Advances in Mathematical Physics

Theory and Applications of Riemannian Submersions

Lead Guest Editor: Meraj Ali Khan
Guest Editors: Mehmet Atçeken and Viqar Azam Khan

Theory and Applications of Riemannian Submersions

Advances in Mathematical Physics

Theory and Applications of Riemannian Submersions

Lead Guest Editor: Meraj Ali Khan
Guest Editors: Mehmet Atçeken and Viqar Azam Khan

Contents

Hindawi
Advances in Mathematical Physics
Volume 2022, Article ID 3232323, 12 pages
https://doi.org/10.1155/2022/3232323

Research Article

A Study of Resolution Improvement in Noncoherent Optical Coherence Imaging

Guoliang Yang,[1] Junhong Su,[1] Yuan Li,[1] Jialin Cai,[1] and Yiren Li[2]

[1]*Optical Engineering, Xi'an Technological University, Xi'an, China*
[2]*Software Engineering, University of Aberdeen, Aberdeen, UK*

Correspondence should be addressed to Junhong Su; sujunhong@xatu.edu.cn

Received 12 April 2022; Revised 10 May 2022; Accepted 17 June 2022; Published 5 July 2022

Academic Editor: Meraj Ali Khan

Noncoherent light, as a common light source in life, can effectively avoid problems such as scattering noise caused by optical components incoherent light imaging, and through the design of the optical path can also trigger interference and holographic imaging of objects, allowing holography to be used in more fields. Various techniques have emerged for recording holograms using incoherent light sources as technology has developed. A recording method has been proposed that exploits the correlation between the object wave information and the Fresnel band sheet to achieve incoherent hologram recording. Using a spatial light modulator (SLM) loaded with a bit-phase mask with multiplexed lens function, the incident light wavefield is phase-modulated to achieve diffraction spectroscopy and phase shifting. And holograms with different phase shifts can be obtained and combined with phase-shifting techniques to eliminate the effects of twin images caused by coaxial holography in the reproduction process. Based on the study of this incoherent holographic imaging system, the influence of the characteristics of the main components of the system and the corresponding parameters on the resolution of the recorded and reproduced holograms is investigated, and optimization methods are given from both theoretical and experimental studies. The empirical analysis of the FINCH imaging system is carried out. The observed optical path is designed, and the method of making a bit-phase mask loaded on a spatial light modulator is presented. The effect of the focal length and recording distance of the dislocation mask on the resolution of the system is investigated by both computer simulation and experimental operation.

1. Introduction

With the continuous progress of science and technology, people's requirements for optical imaging technology and imaging systems have increased. The improvement of imaging resolution has become an essential issue in modern scientific research. The development of holography was greatly facilitated by the advent of the laser in 1960. The highly coherent nature of the laser light source produced excellent interference effects, which significantly improved the quality of holograms. The advent of the laser improved the quality of holography but limited its application.

On the other hand, it has been found under incoherent light source illumination conditions. The emergence of incoherent holography has adapted to the development of holographic imaging, expanding the field of application and freeing it from the requirement of high coherence of light sources. Holographic imaging results from the interference effect between two light beams, which can record the amplitude and phase information of an object in the resulting interference fringe, which is the hologram of the object. According to the principle of reversibility of the optical path, the reproduction process can be seen as a plane wave irradiating the hologram vertically, producing diffraction phenomena to recover the wavefront information of the object's light field. The quality of the reproduced hologram image is affected by the fact that the former is not as effective as the latter compared with the light field interference produced by an object illuminated by a noncoherent light source. Therefore, improving holographic imaging resolution under noncoherent light has become an important research topic.

2. Related Work

2.1. Holographic Display. In conventional imaging techniques, based on the principle of geometrical optics, the image detector can only receive the object's light intensity (i.e., amplitude), and the object's light intensity in three dimensions is superimposed on a flat surface. Holographic imaging is achieved by introducing a reference light that interferes with the light waves reflected or emitted from the object and records interference fringes that correlate the amplitude and phase of the thing. The reproduction process uses the principle of diffraction to recover the wavefront information of the object, and the recorded interference fringe pattern is known as a 'hologram.' It is a two-step imaging technique and an accurate three-dimensional imaging technique.

The Fresnel incoherent correlation holography (FINCH) technique was first proposed by Park and Yu's groups [1, 2] in 2007. The FINCH technique uses a spatial light modulator to diffract and phase shift the incoherent light emitted from an object. Joseph Rosen et al. demonstrated the feasibility and nonscanning nature of this technique.

In addition to Joseph Rosen's group, Czech scientists such as Lavlesh et al. studied the FINCH system's point spread function and resolution [3]. They found that adjusting the optical path increases the interference area of the two beams on the surface of the image detector [4–6] and loading the spatial light modulator with a vortex phase mask improves the contrast at the edges of the object [7]. By enhancing the Michelson interferometric optical path, Rajput's group used two concave mirrors with different curvatures to replace the diffraction spectroscopy effect of the SLM, which is no longer limited by the resolution of the SLM [8–11] reproduction.

2.2. Noncoherent Optical Digital Holographic Imaging Technology. Wang Pan used synthetic aperture imaging technology to improve the resolution of incoherent digital holography [12]. Teruyoshi and Horisaki's group at Jinan University used light-emitting diodes (LEDs) as the illumination source and studied the effect of light source size and diffraction distance on the resolution of hologram reproduction [13] and optimized the quality of phase reconstruction [14]. Teruyoshi et al. from Huazhong University of Science and Technology improved the quality of incoherent light imaging by investigating the imaging system's signal-to-noise ratio and edge contrast [15]. Tatsuki et al. from Zhengzhou University used the FINCH system to perform color holographic imaging of dice, verifying the feasibility of the incoherent light imaging system to record color holograms [16]. Ying et al. investigated the imaging characteristics of the FINCH microscope imaging system by building a reflective incoherent digital holographic microscope imaging system [17]. Changwon's group at Xi'an Institute of Optics and Mechanics studied digital holographic microscopy systems for LED light source illumination and partially coherent light holographic based on point diffraction interferometry [18]. In 2013, Yuhong et al. from South China Normal University conducted a simulation analysis and experimental validation of incoherent digital holography's recording and reproduction process with white light irradiation [19, 20]. In 2007, Yun's group at Beijing University of Technology summarized the characteristics and research progress of incoherent optical holographic imaging [21]. Further improving the resolution of incoherent light holographic imaging is an important aspect to advance the development of this technology [22]. In future practical applications, holographic imaging technology under incoherent light illumination still has an important role and research value in this field.

Although some progress has been made in FINCH imaging technology through the research of Liu Yingchen's group, the existing analysis of noncoherent optical imaging systems is primarily complex and limited to the influence of a specific parameter on the imaging quality, lacking a comprehensive analysis method. Therefore, the thorough analysis of noncoherent optical imaging system parameters is of great importance for optimizing the optical path and improving the imaging system's resolution.

3. Materials and Methods

3.1. Model Design. This experiment uses LED white light with a wide spectral range as the light source to build a Fresnel incoherent correlation imaging system to experimentally investigate the effect of different recording parameters on the resolution. The experimental optical path is shown in Figure 1.

In Figure 1, S is the LED white light source with a central wavelength of about 455 nm and a spectral linewidth of 30 nm. F is the filter with a central wavelength of 450 nm and a spectral linewidth of 20 nm. P is the parallel light tube. O is the target object steel ruler. D is the polarizer (the SLM sensitivity axis's polarization direction). I is the diaphragm. L is the collimated lens ($f = 150$ mm), and BS is the beam splitter. The LCD spatial light modulator used in the experiment is a pure phase reflection type HED-450 manufactured by Holy. With an image plane size of $12.5\,\text{mm} \times 7.1\,\text{mm}$, a resolution of 1920×1080 and an image element size of $6.4\,\mu$m of which the CCD camera model is MVCII-1M, with an image element size of $5.4\,\mu$m and a resolution of 1280×1024, actually using pixels of 800×600. When using MATLAB to produce an SLM-loaded multiplexed Fresnel lens, the two-dimensional grayscale matrix to be generated contains the amount of phase modulation of the focal length of the two lenses. Therefore, the mask is generated so that the two focal length values are each half of the pixels and evenly distributed, in five main steps as follows.

(1) Call the rands function to generate a two-dimensional random matrix

(2) Assigning two focal values randomly to a two-dimensional matrix

(3) The amount of phase modulation corresponding to each point in the matrix is calculated from the expression for the phase distribution

(4) Converts the phase modulation quantities into their corresponding gray values and generates a gray matrix

(5) The image shows a function that generates a grayscale map, i.e., a bit-phase mask

As shown in Figure 2(a), the gray value of each of its pixels represents the amount of phase modulation. When a well-made grayscale is loaded onto the SLM, its gray value will control the voltage across the SLM, deflecting the liquid crystal molecules and thus changing the refractive index. The phase-modulating effect on the light waves is equivalent to coinciding two Fresnel lenses with different focal lengths, as shown in Figure 2(b).

The mean-square error (MSE) method is used to evaluate the image quality, which is calculated by the following formula.

$$\mathrm{MSE} = \frac{1}{MN} \sum_{0 \le i \le N} \sum_{0 \le j \le M} \left(f_{ij} - f'_{ij} \right)^2. \tag{1}$$

The mean square error method calculates the mean square value of the pixel difference between the original image and the j distorted image and determines the distortion of the distorted image by the size of the mean square value,M,f_{ij}; the smaller the mean square error value, the smaller the distortion of the image, and the closer the resolution to the original image. The smaller the RMS error value, the smaller the distortion and the closer the resolution to the original image. A comparison of the mean square error of the reconstructed image and the simulated target at different recording distances are shown in Table 1.

As the recording distance increases, the mean square error value decreases, representing a better image quality, i.e., an increase in resolution. The results are consistent with the results of the subjective evaluation method, which justifies the mean square error method for assessing image quality.

Next, fixing the other parameters constant, the effect on the imaging resolution of the system is investigated by varying the mask focal length. Set the recording distances z_h = 150mm to f_1 = 160mm, f_1 = 200mm, f_1 = 240mm, respectively, and the reconstructed image at its corresponding position is shown in Figure 3.

As shown in Figures 3(a)–3(c), the resolution of the reproduced image decreases as the mask focal length f_1 increases, in line with the theoretical analysis that f_1 increasing leads to a decrease in numerical aperture and a reduction in z_h/f_1 ratio. A comparison of the mean square error of the reconstructed image and the simulated target object when loaded with different mask focal lengths are shown in the following Table 2.

As can be seen from Table 2, the mean square error value of the reproduced image becomes more significant as the focal length of the mask increases, in line with the theoretical analysis.

The experiments also simulated the effect of two different loading modes of the SLM on the imaging quality. The

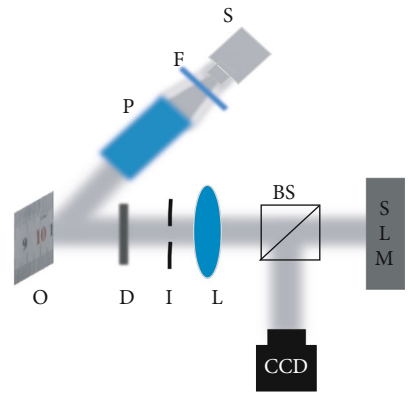

Figure 1: Schematic diagram of the experimental optical path of the FINCH system.

first one loads the SLM with a plane wave and a spherical wave bit-phase mask with a focal distance of f_1 = 145mm, and the second one packs the SLM with two spherical wave bit-phase masks with the mask focal distance set to f_1 = 145mm and f_2 = 155mm. The recording distances for both loading modes are assigned to z_h = 150mm, and the reconstructed images after phase shifting for both loading modes are given in Figure 4.

As shown from Figures 4(a) and 4(b), when the SLM is loaded with planar and spherical wave bit-phase masks, the image background information interferes with the reconstructed image, and the quality of the reproduced image is not as good as when loaded with two spherical wave bit-phase masks. In essence, when the SLM is loaded with only one focal length mask, half of the spatial light modulator pixels can phase modulate. Still, because its fill factor is less than 100%, the light waves incident to the effective pixels will be reflected without modulation. The proportion of the reflected light as reference light is greater than the proportion of the signal light after phase modulation by the SLM, which causes part of the reference light to not participate in the interference. For a mask with two focal lengths, the ratio of the object wave to the reference light is close to 1 : 1, so the contrast of the recorded interference fringe is higher than for a mask loaded with only one focal length, and the resolution of the reconstructed image is relatively better. The mean square error values for comparing the reconstructed image with the simulated target for the two diffraction modes are shown in the following table.

As can be seen from Table 3, the mean square error value of SLM loaded with two spherical wave potential phase masks is smaller than that of the loaded plane and spherical wave likely phase masks, which is in line with the theoretical analysis. Therefore, the imaging quality of loading the two spherical wave phase factors during incoherent optical coherence imaging is more excellent than that of loading the plane and spherical wave phase factors.

Photodetectors cannot directly record the phase information of light waves emitted from an object. They can only sense the light intensity and need to encode the phase information in the intensity information map received by the

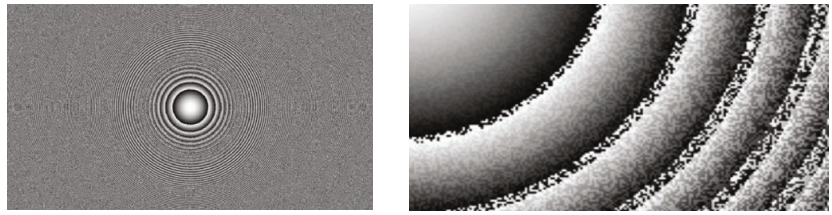

(a) Schematic diagram of the bit-phase mask (b) Enlarged view of part of the bit-phase mask

Figure 2: SLM loaded bit-phase mask.

Table 1: Comparison of reconstruction errors at different recording distances.

	$z_h = 160$mm	$z_h = 200$mm	$z_h = 240$mm
MSE	0.4279	0.3812	0.048

detector and then decode the object light field information through diffraction phenomena. The reproduction process is equivalent to irradiating a hologram vertically with a monochromatic plane wave. The diffraction pattern differs from position to position because of the different shapes of the interference fringes at each place, thus allowing the recording and reproduction of the original object light field distribution. This is analogous to Morse code, where the 26 letters of the alphabet correspond to the length and order of the different electrical pulse response times. The electrical signals are decoded through a previously agreed translation.

The recording process of coherent light digital holographic imaging technology is shown in Figure 5. The object transmitted or emitted light waves carrying the phase and amplitude information of the thing. After a distance to the CCD recording plane, while allowing a beam of light waves with coherence with the object light waves to irradiate the recording plane, the two beams of light waves will interfere, the interference pattern in the form of stripes intensity information recorded by the CCD.

In Figure 5, $O(x, y)$ and $R(x, y)$ denote the object-wave complex amplitude and the reference-wave complex amplitude, respectively, the hologram recorded by the CCD is $I(x, y)$ represented as

$$I(x,y) = |O(x,y) + R(x,y)|^2 = |O(x,y)|^2 + |R(x,y)|^2 + O(x,y)R^*(x,y) + O^*(x,y)R(x,y). \quad (2)$$

In Equation (2), the first term indicates the intensity distribution of the light object field. The second term means the intensity distribution of the reference light wave, which $R(x, y)$ can be taken as a natural constant incoherent light illumination due to better interference. In general, monochromatic plane waves can be used as reference light waves. The third and fourth terms encode the object light wave's complex amplitude and phase information, which can be regarded as the distribution function of the interference fringe.

In digital holography, the holographic dry plate is replaced by an image detector component, a continuously distributed recording medium, whereas the target surface of the image detector is not continuous. For example, in the case of CCDs, the target surface is a combination of many discontinuously distributed pixel units so that the recorded hologram is a discrete intensity distribution.

$$I'(x,y) = I(x,y)\mathrm{rect}\left(\frac{x}{N_x\Delta x}, \frac{y}{N_y\Delta y}\right) \times \sum_{k}^{N_x}\sum_{l}^{N_x}\delta(x - k\Delta x, y - l\Delta y). \quad (3)$$

In formula (3), kl is an integer $(-N_x/2 \le k \le N_x/2 - 1, -N_y/2 \le l \le N_y/2 - 1)$, Δx, Δy are the horizontal and vertical pixel cell size of the CCD, N_x and N_y are the number of horizontal and vertical pixels, respectively, and then, the CCD detection surface width can be expressed as $L_x = N_x\Delta x$ height is $L_y = N_y\Delta y$.

Consider the integration effect of the CCD's pixel cells during sampling.

$$I'(x,y) = I(x,y) * \mathrm{rect}\left(\frac{x}{N_x\Delta x}, \frac{y}{N_y\Delta y}\right)\mathrm{comb}\left(\frac{x}{\Delta x}, \frac{y}{\Delta y}\right)\mathrm{rect} \cdot \left(\frac{x}{N_x\Delta x}, \frac{y}{N_y\Delta y}\right). \quad (4)$$

The symbol "$*$" indicates a convolution operation. It can be seen that a discrete intensity score is stored in a computer in the form of a numerical matrix, which is reproduced through the process and processing of the numerical matrix.

3.2. Recording of Incoherent Digital Holograms. Noncoherent digital holography uses a noncoherent light source, which is very different from coherent digital holographic imaging. Due to the large width of the noncoherent light spectrum and the existence of different wavelengths of light waves, it is difficult to interfere using reference light that is coherent with the object's soft waves. To obtain a hologram of an object under incoherent illumination light, one has to solve the problem of how interference occurs. In incoherent light, digital holography, the thing is composed of many independent point sources, and the light waves emitted between these independent point sources do not satisfy coherence.

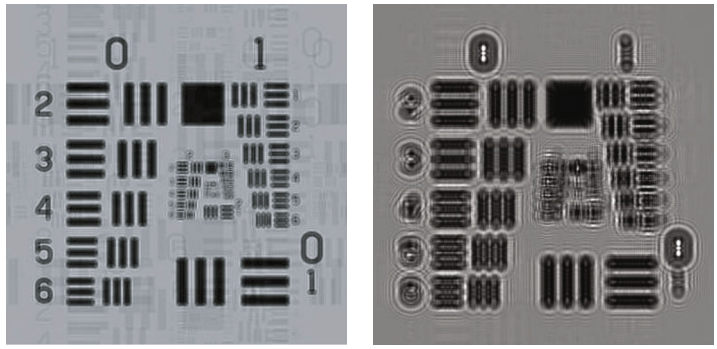

(a) $f_1 = 160$mm (b) $f_1 = 200$mm

(c) $f_1 = 240$mm

Figure 3: SLM simulation of reproduced images loaded with different mask focal lengths.

Table 2: Comparison of reconstruction errors for different mask focal lengths.

	$f_1 = 160$mm	$f_1 = 200$mm	$f_1 = 240$mm
MSE	0.1741	0.3639	0.4102

Still, the light waves emitted from the same point satisfy coherence. According to this property, interference can be triggered to achieve incoherent holographic recording.

Using beam-splitting techniques, the light from each point source is split into two beams, and the optical path is designed so that the two beams converge and interfere to form a point source hologram. In other words, point sources are spatially self-coherent, and incoherent optical coherence imaging takes advantage of this property. A point source hologram can record the amplitude and phase information of the point. By superimposing the holograms of all the independent point sources in a non-coherent manner, all the amplitude and phase information of the object can be recorded. As shown in Figure 6, the recording process of incoherent optical digital holograms can be simply expressed as follows.

Suppose there exists a point $P(x_0, y_0, z_0)$ at a particular position of an object in space, the light wave from this point arrives at the wave splitting plane and is decomposed U_1 into U_2 two light waves by the optical element with separating effect, and they come on the CCD plane when the complex amplitude distribution is expressed as $U_1(x - x_0, y - y_0; z_0)$ and $U_2(x - x_0, y - y_0; z_0)$, U_1 and U_2 satisfy the spatial coherence, and the point source hologram formed on the CCD recording plane expresses the formula as

$$I(x - x_0, y - y_0; z) = |U_1 + U_2|^2 = A_{o1}^2 + A_{o2}^2 + A_{o1}^2 A_{o2}^2 \cos \cdot [\phi_1(x - x_0, y - y_0; z) - \phi_2(x - x_0, y - y_0; z)]. \quad (5)$$

where A_{o1} and A_{o2}, respectively, are the U_1 and U_2 amplitude, representing the intensity information of the point source; ϕ_1 and ϕ_2, respectively, are the U_1 and U_2 phases, carrying the three-dimensional position information of the point source. From the hologram expression, when the complex amplitude U_1 and U_2, the phase part of the difference, that is ϕ_1 and ϕ_2 is not equal, and the phase term is not constant. The intensity distribution associated with the spatial location, the amplitude, and phase information of the point source can be recorded in full. An object can be seen as a combination of many point sources. Assuming that an object has an intensity distribution function $g(x_0, y_0, z_0)$, its incoherent hologram $H(x, y)$ is a noncoherent correlation superimposed on the hologram formed by the object's point interference on the CCD, with the expression

$$H(x, y) = \iiint g(x_0, y_0, z_0) I(x - x_0, y - y_0; z_0) dx_0 dy_0 dz_0. \quad (6)$$

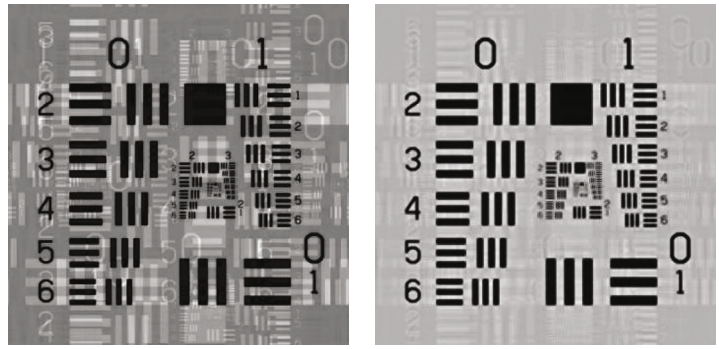

(a) $f_1 = 145\text{mm}$ (b) $f_2 = 155\text{mm}$

Figure 4: Comparison of the resolution of the two diffraction modes.

Table 3: Comparison of reconstruction errors between the two diffraction modes.

	Plane-wave vs. $f_1 = 145\text{mm}$	$f_1 = 145\text{mm} f_2 = 155\text{mm}$
MSE	0.1903	0.0895

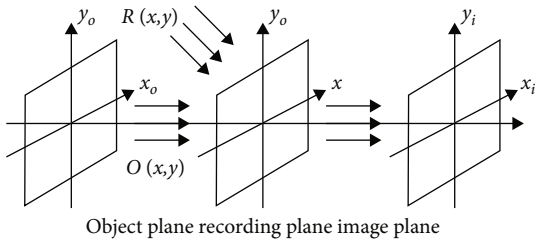

Figure 5: Diagram of the 5 digital holographic recording process.

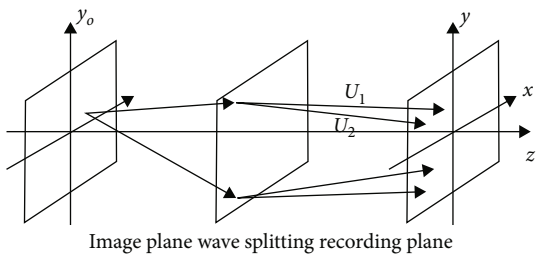

Figure 6: Schematic diagrams of the incoherent digital holographic recording process.

In contrast to the coherently superimposed hologram, the hologram is the intensity distribution of all point sources after superimposing the complex amplitude. In incoherent light, the complex amplitude superimposition is not satisfied, and the hologram is the convolution integral between the intensity distribution of all independent point sources and the point spread function, satisfying the intensity superimposition. In the study of incoherent digital holography, it is necessary to start with the point spread function, which gives a more intuitive view of the imaging system's response to the input light wavefield.

Assuming a CCD detection plane of size $L_x \times L_y$, expressed as a function $\text{rect}(x/L_x, y/L_y)$, the expression for the hologram after discretization is

$$H'(x,y) = H(x,y)\text{rect}\left(\frac{x}{L_x}, \frac{y}{L_y}\right)\text{comb}\left(\frac{x}{\Delta x}, \frac{y}{\Delta y}\right), \quad (7)$$

where $\Delta x \times \Delta y$ is the interval between adjacent pixels of the CCD, and the function $\text{comb}(x/\Delta x, y/\Delta y)$ can be expressed as

$$\text{comb}\left(\frac{x}{\Delta x}, \frac{y}{\Delta y}\right) = \sum_{m}^{M}\sum_{n}^{N}\delta(x - m\Delta x, y - n\Delta y). \quad (8)$$

In Equation (8), M and N indicate the number of pixels of the CCD, m and n take a range of integers $-N/2 \le n \le N/2 - 1$ between $-M/2 \le m \le M/2 - 1$, and the product between $H(x,y)$ and $\text{rect}(x/L_x, y/L_y)$ in expression (7) represents the relationship between the CCD size and the hologram. Multiplying $\text{comb}(x/\Delta x, y/\Delta y)$ by indicates a discrete sampling of the hologram received by the CCD.

Figure 7simulates a comparison of the reconstructed image of the obtained hologram without phase shift and after a three-step phase shift, under identical optical path conditions.

Figure 7(a) shows the diffraction template used in the simulation. When the hologram is not phase-shifted, the reconstructed image in Figures 7(b) and 7(c) is disturbed by the zero-level and conjugate images.

4. Results

4.1. Effect of Nonmonochromatic Light Sources on Interference. From a spectroscopic point of view, any light

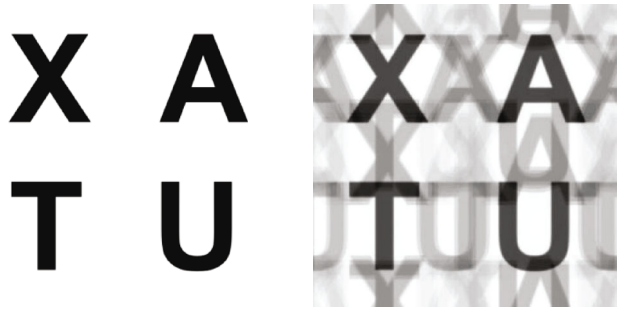

(a) Diffraction template (b) Reconstructed image without phase shift

(c) Reconstructed image after three steps of phase shift

Figure 7: Comparison of reconstructed images without phase shift and after three steps of phase shift.

source has a specific spectral line width, and the spectral linewidth of a noncoherent source is greater than that of a coherent source. Compared to quasimonochromatic light sources, the degree of interference fringe lining captured by the CCD is significantly affected when performing interference experiments. Many wave trains of finite length are emitted from an object illuminated by incoherent light. A point in space is chosen where many trains pass through at a single observation time, with uncertainty in the phase relationship between these trains and each other. For the Fresnel incoherent correlation imaging system studied in this paper, a wave train emitted from any object is modulated by a spatial light modulator into two twin wave trains with different radii of curvature but equal wave train lengths. For a point on the CCD, the two wave trains are divided into two beams after each has passed a certain distance and then combined at the end when the difference between the two wave trains traveled is more significant than the coherence length. The two wave trains are recorded at the exact moment from different incident wave trains; that is, the twin wave trains do not overlap. In a single observation time, many through the wave train on the interference contribution to cancel each other out can not observe stable interference fringes when the difference in the optical range of the two twin wave trains tends to zero. It can be considered that they arrive at the point simultaneously. At this time, they superimpose on each other to produce interference, and stable interference fringes can be observed. This situation is self-coherent.

Spectral lines with $i(\lambda) = dI_\lambda/d\lambda$ spectral density and total optical intensity as the integral of spectral density over the width of the spectral lines:

$$I_0 = \int_0^\infty i(\lambda)d\lambda = \frac{1}{\pi}\int_0^\infty i(k)dk, \tag{9}$$

where $k = 2\pi/\lambda$. The light intensities corresponding to different wavelengths vary with the optical range difference Δl, and the non-coherent superposition of the light intensities at all wavelengths can be expressed as

$$I(\Delta l) = \frac{1}{\pi}\int_0^\infty i(k)[1 + \cos(k\Delta l)]dk = I_0 + \frac{1}{\pi}\int_0^\infty i(k)\cos(k\Delta l)dk. \tag{10}$$

The first term of Equation (10) is constant, and the second term is a quantity related to the optical range difference Δl. For the sake of discussion, the above equation is simplified by considering $i(k)$ that it is equal to a constant $\pi I_0/\Delta k$ in the $k_0 \pm \Delta k/2$ range and 0 in the rest, which can be simplified as follows:

$$I(\Delta l) = I_0\left[1 + \frac{1}{\Delta k}\int_{k_0-\Delta k/2}^{k_0+\Delta k/2}\cos(k\Delta l)dk\right] = I_0\left[1 + \frac{\sin(\Delta k\Delta l/2)}{\Delta k\Delta l/2}\cos(k\Delta l)\right]. \tag{11}$$

The liner ratio of the interference fringe can be derived as

$$V = \left| \frac{\sin(\Delta k \Delta l/2)}{\Delta k \Delta l/2} \right|. \quad (12)$$

The above equation shows that the optical range difference corresponding to an interference fringe with a liner ratio equal to zero is the maximum visual range difference to achieve coherence, and the coherence length can be expressed as

$$\Delta l_{\max} = \frac{2\pi}{\Delta k} = \frac{\lambda^2}{\Delta \lambda}. \quad (13)$$

In a Fresnel, incoherent correlation digital holographic imaging system, the difference in optical range between the two twin wave trains after being split by a spatial light modulator is more significant than the coherence length. This will reduce the quality of the interference fringe or even failure to interfere only when the coherence length is less than that. A clear interference fringe can be recorded on the CCD, and a higher quality reproduction image can be obtained when reconstructing. For nonmonochromatic light sources, the greater the coherence length, the more wave trains will interfere with each other at one point of observation, making the interference fringe clearer. Therefore, when using noncoherent light interference for digital holographic recording, a source with a significant coherence length can be chosen to improve the image quality.

The light source used in this paper is the GCI-060411 type produced by Daheng Optoelectronics. The electrical power is 3 W LED white. The added filter center wavelength is 450 nm, the spectral line bandwidth is about 20 nm and belongs to the visible light band, and the more extensive spectral range is closer to the actual application. The noncoherent light source and spectral diagram are shown in Figures 8(a)–8(d).

As can be seen from Figure 9, the central wavelength of the LED white light source is about 455 nm, and the spectral line width is 30 nm. According to Equation (13) calculation, the coherence length of the light source is about 6.9 μm. After filtering by the filter, the coherence length is approximately 10.1 μm.

To obtain good interference fringes, the maximum optical range difference in the imaging system must be less than 10.1 m. In the FINCH imaging system, the visual range difference of the imaging system is related to the phase mask loaded on the spatial light modulator and the CCD recording position. The imaging system's resolution can be improved by adjusting the focal value of the phase mask and the recording distance to meet the coherence length while determining the light source.

The relationship between the recording distance z_h and the optical range difference of the imaging system is first investigated for a light source with a coherence length of $l_c = 10.1\,\mu$m, assumed $R_0 = 2.5$ mm, 180 mm, 230 mm, and 280 mm, f_1, respectively, and the relationship curve between the optical range difference and the recording distance z_h is given.

The relationship between the recording distance and the optical range difference when the SLM is loaded with three different sets of plane wave and spherical wave bit phase masks is given in Figure 9. The horizontal line is the coherence length of the light source. For the part of the system located below the horizontal line, the optical range difference is less than the coherence length. It satisfies the coherence condition, while the visual range difference for the part above the horizontal line is more significant than the coherence length and does not satisfy the coherence condition.

As can be seen from diagram 10, the maximum optical range difference $\delta_{\max}$ of the system changes proportionally with the recording distance z_h. Keeping the value of the bit phase mask focal length loaded by the SLM unchanged, the optical range difference of the imaging system increases with the distance between the CCD position and the SLM position. Suppose the CCD recording distance continues to grow. In that case, it will cause the CCD to record to the edge of the hologram where the overlap of the two beams will not interfere, reducing the radius of the hologram, and the quality of the reproduced image will be reduced. If the recording distance is kept constant, i.e., the position of the CCD is not moved. The focal length of the mask loaded on the SLM is increased. The curve of the optical range difference will become more inclined, i.e., the visual range difference at this position is reduced, and the coherence condition can be better met. The CCD sampling interval limits the minimum recording distance. The optical range difference is $z_h = 115$ mm less than the coherence length when the SLM is loaded with a bit-phase mask focal length $f_1 = 180$mm, $z_h \le 105$mm. Still, the CCD placed at this position will cause the information sampled to be incomplete, resulting in a decline in imaging quality. According to calculations, only when the SLM is loaded with a mask focal length $f_1 \ge 190$mm that $z_h = 115$mm meets the coherence condition can the CCD record complete information. Therefore, the recording distance is limited in two ways, both by the CCD meeting the sampling interval and by the fact that it cannot be greater than the coherence length.

From the above analysis, it can be seen that the maximum optical range difference of the system is related to the recording position of the CCD, the focal length of the bit-phase mask loaded on the SLM f_1 and the radius R_0 of the modulated spot, fixed $R_0 = 2.5$mm. To study the relationship between the focal length of the front-loaded on the SLM f_1 and the maximum optical range difference,z_h was 130 mm, 150 mm, and 170 mm, respectively. Figure 10 gives the variation curve f_1 of the leading visual range difference $\delta_{\max}$ with the focal length of the loaded mask.

Figure 10 shows that the optical range difference of the imaging system decreases $\delta_{\max}$ as the focal length f_1 of the SLM loading mask increases. Keeping the recording position of the CCD unchanged, and only when the focal length of the mask is f_1 more significant than a specific value will the coherence condition be satisfied at that recording position. At a fixed value of the focal length of the lens loading,

(a) LED white light source

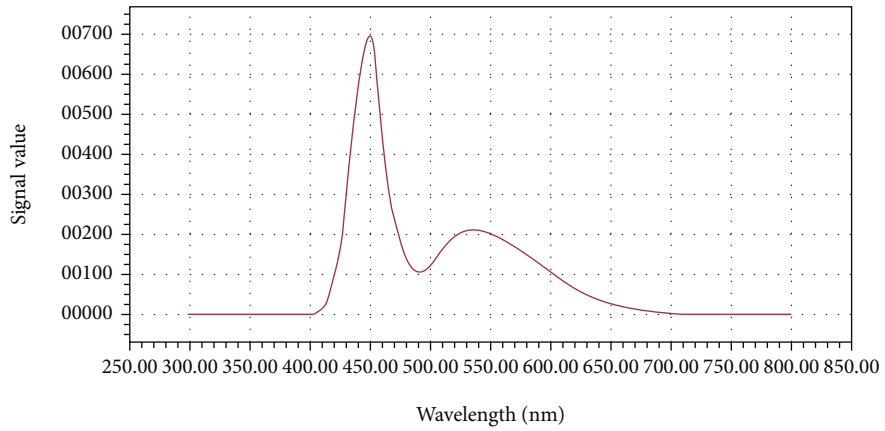

(b) LED white light source spectrum

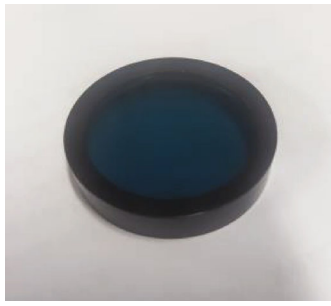

(c) Filter

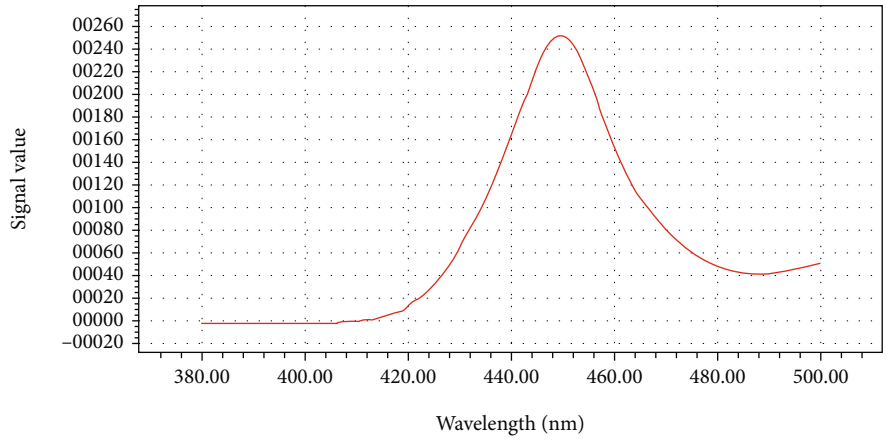

(d) Filtered spectrum of an LED white light source

Figure 8: LED light sources and spectrum.

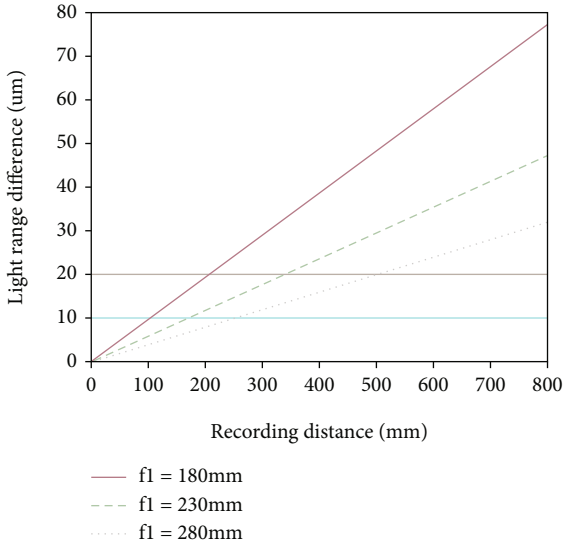

Figure 9: Variation curve of 10 optical range difference δ_{max} with recording distance z_h (plane wave plus spherical wave).

it is to fulfill the coherence condition, but not less than the minimum recording distance limited by the sampling interval.

5. Evaluation

In summary, when the SLM is loaded with planar and spherical waves, the recording distance of the CCD must satisfy both the minimum distance limited by the sampling interval and the requirement that the optical range difference corresponding to the CCD at that position is less than the minimum coherence length. According to Rayleigh's criterion, the resolution of the system increases with z_h/f_1 the increase of the recording distance. When the recording distance is equal to 2 f_1, the solution of the system reaches its maximum. As the recording distance increases, the optical range difference also increases, the z_h/f_1 maximum value being when the visual range difference at that location is precisely equal to the coherence length. With the light source unchanged, i.e., the minimum coherence length is entire. In the case of satisfying the coherence condition z_h, the focal f_1 length of the SLM-loaded mask has to be increased. The

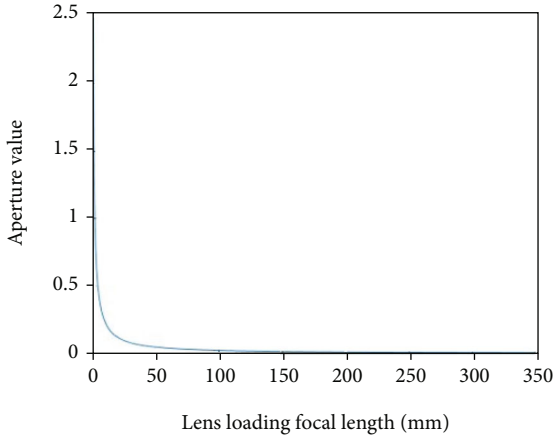

Figure 10: Variation curve of optical 11 range difference $\delta_{\max}$ versus mask focal length f_1 (plane wave plus spherical wave).

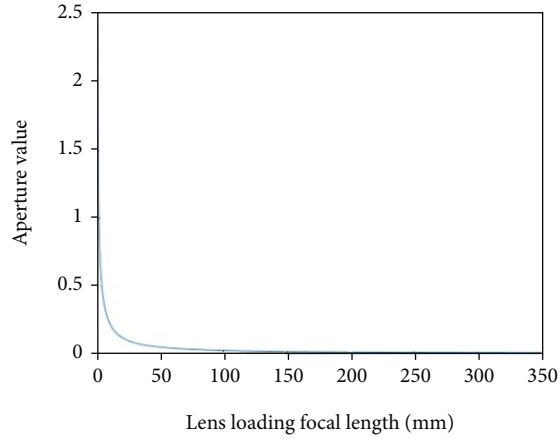

Figure 11: Variation curve of mask focal length f_1 versus numerical aperture.

improvement of the imaging resolution by the ratio change at this z_h/f_1 point is no longer noticeable.

When the recording distance is fixed constant, from the numerical aperture of the imaging system, which directly determines the resolution of the imaging system, NA_{out} the larger the value, the higher the imaging quality, which in this diffraction mode NA_{out} can be expressed as

$$NA_{\text{out}} = \frac{r}{z_r} = \frac{(R_0/f_1)|z_h - f_1|}{|z_h - f_1|} = \frac{R_0}{f_1}. \tag{14}$$

Figure 11 gives the variation of mask focal length f_1 versus numerical aperture.

As can be seen from Figure 11, the system's numerical aperture decreases as f_1 increases, leading to a rapid decrease in resolution and a decrease in z_h/f_1 ratio. At this point, the coherence length of the light source becomes the main factor limiting the key. Assuming that the coherence length of the light source is increased to $l_c = 20\,\mu$m, $R_0 = 2.5$mm, and the mask focal lengths f_1 are set to 180 mm, 230 mm, and 280 mm, respectively; the relationship between the optical range difference and the recording distance z_h is shown in Figure 11.

As shown in Figure 12, the lower horizontal line is $l_c = 10.1\,\mu$m, and the upper horizontal line is $l_c = 20\,\mu$m, $f_1 =$ 230mm. For example, z_h/f_1 is the the maximum value for a coherence length of $l_c = 10.1\,\mu$m, when the coherence condition is met 0.74; z_h/f_1 is approximately 1.46 when the coherence length is increased to $l_c = 20\,\mu$m, which corresponds to an increase in resolution of roughly two times z_h/f_1.

Therefore, $l_c = 10.1$; the resolution can be improved in three ways: (1) When the focal length of the SLM loading mask is constant, the f_1, z_h larger the recording distance, the better, but the maximum difference in the optical range at this position must not be greater than $10.1\,\mu$m. (2) When the recording distance of the CCD is z_h fixed, the smaller the focal length f_1 of the SLM loading mask, the bigger, but the minimum difference in optical range here must not be greater than $10.1\,\mu$m. (3) Non-coherent light illumination

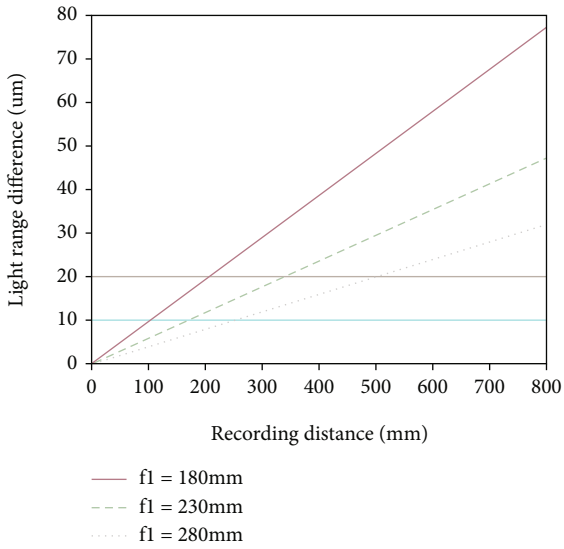

Figure 12: Variation curve of optical range difference $\delta_{\max}$ with recording distance z_h after increasing coherence 13 length (plane wave plus spherical wave).

can change the light source or choose a suitable filter to reduce the spectral line width to improve the minimum coherence length. So that the graph 13 of the horizontal line upward can make in the SLM loaded mask that focal length is f_1 constant. The more considerable recording distance can also meet the minimum coherence length. The recording distance is z_h constant; SLM loaded with a smaller mask focal length can also meet the minimum coherence length. The relative increase z_h/f_1 in the ratio improves the resolution of the imaging system.

6. Conclusion

Holography was first proposed in 1948, and from the beginning, the coherence of the light source limited the imaging resolution. The advent of lasers brought a highly coherent

light source to holography and introduced coherent noise into the optical system. As the technology continued to develop, digital holography emerged as a simple recording and reproduction process but still required lasers as the illumination source. Noncoherent digital holography frees holography from the limitations of light sources. It is based on the principle of spatial self-coherence of point sources, allowing objects to be illuminated by noncoherent light to trigger interference to produce holograms, allowing holography to be applied to a broader range of fields. Noncoherent light imaging based on modulators of spatial light solves the two significant problems of coherence dependence on light sources and twin image overlap. The optical path is simple, and the computer makes the recording reduction. This paper investigates the problem of recording parameters in the FINCH imaging system and finally validates the theoretical analysis through experiments, providing a reference for improving the resolution of incoherent optical coherence imaging.

Data Availability

Data are available upon reasonable request from the corresponding author.

Conflicts of Interest

Author Guoliang Yang has received research support from Xi'an Technological University. The authors declare that no funds, grants, or other support were received during the preparation of this manuscript.

Authors' Contributions

The first draft of the manuscript was written by Guoliang Yang, and all authors commented on previous versions of the manuscript. All authors read and approved the final manuscript.

Acknowledgments

This work is supported by the Shaanxi science and technology plan project-key R & D plan: "development of narrow energy spectrum ion beam emission source" (No.: k20180076).

References

[1] D. Park Samuel, T. Thurman Samuel, R. Lindle James, T. Watnik Abbie, S. Lebow Paul, and A. T. Bratcher, "Singular value decomposition approach to coherent averaging in digital holography," *Journal of the Optical Society of America. A, Optics, Image Science, and Vision*, vol. 37, no. 8, p. 1276, 2020.

[2] N. Yu, S. Xi, X. Wang et al., "Optical implementation of image encryption based on digital holography and computer generated hologram," *Journal of Optics*, vol. 22, no. 7, p. 75702, 2020.

[3] P. Lavlesh, D. Gaurav, and K. Raj, "Effect of displacement in object plane on reconstructed image in lens-based digital holography," *Engineering Research Express*, vol. 3, no. 3, 2021.

[4] Y. He, Z. Xiangchao, W. Feili et al., "Accurate reconstruction for the measurement of tilt surfaces with digital holography," *Optics Communications*, vol. 496, p. 127135, 2021.

[5] P. Matthieu, S. Béatrice, H. Gilles, and P. Pascal, "Theoretical analysis of surface-shape-induced decorrelation noise in multi-wavelength digital holography," *Optics express*, vol. 29, no. 10, pp. 14720–14735, 2021.

[6] A. Betge, H. A. Cura, and E. A. Weitendorf, "Measurement of nuclei content by digital holography in a free surface cavitation tunnel," *Ship Technology Research*, vol. 68, no. 2, pp. 63–69, 2021.

[7] S. Mingguang, D. Pingke, L. Lei, Y. Zhong Zhi, and L. B. Lei, "Single-shot two-wavelength slightly-off-axis flipping digital holography using polarization-splitting modulation," *Optics and Lasers in Engineering*, vol. 143, p. 106629, 2021.

[8] K. Rajput Sudheesh, M. Osamu, T. Yuki et al., "Multimodal sound field imaging using digital holography [invited]," *Applied Optics*, vol. 60, no. 10, pp. B49–B58, 2021.

[9] X. Peng, R. Shien, I. Tomoyoshi, A. Yasuhiro, and M. Osamu, "Dynamic phase measurement of a transparent object by parallel phase-shifting digital holography with dual polarization imaging cameras," *Optics and Lasers in Engineering*, vol. 141, p. 106583, 2021.

[10] L. Adrien, M. A. Al, N. M. Chau, C. Rémi, P. Jérôme, and T. Gilles, "Quantitative temperature measurements in gold nanorods using digital holography," *Acs Applied Materials & Amp; Interfaces*, vol. 13, no. 8, pp. 10313–10320, 2021.

[11] G. B. Karthik, R. S. D. V. S. Jagannadha, and R. K. Divakar, "Novel defocus hologram aberration compensation method in digital holography integrated pathology microscope for label free 3-D imaging," *Optics and Lasers in Engineering*, vol. 140, p. 106514, 2021.

[12] H. Takayuki, T. Tatsuki, I. Yasuyuki, O. Ryutaro, and I. Tomoyoshi, "Multiwavelength-multiplexed phase-shifting incoherent color digital holography," *Optics Express*, vol. 28, no. 7, p. 28(7), 2020.

[13] N. Teruyoshi, K. Yutaro, M. Tetsuhiko, K. Nobuhiro, and I. Norihiko, "Sampling requirements and adaptive spatial averaging for incoherent digital holography," *Optics Express*, vol. 27, no. 23, pp. 33634–33651, 2019.

[14] R. Horisaki, K. Fujii, and J. Tanida, "Single-shot and lensless complex-amplitude imaging with incoherent light based on machine learning," *Optical Review*, vol. 25, no. 5, pp. 593–597, 2018.

[15] N. Teruyoshi, M. Tetsuhiko, K. Yutaro, K. Nobuhiro, and I. Norihiko, "Single-shot phase-shifting incoherent digital holography with multiplexed checkerboard phase gratings," *Optics Letters*, vol. 43, no. 8, p. 1698, 2018.

[16] T. Tatsuki, Q. Xiangyu, O. Reo, T. Yasuhiro, and M. Osamu, "Digital holography and its multidimensional imaging applications: a review," *Microscopy (Oxford, England)*, vol. 67, no. 2, pp. 55–67, 2018.

[17] H. Ying, W. Yuhong, W. Zhou Hongqiang, and M. T. Fan, Eds., *Imaging characteristics of self-interference digital holography with structured illumination*, Beijing Univ. of Technology (China); Univ. Laval (Canada); Beijing Univ. of Posts and Telecommunications (China); Shanghai Institute of Optics and Fine Mechanics (China), 2016.

[18] J. Changwon, C. Clark David, K. Jonghyun, B. Lee, and K. Kim Myung, "Signal enhanced holographic fluorescence microscopy with guide-star reconstruction," *Biomedical Optics Express*, vol. 7, no. 4, p. 1271, 2016.

[19] L. Tatiana, "Iterative phase retrieval for digital holography: tutorial: publisher's note," *Journal of the Optical Society of America. A, Optics, Image Science, and Vision*, vol. 37, no. 1, p. 45, 2020.

[20] W. Yuhong, M. Tianlong, and T. Shiquan, "Optics and optics-based technologies education with the benefit of Lab VIEW," *Beijing Univ. of Technology (China)*, vol. 9793, 2015.

[21] P. Yun, W. Kaifu, and G. Guoqing, "Research and application of dual-camera dynamic in-line digital holography using a two-step phase-shifting cepstrum technique," *Applied Optics*, vol. 59, no. 10, p. 3187, 2020.

[22] R. Li, Y. Gao, and L. Cao, "In situ calibration for a phase-only spatial light modulator based on digital holography," *Optical Engineering*, vol. 59, no. 5, 2020.

Hindawi
Advances in Mathematical Physics
Volume 2022, Article ID 3909552, 15 pages
https://doi.org/10.1155/2022/3909552

Research Article

Mathematical Physics Modelling and Prediction of Oil Spill Trajectory for a Catenary Anchor Leg Mooring (CALM) System

Xuanze Ju,[1,2] **Zili Li**,[1] **Baohui Dong**,[2] **Xianwu Meng**,[2] **and Shuguang Huang**[2]

[1]*College of Pipeline and Civil Engineering, China University of Petroleum (East China)/Shandong Key Laboratory of Oil & Gas Storage and Transportation Safety, Qingdao 266580, China*
[2]*Offshore Oil Engineering Co., Ltd., Engineering Company, Tianjin 300451, China*

Correspondence should be addressed to Xuanze Ju; juxz@cnooc.com.cn

Received 15 April 2022; Revised 11 May 2022; Accepted 19 May 2022; Published 3 June 2022

Academic Editor: Meraj Ali Khan

The catenary anchor leg mooring (CALM) system usually moored a heavy oil tanker; due to its complex working mechanism and special working environment, oil spill accidents are easy to happen. Once the oil spill accident happens, it not only causes huge economic loss, but also kills the marine ecological environment. Oil spill trajectory model considers almost all weathering processes including evaporation, emulsification, dispersion, dissolution, photooxidation, sedimentation, and biodegradation. Model simulations indicated that both tidal currents and wind drag force have significant effect in oil spill movement. The dominant wind in the area is South-westerly wind during the summer monsoon and North-easterly wind during the winter monsoon, but South-westerly wind is far stronger and last longer than the North-easterly wind. As a result, oil spill trajectory is most likely towards offshore to North-east during the summer period (April to September). During the winter period (November–January), oil spill would move towards shore under North-westerly winds. Once oil reaches shore, it would stay at shore permanently and eventually sink to seabed or beach in the simulation. Although the model does not consider longshore drift by waves, oil movement along shore by waves would be a slow process. Therefore, the impact of oil spill during the winter monsoon would be limited to local area around Ras Markaz.

1. Introduction

The transport of petroleum products to export destinations is conducted either by pipeline or in oil terminals. Onshore and offshore terminals are the common types of oil terminals. However, due to geographical and economic conditions, the number of ports available for the construction of oil terminals is limited, resulting in the increase of secondary transport costs, the detention of oil tankers arriving at a port, and other issues. Therefore, it is necessary to study other types of offshore oil loading/offloading facilities to cooperate with or replace oil terminals. The most common type of offshore terminal is the single point mooring (SPM) of catenary anchor leg mooring (CALM) type. A typical schematic for the CALM system is shown in Figure 1 [1]. Since the CALM system was introduced in 1958 [2], it has operated 85% of the world's 700 oil terminals [3, 4], with extensive operations in Southeast Asia, the Middle East, and West Africa. In particular, deepwater offloading CALM buoys are being extensively used in West Africa to allow the efficient loading of spread-moored FPSO [5], and the maximum applied water depth has reached 1435 meters (Agbami oil field, Nigeria) [6]. But for the CALM system, due to its complex working mechanism and special working environment, oil spill accidents are easy to happen [7]. Once the oil spill accident happens, it not only causes huge economic loss, but also kills the Marine ecological environment.

Oil spills have been occurring at sea with increasing frequency, pose significant threats to the marine environment, and often lead to devastating effects on local marine ecology

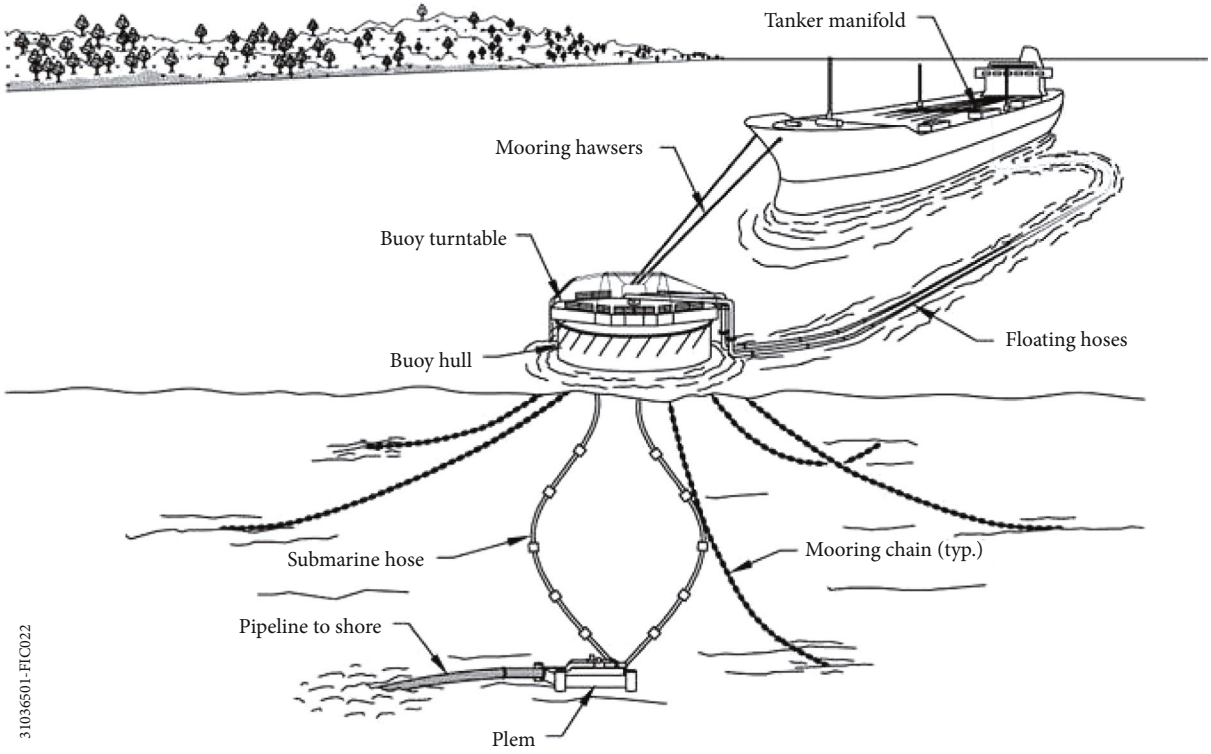

Figure 1: Schematic of a typical catenary anchor leg mooring (CALM) system.

[8]. Numerical modeling has become an important tool for oil spill forecasting, which allows for real time effective clean-up operations immediately after the occurrence of oil spill accidents. Thus, recent years have seen a rapid development of various mathematical models for simulating and predicting oil spills. However, the movement and variation of oil spill in the sea is a complex process, which is influenced by physical, chemical, and biological processes, and is related to the marine hydrodynamic conditions, meteorological conditions, and the oil properties. The processes include oil film expansion, drift, evaporation, emulsification, dissolution, sedimentation, and adsorption. The study on oil spills began in the 1960s. Up to now, many scholars in the world have established and perfected lots of oil spill models. These may include advection, turbulent diffusion, evaporation, dissolution, emulsification, dispersion, auto-oxidation, biodegradation, and sinking/sedimentation [9]. In the last five and six decades, many researchers have studied the processes of oil spills, and various oil spill models have been proposed [10]. Fay [11] divided the oil film expansion into three stages: inertial expansion, viscous expansion, and surface tension expansion, but did not consider the influence of wind on horizontal diffusion. Lehr [12] considered the influence of wind and established a modified Fay-type spreading equation. Elliott [13] proposed the oil particle method for the first time, which regards the oil spill as a large number of oil particles and does not need to solve the diffusion equation. More and more oil spill models begin to use the Lagrange oil particle algorithm, which has become the mainstream method of oil spill trajectory prediction. Chao et al. [14] established two-dimensional and three-dimensional oil spill models in Singapore coastal waters using an oil particle algorithm. Wang et al. [15] established a double-layer oil particle model. Sebastião and Guedes Soares [16] introduced a method to determine the uncertainties in the predictions of oil spill trajectories using a classic oil spill model. The method considers the output of the oil spill model as a function of random variables, which are the input parameters, and calculates the standard deviation of the output results which provides a measure of the uncertainty of the model as a result of the uncertainties of the input parameters. Vethamony et al. [17] presented an oil spill occurred off Goa, west coast of India, on 23 March 2005 due to collision of two vessels. The MIKE21 Spill Analysis model was used to simulate the spill trajectory. The observed spill trajectory and the slick area were in agreement with the model simulations. Díaz et al. [18] used the probabilistic particle tracking model to simulate the oil diffusion after the oil spill from the Prestige wreckage in Galicia. Guo and Wang [19] based on an oil particle algorithm, combined with the 3-D free-surface hydrodynamics model and the third-generation wave model, simulated the oil release in Dalian coastal waters. Mariano et al. [20] developed two oil particle trajectory prediction systems and applied them to the 2010 Deepwater Horizon oil spill in the Gulf of Mexico. Yu et al. [21] proposed a random walk parameterization hindcast method (RWPHM) for the Bohai Sea, in which random walk is initially parameterized and combined with remote sensing data and oil-spill models. Perianez [22] established a Lagrangian oil spill transport model for the

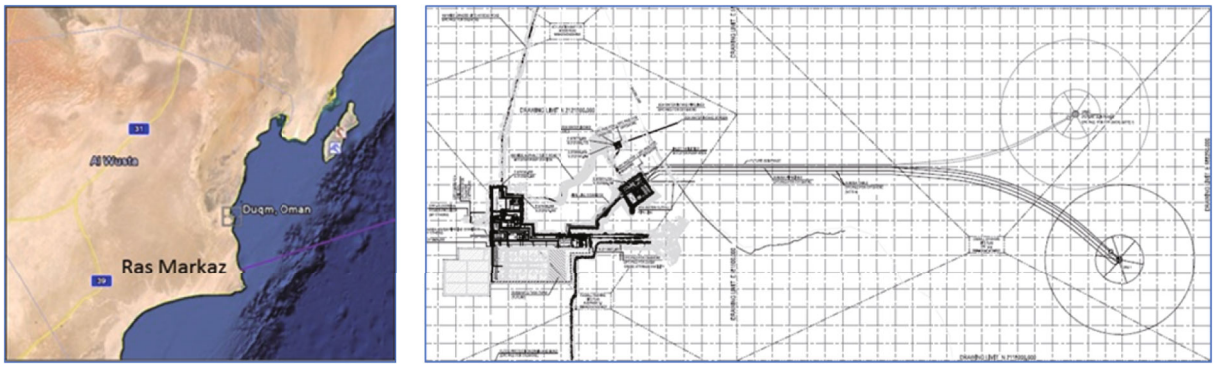

Figure 2: Location of Ras Markaz Crude Oil Park.

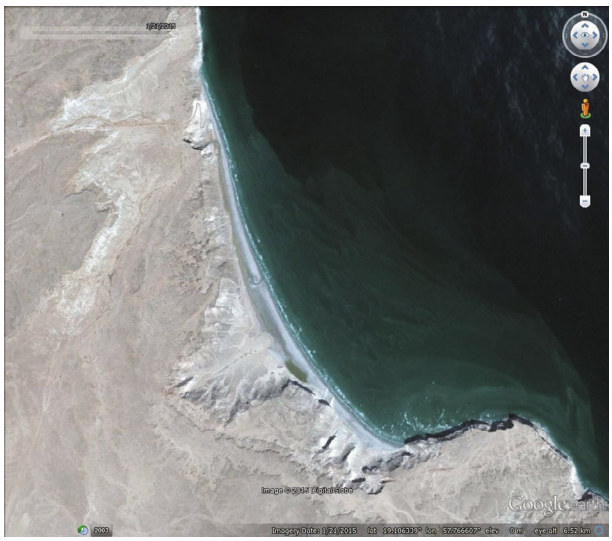

Figure 3: Plan shape of Ras Markaz crenulated bay.

Figure 4: View of the crenulated bay from the northern headland (Ras Markaz is in the background).

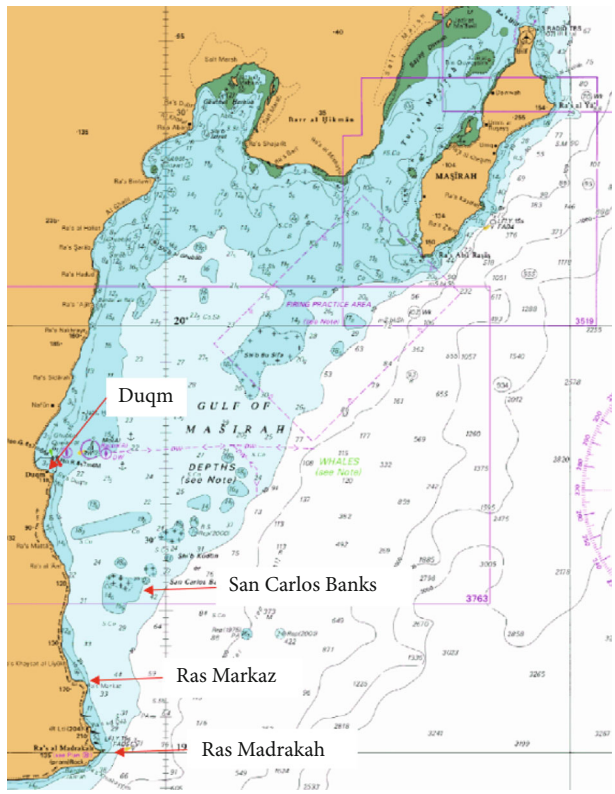

Figure 5: Gulf of Masirah.

Red Sea. The weathering process includes evaporation, emulsification, natural dispersion, dissolution, photooxidation, sedimentation, adhesion to materials, interaction with mineral fines, biodegradation, and the formation of tarballs [23]. Mohamed et al. [24] presented the oil is introduced to the marine environment; it undergoes a series of natural processes known as "weathering." For a successful response operations and protection, it is critical to precisely estimate the behavior of the spilled oil. Debra and William [25] adapted the Fractions Skill Score method, commonly used in weather forecasting, to oil forecasting. A subset of satellite images and trajectory forecasts from the Deepwater Horizon oil spill are used as an example of the method. Pan et al. [26] demonstrated an operational oil spill forecasting system established by National Marine Environmental Forecasting Center (NMEFC). Satellite observations, oil spill models, and operational met-oceanographic forecasts are integrated into the system. Until now, many researchers have

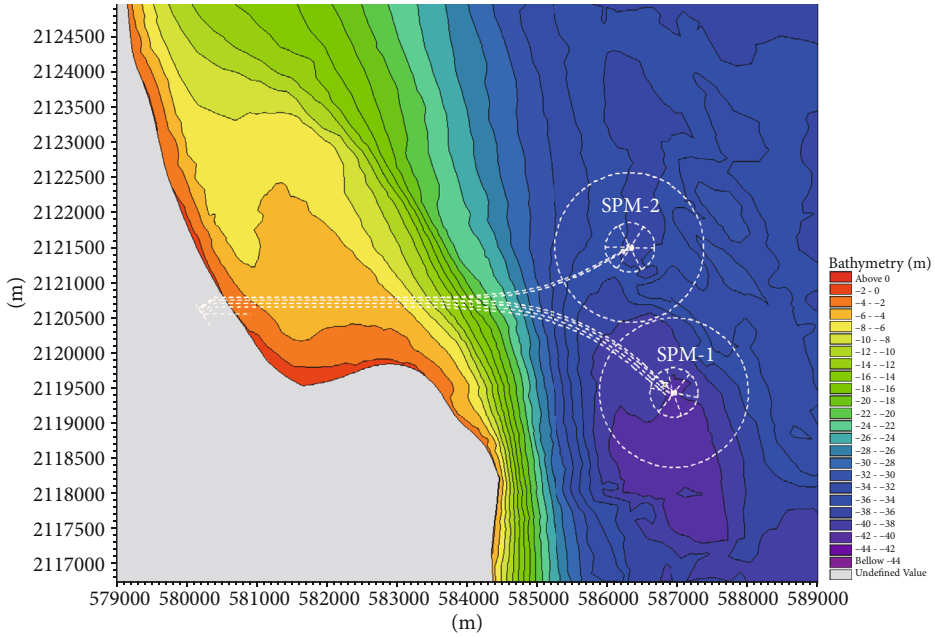

Figure 6: Nearshore bathymetry of Ras Markaz crenulated bay.

investigated the weathering process of the oil spill [27–29], in which empirical formula based on laboratory test is the most commonly used method to calculate oil spill weathering [30]. At present, some of the most widely used oil spill models that can predict the process of oil spill transportation and fate are as follows: Oil Spill Risk Analysis (OSRA), OILTRANS, Oil Modeling Application Package (OILMAP), General National Oceanic and Atmospheric Administration Operational Oil Modeling Environment (GNOME), Oil Spill Contingency and Response (OSCAR), MEDSLIK-II, Estuarine Oil Spill Model (EOSM), and MIKE21 SA model [31–37].

This study presents the oil spill trajectory modelling completed for the planning and design of the Crude Oil Storage Terminal at Ras Markaz on the eastern Arabian Sea coast. The location of the site and layout of the marine facilities, which include two SPMs of CALM type and associated pipelines, are shown in Figure 2. The purpose of the modelling is to investigate the trajectory and fate of potential oil spills through dispersion under the action of the tides, currents, and winds.

2. Site Conditions

2.1. Geological and Geomorphological Setting. The Ras Markaz site is located at the southern end of a large shallow bay extending from Ras Madrakah in the south to Masirah Island in the north. There is a northerly movement of sediment through this large bay driven by wave conditions in the monsoon season. This results in the accretion of sediment at the northern extremity of the bay to the west of Masirah Island and within the channel between the island and the mainland. At Ras Markaz, the oil pipeline trench is located at the southern end of a shallow crenulated bay created by differential erosion between Ras Markaz headland in the south and a less prominent headland in the north (Figure 3). The headland cliffs are composed of layered carbonate rocks (Figure 4).

2.2. Bathymetry and Locations of Oil Pipelines & SPMs of CALM Type. The large bay extending from Ras Madrakah up to Masirah Island has a wide and shallow bathymetry with depths depth generally less than 30 m. This bathymetry is illustrated in Figure 5. The nearshore bathymetry of the smaller bay at Ras Markaz can be broken down into three zones (Figure 6). At the Ras Markaz headland, the bathymetry is steep with the 10 m contour approximately 500 m from the coastline. For most of the crenulated bay, the nearshore gradients are significantly shallower with the 10 m contour that is approximately 2.5 km from the coast. In the southern half of the bay, the nearshore contains a shallow "plateau" at around 3–6 m water depth with steeper slopes inland and seaward of it. This might indicate a significant build-up of sand in these areas, forming a wide nearshore bar. It is likely that sediment transported north has migrated around Ras Markaz headland and into the crenulated bay where the sand bar has formed. There may also be a contribution of sediment from the local Wadi. In the north of the Ras Markaz bay, there is a shallow area, San Carlos Banks (see Figure 5). This shallow water has been identified as a potential risk area of vessel grounding and has been selected for this oil spill trajectory modelling. The oil pipelines and SPM are located to the south of the bay (Figure 6).

2.3. Physical Processes

2.3.1. Wind Climate. The wind climate along the coast between Ras Madrakah and Masirah Island is dominated

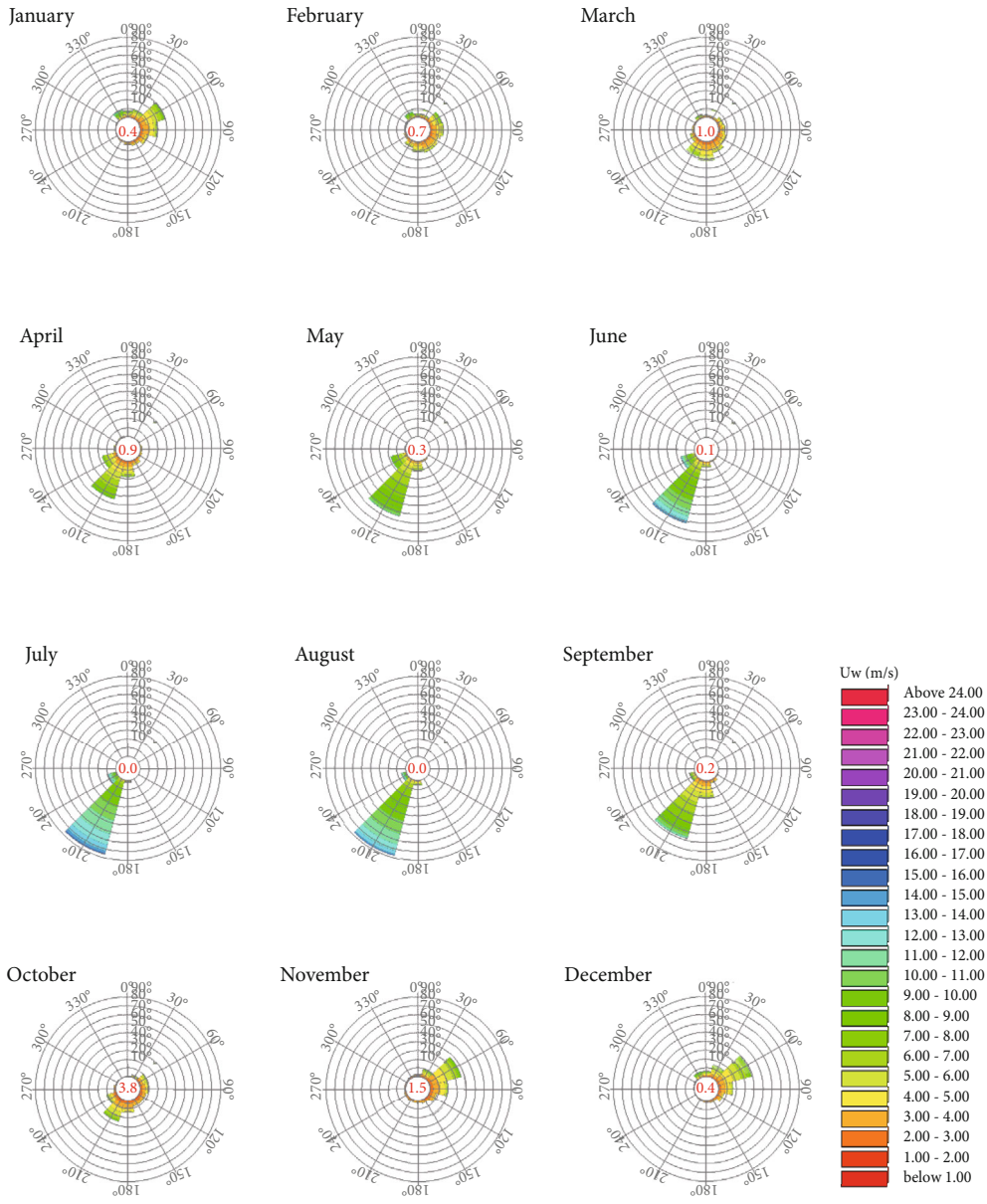

Figure 7: Wind roses (hindcasted wind data from Oceanweather).

Table 1: Wind frequency (hindcasted wind data from Oceanweather).

Wind speed (m/s)	0°N	30°N	60°N	90°N	120°N	150°N	180°N	210°N	240°N	270°N	300°N	330°N	Total
0–3	0.57%	0.74%	1.20%	1.52%	1.64%	1.63%	1.62%	1.40%	0.89%	0.48%	0.40%	0.41%	12.5%
3–5	0.71%	1.41%	5.05%	4.90%	3.06%	2.96%	5.17%	4.83%	1.68%	0.42%	0.35%	0.52%	31.1%
5–7	0.64%	1.07%	4.06%	1.29%	0.39%	0.57%	2.84%	8.77%	2.07%	0.15%	0.13%	0.67%	22.7%
7–9	0.31%	0.49%	1.22%	0.12%	0.02%	0.03%	0.48%	9.70%	1.66%	0.01%	0.02%	0.68%	14.7%
9–11	0.09%	0.09%	0.15%	0.01%	0.00%	0.01%	0.03%	8.30%	1.13%	0.00%	0.01%	0.48%	10.3%
11–13	0.01%	0.01%	0.02%	0.00%	0.00%	0.00%	0.00%	5.56%	0.72%	0.00%	0.00%	0.12%	6.5%
13–15	0.01%	0.01%	0.00%	0.00%	0.00%	0.00%	0.00%	1.92%	0.32%	0.00%	0.00%	0.01%	2.3%
Total	2.45%	3.8%	11.7%	7.8%	5.1%	5.2%	10.1%	40.5%	8.5%	1.2%	0.9%	2.9%	100%

by the two monsoon seasons. In the summer monsoon (April–September), the prevailing conditions are from south-west. Outside this season, the wave climate is more moderate with prevailing winds from the north-east. Figure 7 illustrates monthly and annual wind roses in offshore based on hindcasted wind data provided by

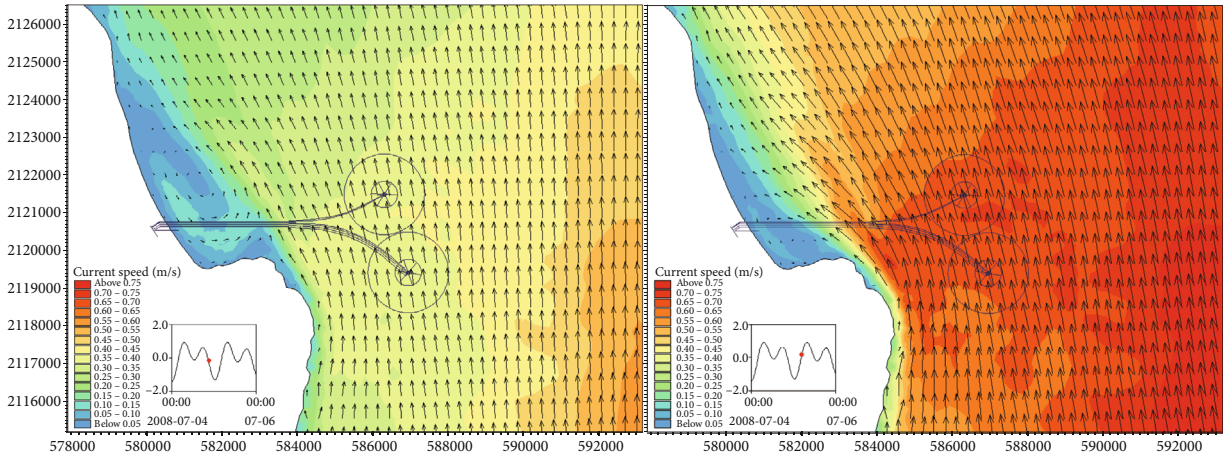

Figure 8: Depth-averaged current velocity during spring tide of the summer monsoon (left: ebb and right: flood tides).

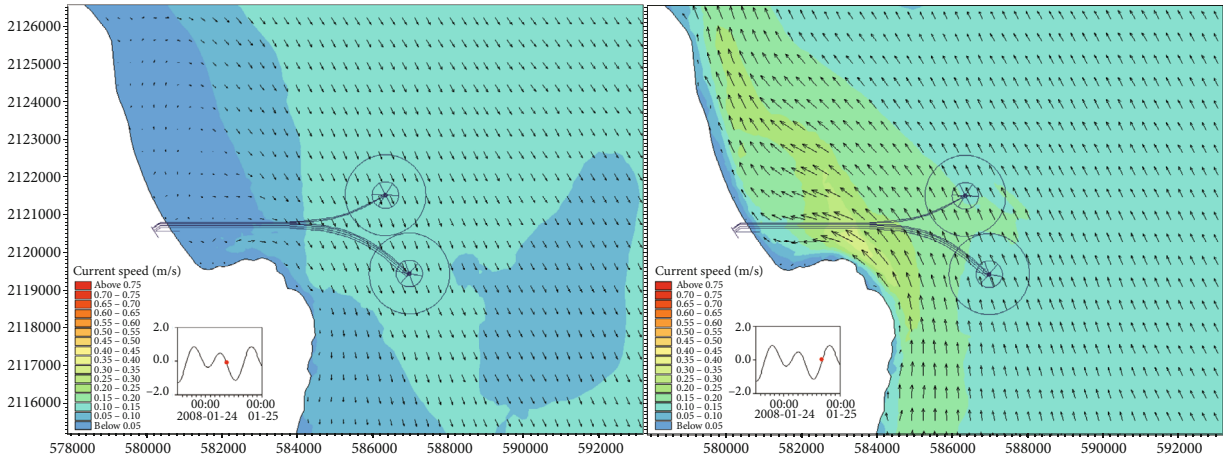

Figure 9: Depth-averaged current velocity during spring tide of the winter monsoon (left: ebb and right: flood tides).

Oceanweather. Table 1 presents the offshore wind data in wind frequency.

2.3.2. Tidal Range. Local tides are mixed semi-diurnal. The range at the Ras Markaz site is approximately 1.5 m (between mean higher high water and mean lower low water) with highest and lowest astronomical tide at +2.54 m CD and +0.14 m CD, respectively.

2.3.3. Tidal Currents. Currents at the site are broadly aligned with the coastline. Flows in a north/north-westerly direction dominate during the summer monsoon season. Outside this season, flows are generally in south easterly direction. Currents are stronger during the monsoon season with flows up 0.5 m/sec at SPM1. The 1 in 1 year current at this location is 1 m/sec driven by strong winds associated with the storm event.

Figures 8 and 9 illustrate modelled peak ebb and flood tidal currents in the area during the summer and winter monsoons, respectively. They show that tidal current velocities (depth-averaged) close to shore are low (less than 0.05 m/s to 0.35 m/s locally) increasing further offshore (greater than 0.5 m/s).

3. Methodology

3.1. Governing Equations of Tidal Current Motion

3.1.1. Continuity Equation.

$$\frac{\partial \zeta}{\partial t} + \frac{\partial[(h+\zeta)u]}{\partial x} + \frac{\partial[(h+\zeta)v]}{\partial y} = 0. \tag{1}$$

3.1.2. Momentum Equation.

$$\frac{\partial u}{\partial t} + u\frac{\partial u}{\partial x} + v\frac{\partial u}{\partial y} - fv = -g\frac{\partial \zeta}{\partial x} + \frac{\partial}{\partial x}\left(N_x\frac{\partial u}{\partial x}\right) + \frac{\partial}{\partial y}\left(N_y\frac{\partial u}{\partial y}\right) - f_b\frac{\sqrt{u^2+v^2}}{h+\zeta}u,$$

$$\frac{\partial v}{\partial t} + u\frac{\partial v}{\partial x} + v\frac{\partial v}{\partial y} + fu = -g\frac{\partial \zeta}{\partial y} + \frac{\partial}{\partial x}\left(N_x\frac{\partial v}{\partial x}\right) + \frac{\partial}{\partial y}\left(N_y\frac{\partial v}{\partial y}\right) - f_b\frac{\sqrt{u^2+v^2}}{h+\zeta}v. \quad (2)$$

where ζ is tide level (relative to a datum level); T is time; x and y are cartesian coordinates; u, v is the flow velocity in x and y directions; h is water depth (relative to a datum level); N_x and N_y are turbulence viscosity coefficients in x and y directions; f is Coriolis parameter; g is the acceleration of gravity; and f_b is the friction coefficient at the bottom.

3.2. Spatial Discrete Calculation of the Model. For shallow water equations in the Cartesian coordinate system, *CFL* can be defined as

$$CFL_{HD} = \left(\sqrt{gh} + |u|\right)\frac{\Delta t}{\Delta x} + \left(\sqrt{gh} + |v|\right)\frac{\Delta t}{\Delta y}, \quad (3)$$

where CFL_{HD} is the Courant–Friedrichs–Lewy condition in the hydrodynamic module, h is the total water depth, u and v are the velocity component in x and y direction, Δx and Δy are the characteristic distance in x and y direction, Δt is the time interval, and g is the gravitational acceleration.

3.3. Oil Spill Trajectory Model

3.3.1. Expansion Process. Take the below equation:

$$\frac{dA_o}{dt} = K_a \bullet A_o^{1/3} \bullet \left[\frac{V_o}{A_o}\right]^{4/3}, \quad (4)$$

where A_o is the oil film area, $A_o = \pi R_o^2$, R_o is oil film diameter, t is time, K_a is diffusion coefficient; $V_o = R_o^2 \pi h$, and h is the initial oil film thickness.

3.3.2. Transport Process

(i) Drift motion

$$U_t = C_w \bullet U_w + U_s. \quad (5)$$

In Δt time, the position change equation of oil particles is

$$X = X_0 + u\Delta t + C_\omega U_\omega \sin\theta\Delta t, \quad Y = Y_0 + v\Delta t + C_\omega U_\omega \cos\theta\Delta t. \quad (6)$$

where X_0 and Y_0 are the initial position of the oil film; U_t is the total drift velocity; U_s is the surface flow velocity; u and v are the current velocity; U_ω is the wind speed (10 m above the sea surface); θ is the wind direction angle; and C_ω is the wind drift coefficient, usually 0.03-0.04.

(ii) Turbulent diffusion

$$S_a = [R]_{-1}^{+1} \bullet \sqrt{6D_a\Delta t}, \quad (7)$$

where S_a is the random walking distance in the a direction within a time step, D_a is the diffusion coefficient in the a direction, t is the diffusion time, and $[R]_{-1}^{+1}$ is the random number from -1 to 1.

3.3.3. Weathering Process. Oil spill model considers almost all weathering processes including evaporation, emulsification, dispersion, dissolution, photooxidation, sedimentation, and biodegradation (see Figure 10).

(i) Evaporation

$$\frac{dQ}{dt} = \frac{K_2 P A_o}{RT} \bullet f \bullet M, \quad K_2 = k \bullet A_o^{0.045} \cdot S_c^{(-2/3)} \cdot U_w^{0.78}, \quad (8)$$

where dQ/dt is the evaporation rate; K_2 is the mass transfer coefficient (k is the evaporation coefficient, S_c is the Schmidt number, and U_w is the wind speed), P is vapor pressure, A_o is the oil film area, f is the evaporation fraction, and R is the constant

(ii) Emulsification

$$Y_w = \frac{K_A\left(1 - e^{-K_A K_B (1+U_w)^2 t}\right)}{K_B}, \quad (9)$$

where Y_w is the moisture content of the emulsion, $K_A = 4.5 \times 10^{-6}$, $K_B = 1/Y_w$, and Y_w is the final moisture content

(iii) Dispersion

$$Q_d = CD^{0.57} S F d^{0.7} \Delta d, \quad (10)$$

where C is the encoder coefficient, D is the wave energy dissipation, S is the fraction of sea surface covered by oil, F is the fraction covered by broken wave, d is the average diameter of oil droplets, and Δd is the size interval of oil droplets

(iv) Dissolution

$$D_v = K_1 \bullet A \bullet \frac{M_v}{M_t} \bullet \rho_1 \bullet f_D \bullet C_V, \quad D_h = K_2 \bullet A \bullet \frac{M_h}{M_t} \bullet \rho_2 \bullet f_D \bullet C_h, \quad (11)$$

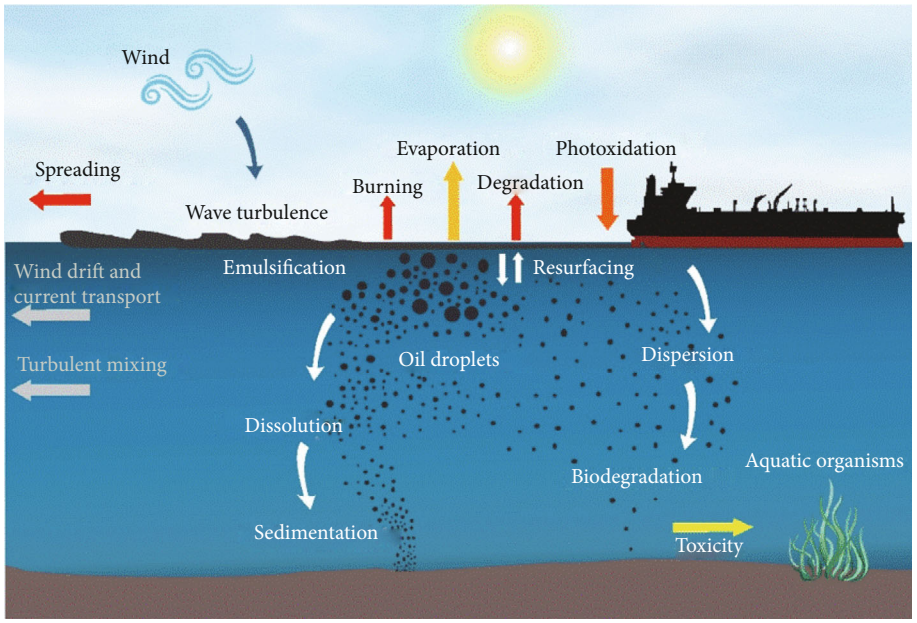

Figure 10: Weathering processes of oil in marine environmental in open water.

Table 2: Model setup main parameters.

Parameters	Settings
Time step (s)	30
Simulation time after oil release (days)	60
Number of vertical layers	8
Horizontal dispersion coefficients (m^2/s)	20 in the area around the site where fine mesh is applied; 200 in other areas where coarse mesh is applied
Vertical dispersion coefficients (m^2/s)	0.01
Number of oil particles release (each run)	720
Oil property	4 fractions of oil (volatile oil, heavy oil, asphaltene and wax) are related to Guafita crude oil)
Spreading (terminal thickness) (m)	0.0001
Biodegradation (decay rate in per day)	Volatile fraction: 0.005 Heavy fraction: 0.0
Emulsification	Maximum water fraction: 0.85 Kao constant: 3.3 Kaw constant: 200 Emulsion rate: 2.0 × 10-6 s/m^3
Water solubility (kg/kg)	Volatire fraction: 2.0×10^{-5} Heavy fraction: 2.0×10^{-7}
Volumentric temperature (1/°C)	Volatire fraction: 0.0007 Heavy fraction: 0.0007
Dissolution (per day)	0.4

where K_1 and K_2 are the volatilization and recombination fraction; M_v and M_h are the volatilization and recombination fraction mass, respectively; M_t is the total mass of oil particles; ρ_1 and ρ_2 are the volatilization and recombination fraction density, respectively; A is the oil film area, f_D is the chemical dispersant effect; and C_V and C_h are the volatilization and recombination fraction water solubility, respectively

3.3.4. Heat Transfer Process

(i) Heat transfer between oil film and air can be expressed as

$$H_T^{\text{oil-air}} = A_{\text{oil}} k_H^{\text{oil-air}} (T_{\text{air}} - T_{\text{oil}}),$$

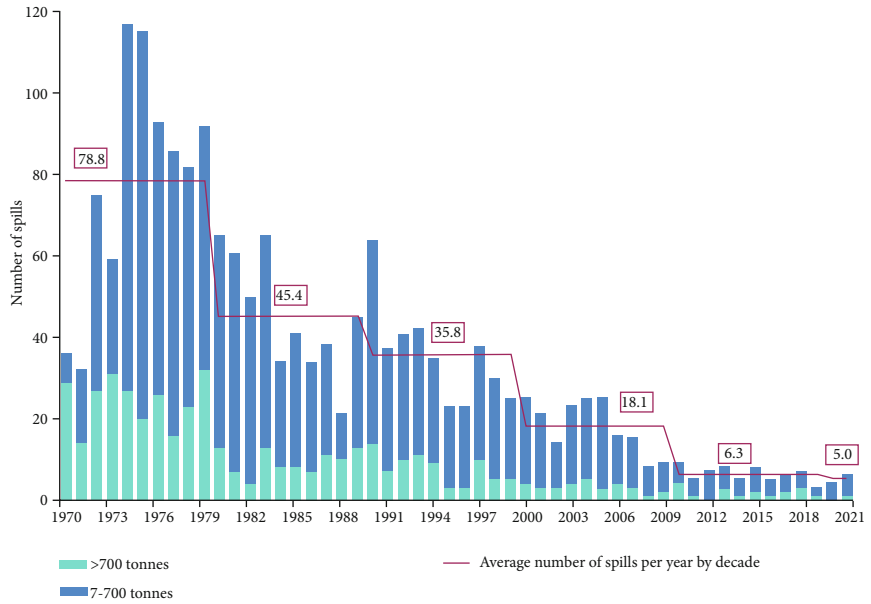

Figure 11: Number of oil spills from tankers worldwide, 1970-2021 (ITOPF, 2021).

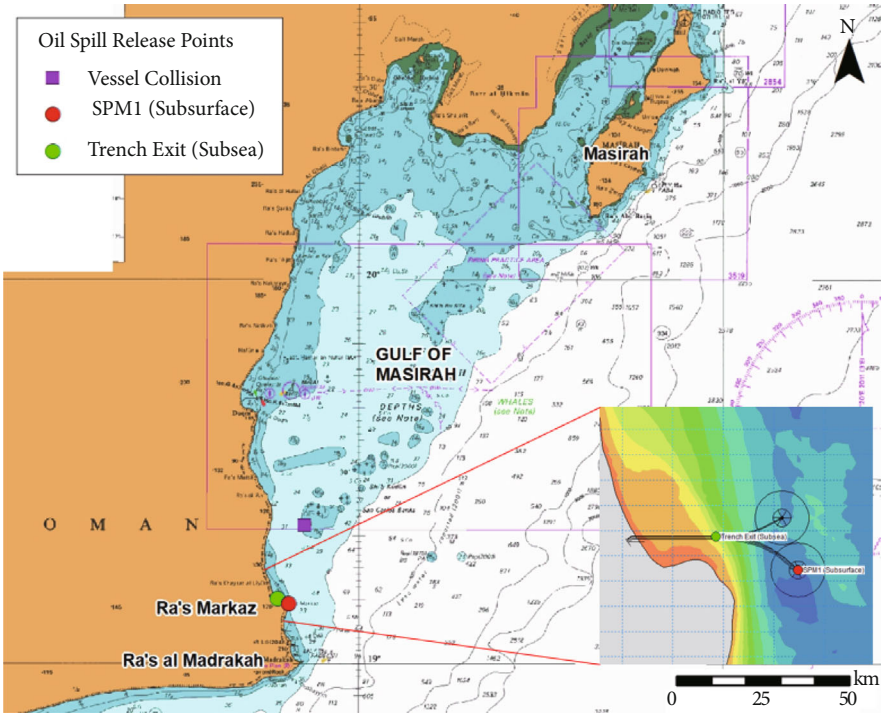

Figure 12: Initial oil spill locations.

$$K_H^{\text{oil-air}} = K_m \rho_a C_{pa} \left(\frac{S_c}{P_r}\right)^{0.67}_{\text{air}},$$

$$P_r = \frac{C_{pa}\rho_a}{0.0241(0.18055 + 0.003T_{\text{air}})}, \quad (12)$$

where S_c is the Schmidt number, $k_H^{\text{oil-air}}$ is the heat transfer coefficient, T_{oil} is the oil film temperature, T_{air} is the air temperature, P_r is the air prandt1 number, C_{pa} is the atmospheric heat capacity, and ρ_a is the atmospheric density

(ii) Heat transfer between oil film and water can be expressed as

$$H_T^{\text{oil-water}} = A_{\text{oil}} k_H^{\text{oil-water}} (T_{\text{water}} - T_{\text{oil}}),$$

$$K_H^{\text{oil-water}} = 0.332 + r_w C_{pw}\, \text{Re}^{-0.5} \text{Pr}_w^{-2/3},$$

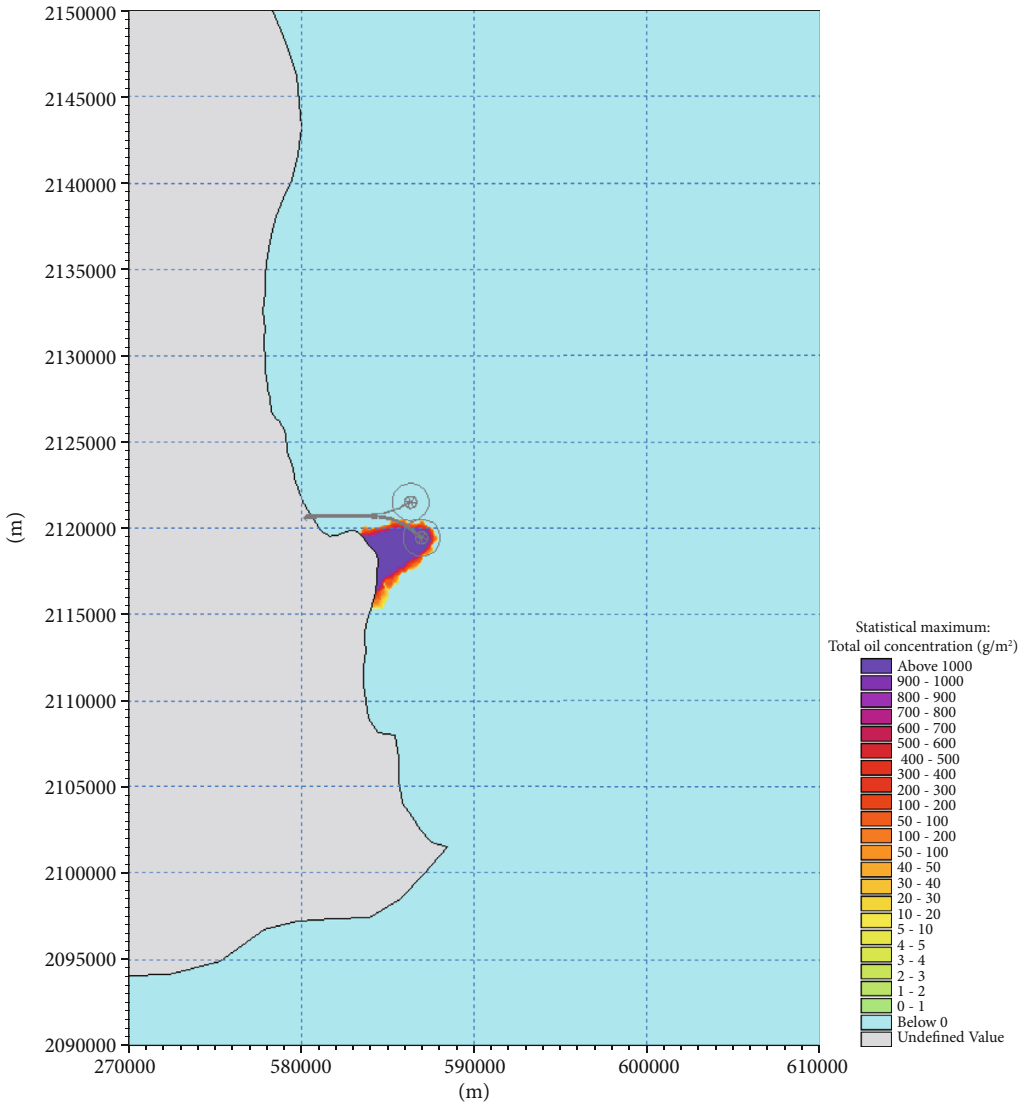

FIGURE 13: Map of maximum oil concentration for scenario 1 (subsurface blowout: 16,000m^3 spill at SPM1) (under typical wind in the winter monsoon).

$$\mathrm{Pr}_w = C_{pw} V_w \rho_w \left(\frac{1}{0.330 + 0.000848\left(T_{w^{-273.15}}\right)} \right), \tag{13}$$

where T_{water} is the temperature of water, Pr_w is the number of prandt1 of water, C_{pw} is the water heat capacity, and ρ_w is the density of water

(iii) Solar radiation

$$H(t) = \begin{cases} K_t \cdot H_o^{\max} \cdot \sin\left(\pi \dfrac{t - t^{\mathrm{sunrise}}}{t^{\mathrm{sunset}} - t^{\mathrm{sunrise}}} \right) t^{\mathrm{sunnrise}} < t < t^{\mathrm{sunset}} \\ 0, \text{otherwise} \end{cases},$$
$$t^{\mathrm{sunset}} = t^{\mathrm{sunrise}} + T_d, \tag{14}$$

where t^{sunrise} is the sunrise time, t^{sunset} is the sunset time, and T_d is the day length

(iv) Transmitting and receiving radiation

$$H_{\mathrm{total}}^{rad} = \sigma\left(l_{\mathrm{air}} \cdot T_{air}^4 + l_{\mathrm{water}} T_{\mathrm{water}}^4 - 2 l_{\mathrm{oil}} T_{\mathrm{oil}}^4 \right), \tag{15}$$

where l_{air} is the atmospheric emissivity, l_{water} is the water emissivity, l_{oil} is the oil emissivity, T_{air} is the air temperature, T_{water} is the water temperature, T_{oil} is the oil temperature, and σ is the Boltzman constant

(v) Evaporative heat loss

$$H^{\mathrm{vapor}} = \sum_{i}^{\mathrm{numberofcomponents}} N_i \cdot \Delta H_{vi},$$

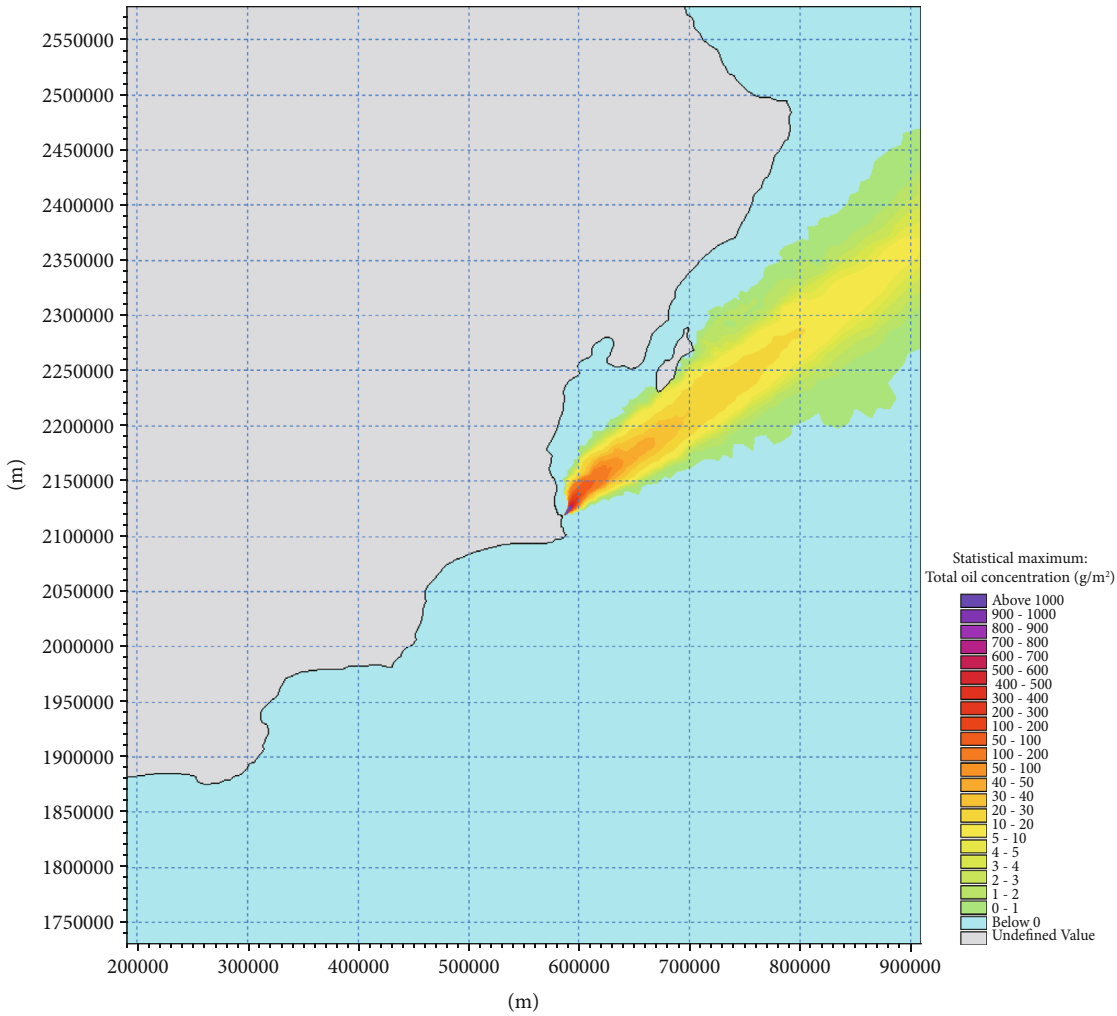

FIGURE 14: Map of maximum oil concentration for scenario 1 (sub-surface blowout: 16,000m^3 spill at SPM1) (under typical wind in the summer monsoon).

$$\frac{dT_{\text{oil}}}{dt} = \frac{1}{\zeta C_p h}\left[(1-a)H + \left(l_{\text{air}}T_{\text{air}}^4 + l_{\text{water}}T_{\text{water}}^4 - 2l_{\text{oil}}\cdot T_{\text{oil}}^4\right)\right] + h_{ow}(T_{\text{water}} - T_{\text{oil}}) + h_{oa}(T_{\text{air}} - T_{\text{oil}}) - \sum N_i \Delta H_{vi} + \left(\frac{dV_{\text{water}}}{dt}\zeta_w \cdot C_{pw} + \frac{dV_{\text{oil}}}{dt}\zeta_{\text{oil}}C_{\text{poil}}\right) \cdot (T_{\text{water}} - T_{\text{oil}}) \cdot A_{\text{oil}}, \tag{16}$$

where ΔH_{vi} is the vaporization heat of i, dV_{water}/dt is the water absorption rate, dV_{oil}/dt is the amount of oil droplets dispersed by upwelling, and C_{po} and C_{pw} are the heat capacity of oil and water, respectively

3.4. Model Setup. The model simulation was carried out for a duration of 60 days covering 4 spring-neap tidal cycles for typical summer and winter monsoon wind conditions, and also all-year wind frequency presented in Table 2.

Sensitivity tests have been carried out for an optimized particle number for sensible balance between accuracy and computational time. The model results have been compared between the use of 720 particles and 7,200 particles, and the difference was found marginal.

3.5. Modelled Oil Type. For more accurate predictions of weathering processes, the oil is divided into fractions (so-called pseudo-components). Therefore, for modelling purpose, it is required to find specific oil characteristics, either from a database or by laboratory tests. In this study, approach of describing an oil by 4 fractions, namely, volatile oil, heavy oil, asphaltene and wax, and the established oil spill template. In this oil spill trajectory modelling, Guafita Crude Oil was simulated, which is described by the following 4 fractions [38]:

(i) Volatile oil: 28.5 (25-32%)

(ii) Heavy oil: 53% (47-59%)

(iii) Asphaltene: 16% (10-22%)

(iv) Wax: 2.5%

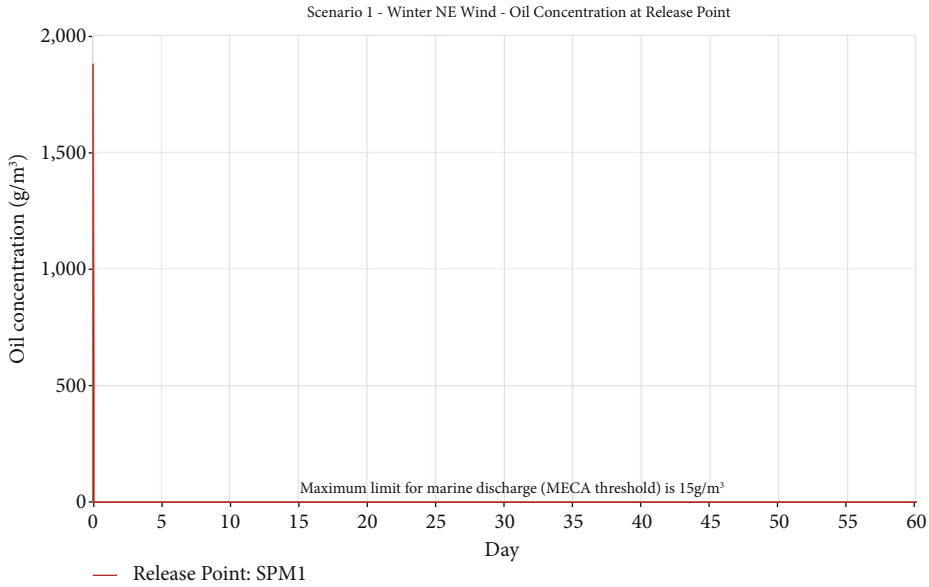

Figure 15: Changes in oil concentration over time at SPM1 spill location for scenario 1 (subsurface blowout: 16,000m^3 spill at SPM1) (under typical winter wind condition).

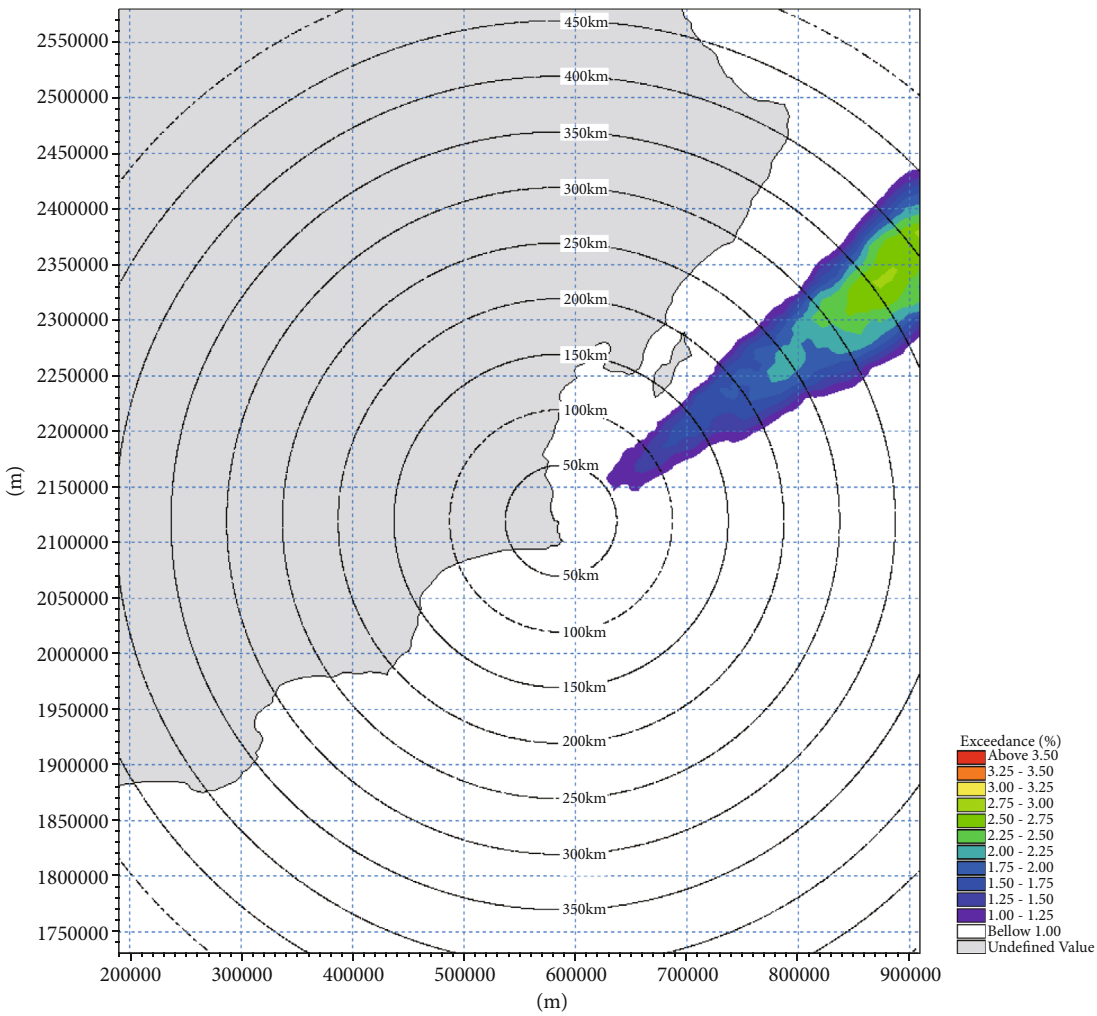

Figure 16: Exceedance probability of water surface oil thickness >10 μm for scenario 1 (sub-surface blowout: 16,000 m3 spill at SPM1)—full model extent.

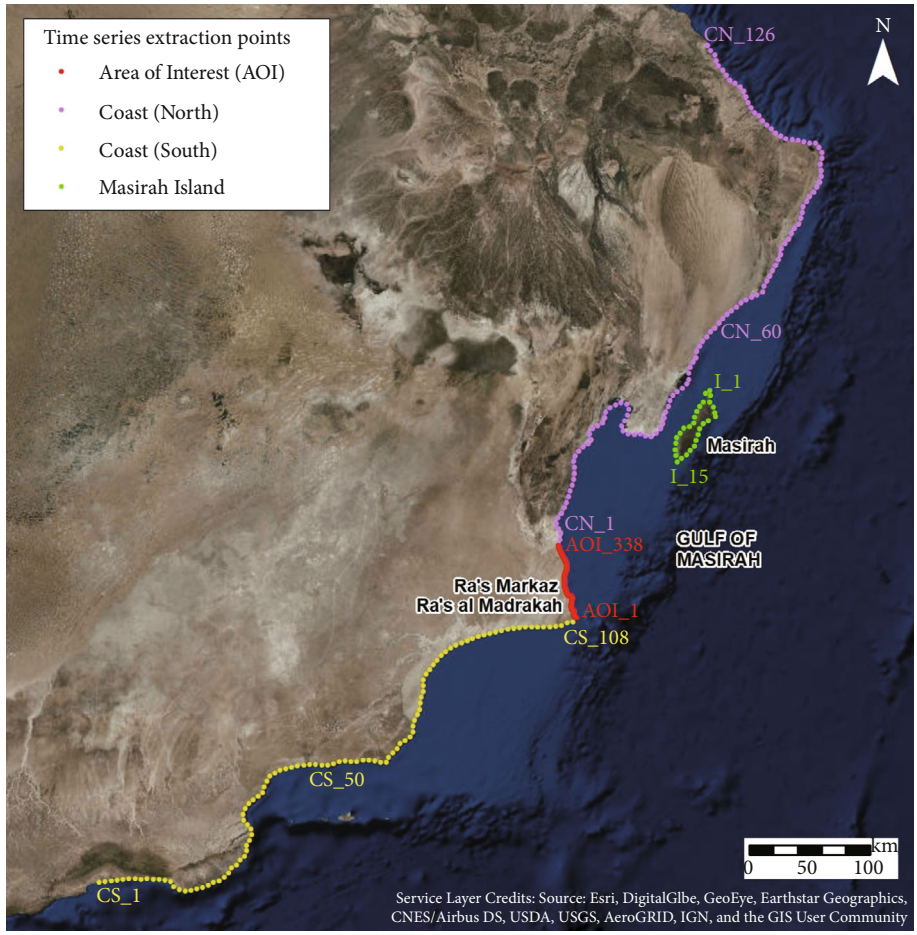

Figure 17: Shoreline points that time series data were extracted for duration statistical analysis.

3.6. Run Scenarios. The following three spill scenarios were simulated:

(a) Surface blowout: 16,000m^3oil release within one hour at SPM1

(b) Subsea blowout; 16,000m^3 oil release within one hour at the trench exit of buried oil pipe

(c) Spill from vessel collision at the mostly likely vessel collision area: 4,500m^3 oil release within six hours

The most likely vessel collision area is at San Carlos Banks (shown in Figure 5) which is approximately 26 km in the north of the site. A comparison of historic oil spills (from ITOPF [39]) shows that spills exceeding 700 tonnes (approx. 700m^3) are rare (and much rarer than oil spills smaller than 700 tonnes) (refer to Figure 11). The oil spill due to grounding of approx. 4,500 tonnes (4,500m^3) is therefore considered a reasonable figure based on historical spill data.

The initial oil spill locations are shown in Figure 12. It should be noted that scenarios I and II above also are deemed to cover, in terms of oil release volume and location, the scenario of two VLCCs colliding at the SPM location. From a planning and response perspective, minor variations in the release point are not considered significant. With regard to oil spills related to hose cleaning, the volumes associated with this type of oil spill is considered minimal, and it is not deemed required to model such a scenario.

4. Model Results and Discussion

4.1. Map of Maximum Oil Concentration. Results were extracted over the entire model domain to investigate the extent of the oil spill plumes. Figures 13 and 14 provide two dimensional maps of maximum oil concentration (of 60-day simulation) for the oil spill scenario 1 under typical summer and winter wind conditions. Maps of maximum oil concentration were selected from oil release at 13 different tidal phases and neap and spring tidal cycles for the worst cases (i.e., maximum extent of oil spreading). It should be noted that concentrations of dissolved aromatics in the water column are usually small and not considered in the oil spill response plan and have therefore not been considered.

4.2. Temporal Changes in Oil Concentration at Initial Spill Locations. The model results were extracted at the initial spill locations (shown in Figure 15) to investigate the changes in oil concentration at those locations. Figure 15 illustrates a sample time-series plot of oil concentration at SPM1 for oil spill scenario 1 under typical winter wind

condition. It is noted that oil concentration raised immediately after oil spill, but oil concentration is reduced to ambient level within 1-2 days. This is because oil movement under prevailing winds is almost in a transverse direction to the tidal flow. As a result, spill oil does not return to its release point under the influence of prevailing winds.

4.3. Probability of Oil Contamination. The probabilities of water surface oiling have been processed from model simulations for annual wind frequency for oil thickness above 0.01 μm, 1 μm, and 10 μm and also for oil concentration above 58 ppb. The contour maps of probabilities of thickness above 0.01 μm, 1 μm, and 10 μm and of oil concentration above 58 ppb are identical. The reason is that the accuracy of this oil spill model was limited to oil thickness above 10 μm. Figure 16 shows a two-dimensional map of probabilities of oil thickness above 10 μm for the oil spill scenario 1.

4.4. Shoreline Impact. In order to analyze shoreline impact by oil spill, time series of oil concentration and thickness were extracted from model results. Those shoreline points are illustrated in Figure 17. Points in the "Area of Interest" (AOI) are set to 200 m interval between Ras Madrakah and South of Duqm. Points in other coastlines, namely "Coast North" (CN series), "Coast South" (CS series) and "Island" (I series), are set at 5 km interval. The impact to "Coast North" is limited to the Gulf of Masirah. "Coast South" received little oil except those points close to Ras Madrakah headland.

5. Conclusive Remarks

The modelling results indicate that both tidal currents and wind drag force have a significant effect in oil spill movement. The dominant wind in the area is South-westerly wind during the summer monsoon and North-easterly wind during the winter monsoon, but South-westerly wind is far stronger and last longer than the North-easterly wind. As a result, oil spill trajectory is most likely towards offshore to North-east during the summer period (April to September). During the winter period (November–January), oil spill would move towards shore under North-westerly winds. Once oil reaches shore, it would stay at shore permanently and eventually sink to seabed or beach in the simulation. Although the model does not consider longshore drift by waves, oil movement along shore by waves would be a slow process. Therefore, the impact of oil spill during the winter monsoon would be limited to local area around Ras Markaz. Oil can spread quickly to offshore under South-westerly wind, and oil can reach to as far as Masirah Island in the north. However, oil concentrations at the key environmentally sensitive locations are low except Coral Head 1. It is noticed that oil movement under prevailing winds is almost in a transverse direction to the tidal flow. As a result, spill oil does not return to its release point under the influence of prevailing winds.

Data Availability

The datasets used and/or analyzed during the current study are available from the corresponding author on reasonable request.

Conflicts of Interest

The author declared no potential conflicts of interest with respect to the research, authorship, and/or publication of this paper.

References

[1] *Shell DEP 37.91.10.10-Gen, Single Point Mooring System*, 2011.

[2] R. Maari, *Single Point Mooring*, Principality of Monaco, 1985.

[3] J. J. Cheng and C. J. Wang, "Crude oil dock development in China: spatial distribution, capacity and problems," *China Transportation Review*, vol. 39, no. 4, pp. 22–27, 2017.

[4] Y. Lv, X. Z. Ju, X. F. Li, G. Li, B. H. Dong, and C. T. Zhong, "Study on construction conditions & site selection of catenary anchor leg mooring (CALM) for offshore oil terminal," *Ocean Engineering Equipment and Technology*, vol. 5, no. 5, pp. 300–304, 2018.

[5] S. Ryu, A. S. Duggal, C. N. Heyl, and Y. Liu, "Prediction of deepwater oil offloading buoy response and experimental validation," *International Journal of Offshore and Polar Engineering*, vol. 16, no. 4, pp. 290–296, 2006.

[6] H. D. Hollister and J. J. Spokes, "The Agbami project: a world class deepwater development," in *Offshore Technology Conference*, Houston, 2004.

[7] Y. F. Wang, D. G. Wang, Y. T. Kang, and H. Jin, "Study on oil spill risk management and prevention for single-point mooring systems," *Ocean Engineering Equipment and Technology*, vol. 1, no. 3, pp. 200–206, 2014.

[8] W. Guo, Y. X. Wang, M. Xie, and Y. J. Cui, "Modeling oil spill trajectory in coastal waters based on fractional Brownian motion," *Marine pollution bulletin*, vol. 58, no. 9, pp. 1339–1346, 2009.

[9] A. H. Al-Rabeh, H. M. Cekirge, and N. Gunay, "A stochastic simulation model of oil spill fate and transport," *Applied Mathematical Modelling*, vol. 13, no. 6, pp. 322–329, 1989.

[10] Z. Liu, Q. Chen, Y. Zhang, C. Zheng, B. Cai, and Y. Liu, "Research on transport and weathering of oil spills in Jiaozhou Bight, China," *Regional Studies in Marine Science*, vol. 51, article 102197, 2022.

[11] J. A. Fay, "Physical processes in the spread of oil on a water surface," in *International Oil Spill Conference Proceedings*no. 1, pp. 463–467, Washington, D. C., 1971.

[12] W. J. Lehr, R. J. Fraga, M. S. Belen, and H. M. Cekirge, "A new technique to estimate initial spill size using a modified fay-type spreading formula," *Marine Pollution Bulletin*, vol. 15, no. 9, pp. 326–329, 1984.

[13] A. J. Elliott, "EUROSPILL: oceanographic processes and NW European shelf databases," *Marine Pollution Bulletin*, vol. 22, no. 11, pp. 548–553, 1991.

[14] X. B. Chao, N. J. Shankar, and H. F. Cheong, "Two- and three-dimensional oil spill model for coastal waters," *Ocean Engineering*, vol. 28, no. 12, pp. 1557–1573, 2001.

[15] S. D. Wang, Y. M. Shen, and Y. H. Zheng, "Two-dimensional numerical simulation for transport and fate of oil spills in seas," *Ocean Engineering*, vol. 32, no. 13, pp. 1556–1571, 2005.

[16] P. Sebastiao and C. G. Soares, "Modeling the fate of oil spills at sea," *Spill Science and Technology Bulletin*, vol. 2, no. 2–3, pp. 121–131, 1995.

[17] P. Vethamony, K. Sudheesh, M. T. Babu et al., "Trajectory of an oil spill off Goa, eastern Arabian Sea: field observations

and simulations," *Environmental pollution*, vol. 148, pp. 438–444, 2007.

[18] B. Díaz, A. Pavón, and M. Gómez-Gesteira, "Use of a probabilistic particle tracking model to simulate the prestige oil spill," *Journal of Marine Systems*, vol. 72, no. 1–4, pp. 159–166, 2008.

[19] W. J. Guo and Y. X. Wang, "A numerical oil spill model based on a hybrid method," *Marine Pollution Bulletin*, vol. 58, no. 5, pp. 726–734, 2009.

[20] A. J. Mariano, V. H. Kourafalou, A. Srinivasan et al., "On the modeling of the 2010 gulf of Mexico oil spill," *Dynamics of Atmospheres and Oceans*, vol. 52, no. 1–2, pp. 322–340, 2011.

[21] F. Yu, J. Li, S. Cui, Y. Zhao, Q. Feng, and C. Ge, "A hindcast method to simulate oil spill trajectories for the Bohai Sea, Northeast China," *Ocean Engineering*, vol. 124, pp. 363–370, 2016.

[22] R. Perianez, "A Lagrangian oil spill transport model for the Red Sea," *Ocean Engineering*, vol. 217, article 107953, 2020.

[23] S. Naz, M. F. Iqbal, I. Mahmood, and M. Allam, "Marine oil spill detection using synthetic aperture radar over Indian ocean," *Marine Pollution Bulletin*, vol. 162, article 111921, 2021.

[24] M. Y. Omar, M. F. Shehada, A. K. Mehanna, A. H. Elbatran, and M. M. Elmesiry, "A case study of the Suez Gulf: modelling of the oil spill behavior in the marine environment," *Egyptian Journal of Aquatic Research*, vol. 47, no. 4, pp. 345–356, 2021.

[25] D. Simecek-Beatty and W. J. Lehr, "Oil spill forecast assessment using fractions skill score," *Marine Pollution Bulletin*, vol. 164, article 112041, 2021.

[26] Q. Pan, X. Zhu, L. Wan et al., "Operational forecasting for Sanchi oil spill," *Applied Ocean Research*, vol. 108, article 102548, 2021.

[27] P. Sebastiao and C. G. Soares, "Uncertainty in predictions of oil spill trajectories in a coastal zone," *Journal of Marine Systems*, vol. 63, no. 3-4, pp. 257–269, 2006.

[28] A. Azevedo, A. Oliveira, A. B. Fortunato, J. Zhang, and A. M. Baptista, "A cross-scale numerical modeling system for management support of oil spill accidents," *Marine Pollution Bulletin*, vol. 80, no. 1-2, pp. 132–147, 2014.

[29] A. K. Mishra and G. S. Kumar, "Weathering of oil spill: modeling and analysis," *Aquatic Procedia*, vol. 4, pp. 435–442, 2015.

[30] M. L. Spaulding, "State of the art review and future directions in oil spill modeling," *Marine Pollution Bulletin*, vol. 115, no. 1-2, pp. 7–19, 2017.

[31] J. M. Price, W. R. Johnson, C. F. Marshall, Z. G. Ji, and G. B. Rainey, "Overview of the oil spill risk analysis (OSRA) model for environmental impact assessment," *Spill Science and Technology Bulletin*, vol. 8, no. 5–6, pp. 529–533, 2003.

[32] A. Berry, T. Dabrowski, and K. Lyons, "The oil spill model OILTRANS and its application to the Celtic Sea," *Marine Pollution Bulletin*, vol. 64, no. 11, pp. 2489–2501, 2012.

[33] A. C. Toz and M. Buber, "Performance evaluation of oil spill software systems in early fate and trajectory of oil spill: comparison analysis of OILMAP and PISCES 2 in Mersin bay spill," *Environmental Monitoring and Assessment*, vol. 190, no. 9, p. 551, 2018.

[34] T. Nordam, C. J. Beegle-Krause, J. Skancke, N. Raymond, and M. Reed, "Improving oil spill trajectory modelling in the arctic," *Marine Pollution Bulletin*, vol. 140, pp. 65–74, 2019.

[35] K. Kampouris, V. Vervatis, J. Karagiorgos, and S. Sofianos, "Oil spill model uncertainty quantification using an atmospheric ensemble," *Ocean Science*, vol. 17, no. 4, pp. 919–934, 2021.

[36] Y. Z. Chen, "Development of an oil spill model adaptable to exposure and submergence conversion of tidal flats: a case study in the Changjiang Estuary," *Marine Pollution Bulletin*, vol. 171, article 112715, 2021.

[37] A.-L. Balogun, S. Yekeen, B. Pradhan, and K. Yusof, "Oil spill trajectory modelling and environmental vulnerability mapping using GNOME model and GIS," *Environmental Pollution*, vol. 268, no. Part A, article 115812, 2021.

[38] L. Lopez and S. L. Monaco-Trupiano, "Comparison of crude oil source-related indicators based on C15-, C15+ and C40+ parameters," *Journal of Oil, Gas, and Alternative Energy Sources*, vol. 6, no. 3, pp. 53–70, 2016.

[39] *ITOPF Handbook*, 2021, https://www.itopf.org/fileadmin/data/Documents/Company_Lit/Oil_Spill_Stats_2019.pdf.

Hindawi
Advances in Mathematical Physics
Volume 2022, Article ID 5718736, 7 pages
https://doi.org/10.1155/2022/5718736

Research Article

Sasakian Manifolds Admitting $*$-η-Ricci-Yamabe Solitons

Abdul Haseeb,[1] **Rajendra Prasad**,[2] **and Fatemah Mofarreh**[3]

[1]*Department of Mathematics, College of Science, Jazan University, Jazan 2097, Saudi Arabia*
[2]*Department of Mathematics and Astronomy, University of Lucknow, Lucknow 226007, India*
[3]*Mathematical Science Department, Faculty of Science, Princess Nourah Bint Abdulrahman University, Riyadh 11546, Saudi Arabia*

Correspondence should be addressed to Abdul Haseeb; malikhaseeb80@gmail.com

Received 13 February 2022; Accepted 12 April 2022; Published 6 May 2022

Academic Editor: Meraj Ali Khan

In this note, we characterize Sasakian manifolds endowed with $*$-η-Ricci-Yamabe solitons. Also, the existence of $*$-η-Ricci-Yamabe solitons in a 5-dimensional Sasakian manifold has been proved through a concrete example.

1. Introduction

In 1982 (resp., 1988), Hamilton introduced the idea of Ricci flow [1] (resp., Yamabe flow [2]). On a smooth Riemannian (or semi-Riemannian manifold), the Yamabe flow is determined as the evolution of the Riemannian (or semi-Riemannian) metric g_0 at time t to $g = g(t)$ using the following equation:

$$\frac{\partial}{\partial t} g(t) = -rg, g(0) = g_0, \tag{1}$$

where $r(t)$ refers to the scalar curvature of the metric $g(t)$. In case $n = 2$, the Yamabe and Ricci flows are related as in the following equation:

$$\frac{\partial}{\partial t} g(t) = -2S(g(t)), \tag{2}$$

where S defines the Ricci tensor. Thus, for the case $n > 2$, there is not such an equivalence, since the Yamabe flow preserves the conformal class of metric but generally this is not true.

The solutions of both Ricci and Yamabe flows are presented as Ricci and Yamabe solitons, respectively. On a Riemannian manifold M, the Ricci and Yamabe solitons are defined by

$$\begin{aligned} \pounds_F g + 2S + 2\lambda g = 0, \\ \pounds_F g + 2(\lambda - r)g = 0, \end{aligned} \tag{3}$$

respectively, where $\pounds_F$ is the Lie derivative operator along vector field F (called soliton vector field) at M and $\lambda \in \mathbb{R}$, where $\mathbb{R}$ is the set of real numbers. Recently in 2018, Deshmukh and Chen ([3, 4]) briefly studied Yamabe solitons to find sufficient conditions at the soliton vector field so that the metric of the Yamabe soliton is of constant scalar curvature. Yamabe solitons have also been studied in ([5–8]) and many others.

In 2019, Ricci-Yamabe flow, as a new class of geometric flows of the type (α, β), was presented by Güler and Crasmareanu [9] and defined as

$$\frac{\partial}{\partial t} g(t) = \beta r(t) g(t) - 2\alpha S(g(t)), g(0) = g_0. \tag{4}$$

After Güler and Crasmareanu, Dey [10] proposed the concept of Ricci-Yamabe solitons; according to him, the Ricci-Yamabe soliton of the type (α, β) is a Riemannian manifold that admits

$$\frac{1}{2}\pounds_F g + \alpha S + \left(\lambda - \frac{\beta r}{2}\right) g = 0, \tag{5}$$

where $\alpha, \beta \in \mathbb{R}$. In addition, it is noted that Ricci-Yamabe solitons of types $(\alpha, 0)$ and $(0, \beta)$ are known as α-Ricci solitons and β-Yamabe solitons, respectively.

The concept of $*$-Ricci soliton was investigated by Kaimakamis and Panagiotidou [11] in case of real hypersurfaces at complex space forms. More specifically, it is noted that the concept of $*$-Ricci tensor was presented firstly by Tachibana [12] in almost Hermitian manifolds, and later by Hamada [13] to consider different case which is the real hypersurfaces of nonflat complex space forms. The Riemannian metric g on the smooth manifold M is named the $*$-Ricci soliton in case F, a smooth vector field and $\lambda \in \mathbb{R}$ obeying:

$$\frac{1}{2}\pounds_F g = -S^* - g, \tag{6}$$

where

$$S^*(K, L) = g(Q^*K, L) = \text{Trace}\{\varphi \circ R(K, \varphi L)\}, \tag{7}$$

for every vector fields K, L on M, as well as Q^* and S^* are the $*$-Ricci operator and the $*$-Ricci tensor, respectively. In this connection, we recommend the papers ([14–21]) for the specific contents regarding Ricci, η-Ricci, and $*$-Ricci solitons in case of contact Riemannian geometry. In [22], the authors studied gradient Yamabe, gradient Einstein, and quasi-Yamabe solitons on almost co-Kähler manifolds.

Recently, Dey and Roy [23] presented the concept of $*$-η-Ricci soliton in Sasakian manifolds. The Riemannian manifold (M, g) is named $*$-η-Ricci soliton in case

$$\frac{1}{2}\pounds_\zeta g + S^* + \lambda g + \mu\eta \otimes \eta = 0. \tag{8}$$

Motivated by previous studies, we introduce the notion of $*$-η-Ricci-Yamabe soliton of type (α, β) which is a Riemannian manifold satisfying

$$\frac{1}{2}\pounds_F g + \alpha S^* + \left(\lambda - \frac{\beta r}{2}\right) g + \mu\eta \otimes \eta = 0, \tag{9}$$

for $\alpha, \beta, \lambda, \mu \in \mathbb{R}$. The $*$-η-Ricci-Yamabe soliton is described as shrinking, steady or expanding if it admits the soliton vector for which $\lambda < 0$, $= 0$ or >0, respectively. Particularly, if $\mu = 0$, then this concept of $*$-η-Ricci-Yamabe soliton $(g, F, \lambda, \mu, \alpha, \beta)$ reduces to a concept of $*$-Ricci-Yamabe soliton $(g, F, \lambda, \alpha, \beta)$.

Throughout the paper, we denote a $(2n+1)$-dimensional Sasakian manifold by M^S_{2n+1}, $*$-Ricci-Yamabe soliton by $*$-RYS, and $*$-η-Ricci-Yamabe soliton by $*$-η-RYS. We present our work as follows: Section 2 includes essential results and some basic definitions of Sasakian manifolds. Section 3 covers the study of $*$-η-RYS on M^S_{2n+1} leading to several significant characterizations of the manifold. Section 4 deals with the study of pseudo-Ricci-symmetric and Ricci recurrent M^S_{2n+1} admitting $*$-η-RYS. The $*$-η-RYS on M^S_{2n+1} satisfying the curvature conditions $R(\zeta, X) \cdot S = 0$ and $Q(g, S) = 0$ have been studied in Sections 5 and 6, respectively.

2. Preliminaries

A $(2n+1)$-dimensional differentiable manifold M is said to admit an almost contact structure, sometimes called a (φ, ζ, η)-structure, in case it admits a (1,1) type tensor field φ, a structure vector field ζ, and a 1-form η satisfying [24]

$$\varphi^2 = -I + \eta \otimes \zeta, \eta(\zeta) = 1, \varphi\zeta = 0, \eta \circ \varphi = 0. \tag{10}$$

The almost contact structure is called normal in case $\aleph + d\eta \otimes \zeta = 0$, where $\aleph$ is the Nijenhuis tensor of φ. Considering the Riemannian metric tensor g that is defined on M and satisfies

$$g(\varphi K, \varphi L) = g(K, L) - \eta(K)\eta(L), \eta(K) = g(K, \zeta), \tag{11}$$

for any $K, L \in \mathfrak{X}(M)$, where $\mathfrak{X}(M)$ refers to the set of all smooth vector fields of M. The structure $(\varphi, \zeta, \eta, g)$ is named the almost contact metric structure. Next, considering Φ, the tensor field of type $(0, 2)$ as $\Phi(K, L) = g(\Phi K, L)$. In case $d\eta = \Phi$, then the structure $(\varphi, \zeta, \eta, g)$ is named as normal metric structure. The normal contact metric structure is named Sasakian structure satisfying ([25–27]):

$$(\nabla_K \varphi)L = g(K, L)\zeta - \eta(L)K, \tag{12}$$

for any $K, L \in \mathfrak{X}(M)$, where ∇ stands for the Levi-Civita connection.

In case of M^S_{2n+1}, we have

$$R(\zeta, K)L = g(K, L)\zeta - \eta(L)K, \tag{13}$$

$$R(K, L)\zeta = \eta(L)K - \eta(K)L, \tag{14}$$

$$S(K, \zeta) = 2n\eta(K) \Leftarrow Q\zeta = 2n\zeta, \tag{15}$$

$$\nabla_K \zeta = -\varphi K, \tag{16}$$

$$(\nabla_K \eta)L = -g(\varphi K, L), \tag{17}$$

for any $K, L \in \mathfrak{X}(M)$; R and Q refers to the curvature tensor and the Ricci operator.

Definition 1. A Sasakian manifold is called an η-Einstein in case the non-vanishing Ricci tensor S is expressed as

$$S(K, L) = ag(K, L) + b\eta(K)\eta(L), \tag{18}$$

where $a, b \in C^\infty(M)$. In particular, if $b = 0$, then M is named as an Einstein manifold.

Definition 2. The vector field V is named as an affine conformal vector field in case it satisfies [28]

$$(\pounds_V \nabla)(K, L) = L(\rho)K + K(\rho)L - g(K, L)grad\rho, \tag{19}$$

where $\rho \in C^{\infty}(M)$. In case $\rho \in \mathbb{R}$, then V is called an affine vector field.

Lemma 3. *The $*$ -Ricci tensor of M^S_{2n+1} is given by [14]*

$$S^*(K,L) = S(K,L) - (2n-1)g(K,L) - \eta(K)\eta(L), \quad (20)$$

for any $K, L \in \mathfrak{X}(M)$.

3. $*$-η-Ricci-Yamabe Solitons on Sasakian Manifolds

First, we prove the following:

Theorem 4. *An M^S_{2n+1} admitting $*$ - η -RYS $(g, \zeta, \lambda, \mu, \alpha, \beta)$ is an η -Einstein manifold of the constant scalar curvature. Moreover, the scalars λ, μ related to each other by $\lambda + \mu = \beta r/2$.*

Proof. Let the metric of an M^S_{2n+1} be $*$-η-RYS $(g, \zeta, \lambda, \mu, \alpha, \beta)$, then Equation (9) turns to

$$g(\nabla_K \zeta, L) + g(K, \nabla_L \zeta) + 2\alpha S^*(K,L) + (2\lambda - \beta r)g(K,L) + 2\mu\eta(K)\eta(L) = 0, \quad (21)$$

for all vector fields K as well L on M. Using (16), Equation (21) leads to

$$S^*(K,L) = -\frac{1}{\alpha}\left(\lambda - \frac{\beta r}{2}\right)g(K,L) - \frac{\mu}{\alpha}\eta(K)\eta(L), \alpha \neq 0. \quad (22)$$

Using (20), (22) takes the form

$$S(K,L) = \sigma_1 g(K,L) + \sigma_2 \eta(K)\eta(L), \quad (23)$$

where $\sigma_1 = 2n - 1 - (1/\alpha)(\lambda - (\beta r/2))$ and $\sigma_2 = 1 - (\mu/\alpha)$.

By putting $L = \zeta$ at (23) as well the use of (10) and (11), we have

$$S(K,\zeta) = (\sigma_1 + \sigma_2)\eta(K), \quad (24)$$

where $\sigma_1 + \sigma_2 = 2n - (1/\alpha)(\lambda + \mu - (\beta r/2))$.

In view of (15), from (24), it follows that

$$\lambda + \mu = \frac{\beta r}{2}, \text{where } \alpha \neq 0. \quad (25)$$

On contracting (23), we find $r = \sigma_1(2n+1) + \sigma_2$, which by using the values of σ_1, σ_2 and (25) leads to

$$r = 2n\left(2n + \frac{\mu}{\alpha}\right), \quad (26)$$

where μ and $\alpha(\neq 0)$ are constants. Thus, (23) together with (25) and (26) leads to the statement of Theorem 4. □

Particularly, taking $\mu = 0$ in (23) as well in (25) resulted in $S(K,L) = (2n-1)g(K,L) + \eta(K)\eta(L)$ and $\lambda = 2n^2\beta$, respectively, being $r = 4n^2$. Thus, we have the following.

Corollary 5. *An M^S_{2n+1} admitting $*$ -RYS $(g, \zeta, \lambda, \alpha, \beta)$ is an η -Einstein manifold, and the soliton is shrinking, steady or expanding according to $\beta < 0$, $= 0$ or >0, respectively.*

Next, we prove the following.

Theorem 6. *If an M^S_{2n+1} admits $*$-η-RYS $(g, F, \lambda, \mu, \alpha, \beta)$ such that the vector field F represents an affine conformal vector field. Then, M^S_{2n+1} is an η-Einstein manifold, and F is an affine vector field.*

Proof. The use of (20) in (9) gives

$$(\pounds_F g)(L,U) = -2\alpha S(L,U) + [2\alpha(2n-1) - (2\lambda - \beta r)]g(L,U) + 2(\alpha - \mu)\eta(L)\eta(U). \quad (27)$$

Referencing Yano [29], the expression

$$\left(\pounds_F \nabla_K g - \nabla_K \pounds_F g - \nabla_{[F,K]} g\right)(L,U) = -g((\pounds_F \nabla)(K,L), U) - g((\pounds_F \nabla)(K,U), L), \quad (28)$$

is well-known for all K, L, U at M. As g is parallel respecting to ∇, the previous equation turns to

$$(\nabla_K \pounds_F g)(L,U) = g((\pounds_F \nabla)(K,U), L) + g((\pounds_F \nabla)(K,L), U), \quad (29)$$

as a result of (19), it leads to

$$(\nabla_K \pounds_F g)(L,U) = 2K(\rho)g(L,U). \quad (30)$$

Taking the covariant derivative of (27) respecting to K and using (17), we have

$$(\nabla_K \pounds_F g)(L,U) = -2\alpha(\nabla_K S)(L,U) + \beta K(r)g(L,U) - 2(\alpha - \mu)(g(\varphi K, L)\eta(U) + g(\varphi K, U)\eta(L)). \quad (31)$$

Putting $L = U = \zeta$ in (31) and using (10), (11), (15), and (30), we get

$$2K(\rho) = \beta K(r). \quad (32)$$

From (30)–(32), we find

$$\alpha(\nabla_K S)(L,U) + (\alpha - \mu)(g(\varphi K, L)\eta(U) + g(\varphi K, U)\eta(L)) = 0, \quad (33)$$

which by replacing $U = \zeta$ gives

$$(\nabla_K S)(L,\zeta) = \left(\frac{\mu}{\alpha} - 1\right) g(\varphi K, L), \alpha \neq 0. \tag{34}$$

Now, the covariant differentiation of (15) yields

$$(\nabla_K S)(L,\zeta) = S(L,\varphi K) - 2ng(\varphi K, L). \tag{35}$$

From (34) and (35), it follows that

$$S(L,\varphi K) = \left(2n - 1 + \frac{\mu}{\alpha}\right) g(\varphi K, L). \tag{36}$$

By replacing K by φK in (36) and using (10), we get

$$S(K,L) = \left(2n - 1 + \frac{\mu}{\alpha}\right) g(K,L) - \left(\frac{\mu}{\alpha} - 1\right)\eta(K)\eta(L), \alpha \neq 0. \tag{37}$$

The contraction of (37) gives $r = 2n(2n + \mu/\alpha)$. Therefore, from (32), it follows that $K(\rho) = 0$. This implies that $\rho \in \mathbb{R}$; therefore, F is an affine vector field. This completes the proof. □

Furthermore, we prove the following.

Lemma 7. *An M^S_{2n+1} satisfies the following equations:*

$$(\nabla_L Q)\zeta = Q\varphi L - 2n\varphi L, \tag{38}$$

$$\left(\nabla_\zeta Q\right)L = 2Q\varphi L, \tag{39}$$

where Q refers to the Ricci operator.

Proof. Differentiating $Q\zeta = 2n\zeta$ along L and using (16), we get (38). Next, differentiating (14) along W and using (16), we find

$$(\nabla_W R)(K,L)\zeta = R(K,L)\varphi W - g(\varphi W, L)K + g(\varphi W, K)L. \tag{40}$$

Taking a frame field and then contracting (40), we get

$$\sum_{i=1}^{2n+1} g\left(\left(\nabla_{e_i} R\right)(e_i, L)\zeta, U\right) = -S(L,\varphi U) + 2ng(\varphi L, U). \tag{41}$$

From Bianchi's second identity, we can easily obtain that

$$\sum_{i=1}^{2n+1} g\left(\left(\nabla_{e_i} R\right)(e_i, L)\zeta, U\right) = (\nabla_U S)(\zeta, L) - \left(\nabla_\zeta S\right)(U, L). \tag{42}$$

By equating (41) and (42), then using (38), Equation (39) follows. □

Now, we prove the next theorem:

Theorem 8. *If an M^S_{2n+1} admits $*$ - η -RYS $(g, F, \lambda, \mu, \alpha, \beta)$ such that the vector field F represents the gradient Dr of r defined by (9), then either F is a pointwise collinear with the structure vector field ζ or $\beta = -2$.*

Proof. Suppose an M^S_{2n+1} admits $*$-η-RYS $(g, F, \lambda, \mu, \alpha, \beta)$ such that the vector field F represents the gradient Dr of r, i.e., $F = Dr$. Then, from (9), we find

$$\nabla_K Dr = -\alpha QK - \left(\lambda - \frac{\beta r}{2} - \alpha(2n-1)\right)K + (\alpha - \mu)\eta(K)\zeta, \tag{43}$$

for any K on M.

The covariant differentiation of (43) respecting to L and the use of (16) and (17) leads to

$$\nabla_L\nabla_K Dr = -\alpha((\nabla_L Q)K + Q(\nabla_L K)) - \left(\lambda - \frac{\beta r}{2} - \alpha(2n-1)\right)\nabla_L K + \frac{\beta}{2}L(r)K + (\alpha - \mu)(-g(\varphi K, L)\zeta + \eta(\nabla_L K)\zeta - \eta(K)\varphi L). \tag{44}$$

Interchanging K and L in (44), we have

$$\nabla_K\nabla_L Dr = -\alpha((\nabla_K Q)L + Q(\nabla_K L)) - \left(\lambda - \frac{\beta r}{2} - \alpha(2n-1)\right)\nabla_K L + \frac{\beta}{2}K(r)L + (\alpha - \mu)(-g(\varphi L, K)\zeta + \eta(\nabla_K L)\zeta - \eta(L)\varphi K). \tag{45}$$

In view of (43), we also have

$$\nabla_{[K,L]} Dr = -\alpha Q(\nabla_K L) + \alpha Q(\nabla_L K) - \left(\lambda - \frac{\beta r}{2} - \alpha(2n-1)\right)\nabla_K L + \left(\lambda - \frac{\beta r}{2} - \alpha(2n-1)\right)\nabla_L K + (\alpha - \mu)(\eta(\nabla_K L)\zeta - \eta(\nabla_L K)\zeta). \tag{46}$$

From (44)–(46), we get

$$R(K,L)Dr = \alpha((\nabla_L Q)K - (\nabla_K Q)L) + \frac{\beta}{2}(K(r)L - L(r)K) + (\alpha - \mu)(2g(K,\varphi L)\zeta + \eta(K)\varphi L - \eta(L)\varphi K). \tag{47}$$

By replacing K by ζ in (47) and using (10), (13), (38), and (39), we get

$$L(r)\zeta - \zeta(r)L = -\alpha(Q\varphi L + 2n\varphi L) + \frac{\beta}{2}(\zeta(r)L - L(r)\zeta) + (\alpha - \mu)\varphi L. \tag{48}$$

The inner product of (48) with ζ leads to

$$\left(1 + \frac{\beta}{2}\right)(L(r) - \xi(r)\eta(L)) = 0. \tag{49}$$

Therefore, we have either $\beta = -2$ or $F = Dr = \xi(r)\xi$, that is, F is pointwise collinear with ζ. The proof is completed. □

4. Pseudo-Ricci-Symmetric and Ricci-Recurrent Sasakian Manifolds Admitting $*$-η-Ricci-Yamabe Solitons

Definition 9. The non-flatM^S_{2n+1} is named pseudo-Ricci-symmetric and is represented by $(PRS)_{2n+1}$, in case the Ricci tensor $S(\neq 0)$ of the manifold satisfies the condition [30]

$$(\nabla_U S)(K, L) = 2A(U)S(K, L) + A(K)S(U, L) + A(L)S(U, K), \tag{50}$$

where the non-zero 1-form A is given by $g(U, \zeta) = A(U)$, $\forall$ vector fields U ; ζ being the vector field that corresponds to the associated 1-form A. In particular, if $A = 0$, then M^S_{2n+1} is called Ricci-symmetric.

The covariant derivative of (23) leads to

$$(\nabla_U S)(K, L) = \sigma_2[g(U, \varphi K)\eta(L) + g(U, \varphi L)\eta(K)]. \tag{51}$$

Now, using (23) and (51), (50) becomes

$$\begin{aligned} &\sigma_2[g(U, \varphi K)\eta(L) + g(U, \varphi L)\eta(K)] \\ &\quad = 2A(U)[\sigma_1 g(K, L) + \sigma_2\eta(K)\eta(L)] \\ &\qquad + A(K)[\sigma_1 g(U, L) + \sigma_2\eta(U)\eta(L)] \\ &\qquad + A(L)[\sigma_1 g(U, K) + \sigma_2\eta(U)\eta(K)]. \end{aligned} \tag{52}$$

Choosing $U = L = \zeta$, (52) reduces to $A(K) = -3A(\zeta)\eta(K)$ which by putting $K = \zeta$ gives $A(\zeta) = 0$. This implies that $A(K) = 0$. Thus, we have the following.

Theorem 10. *A pseudo-Ricci-symmetric M^S_{2n+1} admitting $*$ - η -RYS $(g, \zeta, \lambda, \mu, \alpha, \beta)$ is Ricci-symmetric.*

Definition 11 [31]. An M^S_{2n+1} is named as Ricci-recurrent in case there exists a 1-form $\omega(\neq 0)$ holds:

$$(\nabla_K S)(L, U) = \omega(K)S(L, U). \tag{53}$$

for all K, L and U on M and 1-form ω.

By the use of (51) in (53), we find

$$\sigma_2[g(K, \varphi L)\eta(U) + g(K, \varphi U)\eta(L)] = \omega(K)S(L, U), \tag{54}$$

which by putting $U = \zeta$ then using (10) and (15) reduces to

$$\sigma_2 g(K, \varphi L) = 2n\omega(K)\eta(L). \tag{55}$$

By taking $\omega = \eta$, (55) takes the form

$$\sigma_2 g(K, \varphi L) = 2n\eta(K)\eta(L). \tag{56}$$

Now, replacing K by φK in (56) and using (10), we find

$$\sigma_2 g(\varphi K, \varphi L) = 0. \tag{57}$$

Since $g(\varphi K, \varphi L) \neq 0$, therefore, we obtain $\sigma_2 = 0$. This leads to $\mu = \alpha$. Hence, by the use of (25), we have $\lambda = -\alpha + \beta r/2$. Therefore, we give the next theorem.

Theorem 12. *If a Ricci-recurrent M^S_{2n+1} admits $*$ - η -RYS $(g, \zeta, \lambda, \mu, \alpha, \beta)$, then $\lambda = -\alpha + \beta r/2$ as well $\mu = \alpha$.*

Hence, by using these values of λ and μ in (23), we obtain

$$S(K, L) = 2ng(K, L). \tag{58}$$

Thus, we state:

Corollary 13. *A Ricci-recurrent M^S_{2n+1} admitting a $*$ - η -RYS $(g, \zeta, \lambda, \mu, \alpha, \beta)$ defines an Einstein manifold.*

5. Sasakian Manifolds Admitting $*$-η-Ricci-Yamabe Solitons Satisfying $R(\zeta, X) \cdot S = 0$

Considering an M^S_{2n+1} admitting $*$-η-RYS $(g, \zeta, \lambda, \mu, \alpha, \beta)$ which satisfies $R(\zeta, X) \cdot S = 0$, this implies that

$$S(R(\zeta, K)L, U) + S(L, R(\zeta, K)U) = 0, \tag{59}$$

for all K, L, U on M. In view of (23) and the symmetries of R , (59) takes the form

$$\sigma_2(g(K, L)\eta(U) + g(K, U)\eta(L) - 2\eta(K)\eta(L)\eta(U)) = 0, \tag{60}$$

which by taking $U = \zeta$ then using (10) and (11) turns to

$$\sigma_2 g(\varphi K, \varphi L) = 0. \tag{61}$$

From (61), it follows that $\sigma_2 = 0$, which leads to $\mu = \alpha$; hence, (25) gives $\lambda = \beta r/2 - \alpha$. This helps us to state:

Theorem 14. *For an M^S_{2n+1} admitting $*$ - η -RYS $(g, \zeta, \lambda, \mu, \alpha, \beta)$ that satisfies $R(\zeta, X) \cdot S = 0$, we have $\lambda = -\alpha + \beta r/2$ and $\mu = \alpha$.*

Now by using $\lambda = -\alpha + \beta r/2$ and $\mu = \alpha$, (23) takes the form

$$S(K, L) = 2ng(K, L). \tag{62}$$

Thus, we have:

Corollary 15. *In case an M^S_{2n+1} satisfies $R(\zeta, X) \cdot S = 0$ and admits $*$ - η -RYS $(g, \zeta, \lambda, \mu, \alpha, \beta)$, then it defines an Einstein manifold.*

6. Sasakian Manifolds Admitting $*$-η-Ricci-Yamabe Solitons Satisfying $Q(g, S) = 0$

Let an M^S_{2n+1} admitting $*$-η-RYS $(g, \zeta, \lambda, \mu, \alpha, \beta)$ satisfies

$$Q(g, S)(K, L, U, W) = 0, \tag{63}$$

where

$$Q(g, S)(K, L, U, W) = \left(\left(K_{\wedge g} L\right) \cdot S\right)(U, W). \tag{64}$$

This can be expressed as

$$\begin{aligned} Q(g, S)(K, L, U, W) &= g(L, U)S(K, W) - g(K, U)S(L, W) \\ &\quad + g(L, W)S(K, U) - g(K, W)S(L, U), \end{aligned} \tag{65}$$

where $(K_{\wedge g} L)U = g(L, U)K - g(K, U)L$ being used.

From (63), (65), and (23), we get

$$\begin{aligned} &\sigma_2(g(L, U)\eta(K)\eta(W) - g(K, U)\eta(L)\eta(W) \\ &\quad + g(L, W)\eta(K)\eta(U) - g(K, W)\eta(L)\eta(U)) = 0. \end{aligned} \tag{66}$$

From the preceeding equation, it follows that $\sigma_2 = 0$. This implies that $\mu = \alpha$. Hence, from (25), we get $\lambda = -\alpha + \beta r/2$. Thus, we have

Theorem 16. *If an M^S_{2n+1} admits $*$ - η -RYS $(g, \zeta, \lambda, \mu, \alpha, \beta)$ and the manifold satisfies $Q(g, S) = 0$, then $\lambda = -\alpha + \beta r/2$ and $\mu = \alpha$.*

Now, by using these values of λ as well μ, (23) yields

$$S(K, L) = 2ng(K, L). \tag{67}$$

Thus, we give the next corollary:

Corollary 17. *In case an M^S_{2n+1} admitting $*$ - η -RYS $(g, \zeta, \lambda, \mu, \alpha, \beta)$ satisfies $Q(g, S) = 0$, then it is an Einstein manifold.*

Example 1. Let a manifold $M = \{(u, v, w, s, t) \in \mathbb{R}^5\}$ of dimension 5, where (u, v, w, s, t) refer to the usual coordinates at $\mathbb{R}^5$. Suppose ρ_1,ρ_2, ρ_3, ρ_4, and ρ_5 are the vector fields at M defined as

$$\rho_1 = \frac{\partial}{\partial u}, \rho_2 = \left(\frac{\partial}{\partial w} - 2u\frac{\partial}{\partial t}\right), \rho_3 = \frac{\partial}{\partial v}, \rho_4 = \left(\frac{\partial}{\partial s} - 2v\frac{\partial}{\partial t}\right), \rho_5 = \frac{\partial}{\partial t} = \zeta, \tag{68}$$

and these are linearly independent at each point of M.

Suppose g is the Riemannian metric defined as

$$\begin{aligned} g\left(\rho_i, \rho_j\right) &= 0, 1 \le i \ne j \le 5, \\ g\left(\rho_i, \rho_j\right) &= 1, 1 \le i = j \le 5. \end{aligned} \tag{69}$$

Considering η, a 1-form on M determined as $\eta(K) = g(K, \rho_5) = g(K, \zeta)$ of all $K \in \chi(M)$. Let φ be a $(1, 1)$ tensor field on M defined by

$$\varphi\rho_1 = -\rho_2, \varphi\rho_2 = \rho_1, \varphi\rho_3 = -\rho_4, \varphi\rho_4 = \rho_3, \varphi\rho_5 = 0. \tag{70}$$

The linearity of φ and g leads to

$$\begin{aligned} \eta(\zeta) = 1, \varphi^2 K = -K + \eta(K)\zeta, \eta(\varphi K) = 0, \\ g(K, \zeta) = \eta(K), g(\varphi K, \varphi L) = g(K, L) - \eta(K)\eta(L), \end{aligned} \tag{71}$$

for all $K, L \in \chi(M)$. Therefore $[\rho_1, \rho_2] = 2\rho_5$, $[\rho_3, \rho_4] = -2\rho_5$ and $[\rho_i, \rho_j] = 0$ for others i and j. By using well-known Koszul's formula, we can easily calculate

$$\begin{aligned} &\nabla_{\rho_1}\rho_1 = 0, \nabla_{\rho_1}\rho_2 = -\rho_5, \nabla_{\rho_1}\rho_3 = 0, \nabla_{\rho_1}\rho_4 = 0, \nabla_{\rho_1}\rho_5 = \rho_2, \\ &\nabla_{\rho_2}\rho_1 = \rho_5, \nabla_{\rho_2}\rho_2 = 0, \nabla_{\rho_2}\rho_3 = 0, \nabla_{\rho_2}\rho_4 = 0, \nabla_{\rho_2}\rho_5 = -\rho_1, \\ &\nabla_{\rho_3}\rho_1 = 0, \nabla_{\rho_3}\rho_2 = 0, \nabla_{\rho_3}\rho_3 = 0, \nabla_{\rho_3}\rho_4 = -\rho_5, \nabla_{\rho_3}\rho_5 = \rho_4, \\ &\nabla_{\rho_4}\rho_1 = 0, \nabla_{\rho_4}\rho_2 = 0, \nabla_{\rho_4}\rho_3 = \rho_5, \nabla_{\rho_4}\rho_4 = 0, \nabla_{\rho_4}\rho_5 = -\rho_3, \\ &\nabla_{\rho_5}\rho_1 = \rho_2, \nabla_{\rho_5}\rho_2 = -\rho_1, \nabla_{\rho_5}\rho_3 = \rho_4, \nabla_{\rho_5}\rho_4 = -\rho_3, \nabla_{\rho_5}\rho_5 = 0. \end{aligned} \tag{72}$$

It can be easily verified that the manifold satisfies

$$\nabla_K\zeta = -\varphi K \text{ and } (\nabla_K\varphi)L = g(K, L)\zeta - \eta(L)K \text{ for } \zeta = \rho_5. \tag{73}$$

It is clear that this manifold M is a Sasakian manifold.

It is easy to have the following non-vanishing components:

$$\begin{aligned} R(\rho_1, \rho_2)\rho_1 &= 3\rho_2, R(\rho_1, \rho_5)\rho_1 = -\rho_5, R(\rho_1, \rho_2)\rho_2 \\ &= -3\rho_1, R(\rho_2, \rho_5)\rho_2 = -\rho_5, \\ R(\rho_3, \rho_4)\rho_3 &= 3\rho_4, R(\rho_3, \rho_5)\rho_3 = -\rho_5, R(\rho_3, \rho_4)\rho_4 \\ &= -3\rho_3, R(\rho_4, \rho_5)\rho_4 = -\rho_5, \\ R(\rho_1, \rho_5)\rho_5 &= \rho_1, R(\rho_2, \rho_5)\rho_5 = \rho_4, R(\rho_3, \rho_5)\rho_5 \\ &= \rho_3, R(\rho_4, \rho_5)\rho_5 = \rho_4. \end{aligned} \tag{74}$$

Utilizing the previous results we calculate the following:

$$S(\rho_1, \rho_1) = S(\rho_2, \rho_2) = S(\rho_3, \rho_3) = S(\rho_4, \rho_4) = -2, S(\rho_5, \rho_5) = 4. \tag{75}$$

Using (23), we have $S(\rho_5, \rho_5) = 4 - 1/\alpha(\lambda + \mu - \beta r/2)$. By equating both the values of $S(\rho_5, \rho_5)$, we obtain

$$\lambda + \mu = \frac{\beta r}{2}, \alpha \neq 0. \tag{76}$$

Hence, λ as well μ insures Equation (25), and so, g is the $*$-η-RYS on the given 5-dimensional Sasakian manifold.

Data Availability

No data were used to support this study.

Conflicts of Interest

On behalf of all authors, the corresponding author states that there is no conflict of interest.

Authors' Contributions

Correspondence should be addressed to Abdul Haseeb; malikhaseeb80@gmail.com and haseeb@jazanu.edu.sa.

Acknowledgments

The third author (Fatemah Mofarreh) expresses her gratitude to Princess Nourah bint Abdulrahman University Researchers Supporting Project number (PNURSP2022R27), Princess Nourah bint Abdulrahman University, Riyadh, Saudi Arabia.

References

[1] R. S. Hamilton, "Three-manifolds with positive Ricci curvature," *Journal of Differential Geometry*, vol. 17, no. 2, pp. 255–306, 1982.

[2] R. S. Hamilton, "The Ricci flow on surfaces, mathematics and general relativity (Santa Cruz, CA, 1986), 237-262," *Contemporary Mathematics*, vol. 71, 1988.

[3] B. Y. Chen and S. Deshmukh, "Yamabe and quasi-Yamabe solitons on Euclidean submanifolds," *Mediterranean Journal of Mathematics*, vol. 15, no. 5, p. 194, 2018.

[4] S. Deshmukh and B. Y. Chen, "A note on Yamabe solitons," *Balkan Journal of Geometry and its Applications*, vol. 23, no. 1, pp. 37–43, 2018.

[5] C. Dey and U. C. De, "A note on quasi-Yamabe solitons on contact metric manifolds," *Journal of Geometry*, vol. 111, no. 1, p. 11, 2020.

[6] S. Y. Hsu, "A note on compact gradient Yamabe solitons," *Journal of Mathematical Analysis and Applications*, vol. 388, no. 2, pp. 725-726, 2012.

[7] R. Sharma, "A 3-dimensional Sasakian metric as a Yamabe soliton," *International Journal of Geometric Methods in Modern Physics*, vol. 9, no. 4, p. 1220003, 2012.

[8] Y. J. Suh and U. C. De, "Yamabe solitons and Ricci solitons on almost co-Kähler manifolds," *Canadian Mathematical Bulletin*, vol. 62, no. 3, pp. 653–661, 2019.

[9] S. Güler and M. Crasmareanu, "Ricci-Yamabe maps for Riemannian flows and their volume variation and volume entropy," *Turkish Journal of Mathematics*, vol. 43, no. 5, pp. 2631–2641, 2019.

[10] D. Dey, "Almost Kenmotsu metric as Ricci-Yamabe soliton," https://arxiv.org/abs/2005.02322.

[11] G. Kaimakamis and K. Panagiotidou, "$*$-Ricci solitons of real hypersurfaces in non-flat complex space forms," *Journal of Geometry and Physics*, vol. 86, pp. 408–413, 2014.

[12] S. Tachibana, "On almost-analytic vectors in almost-Kählerian manifolds," *Tohoku Mathematical Journal*, vol. 11, no. 2, 1959.

[13] T. Hamada, "Real hypersurfaces of complex space forms in terms of Ricci $*$-Tensor," *Tokyo Journal of Mathematics*, vol. 25, no. 2, pp. 473–483, 2002.

[14] A. Ghosh and D. S. Patra, "$*$-Ricci soliton within the framework of Sasakian and (k, μ)-contact manifold," *International Journal of Geometric Methods in Modern Physics*, vol. 15, no. 7, article 1850120, pp. 1–23, 2018.

[15] A. Haseeb and U. C. De, "η-Ricci solitons in ε-Kenmotsu manifolds," *Journal of Geometry*, vol. 110, no. 2, p. 34, 2019.

[16] A. Haseeb and R. Prasad, "η-Ricci solitons on ε-LP-Sasakian manifolds with a quarter-symmetric metric connection," *Honam Mathematical Journal*, vol. 41, no. 3, pp. 539–558, 2019.

[17] A. Haseeb and R. Prasad, "$*$-conformal η-Ricci solitons in ϵ-Kenmotsu manifolds," *Publications de l'Institut Mathematique*, vol. 108, no. 122, pp. 91–102, 2020.

[18] S. K. Hui, S. K. Yadav, and A. Patra, "Almost conformal Ricci solitons on f-Kenmotsu manifolds," *Khayyam Journal of Mathematics*, vol. 5, pp. 89–104, 2019.

[19] D. G. Prakasha and P. Veeresha, "Para-Sasakian manifolds and $*$-Ricci solitons," *Afrika Matematika*, vol. 30, no. 7-8, pp. 989–998, 2019.

[20] S. Roy, S. Dey, A. Bhattacharyya, and S. K. Hui, "$*$-conformal η-Ricci soliton on Sasakian manifold," *Asian-European Journal of Mathematics*, vol. 15, no. 2, article 2250035, 2022.

[21] M. Turan, C. Yetim, and S. K. Chaubey, "On quasi-Sasakian 3-manifolds admitting η-Ricci solitons," *Univerzitet u Nišu*, vol. 33, no. 15, pp. 4923–4930, 2019.

[22] U. C. De, S. K. Chaubey, and Y. J. Suh, "A note on almost co-Kähler manifolds," *International Journal of Geometric Methods in Modern Physics*, vol. 17, no. 10, article 2050153, p. 14, 2020.

[23] S. Dey and S. Roy, "$*$-η-Ricci soliton within the framework of Sasakian manifold," *Journal of Dynamical Systems and Geometric Theories*, vol. 18, no. 2, pp. 163–181, 2020.

[24] D. E. Blair, *Contact Manifolds in Riemannian Geometry*, vol. 509 of Lecture Notes in Mathematics, Springer-Verlag, Berlin, 1976.

[25] U. K. Gautam, A. Haseeb, and R. Prasad, "Some results on projective curvature tensor in Sasakian manifolds," *Communication of the Korean Mathematical Society*, vol. 34, pp. 881–896, 2019.

[26] S. Sasaki, *Lecture Note on Almost Contact Manifolds*, no. Part I, 1965Tohoku University, 1965.

[27] S. Sasaki, *Lectures Note on Almost Contact Manifolds*, no. Part II, 1967Tohoku University, 1967.

[28] K. L. Duggal, "Affine conformal vector fields in semi-Riemannian manifolds," *Acta Applicandae Mathematicae*, vol. 23, pp. 275–294, 1991.

[29] K. Yano, *Integral Formulas in Riemannian Geometry*, Marcel Dekker, New York, 1970.

[30] M. C. Chaki, "On pseudo Ricci symmetric manifolds," *Bulgarian Journal of Physics*, vol. 15, no. 6, pp. 526–531, 1988.

[31] E. M. Patterson, "Some theorems on Ricci-recurrent spaces," *Journal of the London Mathematical Society*, vol. s1-27, no. 3, pp. 287–295, 1952.

Hindawi
Advances in Mathematical Physics
Volume 2022, Article ID 9881237, 9 pages
https://doi.org/10.1155/2022/9881237

Research Article

Some Geometric Characterizations of f-Curves Associated with a Plane Curve via Vector Fields

Azeb Alghanemi and Abeer AlGhawazi

Department of Mathematics, Faculty of Science, King Abdulaziz University, P.O. Box 80203, Jeddah 21589, Saudi Arabia

Correspondence should be addressed to Azeb Alghanemi; aalghanemi@kau.edu.sa

Received 16 February 2022; Accepted 28 March 2022; Published 27 April 2022

Academic Editor: Meraj Ali Khan

The differential geometry of plane curves has many applications in physics especially in mechanics. The curvature of a plane curve plays a role in the centripetal acceleration and the centripetal force of a particle traversing a curved path in a plane. In this paper, we introduce the concept of the f-curves associated with a plane curve which are more general than the well-known curves such as involute, evolute, parallel, symmetry set, and midlocus. In fact, we introduce the f-curves associated with a plane curve via its normal and tangent for both the cases, a Frenet curve and a Legendre curve. Moreover, the curvature of an f-curve has been obtained in several approaches.

1. Introduction

The differential geometry of a plane curve is an attractive area of research for geometers and physicists, owing to its applications in several areas such as mechanics, computer graphics, computer vision, and medical imaging. In mechanics, for example, the differential geometry of plane curves is used to study the motion of a particle in a plane. Moreover, the curvature of a curved path is used for computing the centripetal acceleration and the centripetal force of a particle moving along that path (cf. [1]).

In this paper, we define the f-curve associated with a given plane curve, for both the cases, a Frenet curve and a Legendre curve. Note that Legendre curves are more general than Frenet curves. Recently, the geometry of Legendre plane curves has been quite extensively studied, and in particular, their evolutes and involutes have been investigated (cf. [2–5]). An important achievement of this paper is that what we find a neat expression for the curvature of an f-curve.

This paper consists of five main sections. The first section is introductory, giving a general idea about the paper. The second section contains basic concepts of the differential geometry of Frenet plane curves and Legendre plane curves which will be used in the rest of this paper. In the third section, we introduce the concept of the f-curves associated with Frenet and Legendre curves via their normals and we study their curvatures in several cases. In the fourth section, we introduce and study the f-curves associated with a Frenet curve and a Legendre curve in a plane via their tangents. Moreover, we give formulae for the curvature of the f-curve associated with a plane curve in both the cases, a Frenet curve and a Legendre curve. In the fifth section, we give nontrivial examples of the f-curve associated with a regular curve via its normal and we draw these curves using the Maple.

2. Preliminaries

In this section, we are going to review basic concepts of the differential geometry of plane curves. For more detail about plane curves and their properties, we refer the reader to [6, 7]. A smooth plane curve γ is a map $\gamma : I \longrightarrow \mathbb{R}^2$ given by $\gamma(t) = (\gamma_1(t), \gamma_2(t))$ such that $\gamma_1(t)$ and $\gamma_2(t)$ are smooth functions on I, where I is an open interval of $\mathbb{R}$. If γ is a

regular parametrized curve (i.e., $\gamma'(t)=0$ for all $t \in I$), then we define the unit tangent vector by $T_\gamma(t) = \gamma'(t)/\|\gamma'(t)\|$ and the unit normal vector by $N_\gamma(t) = J(T_\gamma(t))$, where J is the counterclockwise rotation by $\pi/2$ and $\|\gamma'(t)\| = \sqrt{\gamma'(t) \cdot \gamma'(t)}$. Now, the Frenet formula is given by

$$\begin{pmatrix} T_\gamma'(t) \\ N_\gamma'(t) \end{pmatrix} = \begin{pmatrix} 0 & \|\gamma'(t)\|\kappa_\gamma(t) \\ -\|\gamma'(t)\|\kappa_\gamma(t) & 0 \end{pmatrix} \begin{pmatrix} T_\gamma(t) \\ N_\gamma(t) \end{pmatrix}, \tag{1}$$

where prime is the derivative with respect to the parameter t and $\kappa_\gamma(t)$ is the curvature of γ which is given by $\kappa_\gamma(t) = (T_\gamma'(t) \cdot N_\gamma(t))/\|\gamma'(t)\|$. The pair $\{T_\gamma(t), N_\gamma(t)\}$ is called the moving frame of the regular curve γ. If γ is parametrized by its arc-length s, then the Frenet formula is given by

$$\begin{pmatrix} T_\gamma'(s) \\ N_\gamma'(s) \end{pmatrix} = \begin{pmatrix} 0 & \kappa_\gamma(s) \\ -\kappa_\gamma(s) & 0 \end{pmatrix} \begin{pmatrix} T_\gamma(s) \\ N_\gamma(s) \end{pmatrix}, \tag{2}$$

where $T_\gamma(s) = \gamma'(s)$ is the unit tangent vector, $N_\gamma(s) = J(T_\gamma(s))$ is the unit normal vector, and $\kappa_\gamma(s) = \pm\|T_\gamma'(s)\|$. Also, the curvature is defined by $\kappa_\gamma(s) = d\chi(s)/ds$, where χ is the angle function between the horizontal lines and the tangent of γ and s is the arc length of γ.

Definition 1. Let $\gamma : I \longrightarrow \mathbb{R}^2$ be a regular parametrized curve and $\tilde{\gamma}(t) = \gamma(t) + \lambda N_\gamma(t)$, where λ is a constant. Then, $\tilde{\gamma}$ and γ are parallel curves.

Definition 2. Let $\gamma : I \longrightarrow \mathbb{R}^2$ be a regular parametrized curve with nonvanishing curvature. Then, the evolute of γ is given by

$$E_\gamma(t) = \gamma(t) + \frac{1}{\kappa_\gamma(t)} N_\gamma(t). \tag{3}$$

It is a well-known result that E_γ is regular at $t_0 \in I$ if and only if $\kappa_\gamma'(t_0) \neq 0$.

In the rest of this section, we review some basic concepts of Legendre plane curves, and for more information, we refer the reader to [2–5, 8].

Definition 3. The map (γ, ω): $I \longrightarrow \mathbb{R}^2 \times S^1$ is called a Legendre curve if $\gamma'(t) \cdot \omega(t) = 0$ for all $t \in I$, where S^1 is the unit circle and $\omega : I \longrightarrow S^1$ is a smooth unit vector field. The map (γ, ω) is a Legendre immersion if it is an immersion.

We call $\gamma : I \longrightarrow \mathbb{R}^2$ a frontal if there exists a smooth function $\omega : I \longrightarrow S^1$ such that (γ, ω) is a Legendre curve, and we call $\gamma : I \longrightarrow \mathbb{R}^2$ a wavefront if there exists a smooth function $\omega : I \longrightarrow S^1$ such that (γ, ω) is a Legendre immersion.

For a Frenet curve γ, if γ has a singular point, then the moving frame is not well-defined. For a Legendre curve, (γ, ω): $I \longrightarrow \mathbb{R}^2 \times S^1$, an alternative frame is well-defined at any point. This frame is given by $\{\omega, \mu\}$, where $\mu(t) = J(\omega(t))$. Also, we have the following formula:

$$\begin{pmatrix} \omega'(t) \\ \mu'(t) \end{pmatrix} = \begin{pmatrix} 0 & \ell(t) \\ -\ell(t) & 0 \end{pmatrix} \begin{pmatrix} \omega(t) \\ \mu(t) \end{pmatrix}, \tag{4}$$

where $\ell(t) = \omega'(t) \cdot \mu(t)$. We call the pair $\{\omega(t), \mu(t)\}$ a moving frame of a Legendre curve γ. In addition, there exists a smooth function $\beta(t)$ such that $\beta(t) = \gamma'(t) \cdot \mu(t)$. The curvature of the Legendre curve is $(\ell(t), \beta(t))$.

Definition 4 (see [4]). Suppose that γ is a frontal with the curvature (ℓ, β). If there exists a unique smooth function $\rho : I \longrightarrow \mathbb{R}$ such that $\beta(t) = \rho(t)\ell(t)$ for all $t \in I$, then the evolute $E_\gamma : I \longrightarrow \mathbb{R}^2$ of γ is given by $E_\gamma(t) = \gamma(t) - \rho(t)\omega(t)$. Moreover, E_γ is a frontal with the curvature $(\ell(t), \rho'(t))$. This means that $(E_\gamma, J(\omega))$: $I \longrightarrow \mathbb{R}^2 \times S^1$ is a Legendre curve, where J is the counterclockwise rotation by $\pi/2$ on $\mathbb{R}^2$.

Definition 5 (see [4]). Suppose that γ is a frontal with the curvature (ℓ, β). The involute of frontal γ at $t_0 \in I$ is given by $I_\gamma(t_0) = \gamma(t) - \int_{t0}^{t} \beta(u)du$, and $(I_\gamma, J^{-1}(\omega))$: $I \longrightarrow \mathbb{R}^2 \times S^1$ is a Legendre curve with curvature $(\ell(t), (\int_{t_0}^{t} \beta(u)du)\ell)$, where J^{-1} is the clockwise rotation by $\pi/2$ on $\mathbb{R}^2$.

3. f-Curve via the Normal Vector Associated with a Plane Curve

3.1. Regular Curve. In this section, we study the f-curve via the normal vector associated with a regular plane curve. Also, the curvature of this curve will be obtained in two different ways.

Definition 6. Let $\gamma : I \longrightarrow \mathbb{R}^2$ be a regular parametrized curve. Then, the f-curve via the normal vector associated with γ is defined by $\alpha(t) = \gamma(t) + f(t)N_\gamma(t)$, where $f : I \longrightarrow \mathbb{R}$ is a smooth function.

In the following lemma, we give the necessary and sufficient condition for the curve α to be a regular curve.

Lemma 7. *Let $\gamma : I \longrightarrow \mathbb{R}^2$ be a unit speed curve. Then, the curve α is regular if and only if $f\kappa_\gamma \neq 1$ or $f' \neq 0$.*

Proof. The proof of this lemma is obvious. □

Remark 8. From Lemma 7, it can be easily obtained that all singular points of the f-curve via the normal vector associated with γ lie on the evolute of γ.

The following theorem provides a useful formula for the curvature of the f-curve via the normal vector associated with γ in the case of its regularity.

Theorem 9. *Let $\gamma : I \longrightarrow \mathbb{R}^2$ be a unit speed curve and α be its associated f-curve via the normal vector.*

(1) If $f\kappa_\gamma \neq 1$, then $\kappa_\alpha = ((\kappa_\gamma \pm \theta')\cos\theta)/(1 - f\kappa_\gamma)$, where θ is the angle between the tangent vector of α and the unit tangent vector of γ

(2) If $f' \neq 0$, then $\kappa_\alpha = ((\kappa_\gamma \mp \phi')\cos\phi)/f'$, where ϕ is the angle between the tangent vector of α and the unit normal vector of γ

Proof. Let $\gamma : I \longrightarrow \mathbb{R}^2$ be a unit speed curve and α be its associated f-curve via the normal vector. Then, we have

$$\alpha' = (1 - f\kappa_\gamma)T_\gamma + f'N_\gamma. \tag{5}$$

Case 1. If $f\kappa_\gamma$=1, then from Lemma 7, α is a regular curve, and we have

$$\alpha' \cdot T_\gamma = 1 - f\kappa_\gamma, \tag{6}$$

which gives

$$\|\alpha'\|\|T_\gamma\| \cos\theta = 1 - f\kappa_\gamma. \tag{7}$$

So, we have

$$\|\alpha'\| \cos\theta = 1 - f\kappa_\gamma. \tag{8}$$

Equation (8) can be rewritten as

$$\|\alpha'\| = (1 - f\kappa_\gamma)\sec\theta. \tag{9}$$

From equation (5), we have

$$\|\alpha'\|^2 = (1 - f\kappa_\gamma)^2 + (f')^2. \tag{10}$$

Now, using equation (8) in equation (10), we get

$$\|\alpha'\|^2 = \|\alpha'\|^2 \cos^2\theta + (f')^2. \tag{11}$$

So,

$$f' = \pm\|\alpha'\| \sin\theta. \tag{12}$$

Substituting (8) and (12) in (5), we have

$$\alpha' = (\|\alpha'\| \cos\theta)T_\gamma \pm (\|\alpha'\| \sin\theta)N_\gamma. \tag{13}$$

The unit tangent vector of α, T_α, can be written as

$$T_\alpha = (\cos\theta)T_\gamma \pm (\sin\theta)N_\gamma, \tag{14}$$

and the unit normal vector of α, N_α, can be written as

$$N_\alpha = (\mp\sin\theta)T_\gamma + (\cos\theta)N_\gamma. \tag{15}$$

Now,

$$T_\alpha' \cdot N_\alpha = \kappa_\gamma \pm \theta'. \tag{16}$$

Hence,

$$\kappa_\alpha = \frac{T_\alpha' \cdot N_\alpha}{\|\alpha'\|} = \frac{(\kappa_\gamma \pm \theta')\cos\theta}{1 - f\kappa_\gamma}. \tag{17}$$

Case 2. If f'=0, then from Lemma 7, α is a regular curve, and we have

$$\alpha' \cdot N_\gamma = f', \tag{18}$$

which gives

$$\|\alpha\|\|N_\gamma\| \cos\phi = f'. \tag{19}$$

So, we have

$$\|\alpha'\| \cos\phi = f'. \tag{20}$$

Equation (20) can be rewritten as

$$\|\alpha'\| = f' \sec\phi. \tag{21}$$

Now, using equation (20) in equation (10), we get

$$\|\alpha'\|^2 = (1 - f\kappa_\gamma)^2 + \|\alpha'\|^2 \cos^2\phi. \tag{22}$$

Now,

$$1 - f\kappa_\gamma = \pm\|\alpha'\| \sin\phi. \tag{23}$$

Substituting (20) and (23) in (5), we get

$$\alpha' = (\pm\|\alpha'\| \sin\phi)T_\gamma + (\|\alpha'\| \cos\phi)N_\gamma. \tag{24}$$

So,

$$T_\alpha = (\pm\sin\phi)T_\gamma + (\cos\phi)N_\gamma, \tag{25}$$

$$N_\alpha = -(\cos\phi)T_\gamma \pm (\sin\phi)N_\gamma. \tag{26}$$

Now,

$$T_\alpha' \cdot N_\alpha = \kappa_\gamma \mp \phi'. \tag{27}$$

Hence,

$$\kappa_\alpha = \frac{\left(\kappa_\gamma \mp \phi'\right)\cos\phi}{f'}. \tag{28}$$

□

As an application of Theorem 9, the curvatures of parallel curves and evolute become special cases of this theorem. Precisely, we have the following corollary.

Corollary 10. *Let $\gamma : I \longrightarrow \mathbb{R}^2$ be a unit speed curve with nonvanishing curvature and α be its associated f-curve via the normal vector.*

(1) If f is a constant and $f \neq 1/\kappa_\gamma$, then (γ, α) are parallel curves and $\kappa_\alpha = \kappa_\gamma/|1 - f\kappa_\gamma|$

(2) If $f' \neq 0$ and $f = 1/\kappa_\gamma$, then α is the evolute of γ and $\kappa_\alpha = \mp\kappa_\gamma^3/\kappa_\gamma'$

3.2. Legendre Curve. In this section, we consider the case when γ is a Legendre curve.

Definition 11. Let (γ, ω): $I \longrightarrow \mathbb{R}^2 \times S^1$ be a Legendre curve. Then, the f-curve via the vector field ω associated with γ is given by $\tilde{\alpha}(t) = \gamma(t) + f(t)\omega(t)$, where $f : I \longrightarrow \mathbb{R}$ is a smooth function.

Lemma 12. *Let (γ, ω): $I \longrightarrow \mathbb{R}^2 \times S^1$ be a Legendre curve. Then, the f-curve via the vector field ω associated with γ is regular if and only if $f \neq (-\beta)/\ell$ or $f' \neq 0$.*

Proof. Let $\tilde{\alpha} = \gamma + f\omega$ be associated with f-curve via the vector field ω, then we have

$$\tilde{\alpha}' = \gamma' + f'\omega + f\omega'. \tag{29}$$

Since $\gamma' = \beta\mu$ and $\omega' = \ell\mu$, we have

$$\tilde{\alpha}' = f'\omega + (\beta + f\ell)\mu. \tag{30}$$

Now, $\tilde{\alpha}' \neq \vec{0}$ if and only if $\beta + f\ell \neq 0$ or $f' \neq 0$. □

Theorem 13. *Let (γ, ω): $I \longrightarrow \mathbb{R}^2 \times S^1$ be a Legendre curve and $\tilde{\alpha}$ be its associated f-curve via the vector field ω.*

(1) If $f \neq -\beta/\ell$, then $\kappa_{\tilde{\alpha}} = ((\ell \mp \psi')\cos\psi)/(\beta + \ell f)$, where ψ is the angle between the tangent vector of $\tilde{\alpha}$ and the unit vector field μ

(2) If $f' \neq 0$, then $\kappa_{\tilde{\alpha}} = ((\ell \pm \xi')\cos\xi)/f'$, where ξ is the angle between the tangent vector of $\tilde{\alpha}$ and the unit vector field ω

Proof. Let (γ, ω): $I \longrightarrow \mathbb{R}^2 \times S^1$ be a Legendre curve and $\tilde{\alpha}$ be its associated f-curve via the vector field ω. Then, we have

$$\tilde{\alpha}' = f'\omega + (\beta + f\ell)\mu. \tag{31}$$

Case 1. If $f = -\beta/\ell$, then from Lemma 12, $\tilde{\alpha}$ is a regular curve, and we have

$$\tilde{\alpha}' \cdot \mu = \beta + f\ell, \tag{32}$$

which gives

$$\left\|\tilde{\alpha}'\right\|\|\mu\|\cos\psi = \beta + f\ell. \tag{33}$$

So, we have

$$\left\|\tilde{\alpha}'\right\|\cos\psi = \beta + f\ell. \tag{34}$$

Equation (34) can be rewritten as

$$\left\|\tilde{\alpha}'\right\| = (\beta + f\ell)\sec\psi. \tag{35}$$

From equation (31), we have

$$\left\|\tilde{\alpha}'\right\|^2 = (\beta + f\ell)^2 + \left(f'\right)^2. \tag{36}$$

Now, using equation (34) in (36), we get

$$\left\|\tilde{\alpha}'\right\|^2 = \left\|\tilde{\alpha}'\right\|^2\cos^2\psi + \left(f'\right)^2. \tag{37}$$

So,

$$f' = \pm\left\|\tilde{\alpha}'\right\|\sin\psi. \tag{38}$$

From (34) and (38), equation (31) becomes

$$\tilde{\alpha}' = \left(\pm\left\|\tilde{\alpha}'\right\|\sin\psi\right)\omega + \left(\left\|\tilde{\alpha}'\right\|\cos\psi\right)\mu. \tag{39}$$

Now,

$$\begin{aligned} T_{\tilde{\alpha}} &= (\pm\sin\psi)\omega + (\cos\psi)\mu, \\ N_{\tilde{\alpha}} &= (-\cos\psi)\omega \pm (\sin\psi)\mu. \end{aligned} \tag{40}$$

Thus,

$$T_{\tilde{\alpha}}' \cdot N_{\tilde{\alpha}} = \ell \mp \psi'. \tag{41}$$

Hence,

$$\kappa_{\tilde{\alpha}} = \frac{\left(\ell \mp \psi'\right)\cos\psi}{\beta + \ell f}. \tag{42}$$

Case 2. If $f'=0$, then from Lemma 12, $\tilde{\alpha}$ is a regular curve, and we have

$$\tilde{\alpha}' \cdot \omega = f', \tag{43}$$

which gives

$$\left\|\tilde{\alpha}'\right\| \|\omega\| \cos \xi = f'. \tag{44}$$

So, we have

$$\left\|\tilde{\alpha}'\right\| \cos \xi = f'. \tag{45}$$

Equation (45) can be rewritten as

$$\left\|\tilde{\alpha}'\right\| = \left(f'\right) \sec \xi. \tag{46}$$

Now, using equation (45) in (36), we have

$$\left\|\tilde{\alpha}'\right\|^2 = (\beta + \ell f)^2 + \left\|\tilde{\alpha}'\right\|^2 \cos^2 \xi. \tag{47}$$

So,

$$\beta + \ell f = \pm \left\|\tilde{\alpha}'\right\| \sin \xi. \tag{48}$$

Substituting (45) and (48) in (31), we get

$$\tilde{\alpha}' = \left(\left\|\tilde{\alpha}'\right\| \cos \xi\right)\omega \pm \left(\left\|\tilde{\alpha}'\right\| \sin \xi\right)\mu. \tag{49}$$

Now,

$$\begin{aligned} T_{\tilde{\alpha}} &= (\cos \xi)\omega \pm (\sin \xi)\mu, \\ N_{\tilde{\alpha}} &= \mp(\sin \xi)\omega + (\cos \xi)\mu. \end{aligned} \tag{50}$$

Thus,

$$T'_{\tilde{\alpha}} \cdot N_{\tilde{\alpha}} = \ell \pm \xi'. \tag{51}$$

Hence,

$$\kappa_{\tilde{\alpha}} = \frac{\left(\ell \pm \xi'\right) \cos \xi}{f'}. \tag{52}$$

□

Now, we have the following corollary of Theorem 13.

Corollary 14. *Let γ be a frontal and $\tilde{\alpha}$ be its associated f-curve via the vector field ω.*

(1) If f is a unique smooth function such that $f = -\beta/\ell$ and $f'=0$, then $\tilde{\alpha}$ is the evolute of γ and it is a regular curve with $\kappa_{\tilde{\alpha}} = \pm\ell^3/(\ell'\beta - \ell\beta')$

(2) If f is a constant and $f \neq -\beta/\ell$, then $\kappa_{\tilde{\alpha}} = \pm\ell/(\beta + f\ell)$

4. f-Curve via the Tangent Vector Associated with a Plane Curve

4.1. Regular Curve

Definition 15. Let $\gamma : I \longrightarrow \mathbb{R}^2$ be a regular parametrized curve. Then, the f-curve via the tangent vector associated with γ is given by $\Omega(t) = \gamma(t) + f(t)T_\gamma(t)$, where $f : I \longrightarrow \mathbb{R}$ is a smooth function.

Now, we state the following lemma.

Lemma 16. *Let $\gamma : I \longrightarrow \mathbb{R}^2$ be a unit speed curve. Then, the curve Ω associated with γ is regular if and only if $f' \neq -1$ or $f\kappa_\gamma \neq 0$.*

Remark 17. From Lemma 16, if Ω has a singularity at t_0, then γ has an inflexion point at t_0 or $\Omega(t_0) = \gamma(t_0)$.

Theorem 18. *Let $\gamma : I \longrightarrow \mathbb{R}^2$ be a unit speed curve and Ω be its associated f-curve via the tangent vector.*

(1) If $f' \neq -1$, then $\kappa_\Omega = ((\kappa_\gamma \pm \zeta') \cos \zeta)/(1 + f')$, where ζ is the angle between the tangent vector of Ω and the unit tangent vector of γ

(2) If $f\kappa_\gamma \neq 0$, then $\kappa_\Omega = ((\kappa_\gamma \mp \Psi') \cos \Psi)/f\kappa_\gamma$, where Ψ is the angle between the tangent vector of Ω and the unit normal vector of γ

Proof. Let $\gamma : I \longrightarrow \mathbb{R}^2$ be a unit speed curve and Ω be its associated f-curve via the tangent vector. Then, we have

$$\Omega' = \left(1 + f'\right) T_\gamma + f\kappa_\gamma N_\gamma. \tag{53}$$

Case 1. If $f' \neq -1$, then from Lemma 16, Ω is a regular curve, and we have

$$\Omega' \cdot T_\gamma = 1 + f', \tag{54}$$

which gives

$$\left\|\Omega'\right\| \cos \zeta = 1 + f'. \tag{55}$$

From equation (53), we have

$$\left\|\Omega'\right\|^2 = \left(1 + f'\right)^2 + \left(f\kappa_\gamma\right)^2. \tag{56}$$

Substituting equation (55) in equation (56), we obtain that

$$f\kappa_\gamma = \pm \left\|\Omega'\right\| \sin \zeta. \tag{57}$$

From equation (55) and equation (57), equation (53) becomes

$$\Omega' = \left(\left\|\Omega'\right\| \cos\zeta\right) T_\gamma \pm \left(\left\|\Omega'\right\| \sin\zeta\right) N_\gamma. \tag{58}$$

Therefore,

$$\begin{aligned} T_\Omega &= (\cos\zeta) T_\gamma \pm (\sin\zeta) N_\gamma, \\ N_\Omega &= \mp(\sin\zeta) T_\gamma + (\cos\zeta) N_\gamma. \end{aligned} \tag{59}$$

Hence,

$$\kappa_\Omega = \frac{T_\Omega' \cdot N_\Omega}{\left\|\Omega'\right\|} = \frac{\left(\kappa_\gamma \pm \zeta'\right)\cos\zeta}{1 + f'}. \tag{60}$$

Case 2. If $f\kappa_\gamma$=0, then from Lemma 16, Ω is a regular curve, and we have

$$\Omega' \cdot N_\gamma = f\kappa_\gamma, \tag{61}$$

which gives

$$\left\|\Omega'\right\| \cos\Psi = f\kappa_\gamma. \tag{62}$$

Substituting (62) in (56), we obtain that

$$1 + f' = \pm\|\Omega\| \sin\Psi. \tag{63}$$

From equation (62) and equation (63), equation (53) becomes

$$\Omega' = \left(\pm\left\|\Omega'\right\| \sin\Psi\right) T_\gamma + \left(\left\|\Omega'\right\| \cos\Psi\right) N_\gamma. \tag{64}$$

Therefore,

$$\begin{aligned} T_\Omega &= (\pm\sin\Psi) T_\gamma + (\cos\Psi) N_\gamma, \\ N_\Omega &= -(\cos\Psi) T_\gamma \pm (\sin\Psi) N_\gamma. \end{aligned} \tag{65}$$

Hence,

$$\kappa_\Omega = \frac{T_\Omega' \cdot N_\Omega}{\left\|\Omega'\right\|} = \frac{\left(\kappa_\gamma \mp \Psi'\right)\cos\Psi}{f\kappa_\gamma}. \tag{66}$$

□

The following corollary can be easily obtained from Theorem 18.

Corollary 19. *Let $\gamma : I \longrightarrow \mathbb{R}^2$ be a unit speed curve and Ω be its associated f-curve via the tangent vector. If $f' = -1$ (that is, $f(s) = C - s$ for some constant C) and $f \neq 0$, then Ω is the involute of γ and $\kappa_\Omega = sing(\kappa_\gamma)/|f|$.*

From Theorem 18, it can be easily obtained a simple and neat formula for the curvature of the regular part of the midlocus associated with a regular part of the symmetry set of a plane curve. The symmetry set of a plane curve is the closure of the locus of centers of the bitangent circles, and the associated midlocus is the set of all midpoints of the chords joining the tangency points. For more detail in the symmetry set of a plane curve and the associated midlocus, we refer the reader to [9–12].

In [9], the first author of this paper obtained the curvature of the midlocus associated with the regular part of the symmetry set of a plane curve. This curvature is given by the following formula:

$$\kappa_\Omega = \frac{\cos\Theta\left(\kappa_\gamma + \Theta'\right)}{\sin\varphi\left(\sin\varphi + r\varphi'\right)}, \tag{67}$$

where φ is the angle between the normal of a given curve γ and the tangent of its symmetry set and Θ is the angle between the tangent of the symmetry set and the tangent of midlocus and prime denotes the derivative with respect to the arc length of the symmetry set. This formula contains more factors than the following formula in the next corollary which gives a simple formula of the curvature of the midlocus. In the following corollary, γ is the symmetry set of a given curve, r is the radius function of the bitangent circles, and the associated f-curve via the tangent of γ is the associated midlocus.

Corollary 20. *Let $\gamma : I \longrightarrow \mathbb{R}^2$ be a unit speed curve and Ω be its associated f-curve via the tangent vector such that $f = -rr'$.*

(1) If $f' \neq -1$, then $\kappa_\Omega = ((\kappa_\gamma \pm \zeta')\cos\zeta)/(1 - r'2 - rr'')$

(2) If $f\kappa_\gamma \neq 0$, then $\kappa_\Omega = (-(\kappa_\gamma \mp \Psi')\cos\Psi)/rr'\kappa_\gamma$

4.2. Legendre Curve

Definition 21. Let (γ, ω): $I \longrightarrow \mathbb{R}^2 \times S^1$ be a Legendre curve. The f -curve via the vector filed μ associated with γ is given by $\tilde{\Omega}(t) = \gamma(t) + f(t)\mu(t)$, where $f : I \longrightarrow \mathbb{R}$ is a smooth function.

Lemma 22. *Let (γ, ω): $I \longrightarrow \mathbb{R}^2 \times S^1$ be a Legendre curve. The f-curve via the vector field μ associated with γ is regular if and only if $\beta + f' \neq 0$ or ℓf=0.*

Theorem 23. *Let (γ, ω): $I \longrightarrow \mathbb{R}^2 \times S^1$ be a Legendre curve and $\tilde{\Omega}$ be its associated f-curve via the vector field μ.*

(1) If $\beta + f' \neq 0$, then $\kappa_{\tilde{\Omega}} = ((\ell \mp \eta')\cos\eta)/(\beta + f')$, where η is the angle between the tangent vector of $\tilde{\Omega}$ and the unit vector field μ

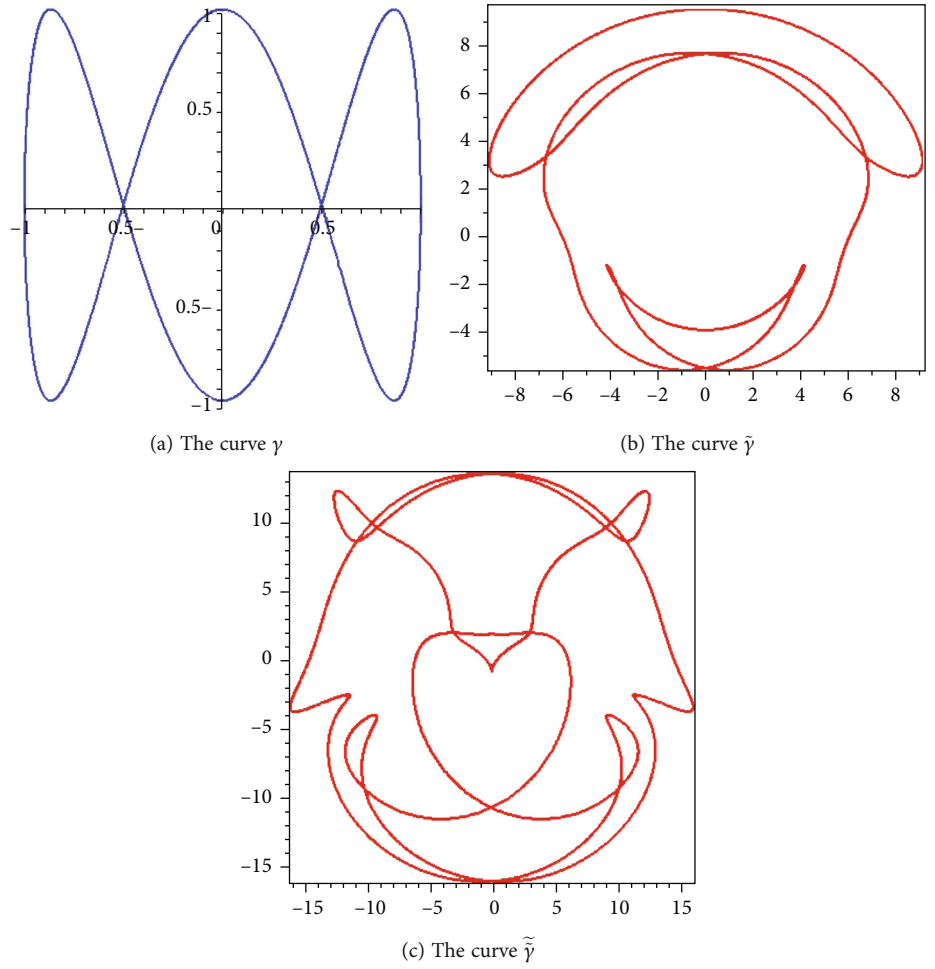

(a) The curve γ

(b) The curve $\tilde{\gamma}$

(c) The curve $\widetilde{\tilde{\gamma}}$

FIGURE 1: The curve γ and its resulting f-curves.

(2) If $\ell f \neq 0$, then $\kappa_{\tilde{\Omega}} = ((\ell \pm \varepsilon')\cos\varepsilon)/\ell f$, where ε is the angle between the tangent vector of $\tilde{\Omega}$ and the unit vector field ω

Proof. Let (γ, ω): $I \longrightarrow \mathbb{R}^2 \times S^1$ be a Legendre curve and $\tilde{\Omega}$ be its associated f-curve via the vector field μ. Then, we have

$$\tilde{\Omega}' = \left(\beta + f'\right)\mu - (\ell f)\omega. \tag{68}$$

Case 1. If $\beta + f' = 0$, then from Lemma 22, $\tilde{\Omega}$ is a regular curve, and we have

$$\tilde{\Omega}' \cdot \mu = \beta + f', \tag{69}$$

which gives

$$\left\|\tilde{\Omega}'\right\| \cos\eta = \beta + f'. \tag{70}$$

From equation (68), we have

$$\left\|\tilde{\Omega}'\right\|^2 = (\beta + f)^2 + (\ell f)^2. \tag{71}$$

Substituting (70) in (71), it can be shown that

$$\ell f = \pm\left\|\tilde{\Omega}'\right\| \sin\eta. \tag{72}$$

From (70) and (72), equation (68) becomes

$$\tilde{\Omega}' = \left(\left\|\tilde{\Omega}'\right\| \cos\eta\right)\mu \mp \left(\left\|\tilde{\Omega}'\right\| \sin\eta\right)\omega. \tag{73}$$

Now,

$$\begin{aligned} T_{\tilde{\Omega}} &= (\mp\sin\eta)\omega + (\cos\eta)\mu, \\ N_{\tilde{\Omega}} &= (-\cos\eta)\omega \mp (\sin\eta)\mu. \end{aligned} \tag{74}$$

Hence,

$$\kappa_{\tilde{\Omega}} = \frac{\left(\ell \pm \eta'\right)\cos\eta}{\beta + \ell f'}. \tag{75}$$

Case 2. If $\ell f \neq 0$, then from Lemma 22, $\tilde{\Omega}$ is a regular curve, and we have

$$\tilde{\Omega}' \cdot \omega = -\ell f, \tag{76}$$

which gives

$$\left\|\tilde{\Omega}'\right\| \cos\varepsilon = -\ell f. \tag{77}$$

Using equation (77) in (71), it can be shown that

$$\beta + f' = \pm\left\|\tilde{\Omega}'\right\| \sin\varepsilon. \tag{78}$$

From (77) and (78), equation (68) becomes

$$\tilde{\Omega}' = \left(\left\|\tilde{\Omega}'\right\| \cos\varepsilon\right)\omega \pm \left(\left\|\tilde{\Omega}'\right\| \sin\varepsilon\right)\mu. \tag{79}$$

Now,

$$\begin{aligned} T_{\tilde{\Omega}} &= (\cos\varepsilon)\omega \pm (\sin\varepsilon)\mu, \\ N_{\tilde{\Omega}} &= (\mp\sin\varepsilon)\omega + (\cos\varepsilon)\mu. \end{aligned} \tag{80}$$

Hence,

$$\kappa_{\tilde{\Omega}} = \frac{\left(\ell \pm \varepsilon'\right)\cos\varepsilon}{\ell f}. \tag{81}$$

□

Corollary 24. *Let (γ, ω): $I \longrightarrow \mathbb{R}^2 \times S^1$ be a Legendre curve with the curvature (ℓ, β) and $\tilde{\Omega}$ be its associated f-curve via the vector field μ. If $f = -\int_{t_0}^{t}\beta(u)du$ and $\ell f \neq 0$, then $\tilde{\Omega}$ is the involute of the frontal and it is a regular curve with $\kappa_{\tilde{\Omega}} = \pm 1/\int_{t_0}^{t}\beta(u)du$.*

5. Examples

In this section, we give an example in the case of a regular curve and we repeat the process to the resulting curve but with different function f. We use the Maple for calculation and drawing pictures. First, let us consider the curve $\gamma(t) = (\cos(t), \sin(3t))$, $t \in (0, 2\pi)$. It is clear that γ is a closed curve (see Figure 1(a)), and we choose $f_1(t) = 3\sin(t) - 5e^{\sin(t)}$. The f_1-curve via the normal vector associated with γ is given by $\tilde{\gamma}(t) = \gamma(t) + f_1(t)N_\gamma(t) = (\tilde{\gamma}_1(t), \tilde{\gamma}_2(t))$, where

$$\begin{aligned} \tilde{\gamma}_1(t) &= \cos(t) + \frac{15\cos(3t)e^{\sin(t)} - 9\cos(3t)\sin(t)}{\sqrt{144\cos^6(t) - 216\cos^4(t) + 80\cos^2(t) + 1}}, \\ \tilde{\gamma}_2(t) &= \sin(t) + \frac{5\sin(t)e^{\sin(t)} + 3\cos^2(t) - 3}{\sqrt{144\cos^6(t) - 216\cos^4(t) + 80\cos^2(t) + 1}}. \end{aligned} \tag{82}$$

The graph of $\tilde{\gamma}$ is shown in Figure 1(b), and we may call this graph Clown's face.

In what follows, we consider the f-curve via the normal vector associated with $\tilde{\gamma}$ with $f(t) = f_2(t) = -5 - 2e^{\sin(9t)}$; this curve is given by $\tilde{\tilde{\gamma}}(t) = \tilde{\gamma}(t) + f_2(t)N_{\tilde{\gamma}}$. The calculation becomes very tedious, and the forms of $\tilde{\tilde{\gamma}}_1$ and $\tilde{\tilde{\gamma}}_2$ are too long and very complicated. We just use the Maple for drawing the graph of this curve which is shown in Figure 1(c). Again, the resulting graph is interesting as well as the graph of $\tilde{\gamma}$ and we may call this graph Tiger's face.

Remark 25. From this section, one can observe the importance of f-curves associated with a plane curve in the theory of computer graphics. We hope this method for creating curves from a given curve will find its applications to computer graphics and related topics soon.

6. Final Remark

Throughout this paper, we introduce the concept of the f-curves associated with a plane curve in the cases of Frenet and Legendre curves. The curvatures of these new curves have been obtained in several ways. This work has direct applications to the motion of particles in the plane. Also, it is useful for calculating the centripetal acceleration and the centripetal force of a particle traversing a curved path such as f-curve in the plane.

Data Availability

No external data has been used in this study.

Conflicts of Interest

The authors declare that they have no conflicts of interest.

References

[1] C. E. Mungan, "A refresher on curvature for application to centripetal acceleration," *Latin-American Journal of Physics Education*, vol. 4, pp. 27–30, 2010.

[2] T. Fukunaga and M. Takahashi, "Existence and uniqueness for Legendre curves," *Journal of Geometry*, vol. 104, no. 2, pp. 297–307, 2013.

[3] T. Fukunaga and M. Takahashi, "Evolutes of fronts in the Euclidean plane," *Journal of Singularities*, vol. 10, pp. 92–107, 2014.

[4] T. Fukunaga and M. Takahashi, "Evolutes and involutes of frontals in the Euclidean plane," *Demonstratio Mathematica*, vol. 48, no. 2, pp. 147–166, 2015.

[5] S. Isumiya and N. Takahashi, "Evolutoids and pedaloids of plane curves," *Note di Matematica*, vol. 39, pp. 13–24, 2019.

[6] A. Pressley, *Elementary Differential Geometry*, 2010, Springer London.

[7] M. Carmo, *Differential Geometry of Curves and Surfaces*, Prentice-Hall, New Jersey, 1976.

[8] T. Fukunaga and M. Takahashi, "Involutes of fronts in the Euclidean plane," *Beiträge zur Algebra und Geometrie/Contributions to Algebra and Geometry*, vol. 57, no. 3, pp. 637–653, 2016.

[9] A. Alghanemi, "The curvature of the midlocus in the plane," *International Journal of Scientific and Innovative Mathematical Research*, vol. 4, pp. 1–6, 2016.

[10] A. Alghanemi, *Geometry of skeletal structures and symmetry sets, [Ph. D. thesis]*, University of Leeds, 2012.

[11] J. W. Bruce, P. J. Giblin, and C. G. Gibson, "Symmetry sets," *Proceedings of the Royal Society of Edinburgh*, vol. 101, no. 1-2, pp. 163–186, 1985.

[12] P. J. Giblin and S. A. Barassett, "Local symmetry of plane curves," *The American Mathematical Monthly*, vol. 92, no. 10, pp. 689–707, 1985.

Hindawi
Advances in Mathematical Physics
Volume 2022, Article ID 6350959, 12 pages
https://doi.org/10.1155/2022/6350959

Research Article

Certain Concepts of Interval-Valued Intuitionistic Fuzzy Graphs with an Application

Peng Xu,[1,2] **Hao Guan**,[1] **A. A. Talebi**,[3] **M. Ghassemi**,[3] **and Hossein Rashmanlou**[3]

[1]*Institute of Computational Science and Technology, Guangzhou University, Guangzhou, Guangdong 510006, China*
[2]*School of Computer Science of Information Technology, Qiannan Normal University for Nationalities, Duyun, Guizhou 558000, China*
[3]*Department of Mathematics, University of Mazandaran, Babolsar, Iran*

Correspondence should be addressed to Hao Guan; guanhao@gzhu.edu.cn

Received 9 February 2022; Accepted 30 March 2022; Published 19 April 2022

Academic Editor: Meraj Ali Khan

Interval-valued intuitionistic fuzzy graph (IVIFG), belonging to the FGs family, has good capabilities when facing with problems that cannot be expressed by FGs. When an element membership is not clear, neutrality is a good option that can be well supported by an IVIFG. The previous definitions of limitations in edge irregular FG have led us to offer new definitions in IVIFGs. Hence, in this paper, some types of edge irregular interval-valued intuitionistic fuzzy graphs (EI-IVIFGs) such as neighborly edge totally irregular (NETI), strongly edge irregular (SEI), and strongly edge totally irregular (SETI) are introduced. A comparative study between NEI-IVIFGs and NETI-IVIFGs is done. With the help of IVIFGs, the most efficient person in an organization can be identified according to the important factors that can be useful for an institution. Finally, an application of IVIFG has been introduced.

1. Introduction

The FG concept serves as one of the most dominant and extensively employed tools for multiple real-word problem representations, modeling, and analysis. To specify the objects and the relations between them, the graph vertices or nodes and edges or arcs are applied, respectively. Graphs have long been used to describe objects and the relationships between them. Many of the issues and phenomena around us are associated with complexities and ambiguities that make it difficult to express certainty. These difficulties were alleviated by the introduction of fuzzy sets by Zadeh [1]. The fuzzy set focuses on the membership degree of an object in a particular set. Kaufman [2] represented FGs based on Zadeh's fuzzy relation [3, 4]. Rosenfeld [5] described the structure of FGs obtaining analogs of several graph theoretical concepts. Bhattacharya [6] gave some remarks on FGs. Several concepts on FGs were introduced by Mordeson and Nair [7]. The existence of a single degree for a true membership could not resolve the ambiguity on uncertain issues, so the need for a degree of membership was felt. Afterward, to overcome the existing ambiguities, Atanassov [8] defined an extension of fuzzy set by introducing nonmembership function and defined intuitionistic fuzzy set (IFS). But after a while, Atanassov and Gargov [9] developed IFS and presented interval-valued intuitionistic fuzzy set (IVIFS). In 1999, Atanassov [10] defined intuitionistic fuzzy graph (IFG), but Akram and Davvaz investigated it in more details in [11]. Hongmei and Lianhua [12] defined interval-valued fuzzy graph and studied its properties. Karunambigai et al. [13] discussed edge regular IFG. Mishra and Pal [14] introduced product of IVIFG. Nagoorgani and Radha [15, 16] studied the concept of regular fuzzy graphs and defined degree of a vertex in FGs. Nagoorgani and Latha [17] investigated the concept of IFGs, NI-FGs, and HI-FGs in 2008. Shao et al. [18] discussed new concepts in IFG. Nandhini and Nandhini [19] described the concept of SI-FGs and studied its properties. Santhi Maheswari and Sekar defined the concepts of edge

irregular FGs and edge totally irregular FGs [20]. Also, they analyzed some properties of NEI-FGs, NETI-FGs, SEI-FGs, and SETI-FGs [21, 22]. Rao et al. [23–25] studied dominating set, equitable dominating set, valid degree, isolated vertex, and some properties of VGs with novel application. Shi and Kosari [26] introduced total dominating set and global dominating set in product vague graphs. Talebi et al. [27–30] defined new concepts of irregularity in single-valued neutrosophic graphs and intuitionistic fuzzy graphs. Kou et al. [31] studied vague graphs with application in transportation systems. Kalaiarasi and Mahalakshmi [32] investigated regular and irregular m -polar fuzzy graphs. Selvanayaki [33] introduced strong and balanced irregular interval-valued fuzzy graphs. Rashmanlou et al. [34] investigate new results in cubic graphs. Poulik and Ghorai [35–37] initiated degree of nodes, detour g-interior nodes, and indices of bipolar fuzzy graphs with applications in real-life systems. Pramanik et al. [38] defined fuzzy competition graph and its uses in manufacturing industries. Muhiuddin et al. [39] introduced reinforcement number of a graph with respect to half-domination. Amanathulla et al. [40] studied on distance two surjective labeling of paths and interval graphs. Ramprasad et al. [41] investigated some properties of highly irregular, edge regular, and totally edge regular m -polar fuzzy graphs. Nazeer et al. [42] introduced an application of product intuitionistic fuzzy incidence graphs in textile industry. Bhattacharya and Pal [43] studied fuzzy covering problem of fuzzy graphs and its application. Borzooei et al. [44] defined inverse fuzzy graphs.

IVIFGs have a wide range of applications in the field of psychological sciences as well as the identification of individuals based on oncological behaviors. With the help of IVIFGs, the most efficient person in an organization can be identified according to the important factors that can be useful for an institution. So, in this paper, some types of EI-IVIFGs such as neighborly edge totally irregular- (NETI-) IVIFGs, strongly edge irregular- (SEI-) IVIFGs, and strongly edge totally irregular- (SETI-) IVIFGs are introduced. Also, we have given some interesting results about EI-IVIFGs, and several examples are investigated. Finally, an application of IVIFG is presented.

2. Preliminaries

A graph $G = (V, E)$ is a mathematical model consisting of a set of nodes V and a set of edges E, where each is an unordered pair of distinct nodes.

Definition 1 (see [5]). A FG $Z = (V, \nu, \xi)$ is a nonempty set V together with a pair of functions $\nu : V \longrightarrow [0, 1]$ and $\xi : V \times V \longrightarrow [0, 1]$ so that $\xi(xy) \leq \min\{\nu(x), \nu(y)\}, \forall x, y \in V$.

Definition 2 (see [11]). An IFG is of the form $G : (\eta, \varsigma)$ which $\eta = (\eta_1, \eta_2)$ and $\varsigma = (\varsigma_1, \varsigma_2)$ so that

(i) The functions $\eta_1 : V \longrightarrow [0, 1]$ and $\eta_2 : V \longrightarrow [0, 1]$ denotes the MD and NM-D of the element $w \in V$, respectively, and $0 \leq \eta_1(w) + \eta_2(w) \leq 1$ for each $w \in V$

(ii) The functions $\varsigma_1 : V \times V \longrightarrow [0, 1]$ and $\varsigma_2 : V \times V \longrightarrow [0, 1]$ are the MD and NM-D of the edge $xw \in E$, respectively, so that $\varsigma_1(xw) \leq \min(\eta_1(x), \eta_1(w))$ and $\varsigma_2(xw) \geq \max(\eta_2(x), \eta_2(w))$ and $0 \leq \varsigma_1(xw) + \varsigma_2(xw) \leq 1$, for each xw in E

Definition 3 (see [11]). An IVFG is of the form $G : (\theta, \zeta)$ which $\theta = [\theta^-, \theta^+]$ is an IVFS in V and $\zeta = (\zeta^-, \zeta^+)$ is an IVFS in $E \subseteq V \times V$ so that $\zeta^-(xw) \leq \min(\theta^-(x), \theta^-(w))$ and $\zeta^+(xw) \leq \min(\theta^+(x), \theta^+(w))$ for each xw in E.

All the basic notations are shown in Table 1.

3. New Concepts of Irregular IVIFGs

Definition 4. An IVIFG is of the form $G : (\sigma, \mu)$ which $\sigma = (\sigma_1, \sigma_2) = ((\sigma_1^-, \sigma_1^+), (\sigma_2^-, \sigma_2^+))$ and $\mu = (\mu_1, \mu_2) = ((\mu_1^-, \mu_1^+), (\mu_2^-, \mu_2^+))$ so that

(i) The functions $\sigma_1 : V \longrightarrow D[0, 1]$ and $\sigma_2 : V \longrightarrow D[0, 1]$ denote the degree of IVM and IV-NM of the element $w \in V$, respectively, so that $0 \leq \sigma_1^+(w) + \sigma_2^+(w) \leq 1$, for each $w \in V$

(ii) The functions $\mu_1 : V \times V \longrightarrow D[0, 1]$ and $\mu_2 : V \times V \longrightarrow D[0, 1]$ denote the degree of IVM and IV-NM of the edge $wz \in E$, respectively, are defined by the following:

(i) $\mu_1^-(wz) \leq \min(\sigma_1^-(w), \sigma_1^-(z))$ and $\mu_1^+(wz) \leq \min(\sigma_1^+(w), \sigma_1^+(z))$

(ii) $\mu_2^-(wz) \geq \max(\sigma_2^-(w), \sigma_2^-(z))$ and $\mu_2^+(wz) \geq \max(\sigma_2^+(w), \sigma_2^+(z))$

so that $0 \leq \mu_1^+(wz) + \mu_2^+(wz) \leq 1$, for each wz in E.

Definition 5. Let G be an IVIFG. Then, the degree of a node w is defined as $d_G(w) = ((d_{\sigma_1^-}(w), d_{\sigma_1^+}(w)), (d_{\sigma_2^-}(w), d_{\sigma_2^+}(w)))$, where $d_{\sigma_1^-}(w) = \Sigma_{z \neq w}\mu_1^-(w, z)$, $d_{\sigma_1^+}(w) = \Sigma_{z \neq w}\mu_1^+(w, z)$, $d_{\sigma_2^-}(w) = \Sigma_{z \neq w}\mu_2^-(w, z)$, and $d_{\sigma_2^+}(w) = \Sigma_{z \neq w}\mu_2^+(w, z)$.

Definition 6. Let G be an IVIFG. Then, the TD of a node w is defined as $td_G(w) = ((td_{\sigma_1^-}(w), td_{\sigma_1^+}(w)), (td_{\sigma_2^-}(w), td_{\sigma_2^+}(w)))$ which $td_{\sigma_1^-}(w) = \Sigma_{z \neq w}\mu_1^-(w, z) + \sigma_1^-(w)$, $td_{\sigma_1^+}(w) = \Sigma_{z \neq w}\mu_1^+(w, z) + \sigma_1^+(w)$, $td_{\sigma_2^-}(w) = \Sigma_{z \neq w}\mu_2^-(w, z) + \sigma_2^-(w)$, and $td_{\sigma_2^+}(w) = \Sigma_{z \neq w}\mu_2^+(w, z) + \sigma_2^+(w)$.

Definition 7. Let G be an IVIFG on. Then,

(i) G is irregular, if there is a node which is a neighbor to nodes with VDs

(ii) G is TI, if there is a node which is a neighbor to nodes with various TDs

Table 1: Some basic notations.

Notation	Meaning
IFG	Intuitionistic fuzzy graph
IVFG	Interval-valued fuzzy graph
IVIFG	Interval-valued intuitionistic fuzzy graph
IVM	Interval valued membership
IV-NM	Interval-valued nonmembership
I-FG	Irregular fuzzy graph
SI	Strongly irregular
HI	Highly irregular
NI	Neighborly irregular
VD	Various degree
TD	Total degree
TI	Total irregular
MD	Membership degree
NE	Neighbor edge
NEI-IVIFG	Neighborly edge irregular interval-valued intuitionistic fuzzy graph
CIVIFG	Connected interval-valued intuitionistic fuzzy graph
IVFS	Interval-valued fuzzy set
NEI	Neighborly edge irregular
NETI	Neighborly edge totally irregular
TER	Totally edge regular
SETI	Strongly edge totally irregular
SEI	Strongly edge irregular
HEI	Highly edge irregular
HETI	Highly edge totally irregular
CF	Constant function

Definition 8. Let G be a CIVIFG. Then, G is called an

(i) NI-IVIFG if each pair of neighbor nodes has VDs

(ii) NTI-IVIFG if each pair of neighbor nodes has various TDs

(iii) SI-IVIFG if each pair of nodes has VDs

(iv) STI-IVIFG if each pair of nodes has various TDs

(v) HI-IVIFG if each node in G is neighbor to the nodes having VDs

(vi) HTI-IVIFG if each node in G is neighbor to the nodes having various TDs

Definition 9. Let G be an IVIFG on. The degree of an edge wz is described as $d_G(wz) = ((d_{\mu_1^-}(wz), d_{\mu_1^+}(wz)), (d_{\mu_2^-}(wz), d_{\mu_2^+}(wz)))$ which $d_{\mu_i^-}(wz) = d_{\sigma_i^-}(w) + d_{\sigma_i^-}(z) - 2\mu_i^-(wz)$ and $d_{\mu_i^+}(wz) = d_{\sigma_i^+}(w) + d_{\sigma_i^+}(z) - 2\mu_i^+(wz)$, for $i = 1, 2$.

Definition 10. Let G be an IVIFG. The TD of an edge wz is presented as $td_G(wz) = ((td_{\mu_1^-}(wz), td_{\mu_1^+}(wz)), (td_{\mu_2^-}(wz), td_{\mu_2^+}(wz)))$ where $td_{\mu_i^-}(wz) = d_{\sigma_i^-}(w) + d_{\sigma_i^-}(z) - \mu_i^-(wz) = d_{\mu_i^-}(wz) + \mu_i^-(wz)$ and $td_{\mu_i^+}(wz) = d_{\sigma_i^+}(w) + d_{\sigma_i^+}(z) - \mu_i^+(wz) = d_{\mu_i^+}(wz) + \mu_i^+(wz)$, for $i = 1, 2$.

Definition 11. Let G be a CIVIFG. Then, G is called an

(i) NEI-IVIFG if each pair of NEs has VDs

(ii) NETI-IVIFG if each pair of NEs has various TDs

Example 12. Graph which is both NEI-IVIFG and NETI-IVIFG.

Consider G^* which $V = \{u, v, w, x\}$ and $E = \{uv, vw, wx, xu\}$.

From Figure 1, $d_G(u) = d_G(v) = d_G(w) = d_G(x) = ((0.3,0.5), (0.5,1.0))$, $d_G(uv) = d_G(wx) = ((0.4,0.6), (0.4,0.8))$, and $d_G(vw) = d_G(xu) = ((0.2,0.4), (0.6,1.2))$.

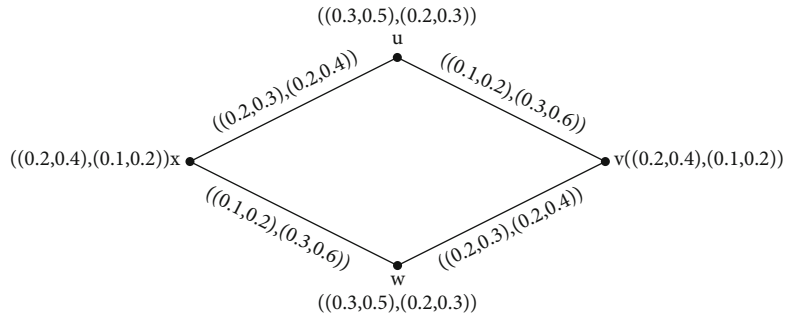

Figure 1: G is both NEI-IVIFG and NETI-IVIFG.

Clearly, neighbor edges have VDs. Hence, G is a NEI-IVIFG.

For TDs, we have the following:

$$\begin{aligned} td_G(uv) = td_G(wx) = ((0.5,0.8),(0.7,1.4)),\\ td_G(vw) = td_G(xu) = ((0.4,0.7),(0.8,1.6)). \end{aligned} \tag{1}$$

Obviously, neighbor edges have various TDs. So, G is a NETI-IVIFG. Hence, G is both NEI-IVIFG and NETI-IVIFG.

Example 13. NEI-IVIFG needs not to be NETI-IVIFG.

Consider G be an IVIFG and G^* a star includes four nodes.

From Figure 2, $d_G(u) = ((0.2,0.3),(0.3,0.4))$, $d_G(v) = ((0.1,0.2),(0.4,0.5))$, $d_G(w) = ((0.0,0.1),(0.5,0.6))$, $d_G(x) = ((0.3,0.6),(1.2,1.5))$, $d_G(ux) = ((0.1,0.3),(0.9,1.1))$, $d_G(vx) = ((0.2,0.4),(0.8,1.0))$, $d_G(wx) = ((0.3,0.5),(0.7,0.9))$, and $td_G(ux) = td_G(vx) = td_G(wx) = ((0.3,0.6),(1.2,1.5))$.

Here, $d_G(ux) \neq d_G(vx) \neq d_G(wx)$. Hence, G is a NEI-IVIFG. But G is not a NETI-IVIFG, since all edges have same TDs.

Example 14. NETI-IVIFGs need not to be NEI-IVIFGs. The following shows this subject:

Consider G be an IVIFG so that G^* a path consists of 4 nodes.

From Figure 3, $d_G(u) = d_G(x) = ((0.05,0.20),(0.15,0.25))$, $d_G(v) = d_G(w) = ((0.15,0.60),(0.45,0.75))$, $d_G(uv) = d_G(vw) = d_G(wx) = ((0.1,0.4),(0.3,0.5))$, $td_G(uv) = ((0.15,0.60),(0.45,0.75))$, $td_G(vw) = ((0.2,0.8),(0.6,1.0))$, and $td_G(wx) = ((0.15,0.60),(0.45,0.75))$.

Here, $d_G(uv) = d_G(vw) = d_G(wx)$. Hence, G is not a NEI-IVIFG. But G is a NETI-IVIFG, since $td_G(uv) \neq td_G(vw)$ and $td_G(vw) \neq td_G(wx)$.

Theorem 15. *Suppose G is a CIVIFG and μ is a CF. Then, G is a NEI-IVIFG if G is a NETI-IVIFG.*

Proof. Assume that μ is a CF and $\mu(wz) = f, \forall wz$ in E, which $f = ((f_1^-, f_1^+), (f_2^-, f_2^+))$ is constant.

Let wz and zy be pairs of neighbor edges in E; then, we have the following:

$$\begin{aligned} &d_G(wz) \neq d_G(zy) \Leftrightarrow d_G(wz) + d \neq d_G(zy) + d \Leftrightarrow \left(\left(d_{\mu_1^-}(wz), d_{\mu_1^+}(wz)\right), \left(d_{\mu_2^-}(wz), d_{\mu_2^+}(wz)\right)\right)\\ &\quad + ((f_1^-, f_1^+), (f_2^-, f_2^+)) \neq \left(\left(d_{\mu_1^-}(zy), d_{\mu_1^+}(zy)\right), \left(d_{\mu_2^-}(zy), d_{\mu_2^+}(zy)\right)\right)\\ &\quad + ((f_1^-, f_1^+), (f_2^-, f_2^+)) \Leftrightarrow \left(\left(d_{\mu_1^-}(wz) + f_1^-, d_{\mu_1^+}(wz) + f_1^+\right), \left(d_{\mu_2^-}(wz)\right.\right.\\ &\quad \left.\left. + f_2^-, d_{\mu_2^+}(wz) + f_2^+\right)\right) \neq \left(\left(d_{\mu_1^-}(zy) + f_1^-, d_{\mu_1^+}(zy) + f_1^+\right),\right.\\ &\quad \left.\cdot\left(d_{\mu_2^-}(zy) + f_2^-, d_{\mu_2^+}(zy) + f_2^+\right)\right) \Leftrightarrow \left(\left(d_{\mu_1^-}(wz) + \mu_1^-(wz), d_{\mu_1^+}(wz) + \mu_1^+(wz)\right),\right.\\ &\quad \left.\cdot\left(d_{\mu_2^-}(wz) + \mu_2^-(wz), d_{\mu_2^+}(wz) + \mu_2^+(wz)\right)\right) \neq \left(\left(d_{\mu_1^-}(zy) + \mu_1^-(zy), d_{\mu_1^+}(zy)\right.\right.\\ &\quad \left.\left. + \mu_1^+(zy)\right), \left(d_{\mu_2^-}(zy) + \mu_2^-(zy), d_{\mu_2^+}(zy) + \mu_2^+(zy)\right)\right) \Leftrightarrow \left(\left(td_{\mu_1^-}(wz), td_{\mu_1^+}(wz)\right),\right.\\ &\quad \left.\cdot\left(td_{\mu_2^-}(wz), td_{\mu_2^+}(wz)\right)\right) \neq \left(\left(td_{\mu_1^-}(zy), td_{\mu_1^+}(zy)\right),\right.\\ &\quad \left.\cdot\left(td_{\mu_2^-}(zy), td_{\mu_2^+}(zy)\right)\right) \Leftrightarrow td_G(wz) \neq td_G(zy). \end{aligned} \tag{2}$$

Therefore, neighbor edges have VDs if they have various TDs. Hence, G is a NEI-IVIFG if G is a NETI-IVIFG. □

Remark 16. Let G be a CIVIFG. If G is both NEI-IVIFG and NETI-IVIFG, then μ needs not to be a CF.

Example 17. Suppose G is an IVIFG and G^* a path consists of four nodes.

From Figure 4, $d_G(u) = d_G(x) = ((0.2,0.3),(0.4,0.5))$, $d_G(v) = d_G(w) = ((0.3,0.5),(0.7,0.9))$, $d_G(uv) = ((0.1,0.2),(0.3,0.4))$, $d_G(vw) = ((0.4,0.6),(0.8,1.0))$, $d_G(wx) = ((0.1,0.2),(0.3,0.4))$, $td_G(uv) = ((0.3,0.5),(0.7,0.9))$, $td_G(vw) = ((0.5,0.8),(1.1,1.4))$, and $td_G(wx) = ((0.3,0.5),(0.7,0.9))$.

Here, $d_G(uv) \neq d_G(vw)$ and $d_G(vw) \neq d_G(wx)$. Hence, G is a NEI-IVIFG. Also, $td_G(uv) \neq td_G(vw)$ and $td_G(vw) \neq td_G(wx)$. Hence, G is a NETI-IVIFG but μ is not CF.

Theorem 18. *Let G be a CIVIFG and μ a CF. If G is a SI-IVIFG, then, G is a NEI-IVIFG.*

Proof. Assume G is a CIVIFG, μ is a CF, and $\mu(wz) = f, \forall wz$ in E, which $f = ((f_1^-, f_1^+), (f_2^-, f_2^+))$ is constant.

Let wz and zy be any two NEs in G. Assume that G is a SI-IVIFG. Then, each pair of nodes in G has VDs, and

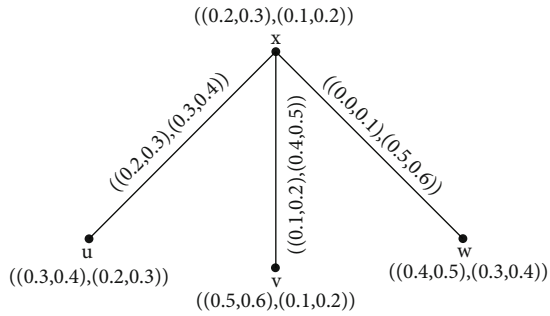

Figure 2: G is NEI-IVIFG but it is not NETI-IVIFG.

hence,

$$\begin{aligned}
&d_G(w) \neq d_G(z) \neq d_G(y) \Rightarrow \left(\left(d_{\sigma_1^-}(w), d_{\sigma_1^+}(w)\right),\right.\\
&\cdot \left.\left(d_{\sigma_2^-}(w), d_{\sigma_2^+}(w)\right)\right) \neq \left(\left(d_{\sigma_1^-}(z), d_{\sigma_1^+}(z)\right),\right.\\
&\cdot \left.\left(d_{\sigma_2^-}(z), d_{\sigma_2^+}(z)\right)\right) \neq \left(\left(d_{\sigma_1^-}(y), d_{\sigma_1^+}(y)\right),\right.\\
&\cdot \left.\left(d_{\sigma_2^-}(y), d_{\sigma_2^+}(y)\right)\right) \Rightarrow \left(\left(d_{\sigma_1^-}(w), d_{\sigma_1^+}(w)\right),\right.\\
&\cdot \left.\left(d_{\sigma_2^-}(w), d_{\sigma_2^+}(w)\right)\right) + \left(\left(d_{\sigma_1^-}(z), d_{\sigma_1^+}(z)\right),\right.\\
&\cdot \left.\left(d_{\sigma_2^-}(z), d_{\sigma_2^+}(z)\right)\right) - 2\left(\left(f_1^-, f_1^+\right), \left(f_2^-, f_2^+\right)\right) \neq \left(\left(d_{\sigma_1^-}(z), d_{\sigma_1^+}(z)\right),\right.\\
&\cdot \left.\left(d_{\sigma_2^-}(z), d_{\sigma_2^+}(z)\right)\right) + \left(\left(d_{\sigma_1^-}(y), d_{\sigma_1^+}(y)\right), \left(d_{\sigma_2^-}(y), d_{\sigma_2^+}(y)\right)\right)\\
&\quad - 2\left(\left(f_1^-, f_1^+\right), \left(f_2^-, f_2^+\right)\right) \Rightarrow \left(\left(d_{\sigma_1^-}(w) + d_{\sigma_1^-}(z) - 2f_1^-, d_{\sigma_1^+}(w) + d_{\sigma_1^+}(z) - 2f_1^+\right),\right.\\
&\cdot \left.\left(d_{\sigma_2^-}(w) + d_{\sigma_2^-}(z) - 2f_2^-, d_{\sigma_2^+}(w) + d_{\sigma_2^+}(z) - 2f_2^+\right)\right) \neq \left(\left(d_{\sigma_1^-}(z) + d_{\sigma_1^-}(y)\right.\right.\\
&\quad \left.\left. - 2f_1^-, d_{\sigma_1^+}(z) + d_{\sigma_1^+}(y) - 2f_1^+\right), \left(d_{\sigma_2^-}(z) + d_{\sigma_2^-}(y) - 2f_2^-, d_{\sigma_2^+}(z) + d_{\sigma_2^+}(y)\right.\right.\\
&\quad \left.\left. - 2f_2^+\right)\right) \Rightarrow \left(\left(d_{\sigma_1^-}(w) + d_{\sigma_1^-}(z) - 2\mu_1^-(wz), d_{\sigma_1^+}(w) + d_{\sigma_1^+}(z) - \mu_1^+(wz)\right),\right.\\
&\cdot \left.\left(d_{\sigma_2^-}(w) + d_{\sigma_2^-}(z) - 2\mu_2^-(wz), d_{\sigma_2^+}(w) + d_{\sigma_2^+}(z) - 2\mu_2^+(wz)\right)\right) \neq \left(\left(d_{\sigma_1^-}(z)\right.\right.\\
&\quad \left.\left. + d_{\sigma_1^-}(y) - 2\mu_1^-(zy), d_{\sigma_1^+}(z) + d_{\sigma_1^+}(y) - 2\mu_1^+(zy)\right), \left(d_{\sigma_2^-}(z) + d_{\sigma_2^-}(y)\right.\right.\\
&\quad \left.\left. - 2\mu_2^-(zy), d_{\sigma_2^+}(z) + d_{\sigma_2^+}(y) - 2\mu_2^+(zy)\right)\right) \Rightarrow \left(\left(d_{\mu_1^-}(wz), d_{\mu_1^+}(wz)\right),\right.\\
&\cdot \left.\left(d_{\mu_2^-}(wz), d_{\mu_2^+}(wz)\right)\right) \neq \left(\left(d_{\mu_1^-}(zy), d_{\mu_1^+}(zy)\right),\right.\\
&\cdot \left.\left(d_{\mu_2^-}(zy), d_{\mu_2^+}(zy)\right)\right) \Rightarrow d_G(wz) \neq d_G(zy).
\end{aligned} \tag{3}$$

Hence, neighbor edges have VDs. Thus, G is a NEIIVIFG. □

Theorem 19. *Let G be a CIVIFG on G^* and μ a CF. If G is a SI-IVIFG, then G is a NETI-IVIFG.*

Proof. It is similar to Theorem 18. □

Remark 20. Converse of Theorem 19 is not generally true.

Example 21. Let G be an IVIFG so that G^* consists of four nodes.

From Figure 5, $d_G(u) = d_G(x) = ((0.1,0.3), (0.2,0.4))$ and $d_G(v) = d_G(w) = ((0.2,0.6), (0.4,0.8))$.

Here, G is not a SI-IVIFG. $d_G(uv) = ((0.1,0.3), (0.2,0.4))$, $d_G(vw) = ((0.2,0.6), (0.4,0.8))$, $d_G(wx) = ((0.1,0.3), (0.2,0.4))$, $td_G(uv) = ((0.2,0.6), (0.4,0.8))$, $td_G(vw) = ((0.3,0.9), (0.6,1.2))$, and $td_G(wx) = ((0.2,0.6), (0.4,0.8))$.

Hence, $d_G(uv) \neq d_G(vw)$ and $d_G(vw) \neq d_G(wx)$. Furthermore, $td_G(uv) \neq td_G(vw)$ and $td_G(vw) \neq td_G(wx)$. Hence, G is both NEI-IVIFG and NETI-IVIFG. But G is not a SI-IVIFG.

Theorem 22. *Let G be a CIVIFG and μ a CF. Then, G is a HI-IVIFG if G is a NEI-IVIFG.*

Proof. Assume G is a CIVIFG and μ is a CF. Consider $\mu(wz) = f, \forall wz$ in E, which $f = ((f_1^-, f_1^+), (f_2^-, f_2^+))$ is CF.

Let wz and zy be any two neighbor edges in G. Then,

$$\begin{aligned}
&d_G(w) \neq d_G(y) \Rightarrow \left(\left(d_{\sigma_1^-}(w), d_{\sigma_1^+}(w)\right), \left(d_{\sigma_2^-}(w), d_{\sigma_2^+}(w)\right)\right) \neq \left(\left(d_{\sigma_1^-}(y), d_{\sigma_1^+}(y)\right),\right.\\
&\quad \cdot \left.\left(d_{\sigma_2^-}(y), d_{\sigma_2^+}(y)\right)\right) \Rightarrow \left(\left(d_{\sigma_1^-}(w), d_{\sigma_1^+}(w)\right), \left(d_{\sigma_2^-}(w), d_{\sigma_2^+}(w)\right)\right)\\
&\quad + \left(\left(d_{\sigma_1^-}(z), d_{\sigma_1^+}(z)\right), \left(d_{\sigma_2^-}(z), d_{\sigma_2^+}(z)\right)\right)\\
&\quad - 2\left(\left(f_1^-, f_1^+\right), \left(f_2^-, f_2^+\right)\right) \neq \left(\left(d_{\sigma_1^-}(z), d_{\sigma_1^+}(z)\right), \left(d_{\sigma_2^-}(z), d_{\sigma_2^+}(z)\right)\right)\\
&\quad + \left(\left(d_{\sigma_1^-}(y), d_{\sigma_1^+}(y)\right), \left(d_{\sigma_2^-}(y), d_{\sigma_2^+}(y)\right)\right)\\
&\quad - 2\left(\left(f_1^-, f_1^+\right), \left(f_2^-, f_2^+\right)\right) \Rightarrow \left(\left(d_{\sigma_1^-}(w) + d_{\sigma_1^-}(z) - 2f_1^-, d_{\sigma_1^+}(w) + d_{\sigma_1^+}(z)\right.\right.\\
&\quad \left.\left. - 2f_1^+\right), \left(d_{\sigma_2^-}(w) + d_{\sigma_2^-}(z) - 2f_2^-, d_{\sigma_2^+}(w) + d_{\sigma_2^+}(z) - 2f_2^+\right)\right)\\
&\quad \neq \left(\left(d_{\sigma_1^-}(z) + d_{\sigma_1^-}(y) - 2f_1^-, d_{\sigma_1^+}(z) + d_{\sigma_1^+}(y) - 2f_1^+\right), \left(d_{\sigma_2^-}(z) + d_{\sigma_2^-}(y)\right.\right.\\
&\quad \left.\left. - 2f_2^-, d_{\sigma_2^+}(z) + d_{\sigma_2^+}(y) - 2f_2^+\right)\right) \Rightarrow \left(\left(d_{\sigma_1^-}(w) + d_{\sigma_1^-}(z) - 2\mu_1^-(wz), d_{\sigma_1^+}(w)\right.\right.\\
&\quad \left.\left. + d_{\sigma_1^+}(z) - \mu_1^+(wz)\right), \left(d_{\sigma_2^-}(w) + d_{\sigma_2^-}(z) - 2\mu_2^-(wz), d_{\sigma_2^+}(w) + d_{\sigma_2^+}(z)\right.\right.\\
&\quad \left.\left. - 2\mu_2^+(wz)\right)\right) \neq \left(\left(d_{\sigma_1^-}(z) + d_{\sigma_1^-}(y) - 2\mu_1^-(zy), d_{\sigma_1^+}(z) + d_{\sigma_1^+}(y)\right.\right.\\
&\quad \left.\left. - 2\mu_1^+(zy)\right), \left(d_{\sigma_2^-}(z) + d_{\sigma_2^-}(y) - 2\mu_2^-(zy), d_{\sigma_2^+}(z) + d_{\sigma_2^+}(y)\right.\right.\\
&\quad \left.\left. - 2\mu_2^+(zy)\right)\right) \Rightarrow \left(\left(d_{\mu_1^-}(wz), d_{\mu_1^+}(wz)\right), \left(d_{\mu_2^-}(wz), d_{\mu_2^+}(wz)\right)\right)\\
&\quad \neq \left(\left(d_{\mu_1^-}(zy), d_{\mu_1^+}(zy)\right), \left(d_{\mu_2^-}(zy), d_{\mu_2^+}(zy)\right)\right) \Rightarrow d_G(wz) \neq d_G(zy).
\end{aligned} \tag{4}$$

Therefore, neighbor edges have VDs, if each node neighbor to the nodes has VDs. Hence, G is a HIIVIFG, if G is a NEIIVIFG. □

Theorem 23. *Suppose G is a CIVIFG and μ is a CF. Then, G is HI-IVIFG if and only if G is NETI-IVIFG.*

Proof. It is clear. □

Theorem 24. *Let G be an IVIFG on G^*, a star $K_{1,n}$. Then, G is a TER-IVIFG. If the degrees of IVM and IV-NM of no two edges are similar, then G is a NEI-IVIFG.*

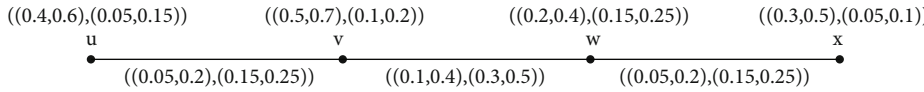

Figure 3: G is NETI-IVIFG but it is not NEI-IVIFG.

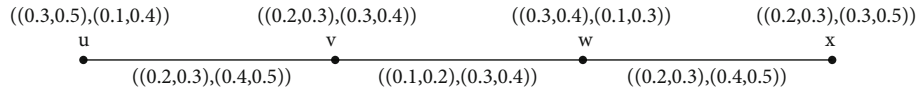

Figure 4: μ is not a CF.

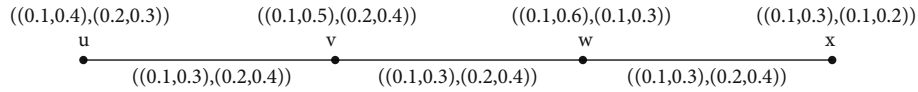

Figure 5: G is both NEI-IVIFG and NETI-IVIFG, not SI-IVIFG.

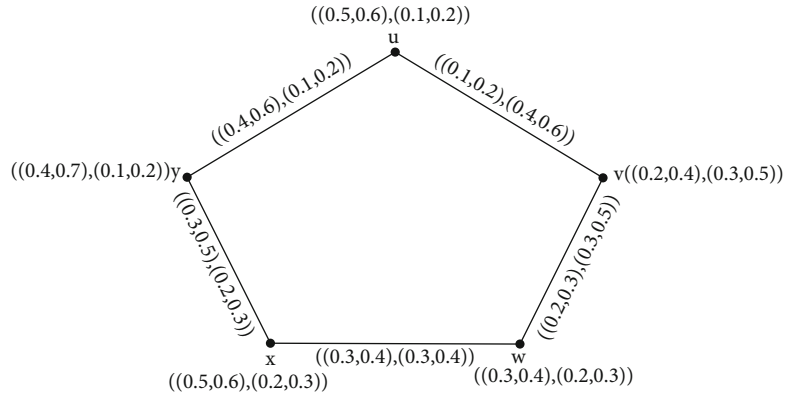

Figure 6: G is both SEI-IVIFG and SETI-IVIFG.

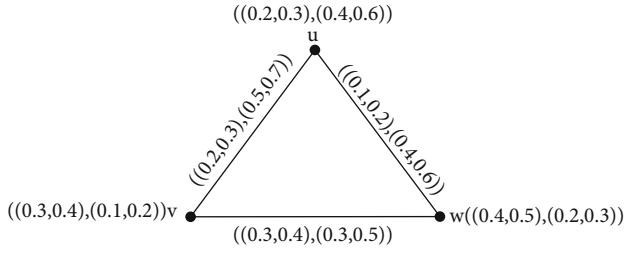

Figure 7: G is SEI-IVIFG but it is not SETI-IVIFG.

Proof. Suppose $v_1, v_2, v_3, \cdots, v_n$ are the nodes neighbor to the node x. Assume $e_1, e_2, e_3, \cdots, e_n$ are the edges of a star G^* in that order having degrees of IVM $m_1, m_2, m_3, \cdots, m_n$ and degrees of IV-NM $n_1, n_2, n_3, \cdots, n_n$ which $m_i = (m_i^-, m_i^+)$ and $n_i = (n_i^-, n_i^+)$, for $i = 1, 2$ so that $0 \le m_i^+ + n_i^+ \le 1$, for each $1 \le i \le n$.

Then,

$$\begin{aligned} td_G(e_i) &= \left(\left(td_{\mu_1^-}(e_i), td_{\mu_1^+}(e_i)\right), \left(td_{\mu_2^-}(e_i), td_{\mu_2^+}(e_i)\right)\right) \\ &= \left(\left(d_{\mu_1^-}(e_i) + \mu_1^-(e_i), d_{\mu_1^+}(e_i) + \mu_1^+(e_i)\right),\right. \\ &\qquad \left.\cdot\left(d_{\mu_2^-}(e_i) + \mu_2^-(e_i), d_{\mu_2^+}(e_i) + \mu_2^+(e_i)\right)\right) \\ &= \left(\left(\sum_{k=1}^{n} m_k^- - m_i^- + m_i^-, \sum_{k=1}^{n} m_k^+ - m_i^+ + m_i^+\right),\right. \\ &\qquad \left.\cdot\left(\sum_{k=1}^{n} n_k^- - n_i^- + n_i^-, \sum_{k=1}^{n} n_k^+ - n_i^+ + n_i^+\right)\right) \\ &= \left(\left(\sum_{k=1}^{n} m_k^-, \sum_{k=1}^{n} m_k^+\right), \left(\sum_{k=1}^{n} n_k^-, \sum_{k=1}^{n} n_k^+\right)\right). \end{aligned} \tag{5}$$

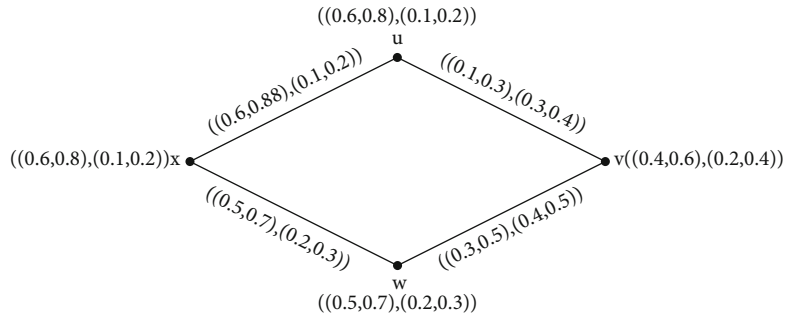

Figure 8: G is SETI-IVIFG but it is not SEI-IVIFG.

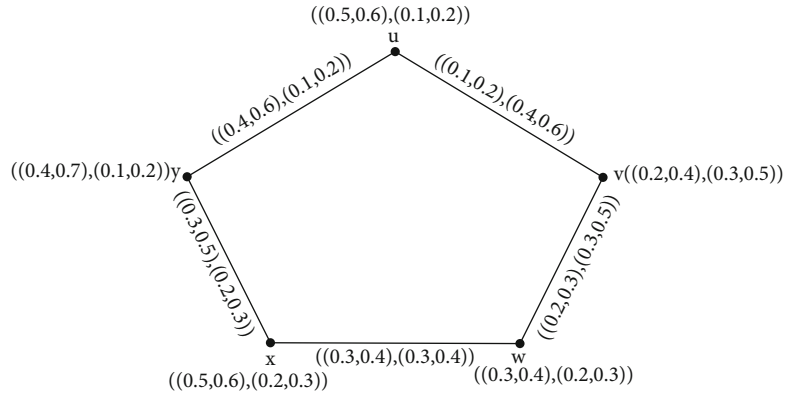

Figure 9: μ is not a CF.

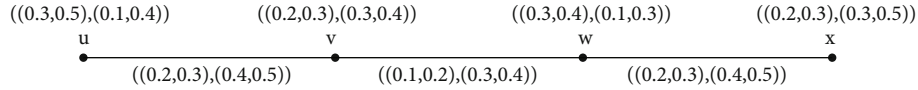

Figure 10: G is NEI and NETI-IVIFG but it is not SEI and SETI-IVIFG.

Table 2: The names of the staff and their specialization in the hospital.

Name	Services
Jafari (Ja)	Medical equipment expert
Mohseni (Mo)	Head of security guard
Alavi (Al)	Head of admissions
Samie (Sa)	Expert radiology and laboratory
Rezai (Re)	Hospital head
Ghoreishi (Gh)	IT expert
Khorami (Kh)	Head of finance

Table 3: Employee power based on degree of membership and nonmembership.

	Jafari	Mohseni	Alavi	Samie	Rezai	Ghoreishi	Khorami
σ_1^-	0.85	0.85	0.75	0.65	0.55	0.55	0.45
σ_1^+	0.95	0.95	0.85	0.75	0.65	0.65	0.55
σ_2^-	0	0	0.05	0.05	0.25	0.25	0.25
σ_2^+	0.05	0.05	0.15	0.15	0.35	0.35	0.35

All edges e_i, $(1 \le i \le n)$, have same TDs. Hence, G is a TER-IVIFG. Now, if $m_i^- \ne m_j^-$, $m_i^+ \ne m_j^+$, $n_i^- \ne n_j^-$, and $n_i^+ \ne n_j^+$, for each $1 \le i, j \le n$, then we have the following:

$$\begin{aligned} d_G(e_i) &= \left(\left(d_{\mu_1^-}(e_i), d_{\mu_1^+}(e_i)\right), \left(d_{\mu_2^-}(e_i), d_{\mu_2^+}(e_i)\right)\right) \\ &= \left(\left(d_{\sigma_1^-}(x) + d_{\sigma_1^-}(v_i) - 2\mu_1^-(xv_i), d_{\sigma_1^+}(x) + d_{\sigma_1^+}(v_i) - 2\mu_1^+(xv_i)\right),\right. \\ &\quad \left.\cdot\left(d_{\sigma_2^-}(x) + d_{\sigma_2^-}(v_i) - 2\mu_2^-(xv_i), d_{\sigma_2^+}(x) + d_{\sigma_2^+}(v_i) - 2\mu_2^+(xv_i)\right)\right) \\ &= \left(\left(\sum_{k=1}^{n} m_k^- + m_i^- - 2m_i^-, \sum_{k=1}^{n} m_k^+ + m_i^+ - 2m_i^+\right),\right. \\ &\quad \left.\cdot\left(\sum_{k=1}^{n} n_k^- + n_i^- - 2n_i^-, \sum_{k=1}^{n} n_k^+ + n_i^+ - 2n_i^+\right)\right) \\ &= \left(\left(\sum_{k=1}^{n} m_k^- - m_i^-, \sum_{k=1}^{n} m_k^+ - m_i^+\right), \left(\sum_{k=1}^{n} n_k^- - n_i^-, \sum_{k=1}^{n} n_k^+ - n_i^+\right)\right), \\ &\quad \text{for each } 1 \le i \le n. \end{aligned} \tag{6}$$

Therefore, all edges e_i,$(1 \le i \le n)$, have VDs. Hence, G is a NEI-IVIFG. □

Definition 25. Let G be a CIVIFG on G^*. Then, G is called to be a:

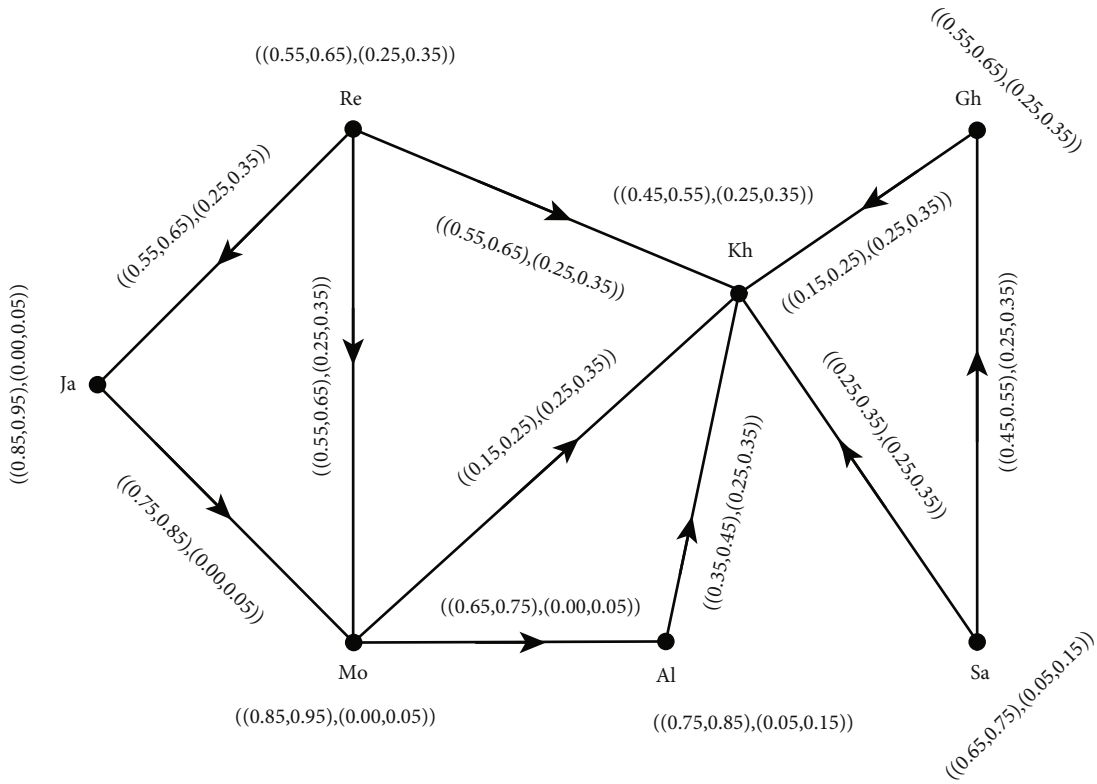

Figure 11: IVIF digraph (influence graph).

Table 4: Adjacency matrix corresponding to Figure 11.

	Ja	Mo	Al	Sa	Re	Gh	Kh
Ja	0	$\begin{pmatrix}(0.75,0.85)\\,\\(0,0.05)\end{pmatrix}$	0	0	0	0	0
Mo	0	0	$\begin{pmatrix}(0.65,0.75)\\,\\(0,0.05)\end{pmatrix}$	0	0	0	$\begin{pmatrix}(0.15,0.25)\\,\\(0.25,0.35)\end{pmatrix}$
Al	0	0	0	0	0	0	$\begin{pmatrix}(0.35,0.45)\\,\\(0.25,0.35)\end{pmatrix}$
Sa	0	0	0	0	0	$\begin{pmatrix}(0.45,0.55)\\,\\(0.25,0.35)\end{pmatrix}$	$\begin{pmatrix}(0.25,0.35)\\,\\(0.25,0.35)\end{pmatrix}$
Re	$\begin{pmatrix}(0.55,0.65)\\,\\(0.25,0.35)\end{pmatrix}$	$\begin{pmatrix}(0.55,0.65)\\,\\(0.25,0.35)\end{pmatrix}$	0	0	0	0	$\begin{pmatrix}(0.25,0.35)\\,\\(0.25,0.35)\end{pmatrix}$
Gh	0	0	0	0	0	0	$\begin{pmatrix}(0.15,0.25)\\,\\(0.25,0.35)\end{pmatrix}$
Kh	0	0	0	0	0	0	0

(i) SEI-IVIFG if each pair of edges has VDs

(ii) SETI-IVIFG if each pair of edges has various TDs

Example 26. Graph that is both SEI-IVIFG and SETI-IVIFG.

Let G be a CIVIFG on G^* which is a cycle of length five.

From Figure 6, $d_G(u) = ((0.5,0.8),(0.5,0.8))$, $d_G(v) = ((0.3,0.5),(0.7,1.1))$, $d_G(w) = ((0.5,0.7),(0.6,0.9))$, $d_G(x) = ((0.6,0.9),(0.5,0.7))$, $d_G(y) = ((0.7,1.1),(0.3,0.5))$, $d_G(uv) = ((0.6,0.9),(0.4,0.7))$, $d_G(vw) = ((0.4,0.6),(0.7,1.0))$, $d_G(wx) = ((0.5,0.8),(0.5,0.8))$, $d_G(xy) = ((0.7,1.0),(0.4,0.6))$, and $d_G(yu) = ((0.4,0.7),(0.6,0.9))$.

Thus, G is a SEI-IVIFG.

$td_G(uv) = ((0.7,1.1),(0.8,1.3))$, $td_G(vw) = ((0.6,0.9),(1.0,1.5))$, $td_G(wx) = ((0.8,1.2),(0.8,1.2))$, $td_G(xy) = ((1.0,1.5),(0.6,0.9))$, and $td_G(yu) = ((0.8,1.3),(0.7,1.1))$.

The above calculations show that each edge has various TD. Therefore, G is a SETI-IVIFG.

So, G is both SEI-IVIFG and SETI-IVIFG.

Example 27. SEI-IVIFG needs not be SETI-IVIFG.

Let G be an IVIFG so that G^*, a cycle of length three.

From Figure 7, $d_G(u) = ((0.3,0.5),(0.9,1.3))$, $d_G(v) = ((0.5,0.7),(0.8,1.2))$, $d_G(w) = ((0.4,0.6),(0.7,1.1))$, $d_G(uv) = ((0.4,0.6),(0.7,1.1))$, $d_G(vw) = ((0.3,0.5),(0.9,1.3))$, $d_G(wu) = ((0.5,0.7),(0.8,1.2))$, and $td_G(uv) = td_G(vw) = td_G(wu) = ((0.6,0.9),(1.2,1.8))$.

Note that G is SEI-IVIFG, since each pair of edges has VDs. Also, G is not SETI-IVIFG, since all the edges have same TDs. Hence, SEI-IVIFG needs not to be SETI-IVIFG.

Example 28. SETI-IVIFG needs not to be SEI-IVIFG.

Suppose G is an IVIFG so that G^*, a cycle of length four.

From Figure 8, $d_G(u) = ((0.7,1.1),(0.4,0.6))$, $d_G(v) = ((0.4,0.8),(0.7,0.9))$, $d_G(w) = ((0.8,1.2),(0.6,0.8))$, $d_G(x) = ((1.1,1.5),(0.3,0.5))$, $d_G(uv) = d_G(wx) = ((0.9,1.3),(0.5,0.7))$, $d_G(vw) = d_G(xu) = ((0.6,1.0),(0.5,0.7))$, $td_G(uv) = ((1.0,1.6),(0.8,1.1))$, $td_G(vw) = ((0.9,1.5),(0.9,1.2))$, $td_G(wx) = ((1.4,2.0),(0.7,1.0))$, and $d_G(xu) = ((1.2,1.8),(0.6,0.9))$.

It is noted that $d_G(uv) = d_G(wx)$. So, G is not SEI-IVIFG.

But G is SETI-IVIFG, since $td_G(uv) \neq td_G(vw) \neq td_G(wx) \neq td_G(xu)$. Hence, SETI-IVIFG needs not to be SEI-IVIFG.

Remark 29. Let G be a CIVIFG on G^*. If G is both SEI-IVIFG and SETI-IVIFG, then μ needs not to be a CF.

Example 30. Consider G be an IVIFG so that G^* is a cycle of length five.

From Figure 9, $d_G(u) = ((0.5,0.8),(0.5,0.8))$, $d_G(v) = ((0.3,0.5),(0.7,1.1))$, $d_G(w) = ((0.5,0.7),(0.6,0.9))$, $d_G(x) = ((0.6,0.9),(0.5,0.7))$, and $d_G(y) = ((0.7,1.1),(0.3,0.5))$. Also, $d_G(uv) = ((0.6,0.9),(0.4,0.7))$, $d_G(vw) = ((0.4,0.6),(0.7,1.0))$, $d_G(wx) = ((0.5,0.8),(0.5,0.8))$, $d_G(xy) = ((0.7,1.0),(0.4,0.6))$, and $d_G(yu) = ((0.4,0.7),(0.6,0.9))$.

Clearly, each edge in G has VD. Therefore, G is a SEI-IVIFG.

Also, $td_G(uv) = ((0.7,1.1),(0.8,1.3))$, $td_G(vw) = ((0.6,0.9),(1.0,1.5))$, $td_G(wx) = ((0.8,1.2),(0.8,1.2))$, $td_G(xy) = ((1.0,1.5),(0.6,0.9))$, and $td_G(yu) = ((0.8,1.3),(0.7,1.1))$.

Thus, each edge in G has various TD. So, G is a SETI-IVIFG. Hence, G is both SEI-IVIFG and SETI-IVIFG. But μ is not a CF.

Theorem 31. *Let G be an IVIFG on G^*. If G is a SEI-IVIFG, then G is a NEI-IVIFG.*

Proof. Let G be an IVIFG on G^* that is SEI-IVIFG. Then, each edge in G has VD. Thus, each neighbor edge has VD. So, G is a NEI-IVIFG. □

Theorem 32. *Let G be an IVIFG on G^*. If G is a SETI-IVIFG, then G is a NETI-IVIFG.*

Proof. Let G be an IVIFG on G^* that is SETI-IVIFG. Then, each pair of edges in G has various TDs. Hence, each pair of neighbor edges has various TDs. Therefore, G is a NETI-IVIFG. □

Remark 33. The inverse of Theorems 31 and 32 is not generally true.

Example 34. Let G be an IVIFG so that G^* is a path with four nodes.

From Figure 10, $d_G(u) = d_G(x) = ((0.2,0.3),(0.4,0.5))$, $d_G(v) = d_G(w) = ((0.3,0.5),(0.7,0.9))$, $d_G(uv) = ((0.1,0.2),(0.3,0.4))$, $d_G(vw) = ((0.4,0.6),(0.8,1.0))$, $d_G(wx) = ((0.1,0.2),(0.3,0.4))$, $td_G(uv) = ((0.3,0.5),(0.7,0.9))$, $td_G(vw) = ((0.5,0.8),(1.1,1.4))$, and $td_G(wx) = ((0.3,0.5),(0.7,0.9))$.

Here, $d_G(uv) \neq d_G(vw)$ and $d_G(vw) \neq d_G(wx)$. Hence, G is a NEI-IVIFG. But G is not a SEI-IVIFG, since $d_G(uv) \neq d_G(wx)$. Also, note that $td_G(uv) \neq td_G(vw)$ and $td_G(vw) \neq td_G(wx)$. So, G is a NETI-IVIFG. But G is not a SETI-IVIFG, since $td_G(uv) \neq td_G(wx)$.

4. Application of IVIF Influence Digraph to Find the Most Effective Person in a Hospital

Serving the people has always been an important duty of any government, and this has also played a significant role in the growth and prosperity of any country, because if the people are satisfied with the government of their country, then they will perform their duties in the best possible way. As a result, a healthier society will be formed with more progress. One of these very important services is taking care of people's health. Hospitals and medical centers must also serve patients in the best possible way and not neglect to admit and treat patients. But a very important issue that can be important in the service and treatment of patients in the fastest possible time is the rapid and correct management

of hospital wards and health centers. If a manager can properly guide the staff under her supervision and give them the necessary training to treat patients, then the service will be provided in the best possible way. Therefore, in this section, we try to introduce the most effective staff of a hospital with the help of an IVIFG. To do this, we consider the nodes of this influence graph as the staff of a hospital and the edges as the influence of one employee on another employee. The names of the staff and their specialization in the hospital are shown in Table 2. For this hospital, the staff is as follows:

$$E = \{\text{Jafari, Mohseni, Alavi, Samie, Rezai, Ghoreishi, Khorami}\}. \tag{7}$$

(i) Mohseni has been working with Samie for 12 years and values his views on issues

(ii) Rezai has been the head of the hospital, and not only Mohseni but also Samie is very satisfied with Rezai's performance

(iii) The safety of hospital staff and also the care of hospital equipment is a very important issue. Mohseni is an expert for this

(iv) Alavi and Ghoreishi have a long history of conflict

(v) Samie is very effective in laboratory and radiology affairs of the hospital

Considering the above points, the influence graph can be very important. But such a graph cannot show the power of employees within a hospital and the degree of influence of employees on each other. Since power and influence do not have defined boundaries, they can be represented as an interval-valued fuzzy set. On the other hand, there can be no fair interpretation of the power and influence of individuals, because evaluations are always accompanied by skepticism. So, here we use the interval-valued intuitionistic fuzzy degrees, which is very useful for influence and conflicts between employees. The interval-valued intuitionistic fuzzy set of employees is shown in Table 3.

We have shown the influence of persons in the IVIF digraph with an edge. This graph is shown in Figure 11, and its adjacency matrix is shown in Table 4.

Hospital staff are the vertices of the IVIF digraph of Figure 11, and their strength in terms of conditions, degrees of IVM, and IV-NM is that it can also be expressed as a percentage. For example, Mr. Alavi has 75% to 85% of power and between 5% and 15% does not have this power. Also, the edges of this graph indicate the influence of one person on another. Degree of IVM and IV-NM can be described in terms of positive and negative influence. For example, between 55% and 65% of the time, Mr. Jafari is influenced by Mr. Rezaei's thoughts and ideas, but 25% to 35% of the time he is not influenced by his opinions.

In Figure 11, it is clear that Mr. Rezaei controls both the medical equipment experts: Mr. Jafari and the head of security guard, Mr. Mohseni. His influence on both of them is the same. Because the IV membership rate in both of them is (0.55, 0.65), i.e., 55% to 65%. But in the case of Mr. Rezaei and Mr. Mohseni, the degree of doubt is between 0% and 20% because

$$(1 - 0.65 - 0.35, 1 - 0.55 - 0.25) = (0, 0.20), \tag{8}$$

and in the case of Mr. Jafari and Mohseni, it is between 10% and 25% because

$$(1 - 0.85 - 0.05, 1 - 0.75 - 0) = (0.10, 0.25). \tag{9}$$

The implication is that Mr. Jafari is more skeptical than Mr. Rezaei. Clearly, Mr. Rezaei has the most influence in the organization, because he dominates both the equipment expert and the security guard; these two people have the most power in the hospital, i.e., between 85% and 95%.

5. Conclusions

Interval-valued intuitionistic fuzzy graphs have various uses in modern science and technology, especially in the fields of neural networks, computer science, operation research, and decision-making. Also, they have a wide range of applications in the field of psychological sciences as well as the identification of individuals based on oncological behaviors. With the help of IVIFGs, the most effective person in an organization can be identified according to the important factors that can be useful for an institution. Therefore, in this research, some types of EI-IVIFGs such as NETI-IVIFGs, SEI-IVIFGs, and SETI-IVIFGs are introduced. A comparative study between NEI-IVIFGs and NETI-IVIFGs is presented. Finally, an application of IVIF influence digraph has presented. In our future work, we will introduce connectivity index, Winer index, and Randic index in interval-valued intuitionistic fuzzy graphs and investigate some of their properties. Also, we will investigate some types of energy, including Laplacian and skew Laplacian in both interval-valued intuitionistic fuzzy graphs and interval-valued intuitionistic fuzzy digraphs.

Data Availability

No data were used to support this study.

Conflicts of Interest

The authors declare that they have no conflict of interest.

Acknowledgments

This work was supported by the Natural Science Foundation of China (grant nos. 62002079).

References

[1] L. A. Zadeh, "Fuzzy sets," *Information and Control*, vol. 8, pp. 338–353, 1965.

[2] A. Kaufman, "Introduction a la theorie des sous-emsembles flous," *Masson et Cie*, vol. 1, 1973.

[3] L. A. Zadeh, "Similarity relations and fuzzy ordering," *Information Sciences*, vol. 3, pp. 177–200, 1971.

[4] L. A. Zadeh, "Is there a need for fuzzy logical," *Information Sciences*, vol. 178, pp. 2751–2779, 2008.

[5] A. Rosenfeld, *Fuzzy Graphs, Fuzzy Sets and Their Applications*, L. A. Zadeh, K. S. Fu, and M. Shimura, Eds., Academic Press, New York, 1975.

[6] P. Bhattacharya, "Some remarks on fuzzy graphs," *Pattern Recognition Letters*, vol. 6, no. 5, pp. 297–302, 1987.

[7] J. N. Mordeson and P. S. Nair, *Fuzzy Graph and Fuzzy Hypergraphs*, PhysicaVerlag, Heidebeg, Second edition, 2001.

[8] K. T. Atanassov, "Intuitionistic fuzzy sets," *International Journal Bioautomation*, vol. 20, pp. 87–96, 1986.

[9] K. T. Atanassov and G. Gargov, "Interval-valued intuitionistic fuzzy sets," *Fuzzy Sets and Systems*, vol. 31, no. 3, pp. 343–349, 1989.

[10] K. T. Atanassov, "Intuitionistic Fuzzy Sets," in *Theory, Applications, Studies in Fuzziness and Soft Computing*, Physica-Verl, Heidelberg, New York, 1999.

[11] M. Akram and B. Davvaz, "Strong intuitionistic fuzzy graphs," *Filomat*, vol. 26, no. 1, pp. 177–196, 2012.

[12] J. Hongmei and W. Lianhua, "Interval-valued fuzzy subsemigroups and subgroups associated by interval-valued fuzzy graphs," *2009 WRz Global Congress on Intelligent Systems*, vol. 1, pp. 484–487, 2009.

[13] M. G. Karunambigai, S. Sivasankar, and K. Palanivel, "Edge regular intuitionistic fuzzy graph," *Advances in Fuzzy Sets and Systems*, vol. 20, no. 1, pp. 25–46, 2015.

[14] S. N. Mishra and A. Pal, "Product of interval-valued intuitionistic fuzzy graph," *Annals of Pure and Applied Mathematics*, vol. 5, no. 1, pp. 37–46, 2013.

[15] A. Nagoorgani and K. Radha, "The degree of a vertex in some fuzzy graphs," *International Journal of Algorithms, Computing and Mathematics*, vol. 2, no. 3, pp. 107–116, 2009.

[16] A. Nagoorgani and K. Radha, "On regular fuzzy graphs," *Journal of Physical Sciences*, vol. 12, pp. 33–44, 2008.

[17] A. Nagoorgani and S. R. Latha, "On irregular fuzzy graphs," *Applied Mathematical Sciences*, vol. 6, no. 11, pp. 517–523, 2012.

[18] Z. Shao, S. Kosari, H. Rashmanlou, and M. Shoaib, "New concepts in intuitionistic fuzzy graph with application in water supplier systems," *Mathematics*, vol. 8, no. 8, p. 1241, 2020.

[19] S. P. Nandhini and E. Nandhini, "Strongly irregular fuzzy graphs," *International Journal of Mathematical Archive*, vol. 5, no. 5, pp. 110–114, 2014.

[20] N. R. Santhi Maheswari and C. Sekar, "On edge irregular fuzzy graphs," *International Journal of Mathematics and Soft Computing*, vol. 6, no. 2, pp. 131–143, 2016.

[21] N. R. Santhi Maheswari and C. Sekar, "On neighbourly edge irregular fuzzy graphs," *International Journal of Mathematical Archive*, vol. 6, no. 10, pp. 224–231, 2015.

[22] N. R. Santhi Maheswari and C. Sekar, "On strongly edge irregular fuzzy graphs," *Kragujevac Journal of Mathematics*, vol. 40, no. 1, pp. 125–135, 2016.

[23] S. Kosari, Y. Rao, H. Jiang, X. Liu, P. Wu, and Z. Shao, "Vague graph structure with application in medical diagnosis," *Symmetry*, vol. 12, no. 10, p. 1582, 2020.

[24] Y. Rao, S. Kosari, and Z. Shao, "Certain properties of vague graphs with a novel application," *Mathematics*, vol. 8, no. 10, p. 1647, 2020.

[25] Y. Rao, S. Kosari, Z. Shao, R. Cai, and L. Xinyue, "A study on domination in vague incidence graph and its application in medical sciences," *Symmetry*, vol. 12, no. 11, p. 1885, 2020.

[26] X. Shi and S. Kosari, "Certain properties of domination in product vague graphs with an application in medicine," *Frontiers of Physics*, vol. 9, article 680634, 2021.

[27] A. A. Talebi, M. Ghassemi, and H. Rashmanlou, "New concepts of irregular-intuitionistic fuzzy graphs with applications," *Annals of the University of Craiova-Mathematics and Computer Science Series*, vol. 47, no. 2, pp. 226–243, 2020.

[28] A. A. Talebi, M. Ghassemi, H. Rashmanlou, and S. Broumi, "Novel properties of edge irregular single valued neutrosophic graphs," *Neutrosophic Sets and Systems (NSS)*, vol. 43, pp. 255–279, 2021.

[29] A. A. Talebi, H. Rashmanlou, and M. Ghassemi, *New Concepts of Strongly Edge Irregular Interval-Valued Neutrosophic Graphs*, Nova Science Publishers, Inc., 2020.

[30] A. A. Talebi, H. Rashmanlou, and S. H. Sadati, "Interval-valued intuitionistic fuzzy competition graph," *Journal of Multiple-Valued Logic and Soft Computing*, vol. 34, pp. 335–364, 2020.

[31] Z. Kou, S. Kosari, and M. Akhoundi, "A novel description on vague graph with application in transportation systems," *Journal of Mathematics*, vol. 2021, Article ID 4800499, 11 pages, 2021.

[32] K. Kalaiarasi and L. Mahalakshmi, "Regular and irreguar m-polar fuzzy graphs," *Global Journal of Mathematical Sciences: Theory and Practical*, vol. 9, no. 2, pp. 139–152, 2017.

[33] S. Selvanayaki, "Strong and balanced irregular interval valued fuzzy graphs," *International Journal of Engineering, Science and Mathematics*, vol. 6, no. 2, pp. 28–37, 2017.

[34] H. Rashmanlou, G. Muhiuddin, S. K. Amanathulla, F. Mofidnakhaei, and M. Pal, "A study on cubic graphs with novel application," *Journal of Intelligent and Fuzzy Systems*, vol. 40, no. 1, pp. 89–101, 2021.

[35] S. Poulik and G. Ghorai, "Detour g-interior nodes and detour g-boundary nodes in bipolar fuzzy graph with applications," *Hacettepe Journal of Mathematics and Statistics*, vol. 49, no. 1, pp. 106–119, 2020.

[36] S. Poulik and G. Ghorai, "Certain indices of graphs under bipolar fuzzy environment with applications," *Soft Computing*, vol. 24, no. 7, pp. 5119–5131, 2020.

[37] S. Poulik and G. Ghorai, "Applications of graph's complete degree with bipolar fuzzy information," in *Complex & Intelligent Systems*, Springer, 2021.

[38] T. Pramanik, G. Muhiuddin, A. M. Alanazi, and M. Pal, "An extension of fuzzy competition graph and its uses in manufacturing industries," *Mathematics*, vol. 8, no. 6, 2020.

[39] G. Muhiuddin, N. Sridharan, D. Al-Kadi, S. Amutha, and M. E. Elnair, "Reinforcement number of a graph with respect to half-domination," *Journal of Mathematics*, vol. 2021, Article ID 6689816, 7 pages, 2021.

[40] S. K. Amanathulla, G. Muhiuddin, D. Al-Kadi, and M. Pal, "Distance two surjective labelling of paths and interval graphs," *Discrete Dynamics in Nature and Society*, vol. 2021, Article ID 9958077, 9 pages, 2021.

[41] C. Ramprasad, P. L. N. Varma, S. Satyanarayana, and N. Srinivasarao, "Morphism of m-polar fuzzy graph,"

Advances in Fuzzy Systems, vol. 2017, Article ID 4715421, 9 pages, 2017.

[42] I. Nazeer, T. Rashid, and A. Keikha, "An application of product of intuitionistic fuzzy incidence graphs in textile industry," *Complexity*, vol. 2021, Article ID 5541125, 16 pages, 2021.

[43] A. Bhattacharya and M. Pal, "Fuzzy covering problem of fuzzy graphs and its application to investigate the Indian economy in new normal," *Journal of Applied Mathematics and Computing*, vol. 68, no. 1, pp. 479–510, 2022.

[44] R. A. Borzooei, R. Almallah, Y. B. Jun, and H. Ghaznavi, "Inverse fuzzy graphs with applications," *New Mathematics and Natural Computation*, vol. 16, no. 2, pp. 397–418, 2020.

Hindawi
Advances in Mathematical Physics
Volume 2022, Article ID 9044567, 9 pages
https://doi.org/10.1155/2022/9044567

Research Article

Darboux Vector in Four-Dimensional Space-Time

Na Hu,[1] **Tingting Zhang**,[1] **and Yang Jiang**[2]

[1]*School of Science, Shenyang University of Technology, Shenyang, China*
[2]*College of Mathematics and Systems Science, Shenyang Normal University, Shenyang, China*

Correspondence should be addressed to Na Hu; huna@sut.edu.cn

Received 8 February 2022; Accepted 25 March 2022; Published 12 April 2022

Academic Editor: Mehmet Atçeken

As the space-time model of the theory of relativity, four-dimensional Minkowski space is the basis of the theoretical framework for the development of the theory of relativity. In this paper, we introduce Darboux vector fields in four-dimensional Minkowski space. Using these vector fields, we define some new planes and curves. We find that the new planes are the instantaneous rotation planes of rigid body moving in four-dimensional space-time. In addition, according to some characteristics of Darboux vectors in geometry, we define some new space curves in four-dimensional space-time and describe them with curvature functions. Finally, we give some examples.

1. Introduction

On the basis of the principle of relativity and Lorentz transformation, in 1907, Minkowski proposed to add a time dimension on the basis of three space dimensions, thus forming a four-dimensional space-time, and this space-time is also called Minkowski 4-space. The metric tensor g in $\mathbb{E}_1^4$ is given by

$$g = dx_1^2 + dx_2^2 + dx_3^2 - dx_4^2, \tag{1}$$

where (x_1, x_2, x_3, x_4) is a standard rectangular coordinate system in $\mathbb{E}_1^4$. Minkowski space is not only closely related to physics but also provides theoretical and methodological support for the study of astrophysics and cosmology [1–4]. The study of submanifolds in Minkowski space is of interest in relativity theory; therefore, more and more geometers and physicists are committed to the study of submanifolds in Minkowski space. For example, in [5], the authors studied some local properties of slant geometry on spacelike submanifolds of codimension two in Lorentz-Minkowski space and investigate spacelike curves in Lorentz-Minkowski 3-space from different viewpoints as another special case. In [6], the authors studied null helices of 1-dimensional lightlike submanifolds and gave some characterizations of null helices in $\mathbb{R}_1^3$. We refer the reader to [7–17] and the references therein for more related works.

The Darboux vector is the local speed vector of the Frenet frame of space curves, which was discovered and named after Gaston Darboux [18]. If an object moves along a regular curve, we can use the Frenet frame of space curves to describe the motion of the object in terms of two vectors: the translation vector and the rotation vector, where the rotation vector is the Darboux vector. Because the Darboux vector is directly related to the angular momentum, it is also called the angular momentum vector.

In the past few decades, many researchers have mainly studied Darboux vectors in 3-dimensional space [19–26] and have obtained some interesting conclusions. For example, in 2012, Ziplar introduced and studied Darboux helices in Euclidean 3-space and proved that Darboux helices coincide with slant helices [19]. In [20], Öztürk and Nešovic′ defined the pseudo null and null Cartan Darboux helices in Minkowski 3-space and obtained the relationship between pseudo null, null Cartan Darboux helices, and slant helices. In [21], the quasi Darboux vector field of null curve in Minkowski 3-space was defined, and some interesting conclusions about osculating developable of null curve which is defined by quasi Darboux vector field of null curve were obtained. Wang and Pei defined the Darboux vector of the null curve in [23] and described the direction of the rotation

axis of the Cartan frame in Minkowski 3-space. Later, in 2017, Düldül [27] extended the Darboux frame field to four-dimensional Euclidean space and gave the relationship between the curvature of Frenet frame and Darboux frame. In [28], Düldül defined some new vector fields in four-dimensional Euclidean space and showed that the determined new planes play the role of the Darboux vector. İlarslan and Yildirim [29] defined the Darboux helices in four-dimensional Euclidean space as a curve whose Darboux vector makes a constant angle with some fixed direction and obtained relation between the curves Darboux helix, general helix, and V_4-slant helix in a special case.

Motivated by those ideas, in this paper, we construct four new vector fields along the space curve whose curvatures do not disappear in four-dimensional space-time. Based on these vector fields, we define some new planes and helices in four-dimensional space-time. The corresponding curvature functions are given when the position vectors of the curves lie on different planes. Moreover, we define Darboux helices in Minkowski 4-space and give some descriptions of their curvature functions.

2. Preliminaries

Four-dimensional space-time $\mathbb{E}_1^4$ is the real four-dimensional vector space $\mathbb{R}^4$ equipped with the standard flat metric given by

$$\langle x, y\rangle = x_1y_1 + x_2y_2 + x_3y_3 - x_4y_4. \tag{2}$$

For any three vectors $x = (x_1, x_2, x_3, x_4)$, $y = (y_1, y_2, y_3, y_4)$, and $z = (z_1, z_2, z_3, z_4)$ in $\mathbb{E}_1^4$, their exterior product is given by

$$x \times y \times z = \begin{vmatrix} e_1 & e_2 & e_3 & -e_4 \\ x_1 & x_2 & x_3 & x_4 \\ y_1 & y_2 & y_3 & y_4 \\ z_1 & z_2 & z_3 & z_4 \end{vmatrix}, \tag{3}$$

where $\{e_1, e_2, e_3, e_4\}$ is an orthogonal basis in $\mathbb{E}_1^4$, that is,

$$e_1 = (1, 0, 0, 0), e_2 = (0, 1, 0, 0), e_3 = (0, 0, 1, 0), e_4 = (0, 0, 0, 1). \tag{4}$$

A vector v in $\mathbb{E}_1^4$ is called spacelike, timelike, or null (lightlike), if $\langle v, v\rangle > 0$ or $\langle v, v\rangle < 0$, $\langle v, v\rangle = 0$, respectively. In particular, the vector $v = 0$ is said to be spacelike. A curve $\gamma(s)$: $I \longrightarrow \mathbb{E}_1^4$ is called spacelike, timelike, or null (lightlike) if all of its velocity vectors $\gamma'(s)$ satisfy $\langle \gamma', \gamma'\rangle > 0$, $\langle \gamma', \gamma'\rangle < 0$, or $\langle \gamma', \gamma'\rangle = 0$, respectively. The norm of a vector v in $\mathbb{E}_1^4$ is given by $\|v\| = \sqrt{|\langle v, v\rangle|}$ [15].

Definition 1 (see [30]). Let $\gamma(s)$ be a null curve parameterized by null arc length s (i.e., $\|\gamma''(s)\| = 1$) in $\mathbb{E}_1^4$. Then, $\gamma(s)$ can be framed by a Cartan Frenet frame $\{T, N, B_1, B_2\}$ such that

$$\begin{bmatrix} T' \\ N' \\ B_{1'} \\ B_{2'} \end{bmatrix} = \begin{bmatrix} 0 & 1 & 0 & 0 \\ k_2 & 0 & -1 & 0 \\ 0 & -k_2 & 0 & k_3 \\ -k_3 & 0 & 0 & 0 \end{bmatrix} \begin{bmatrix} T \\ N \\ B_1 \\ B_2 \end{bmatrix}, \tag{5}$$

where

$$\begin{aligned} &\langle N, B_2\rangle = \langle T, B_2\rangle = \langle N, B_1\rangle = \langle T, N\rangle = \langle T, T\rangle \\ &\quad = \langle B_1, B_1\rangle = \langle B_1, B_2\rangle = 0, \\ &\langle N, N\rangle = \langle B_2, B_2\rangle = \langle T, B_1\rangle = 1, \\ &T \times N \times B_1 = B_2, N \times B_1 \times B_2 = B_1, B_1 \times B_2 \times T \\ &\quad = N, B_2 \times T \times N = T. \end{aligned} \tag{6}$$

In sequence, T, N, B_1, B_2 are called the tangent, principal normal, first binormal, and second binormal vector field of $\gamma(s)$ and k_2 and k_3 are first curvature and second curvature of the curve $\gamma(s)$, respectively.

Definition 2 (see [16]). Let$\gamma(s)$ be a pseudo null curve parameterized by arc length s (i.e., $\|\gamma''(s)\| = 0$) in $\mathbb{E}_1^4$. Then, the Frenet equation is defined by

$$\begin{bmatrix} T' \\ N' \\ B_{1'} \\ B_{2'} \end{bmatrix} = \begin{bmatrix} 0 & 1 & 0 & 0 \\ 0 & 0 & k_1 & 0 \\ 0 & k_2 & 0 & -k_1 \\ -1 & 0 & -k_2 & 0 \end{bmatrix} \begin{bmatrix} T \\ N \\ B_1 \\ B_2 \end{bmatrix}, \tag{7}$$

where

$$\begin{aligned} &\langle B_2, B_2\rangle = \langle B_1, B_2\rangle = \langle N, B_1\rangle = \langle T, B_1\rangle \\ &\quad = \langle T, N\rangle = \langle T, B_2\rangle = \langle N, N\rangle = 0, \\ &\langle N, B_2\rangle = \langle B_1, B_1\rangle = \langle T, T\rangle = 1, \\ &T \times N \times B_1 = N, N \times B_1 \times B_2 = T, B_1 \times B_2 \times T \\ &\quad = B_2, B_2 \times T \times N = B_1, \end{aligned} \tag{8}$$

and k_1 and k_2 are first curvature and second curvature of the curve $\gamma(s)$, respectively.

3. Darboux Helix and Planes of Null Curve

When the Frenet frame $\{T, N, B_1, B_2\}$ of a nongeodesic null curve makes an instantaneous helix motion in $\mathbb{E}_1^4$, there exists an axis of the frame's rotation. The direction of such axis is given by the vector

$$D_1 = k_2T + B_1, D_2 = B_2, D_3 = T, D_4 = k_3N + k_2B_2, \tag{9}$$

and we call them the Darboux vectors for the null curves in $\mathbb{E}_1^4$. The Darboux vectors satisfy the Darboux equations

$$\begin{aligned} T' &= D_1 \times D_2 \times T, \\ N' &= D_2 \times D_1 \times N, \\ B_{1'} &= D_3 \times D_4 \times B_1, \\ B_{2'} &= D_4 \times D_3 \times B_2. \end{aligned} \tag{10}$$

From (10), we know that Frenet vectors T and N rotate around the D_1D_2 plane, and Frenet vectors B_1 and B_2 rotate around the D_3D_4 plane. We find that the D_1D_2 plane and D_3D_4 plane play the role of Darboux vector in three-dimensional space. We also note that D_2 and D_3 are Frenet vectors of the null curve, $\{D_1, D_2, D_3, D_4\}$ is linearly independent, and D_1 is orthogonal to D_2 and D_4. We are going to use the subspace spanned by $\{D_1, D_2\}$ and $\{D_1, D_4\}$ to represent D_1D_2 plane and D_1D_4 plane, respectively.

Inspired by [10, 28], we discuss the situation when the curve $\gamma(s)$ lies in D_1D_2 and D_1D_4 planes.

Theorem 3. *Let $\gamma(s)$: $I \longrightarrow \mathbb{E}_1^4$ be a null curve parameterized by null arc length s. k_2, k_3 are the curvature functions of the null curve $\gamma(s)$. If $\gamma(s)$ lies in D_1D_2 plane, then the curvature functions k_2, k_3 satisfy*

$$\left[\frac{(1/k_3)'}{k_3 + (k_{2'}/k_3)'}\right]' = 0, \tag{11}$$

and in addition, the curve $\gamma(s)$ can be expressed as

$$\gamma(s) = cD_1 + \frac{ck_{2'} - 1}{k_3} D_2, \tag{12}$$

where c is nonzero constant.

Proof. We may assume that

$$\gamma(s) = \lambda(s)D_1 + \mu(s)D_2, \tag{13}$$

and we take the derivative of (13) according to s, and we obtain

$$T = \gamma'(s) = \left((\lambda k_2)' - \mu k_3\right)T + \lambda' B_1 + \left(\lambda k_3 + \mu'\right)B_2. \tag{14}$$

Hence,

$$\begin{cases} (\lambda k_2)' - \mu k_3 = 1, \\ \lambda' = 0, \\ \lambda k_3 + \mu' = 0. \end{cases} \tag{15}$$

From the second equation of (15), we get

$$\lambda = c, \tag{16}$$

and substituting (16) into the first equation of (15), we have

$$\mu = \frac{ck_{2'} - 1}{k_3}. \tag{17}$$

Then, the curve $\gamma(s)$ can be denoted as

$$\gamma(s) = cD_1 + \frac{ck_{2'} - 1}{k_3} D_2. \tag{18}$$

From the third equation of (15), we get

$$c = \frac{(1/k_3)'}{k_3 + (k_{2'}/k_3)'}, \tag{19}$$

that is,

$$\left[\frac{(1/k_3)'}{k_3 + (k_{2'}/k_3)'}\right]' = 0. \tag{20}$$

This ends the proof. □

Corollary 4. *In particular, when $k_3 = a = \text{constant} \neq 0$, we have $k_2 = (a^2/2)s^2 + b$, and the curve $\gamma(s)$ can be expressed as*

$$\gamma(s) = cD_1 + \frac{ca^2 s - 1}{a} D_2, \tag{21}$$

where a and b are constants.

Theorem 5. *Let $\gamma(s)$: $I \longrightarrow \mathbb{E}_1^4$ be a null curve parameterized by null arc length s. k_2, k_3 are the curvature functions of the pseudonull curve $\gamma(s)$. If the $\gamma(s)$ lies in D_1D_4 plane, then the curvature functions k_2, k_3 satisfy*

$$k_2 = \frac{s + c_3}{c_1 s + c_2}, k_3^2 = \frac{c_1 (s + c_3)^2}{(c_1 s + c_2)^2 \left(1 - (s + c_3)^2\right)}, \tag{22}$$

and in addition, the curve $\gamma(s)$ can be expressed as

$$\gamma(s) = (c_1 s + c_2)D_1 + \frac{c_1}{k_3} D_4, \tag{23}$$

where c_1, c_2, and c_3 are constants.

Proof. Assume that

$$\gamma(s) = \lambda D_1 + \mu D_4. \tag{24}$$

Differentiating equation (24) with respect to s, we have

$$\begin{aligned} T = \gamma' = (\lambda k_2)' T + (\mu k_3)' N + \left(\lambda' - \mu k_3\right) B_1 \\ + \left((\mu k_2)' + \lambda k_3\right) B_2. \end{aligned} \tag{25}$$

Then, we obtain the system of differential equations

$$\begin{cases} (\lambda k_2)' = 1, \\ (\mu k_3)' = 0, \\ \lambda' - \mu k_3 = 0, \\ (\mu k_2)' + \lambda k_3 = 0. \end{cases} \tag{26}$$

From the second equation of (26), we get

$$\mu k_3 = c_1. \tag{27}$$

Substituting (27) into the third equation of (26), we have

$$\lambda = c_1 s + c_2. \tag{28}$$

Then, the curve $\gamma(s)$ can be denoted as

$$\gamma(s) = (c_1 s + c_2) D_1 + \frac{c_1}{k_3} D_4. \tag{29}$$

Substituting (28) into the first equation of (26), we have

$$k_2 = \frac{s + c_3}{c_1 s + c_2}. \tag{30}$$

Substituting (27) and (28) into the fourth equation of (26), we can calculate that

$$k_3^2 = \frac{c_1 (s + c_3)^2}{(c_1 s + c_2)^2 \left(1 - (s + c_3)^2\right)}. \tag{31}$$

This ends the proof. □

Definition 6. Let $\gamma(s)$: $I \longrightarrow \mathbb{E}_1^4$ be a null curve with parameterized by null arc length s. If there exists a fixed direction $V \neq 0$ such that

$$\langle D_1, V \rangle = a, a \in \mathbb{R}, \tag{32}$$

then the null curve $\gamma(s)$ is called the null Darboux helix, and the fixed direction V is called an axis of the null Darboux helix.

Theorem 7. *Let $\gamma(s)$: $I \longrightarrow \mathbb{E}_1^4$ be a null curve with parameterized by null arc length s. If $\gamma(s)$ is a null Darboux helix in $\mathbb{E}_1^4$ whose fixed direction V satisfies*

$$\langle D_1, V \rangle = a, a \in \mathbb{R}, \tag{33}$$

then V is given by

$$\begin{aligned} V = &\left(a - b k_2 e^{\int \xi ds}\right) T + b \xi e^{\int \xi ds} N \\ &+ b e^{\int \xi ds} B_1 - \frac{b k_{2'}}{k_3} e^{\int \xi ds} B_2, \end{aligned} \tag{34}$$

and the curvature functions k_2, k_3 satisfy

$$\left(2k_2 - \xi^2 - \xi'\right) e^{\int \xi ds} = \frac{a}{b}, \tag{35}$$

where

$$\xi = \frac{k_3 - (k_{2'}/k_3)'}{k_{2'}/k_3}, \tag{36}$$

and $b \in \mathbb{R}_0, k_3 \neq 0, k_2 \neq const.$

Proof. Let $\gamma(s)$: $I \longrightarrow \mathbb{E}_1^4$ be a null Darboux helix with parameterized by null arc length s. Then, for a fixed direction V satisfying

$$\langle D_1, V \rangle = a, a \in \mathbb{R}, \tag{37}$$

we can assume

$$V = u_1 T + u_2 N + u_3 B_1 + u_4 B_2. \tag{38}$$

By using (5), we can obtain

$$\langle D_1, V \rangle = k_2 u_3 + u_1 = a, \tag{39}$$

$$\langle D_{1'}, V \rangle = k_{2'} u_3 + k_3 u_4 = 0. \tag{40}$$

Taking the derivative of equation (39) according to s, we obtain

$$u_{1'} = -(k_2 u_3)'. \tag{41}$$

Differentiating equation (38) and using the Frenet equation (5), we have

$$\begin{cases} u_{1'} - k_3 u_4 + k_2 u_2 = 0, \\ u_1 + u_{2'} - k_2 u_3 = 0, \\ u_2 - u_{3'} = 0, \\ u_{4'} + k_3 u_3 = 0. \end{cases} \tag{42}$$

By (40), we can obtain

$$u_4 = -\frac{k_{2'}}{k_3} u_3, \tag{43}$$

Substituting (43) into the fourth equation of (42), we can obtain

$$u_3 = b e^{\int \xi ds}, \xi = \frac{k_3 - (k_{2'}/k_3)'}{k_{2'}/k_3}. \tag{44}$$

From (39), (44), and the third equation of (42), we have

$$\begin{aligned} u_2 &= u_{3'} = b \xi e^{\int \xi ds}, \\ u_1 &= a - k_2 u_3 = -b \xi e^{\int \xi ds} + a. \end{aligned} \tag{45}$$

Thus,

$$V = \left(a - bk_2 e^{\int \xi ds}\right) T + b\xi e^{\int \xi ds} N + be^{\int \xi ds} B_1 - \frac{bk_{2'}}{k_3} e^{\int \xi ds} B_2. \tag{46}$$

From the second equation of (42), the relationship between k_2 and k_3 can be expressed as

$$\left(2k_2 - \xi^2 - \xi'\right) e^{\int \xi ds} = \frac{a}{b}, \tag{47}$$

where b is given by the relation (44), and if $b = 0$, the axis $V = 0$, which is a contradiction. Hence, $b \neq 0$, which completes the proof. □

Corollary 8. *In particular, when $a = 0, b = 1$, we have*

$$V = \left(-k_2 T + \xi N + B_1 - \frac{k_{2'}}{k_3} B_2\right) e^{\int \xi ds}, \tag{48}$$

and the curvature functions k_2, k_3 satisfy

$$\xi' + \xi^2 - 2k_2 = 0, \tag{49}$$

where

$$\xi = \frac{k_3 - (k_{2'}/k_3)'}{k_{2'}/k_3}. \tag{50}$$

Some examples of null Darboux helix in $\mathbb{E}_1^4$ are given below.

Example 1. Let $\gamma(s)$: $I \longrightarrow \mathbb{E}_1^4$ be a null curve with the arc length s and the curvature

$$k_2 = \frac{s^2 + 1}{2}, k_3 = \frac{s}{\sqrt{e^{-s^2} + 1}}, \tag{51}$$

and then, $\gamma(s)$ is a Darboux helix whose fixed direction is given by

$$V = \left(-\frac{s^2 + 1}{2} T + sN + B_1 - \sqrt{s^2 + 1} B_2\right) e^{s^2/2}. \tag{52}$$

Example 2. Let $\gamma(s)$: $I \longrightarrow \mathbb{E}_1^4$ be a null curve with the arc length s and the curvature

$$k_2 = \frac{\sec^2 s + \tan^2 s}{2}, k_3 = 2 \sec s \tan s, \tag{53}$$

and then, $\gamma(s)$ is a Darboux helix whose fixed direction is given by

$$V = \left(-\frac{1 + \sin^2 s}{2 \cos^2 s} T + \tan sN + B_1 - \sec sB_2\right) \sec s. \tag{54}$$

Example 3. Let $\gamma(s)$: $I \longrightarrow \mathbb{E}_1^4$ be a null curve with the arc length s and the curvature

$$k_2 = \frac{1}{s^2}, \quad k_3 = -\frac{2}{s^2}, \tag{55}$$

and then, $\gamma(s)$ is a Darboux helix whose fixed direction is given by

$$V = \left(-\frac{1}{s^2} T - \frac{1}{s} N + B_1 - \frac{1}{s} B_2\right) \frac{1}{s}. \tag{56}$$

4. Darboux Helix and Planes of Pseudo null Curve

When the Frenet frame $\{T, N, B_1, B_2\}$ of a nongeodesic pseudonull curve makes an instantaneous helix motion in $\mathbb{E}_1^4$, there exists an axis of the frame's rotation. The direction of such axis is given by the vector

$$D_1 = N, D_2 = k_2 T, D_3 = T, D_4 = -k_2 N - k_1 B_2, \tag{57}$$

and we call them the Darboux vectors for the pseudo null curves in $\mathbb{E}_1^4$. The Darboux vectors satisfy the Darboux equations

$$\begin{aligned} T' &= D_1 \times D_2 \times T, \\ N' &= D_3 \times D_4 \times N, \\ B_{1'} &= D_4 \times D_3 \times B_1, \\ B_{2'} &= D_2 \times D_1 \times B_2. \end{aligned} \tag{58}$$

From (58), we know that Frenet vectors T and B_2 rotate around the D_1D_2 plane, and Frenet vectors N and B_1 rotate around the D_3D_4 plane. We find that the D_1D_2 plane and D_3D_4 plane play the role of Darboux vector in three-dimensional space. We also note that D_1 and D_3 are Frenet vectors of the pseudonull curve, $\{D_1, D_2, D_3, D_4\}$ is linearly independent, and D_4 is orthogonal to D_2 and D_3. We are going to use the subspace spanned by $\{D_2, D_4\}$ and $\{D_3, D_4\}$ to represent D_2D_4 plane and D_3D_4 plane, respectively.

Similar to Section 3, we discuss the situation when the curve $\gamma(s)$ is in D_2D_4 and D_3D_4 planes.

Theorem 9. *Let $\gamma(s)$: $I \longrightarrow \mathbb{E}_1^4$ be a pseudonull curve with parameterized by arc length s. k_1, k_2 are the curvature functions of the pseudonull curve $\gamma(s)$. If $\gamma(s)$ lies in D_2D_4 plane, then the curvature functions k_1, k_2 satisfy*

$$c_2 k_{2''} + c_1 k_2 k_{2'} + k_2 = 0, \tag{59}$$

and in addition, the curve $\gamma(s)$ can be expressed as

$$\gamma(s) = c_1 D_2 + \frac{c_2}{k_2} D_4, \tag{60}$$

where c_1 and c_2 are nonzero constants.

Proof. We may assume that

$$\gamma(s) = \lambda D_2 + \mu D_4, \tag{61}$$

and we take the derivative of (61) according to s, and we obtain

$$\begin{aligned} T = \gamma' = \left(\mu k_1 - (\lambda k_2)'\right) T - (\mu k_2)' N \\ + \lambda' B_1 - \left(\lambda k_1 + (\mu k_1)'\right) B_2. \end{aligned} \tag{62}$$

Hence,

$$\begin{cases} u_1 k_1 - (\lambda k_2)' = 1, \\ (\mu k_2)' = 0, \\ \lambda' = 0, \\ \lambda k_1 + (\mu k_1)' = 0. \end{cases} \tag{63}$$

From the second and the third equations of (63), we get

$$\lambda = c_1, \mu k_2 = c_2, \tag{64}$$

where c_1 and c_2 are nonzero constants.

Then, the curve $\gamma(s)$ can be denoted as

$$\gamma(s) = c_1 D_2 + \frac{c_2}{k_2} D_4. \tag{65}$$

Substituting (64) into the fourth equation of (63), we have

$$c_2 k_1 = c_1 k_2 k_{2'} + k_2. \tag{66}$$

From (66) and the first equation of (63), we get

$$c_2 k_{2''} + c_1 k_2 k_{2'} + k_2 = 0. \tag{67}$$

This ends the proof. □

Theorem 10. *Let $\gamma(s)$: $I \longrightarrow \mathbb{E}_1^4$ be a pseudonull curve with parameterized by arc length s. k_1, k_2 are the curvature functions of the pseudonull curve $\gamma(s)$. If the $\gamma(s)$ lies in D_3D_4 plane, then the curvature functions k_1, k_2 satisfy*

$$\frac{k_2}{k_1} = \frac{(1 - c_1)s^2}{2c_1} + \frac{c_2 s}{c_1} + \frac{c_3}{c_1}, \tag{68}$$

and in addition, the curve can be expressed as

$$\gamma(s) = (c_2 + (1 - c_1)s) D_3 + \frac{c_1}{k_1} D_4, \tag{69}$$

where c_1, c_2, c_3 are constants.

Proof. Assume that

$$\gamma(s) = \lambda D_3 + \mu D_4. \tag{70}$$

Differentiating equation (70) with respect to s, we have

$$T = \gamma' = \left(\mu k_1 + \lambda'\right) T - \left(\lambda - (\mu k_2)'\right) N - (\mu k_1)' B_2. \tag{71}$$

So we obtain the system of differential equations

$$\begin{cases} \mu k_1 + \lambda' = 1, \\ \lambda - (\mu k_2)' = 0, \\ (\mu k_1)' = 0. \end{cases} \tag{72}$$

From the first and the third equations of (72), we get

$$\lambda = (1 - c_1)s + c_2, \tag{73}$$

$$\mu k_1 = c_1. \tag{74}$$

Then, the curve $\gamma(s)$ can be denoted as

$$\alpha(s) = ((1 - c_1)s + c_2) D_3 + \frac{c_1}{k_1} D_4. \tag{75}$$

Substituting (73) and (74) into the second equation of (72), we have

$$\mu k_2 = \frac{1}{2}(1 - c_1)s^2 + c_2 s + c_3. \tag{76}$$

From equations (74) and (76), we can obtain

$$\frac{k_2}{k_1} = \frac{(1 - c_1)s^2}{2c_1} + \frac{c_2 s}{c_1} + \frac{c_3}{c_1}, \tag{77}$$

where c_1, c_2, c_3 are constants. □

Corollary 11. *In particular, when $c_1 = 1/1$, $c_2 = c_3 = 0$, we have $k_2/k_1 = s^2$. Let $k_1 = 3s/(s^2 + 1)^2$ and $k_2 = 3s^3/(s^2 + 1)^2$. Then, the curve $\gamma(s)$ can be expressed as*

$$\gamma'' = \frac{3s\sqrt{s^2 + 1}}{2(s^2 + 1)^3} \left(2s, s^2, 1 - s^2 - \frac{s^4}{4}, 1 + s^2 + \frac{s^4}{4}\right). \tag{78}$$

Definition 12. Let $\gamma(s)$: $I \longrightarrow \mathbb{E}_1^4$ be a pseudo null curve with parameterized by arc length s. If there exists a fixed direction $V \neq 0$ such that

$$\langle D_2, V \rangle = a, a \in \mathbb{R}, \tag{79}$$

then the pseudo null curve $\gamma(s)$ is called the pseudo null Darboux helix, and the fixed direction V is called an axis of the pseudo null Darboux helix.

Theorem 13. *Let $\gamma(s)$: $I \longrightarrow \mathbb{E}_1^4$ be a pseudonull curve with parameterized by arc length s. If $\gamma(s)$ is a pseudonull Darboux*

helix in $\mathbb{E}_1^4$ whose fixed direction V satisfies

$$\langle D_2, V\rangle = a, a \in \mathbb{R}, \tag{80}$$

then V is given by

$$V = u_1 T - \frac{k_{2'}}{k_1} u_1 N + (u_1 k_2 + a) B_1 + u_{1'} B_2, \tag{81}$$

and the curvature functions k_1, k_2 satisfy

$$u_{1''} - k_1 k_2 u_1 = a k_1, \tag{82}$$

where

$$\xi = \frac{1 + k_2^2 - (k_{2'}/k_1)'}{k_{2'}/k_1}, \tag{83}$$

and $a, b \in \mathbb{R}, k_1 \neq 0, k_2 \neq const.$

Proof. Let $\gamma(s)$: $I \longrightarrow \mathbb{E}_1^4$ be a pseudo null Darboux helix with parameterized by arc length s. Then, for a fixed direction V satisfying

$$\langle D_2, V\rangle = a, a \in \mathbb{R}, \tag{84}$$

we can assume

$$V = u_1 T + u_2 N + u_3 B_1 + u_4 B_2. \tag{85}$$

By using (84), we can obtain

$$\langle D_2, V\rangle = u_3 - u_1 k_2 = a, \tag{86}$$

$$\langle D_{2'}, V\rangle = -k_1 u_2 - k_{2'} u_1 = 0. \tag{87}$$

Taking the derivative of equation (86) according to s, we obtain

$$u_{3'} = (k_2 u_1)'. \tag{88}$$

Differentiating equation (85) and using the Frenet equation (7), we have

$$\begin{cases} u_{1'} - u_4 = 0, \\ u_1 + u_{2'} + k_2 u_3 = 0, \\ k_1 u_2 + u_{3'} - k_2 u_4 = 0, \\ u_{4'} - k_1 u_3 = 0. \end{cases} \tag{89}$$

Substituting (86) and (87) into the second equation of (89), we can obtain

$$u_{1'} - \frac{1 + k_2^2 - (k_{2'}/k_1)'}{k_{2'}/k_1} u_1 = a k_2. \tag{90}$$

By (90), we can obtain

$$u_1 = e^{\int \xi ds}\left(a k_2 e^{-\int \xi ds} + b\right), \tag{91}$$

where

$$\xi = \frac{1 + k_2^2 - (k_{2'}/k_1)'}{k_{2'}/k_1}. \tag{92}$$

From (87), (88), and the first equation of (89), we have

$$\begin{aligned} u_2 &= -\frac{k_{2'}}{k_1} u_1 = -\frac{k_{2'}}{k_1} e^{\int \xi ds}\left(a k_2 e^{-\int \xi ds} + b\right), \\ u_3 &= u_1 k_2 + a = k_2 e^{\int \xi ds}\left(a k_2 e^{-\int \xi ds} + b\right) + a, \\ u_4 &= u_{1'} = c_1 k_2 + \xi e^{\int \xi ds}\left(a k_2 e^{-\int \xi ds} + b\right). \end{aligned} \tag{93}$$

Thus,

$$V = u_1 T - \frac{k_{2'}}{k_1} u_1 N + (u_1 k_2 + a) B_1 + u_{1'} B_2. \tag{94}$$

From the fourth equation of (89), the relationship between k_1 and k_2 can be expressed as

$$u_{1''} - k_1 k_2 u_1 = a k_1, a \in \mathbb{R}. \tag{95}$$

This ends the proof. □

Corollary 14. *In particular, when $a = 0, b = 1$, we have*

$$V = \left(T - \frac{k_{2'}}{k_1} N + k_2 B_1 + \xi B_2\right) e^{\int \xi ds}, \tag{96}$$

and the curvature functions k_2, k_3 satisfy

$$\xi' + \xi^2 - k_1 k_2 = 0, \tag{97}$$

where

$$\xi = \frac{1 + k_2^2 - (k_{2'}/k_1)'}{k_{2'}/k_1}. \tag{98}$$

Some examples of pseudo null Darboux helix in $\mathbb{E}_1^4$ are given below.

Example 4. Let $\gamma(s)$: $I \longrightarrow \mathbb{E}_1^4$ be a pseudo null curve, and s is the pseudoarc length. The curvature function k_1, k_2 satisfies

$$k_1 = \frac{1}{s(s^2+1)\sqrt{s^2+1}}, \quad k_2 = \frac{s}{\sqrt{s^2+1}}, \tag{99}$$

and then, $\gamma(s)$ is a Darboux helix whose fixed direction is given by

$$V = \sqrt{s^2+1}T - s\sqrt{s^2+1}N + sB_1 + \frac{s}{\sqrt{s^2+1}}B_2. \quad (100)$$

Example 5. Let $\gamma(s)$: $I \longrightarrow \mathbb{E}_1^4$ be a pseudo null curve with the arc length s and the curvature

$$k_1 = \frac{2\sec^2 s}{\sqrt{2\sec^2 s - 1}}, k_2 = \sqrt{2\sec^2 s - 1}, \quad (101)$$

and then, $\gamma(s)$ is a Darboux helix whose fixed direction is given by

$$V = \tan sT - \tan^2 sN + \tan s\sqrt{2\sec^2 s - 1}B_1 + \sec^2 sB_2. \quad (102)$$

Example 6. Let $\gamma(s)$: $I \longrightarrow \mathbb{E}_1^4$ be a pseudo null curve with the arc length s and the curvature

$$k_1 = \frac{1}{\sqrt{2e^s - 1}}, k_2 = \sqrt{2e^s - 1}, \quad (103)$$

and then, $\gamma(s)$ is a Darboux helix whose fixed direction is given by

$$V = e^s T - e^{2s}N + e^s\sqrt{2e^s - 1}B_1 + e^s B_2. \quad (104)$$

5. Conclusion

In this paper, we discuss some new space curves and planes in four-dimensional space-time and give characterizations of them in terms of the curvature functions. Before this study, most researchers studied Darboux vector in three-dimensional space and four-dimensional Euclidean space. In this paper, the Darboux vector fields in three-dimensional space are extended to four-dimensional space-time by mathematical method. By defining Darboux vector fields in four-dimensional space-time in the form of vector products, we find that the Frenet vectors rotate around a plane spanned by two new vector fields, and this plane plays the role that the Darboux vector plays in three-dimensional space. This paper gives a new description of Darboux vector in four-dimensional space-time, which promotes the further development of angular momentum vector in physics and geometry.

Data Availability

No data were used to support this study.

Conflicts of Interest

The authors declare no conflict of interest.

Authors' Contributions

The authors have made the same contribution.

References

[1] A. Petrov, *Einstein Spaces*, Pergamon Press, 1969.

[2] M. P. Dabrowski, "Null string evolution in black hole and cosmological spacetimes," *Physical Review D.*, vol. 66, no. 4, pp. 427–444, 2002.

[3] A. Ferrández, A. Giménez, and P. Lucas, "Relativistic particles and the geometry of 4-D null curves," *Journal of Geometry and Physics.*, vol. 57, no. 10, pp. 2124–2135, 2007.

[4] K. L. Duggal and D. H. Jin, "A classification of Einstein lightlike hypersurfaces of a Lorentzian space form," *Journal of Geometry and Physics*, vol. 60, no. 12, pp. 1881–1889, 2010.

[5] S. Izumiya and H. Yildirim, "Slant geometry on spacelike submanifolds of codimension two in Lorentz-Minkowski space," *Journal of Geometry and Physics*, vol. 98, pp. 160–180, 2015.

[6] B. Sahin, E. Kiliç, and R. Günes, "Null helices in Minkowski 3-space," *Differential Geometry Dynamical Systems*, vol. 3, pp. 31–36, 2001.

[7] B. O'Neill, *Semi-Riemannian Geometry: With Applications to Relativity*, Academic Press, New York, 1983.

[8] J. A. Aledo, J. M. Espinar, and J. A. Galvez, "Timelike surfaces in the Lorentz–Minkowski space with prescribed Gaussian curvature and Gauss map," *Journal of Geometry and Physics*, vol. 56, no. 8, pp. 1357–1369, 2006.

[9] A. E. Treibergs, "Entire spacelike hypersurfaces of constant mean curvature in Minkowski space," *Inventiones Mathematicae*, vol. 66, no. 1, pp. 39–56, 1982.

[10] B. Y. Chen, "When does the position vector of a space curve always lie in its rectifying plane," *American Mathematical Monthly*, vol. 110, no. 2, pp. 147–152, 2003.

[11] L. J. Alías and J. M. Malacarne, "Spacelike hypersurfaces with constant higher order mean curvature in Minkowski spacetime," *Journal of Geometry and Physics*, vol. 41, no. 4, pp. 359–375, 2002.

[12] Z. Özdemir and I. A. Gök, "New approach on type-3 slant helix in $\mathbb{E}^4$," *Gen. Math*, vol. 28, no. 1, pp. 40–49, 2015.

[13] M. Bektas and M. Yilmaz Yildirim, "(k, m)-type slant helices for partially null and pseudo null curves in Minkowski 4-space $\mathbb{E}14$," *Applied Mathematics and Nonlinear Sciences.*, vol. 5, no. 1, pp. 515–520, 2020.

[14] E. Nešović, "On k-type null Cartan slant helices in Minkowski 3-space," *Mathematical Methods in the Applied Sciences*, vol. 41, no. 17, pp. 7583–7598, 2018.

[15] K. İlarslan and E. Nešović, "Spacelike and timelike normal curves in Minkowski space-time," *Publications de I' Institut Mathematique*, vol. 85, no. 99, pp. 111–118, 2009.

[16] A. Tawfik and M. Turgut, "k-type partially null and pseudo null slant helices in Minkowski 4-space," *Mathematical Communications*, vol. 17, pp. 93–103, 2012.

[17] S. Izumiya and M. Kasedou, "Lightlike flat geometry of spacelike submanifolds in Lorentz-Minkowski space," *International Journal of Geometric Methods in Modern Physics.*, vol. 11, no. 5, pp. 1450049–1450200, 2014.

[18] M. P. Do Carmo, *Differential Geometry of Curves and Surfaces*, Prentice-Hall, New Jersey, 1976.

[19] E. Ziplar and A. Senol, "On Darboux helices in Euclidean 3-space," *Global Journal of Science Frontier Research*, vol. 12, no. 13, pp. 72–80, 2012.

[20] U. Öztürk and E. Nešović, "On k -type pseudo null Darboux helices in Minkowski 3-space," *Kuwait Journal of Science*, vol. 439, no. 2, pp. 690–700, 2016.

[21] E. Kiliç, H. B. Karadağ, and M. Karadağ, "Special null curves on the ruled surfaces in the Minkowski 3-spaces," *Indian Journal of Mathematics Special Memorial*, vol. 51, no. 1, 2009.

[22] K. Zhou and Z. Wang, "Pseudo-spherical Darboux images and lightcone images of principal-directional curves of nonlightlike curves in Minkowski 3-space," *Mathematical Methods in the Applied Sciences*, vol. 43, no. 1, pp. 35–77, 2020.

[23] Z. Wang and D. H. Pei, "Null Darboux developable and pseudo-spherical Darboux image of null Cartan curve in Minkowski 3-space," *Hokkaido Mathematical Journal*, vol. 40, no. 2, pp. 219–240, 2011.

[24] J. Qian, X. Fu, and S. D. Jung, "Darboux associated curves of a null curve on pseudo-Riemannian space forms," *Mathematics*, vol. 8, no. 3, p. 395, 2020.

[25] E. Nešović and U. Öztürk, "On k-type pseudo null Darboux helices in Minkowski 3-space," *Journal of Mathematical Analysis and Applications*, vol. 439, no. 2, pp. 690–700, 2016.

[26] S. Izumiya, H. Katsumi, and T. Yamasaki, "The rectifying developable and the spherical Darboux image of a space curve," *Banach Center Publications*, vol. 50, no. 1, pp. 137–149, 1999.

[27] M. Düldül, "Extension of the Darboux frame into Euclidean 4-space and its invariants," *Turkish Journal of Mathematics*, vol. 41, no. 6, pp. 1628–1639, 2017.

[28] M. Düldül, "Vector fields and planes in $\mathbb{E}^4$ which play the role of Darboux vector," *Turkish Journal of Mathematics*, vol. 44, no. 1, pp. 274–283, 2020.

[29] K. İlarslan and M. Yildirim, "On Darboux helices in Euclidean 4-space," *Mathematical Methods in the Applied Sciences*, vol. 42, no. 16, pp. 5184–5189, 2019.

[30] J. Walrave, *Curves and Surfaces in Minkowski Space, [Ph.D. thesis]*, K. U. Leuven, Fac. of Science, Leuven, 1995.

Hindawi
Advances in Mathematical Physics
Volume 2022, Article ID 9239897, 6 pages
https://doi.org/10.1155/2022/9239897

Research Article

On Compact Trans-Sasakian Manifolds

Ibrahim Al-Dayel[1] **and Sharief Deshmukh**[2]

[1]*Department of Mathematics and Statistics, College of Science, Imam Mohammad Ibn Saud Islamic University, P.O. Box-65892, Riyadh 11566, Saudi Arabia*
[2]*Department of Mathematics, College of Science, King Saud University, P.O. Box-2455, Riyadh 11451, Saudi Arabia*

Correspondence should be addressed to Sharief Deshmukh; shariefd@ksu.edu.sa

Received 17 January 2022; Accepted 16 March 2022; Published 5 April 2022

Academic Editor: P. Areias

We study 3-dimensional compact and simply connected trans-Sasakian manifolds and find necessary and sufficient conditions under which these manifolds are homothetic to Sasakian manifolds. The first two results deal with finding necessary and sufficient conditions on a compact and simply connected trans-Sasakian manifold to be homothetic to an Einstein Sasakian manifold and in the third result deals with finding necessary and sufficient condition on a compact and simply connected trans-Sasakian manifold to be homothetic to a Sasakian manifold.

1. Introduction

It is well known that for an almost contact metric manifold (M, F, ζ, η, g) (cf. [1]), the product $\bar{M} = M \times R$ has an almost complex structure J, which with product metric $\bar{g}$ makes $(\bar{M}, \bar{g})$ an almost Hermitian manifold. The properties of the almost Hermitian manifold $(\bar{M}, J, \bar{g})$ control the properties of the almost contact metric manifold (M, F, ζ, η, g) and provide several structures on M such as a Sasakian structure and a quasi-Sasakian structure (cf. [1–3]). There are known sixteen different types of structures on $(\bar{M}, J, \bar{g})$ (cf. [4]), and using the structure in the class $\mathcal{W}_4$ on $(\bar{M}, J, g)$, a structure $(F, \zeta, \eta, g, \alpha, \beta)$ was introduced on M, which is called trans-Sasakian structure (cf. [5]), that generalizes Sasakian structure, Kenmotsu structure, and cosymplectic structure on a contact metric manifold (cf. [2, 3]), where α and β being the real functions defined on M.

Recall that a trans-Sasakian manifold $(M, F, \zeta, \eta, g, \alpha, \beta)$ is called a trans-Sasakain manifold of type (α, β), and trans-Sasakian manifolds of type $(0, 0)$, $(\alpha, 0)$, and $(0, \beta)$ are called a cosymplectic, a α-Sasakian, and a β-Kenmotsu manifolds, respectively. It is on account of a result proved in [6] that a trans-Sasakian manifold of dimension five or greater than five reduces to a cosymplectic manifold, a α-Sasakian manifold, or a β-Kenmotsu manifold, so there is an emphasis on studying three-dimensional trans-Sasakian manifolds.

Among other questions, finding conditions under which a compact 3-dimensional trans-Sasakian manifold (M, F, ζ, η, g) is homothetic to a Sasakian manifold is of prime importance. The geometry of 3-dimensional trans-Sasakian manifold is also important owing to Thurston's conjecture (cf. [7]), and fetching conditions on a 3-dimensional trans-Sasakian manifold (M, F, ζ, η, g) in matching it among Thurston's eight geometries becomes more interesting. It is worth noting that in Thurston's eight geometries, the first place is occupied by the spherical geometry S^3.

In ([8–13]), the authors have studied compact 3-dimensional trans-Sasakian manifolds with some suitable restrictions on functions α and β appearing in the definition of a trans-Sasakian manifold for getting conditions under which a trans-Sasakian manifold is homothetic to a Sasakian manifold. In particular, it is known that a 3-dimensional compact simply connected trans-Sasakian manifold $(M, F, \zeta, \eta, g, \alpha, \beta)$ satisfying Poisson equations $\Delta\alpha = \beta$ and $\Delta\alpha = \alpha^2\beta$, respectively, is necessarily homothetic to a Sasakian manifold (cf. [10]).

An interesting work on 3-dimensional trans-Sasakian manifolds is found in [14, 15], where the authors have considered other aspects in Thurston's eight geometries. In [10], it is asked whether the function β on a 3-dimensional compact trans-Sasakian manifold $(M, F, \zeta, \eta, g, \alpha, \beta)$ satisfying grad $\beta = \zeta(\beta)\zeta$ necessitates the trans-Sasakian manifold to be homothetic to a Sasakian manifold. In [15], it is shown that this question has negative answer.

Einstein Sasakian manifolds are very important due to their geometric importance (cf. [16]). In this paper, in our first two results, we find necessary and sufficient conditions on a compact simply connected 3-dimensional trans-Sasakian manifold $(M, F, \zeta, \eta, g, \alpha, \beta)$ to be homothetic to an Einstein Sasakian manifold, and in the third, we find a necessary and sufficient condition on a compact simply connected 3-dimensional trans-Sasakian $(M, F, \zeta, \eta, g, \alpha, \beta)$ to be homothetic to a Sasakian manifold.

In the first result, we consider a compact and simply connected trans-Sasakian manifold $(M, F, \zeta, \eta, g, \alpha, \beta)$ of positive constant scalar curvature τ, the function β satisfying Fischer-Marsden equation shows that the functions α and β are related to τ by the inequality $\beta(\alpha^2 - \beta^2 - \tau/4) \geq 0$, and the Ricci operator Q satisfying Codazzi-type equation with respect to vector field ζ necessarily implies that $(M, F, \zeta, \eta, g, \alpha, \beta)$ is homothetic to an Einstein Sasakian manifold. In the second result, we show that a compact simply connected trans-Sasakian manifold with function α constant along the integral curves of ζ, scalar curvature τ satisfying the inequality $\alpha(6\alpha^2 - \tau) \geq 0$, and the Ricci operator Q satisfying Codazzi-type equation with respect to vector field ζ necessarily imply that $(M, F, \zeta, \eta, g, \alpha, \beta)$ is homothetic to an Einstein Sasakian manifold. Finally, in the last result, we show that on a compact and simply connected trans-Sasakian manifold, the function β satisfies the differential inequality $\zeta(\beta^2) \leq -2\beta^3$, and vector fields $(\nabla Q)(\text{grad}\alpha, \zeta), \zeta$ are orthogonal, which necessarily imply that $(M, F, \zeta, \eta, g, \alpha, \beta)$ is homothetic to a Sasakian manifold, where the covariant derivative $(\nabla Q)(U, \zeta) = \nabla_U Q\zeta - Q(\nabla_U \zeta)$ for a smooth vector field U on M.

2. Preliminaries

Let (M, F, ζ, η, g) be an almost contact metric manifold dim $M = 3$, where F being a $(1,1)$-tensor field, ζ a unit vector field, and η smooth 1-form dual to ζ with respect to the Riemannian metric g satisfying

$$F^2 = -I + \eta \otimes \zeta,\ F(\zeta) = 0,\ \eta \circ F = 0,\ g(FU_1, FU_2) = g(U_1, U_2) - \eta(U_1)\eta(U_2),\quad U_1, U_2 \in \Gamma(TM), \tag{1}$$

where $\Gamma(TM)$ is the space of smooth sections of the tangent bundle TM (cf. [1]). If there exist functions α and β on an almost contact metric manifold (M, F, ζ, η, g) satisfying

$$(\nabla F)(U_1, U_2) = \alpha(g(U_1, U_2)\zeta - \eta(U_2)U_1) + \beta(g(FU_1, U_2)\zeta - \eta(U_2)FU_1), \tag{2}$$

then $(M, F, \zeta, \eta, g, \alpha, \beta)$ is said to be a trans-Sasakian manifold, where $(\nabla F)(U_1, U_2) = \nabla_{U_1} FU_2 - F(\nabla_{U_1} U_2)$, $U_1, U_2 \in \Gamma(TM)$, and ∇ is the Levi-Civita connection with respect to the metric g (cf. [8–15]). Using equations (1) and (2), it follows that

$$\nabla_U \zeta = -\alpha F(U) + \beta(U - \eta(U)\zeta), \quad U \in \Gamma(TM). \tag{3}$$

Using the Ricci tensor Ric of a Riemannian manifold (M, g), the Ricci operator Q is defined by $Ric(U_1, U_2) = g(QU_1, U_2)$ and $U_1, U_2 \in \Gamma(TM)$. We have the following for a 3-dimensional trans-Sasakian manifold $(M, F, \zeta, \eta, g, \alpha, \beta)$:

$$\zeta(\alpha) = -2\alpha\beta, \tag{4}$$

$$Q\zeta = F(\text{grad}\,\alpha) - \text{grad}\,\beta + 2\left(\alpha^2 - \beta^2\right)\zeta - \zeta(\beta)\zeta. \tag{5}$$

Note that equation (3) implies

$$\text{div}\,\zeta = 2\beta, \tag{6}$$

and using this equation together with equation (4), we have

$$\text{div}\left(\alpha^k \zeta\right) = k\alpha^{k-1}\zeta(\alpha) + \alpha^k\,\text{div}\,\zeta = -2k\alpha^k\beta + 2\alpha^k\beta = -2(k-1)\alpha^k\beta. \tag{7}$$

Thus, on compact 3-dimensional trans-Sasakian manifold $(M, F, \zeta, \eta, g, \alpha, \beta)$, using equation (6) and the above equation, we have

$$\begin{aligned} \int_M \beta &= 0, \\ \int_M \alpha^k \beta &= 0 \text{for} k \neq 1. \end{aligned} \tag{8}$$

Now, we state the following result of Okumura.

Theorem 1. *[17] Let (M, g) be a Riemannian manifold. If M admits a Killing vector field ζ of constant length satisfying*

$$c^2\left(\nabla_{U_1}\nabla_{U_2}\zeta - \nabla_{\nabla_{U_1}U_2}\zeta\right) = g(U_2, \zeta)U_1 - g(U_1, U_2)\zeta \tag{9}$$

for nonzero constant c and any vector fields U_1 and U_2, then M is homothetic to a Sasakian manifold.

For a smooth function h on the Riemannian manifold (M, g), then the operator A_h defined by

$$A_h(U) = \nabla_U\,\text{grad}\,h, \quad U \in \Gamma(TM) \tag{10}$$

is called the Hessian operator of h, and it is a symmetric operator. Moreover, the Hessian $\text{Hess}(h)$ of h is defined by

$$\text{Hess}(h)(U_1, U_2) = g(A_h(U_1), U_2), \quad U_1, U_2 \in \Gamma(TM). \tag{11}$$

The Laplace operator Δ on (M, g) is defined by $\Delta h = \text{div}\,(\text{grad}\,h)$, and we also have

$$\Delta h = trA_h. \tag{12}$$

Fischer-Marsden differential equation on a Riemannian manifold (M, g) is (cf. [18])

$$(\Delta h)g + h\text{Ric} = \text{Hess}(h). \tag{13}$$

3. Trans-Sasakian Manifolds Homothetic to Einstein Sasakian Manifolds

In this section, we find necessary and sufficient conditions for a compact and simply connected 3-dimensional trans-Sasakian manifold $(M, F, \zeta, \eta, g, \alpha, \beta)$ to be homothetic to an Einstein Sasakian manifold.

Theorem 2. *A compact and simply connected 3-dimensional trans-Sasakian manifold $(M, F, \zeta, \eta, g, \alpha, \beta)$ with positive constant scalar curvature τ and the function β a solution of Fischer-Marsden equation satisfying*

$$\beta\left(\alpha^2 - \beta^2 - \frac{\tau}{4}\right) \geq 0 \tag{14}$$

is homothetic to an Einstein Sasakian manifold of positive scalar curvature, if and only if, the Ricci operator Q satisfies

$$(\nabla Q)(U, \zeta) = (\nabla Q)(\zeta, U), \quad U \in \Gamma(TM). \tag{15}$$

Proof. Suppose $(M, F, \zeta, \eta, g, \alpha, \beta)$ is a compact simply connected 3-dimensional trans-Sasakian manifold satisfying the hypothesis. Then, equation (13) gives

$$(\Delta\beta)g + \beta\text{Ric} = \text{Hess}(\beta), \tag{16}$$

and taking trace in above equation and using equation (12), we have

$$\Delta\beta = -\frac{\tau}{2}\beta. \tag{17}$$

□

Note that by equation (3), we have $\nabla_\zeta \zeta = 0$, and therefore, $\text{Hess}(\beta)(\zeta, \zeta) = \zeta\zeta(\beta)$. Using this equation and equation (17) in equation (16), we get

$$-\frac{\tau}{2}\beta + \beta\text{Ric}(\zeta, \zeta) = \zeta\zeta(\beta). \tag{18}$$

Now, using equation (5), we have $\text{Ric}(\zeta, \zeta) = 2(\alpha^2 - \beta^2 - \zeta(\beta))$. Thus, the above equation becomes

$$-\frac{\tau}{2}\beta + 2\beta\left(\alpha^2 - \beta^2 - \zeta(\beta)\right) = \zeta\zeta(\beta). \tag{19}$$

Using equation (6), we have $\text{div}\,(\zeta(\beta)\zeta) = \zeta\zeta(\beta) + 2\beta\zeta(\beta)$, and inserting it in the above equation, we conclude

$$-\frac{\tau}{2}\beta + 2\beta\left(\alpha^2 - \beta^2\right) = \text{div}\,(\zeta(\beta)\zeta). \tag{20}$$

Integrating the above equation, we get

$$\int_M \beta\left(\alpha^2 - \beta^2 - \frac{\tau}{4}\right) = 0. \tag{21}$$

Using the inequality in the statement, we conclude

$$\beta\left(\alpha^2 - \beta^2 - \frac{\tau}{4}\right) = 0. \tag{22}$$

Since M is simply connected, it is connected, and therefore equation (22) implies either (i) $\beta = 0$ or (ii) $\alpha^2 - \beta^2 - \tau/4 = 0$. Suppose (ii) holds, then as τ is a constant, we get $\zeta(\alpha^2) = \zeta(\beta^2)$, which in view of equation (4) implies $\beta\zeta(\beta) = -2\alpha^2\beta$; that is, $3\beta^2\zeta(\beta) = -6\alpha^2\beta^2$. Thus, we have

$$\zeta\left(\beta^3\right) = -6\alpha^2\beta^2. \tag{23}$$

Using equation (6), we have $\text{div}\,(\beta^3\zeta) = \zeta(\beta^3) + 2\beta^4$, and inserting it in above equation, we get

$$\text{div}\,\left(\beta^3\zeta\right) = 2\beta^2\left(\beta^2 - 3\alpha^2\right). \tag{24}$$

Integrating the above equation, we get

$$\int_M \beta^2\left(3\alpha^2 - \beta^2\right) = 0. \tag{25}$$

Now, using (ii) in above integral, we have

$$\int_M \beta^2\left(2\alpha^2 + \frac{\tau}{4}\right) = 0, \tag{26}$$

and since the scalar curvature $\tau > 0$, through above integral, we conclude that $\beta = 0$. Thus, using equations (2), (3), (4), and (5), take the forms

$$\begin{aligned}(\nabla F)(U_1, U_2) &= \alpha(g(U_1, U_2)\zeta - \eta(U_2)U_1),\\ \nabla_U \zeta &= -\alpha FU,\end{aligned} \tag{27}$$

$$\begin{aligned}\zeta(\alpha) &= 0,\\ Q\zeta &= F(\text{grad}\,\alpha) + 2\alpha^2\zeta.\end{aligned} \tag{28}$$

Taking the covariant derivative in the second equation of equation (28), we get

$$(\nabla Q)(U, \zeta) + Q(\nabla_U \zeta) = (\nabla F)(U, \text{grad}\,\alpha) + F(A_\alpha U) + 4\alpha U(\alpha)\zeta + 2\alpha^2\nabla_U\zeta, \tag{29}$$

and using equation (27) in above equation, we arrive at

$$(\nabla Q)(U,\zeta) - \alpha Q(FU) = 5\alpha U(\alpha)\zeta + F(A_\alpha U) - 2\alpha^3 FU, \quad U \in \Gamma(TM). \tag{30}$$

Now, using the Codazzi equation type condition on Q in the hypothesis, we get

$$(\nabla Q)(\zeta,U) - \alpha Q(FU) = 5\alpha U(\alpha)\zeta + F(A_\alpha U) - 2\alpha^3 FU, \quad U \in \Gamma(TM). \tag{31}$$

Using the second equation in equation (27), we compute the Lie derivative of g with respect to ζ to conclude

$$\left(\pounds_\zeta g\right)(U_1,U_2) = -\alpha g(FU_1,U_2) - \alpha g(FU_2,U_1) = 0, \tag{32}$$

that is, ζ is a Killing vector field and that the flow of ζ consists of isometries of the Riemannian manifold M. Thus, we have

$$\left(\pounds_\zeta Q\right)(U) = 0, \quad U \in \Gamma(TM), \tag{33}$$

and using equation (27), we conclude

$$(\nabla Q)(\zeta,U) = \alpha Q(FU) - \alpha F(QU), \quad U \in \Gamma(TM). \tag{34}$$

Combining the above equation with equation (31), we have

$$-\alpha F(QU) = 5\alpha U(\alpha)\zeta + F(A_\alpha U) - 2\alpha^3 FU, \quad U \in \Gamma(TM). \tag{35}$$

Taking the inner product with ζ in above equation, we conclude

$$\alpha U(\alpha) = 0, \quad U \in \Gamma(TM). \tag{36}$$

We claim that M being simply connected, $\alpha \neq 0$; for if $\alpha = 0$, then by equation (27), we see that ζ is parallel and that η is closed, which implies η is exact; that is, $\eta = df$ for a smooth function f on M. This implies $\zeta = \text{gradf}$, and M being compact, there is a point $q \in M$ such that $(\text{gradf})(q) = 0$, and we get $\zeta(q) = 0$, a contradiction to the fact that ζ is a unit vector field. Hence, $\alpha \neq 0$, and equation (36) implies $U(\alpha) = 0$, $U \in \Gamma(TM)$; that is, α is a nonzero constant.

Now, equation (28) gives $Q(\zeta) = 2\alpha^2\zeta$, and taking the covariant derivative in this equation yields

$$(\nabla Q)(U,\zeta) - \alpha Q(FU) = -2\alpha^3 FU. \tag{37}$$

Using the condition in the hypothesis and equation (34) with $\alpha \neq 0$, in above equation, we get

$$-F(QU) = -2\alpha^2 FU, \quad U \in \Gamma(TM). \tag{38}$$

Operating F on above equation while using equation (1) and $Q(\zeta) = 2\alpha^2\zeta$, we conclude

$$QU = 2\alpha^2 U, \quad U \in \Gamma(TM). \tag{39}$$

This proves that M is an Einstein manifold. Finally, using equation (27), with α a nonzero constant, we compute

$$\begin{aligned}\nabla_{U_1}\nabla_{U_2}\zeta - \nabla_{\nabla_{U_1}U_2}\zeta &= -\alpha\left(\nabla_{U_1}FU_2 - F\left(\nabla_{U_1}U_2\right)\right)\\ &= -\alpha(\nabla F)(U_1,U_2) = \alpha^2\left(g(U_2,\zeta)U_1 - g(U_1,U_2)\zeta\right).\end{aligned} \tag{40}$$

Hence, by Theorem 1, we conclude that M is homothetic to a compact simply connected Einstein Sasakian manifold of positive scalar curvature. The converse is trivial.

Theorem 3. *A compact and simply connected 3-dimensional trans-Sasakian manifold $(M, F, \zeta, \eta, g, \alpha, \beta)$ satisfying $\zeta(\alpha) = 0$ and the scalar curvature τ satisfying*

$$\alpha\left(6\alpha^2 - \tau\right) \geq 0 \tag{41}$$

is homothetic to an Einstein Sasakian manifold, if and only if, the Ricci operator Q satisfies

$$(\nabla Q)(U,\zeta) = (\nabla Q)(\zeta,U), \quad U \in \Gamma(TM). \tag{42}$$

Proof. Suppose $(M, F, \zeta, \eta, g, \alpha, \beta)$ is a compact and simply connected 3-dimensional trans-Sasakian manifold satisfying the hypothesis. Then, using equation (4) and the condition $\zeta(\alpha) = 0$, we get $\alpha\beta = 0$. However, if $\alpha = 0$, then equation (3) implies that η is closed, and as seen in the proof of Theorem 2, we get a contradiction owing to simply connectedness of M. Thus, $\alpha \neq 0$, and on connected M, equation $\alpha\beta = 0$ implies that $\beta = 0$. Therefore, equations (27) and (28) hold. Now, using equation (28), we have $Q\zeta = F(\text{grad}\ \alpha) + 2\alpha^2\zeta$, which gives

$$-\text{grad}\ \alpha = F(Q\zeta). \tag{43}$$

□

Taking covariant derivative in above equation, we have

$$-A_\alpha U = (\nabla F)(U,Q\zeta) + F(\nabla Q)(U,\zeta) + FQ(\nabla_U\zeta), \quad U \in \Gamma(TM), \tag{44}$$

and using equation (27), we get

$$-A_\alpha U = \alpha(\text{Ric}(U,\zeta)\zeta - \text{Ric}(\zeta,\zeta)U) + F(\nabla Q)(U,\zeta) - \alpha FQFU, \quad U \in \Gamma(TM). \tag{45}$$

Using condition in the hypothesis, we have

$$-A_\alpha U = \alpha(Ric(U,\zeta)\zeta - Ric(\zeta,\zeta)U) + F(\nabla Q)(\zeta,U) - \alpha FQFU, \quad U \in \Gamma(TM). \tag{46}$$

Also, equation (27) implies that ζ is a Killing vector field, and therefore, using its outcome equation (34) as well as

equation (28), we conclude

$$-A_\alpha U = \alpha\left(\mathrm{Ric}(U,\zeta)\zeta - 2\alpha^2 U\right) + F(\alpha Q(FU) - \alpha F(QU)) - \alpha FQFU, \quad U \in \Gamma(TM). \tag{47}$$

That is, on using equation (1), we have

$$A_\alpha U = \alpha\left(2\alpha^2 U - QU\right), \quad U \in \Gamma(TM). \tag{48}$$

Thus, we have

$$\Delta\alpha = \alpha\left(6\alpha^2 - \tau\right), \tag{49}$$

and integrating the above equation, we get

$$\int_M \alpha\left(6\alpha^2 - \tau\right) = 0. \tag{50}$$

Using the condition in the hypothesis, we have $\alpha(6\alpha^2 - \tau) = 0$, and as $\alpha \neq 0$, we conclude $\tau = 6\alpha^2$. Consequently, equation (49) implies that $\Delta\alpha = 0$, and M being compact, we conclude that α is a constant. Thus, α being nonzero constant, equation (48) gives

$$QU = 2\alpha^2 U, \quad U \in \Gamma(TM). \tag{51}$$

This proves that M is an Einstein manifold, and using equation (27), we see that the unit Killing vector field ζ satisfies

$$\nabla_{U_1}\nabla_{U_2}\zeta - \nabla_{\nabla_{U_1}U_2}\zeta = \alpha^2(g(U_2,\zeta)U_1 - g(U_1,U_2)\zeta), \quad U_1, U_2 \in \Gamma(TM). \tag{52}$$

Hence, in view of Theorem 1, we conclude that M is homothetic to an Einstein Sasakian manifold. The converse is trivial.

Theorem 4. *A compact and simply connected 3-dimensional trans-Sasakian manifold $(M, F, \zeta, \eta, g, \alpha, \beta)$ satisfying*

$$\zeta\left(\beta^2\right) \leq -2\beta^3 \tag{53}$$

is homothetic to a Sasakian manifold, if and only if, the vector fields $(\nabla Q)(\mathrm{grad}\,\alpha, \zeta)$ and ζ are orthogonal.

Proof. Suppose $(M, F, \zeta, \eta, g, \alpha, \beta)$ is a compact and simply connected 3-dimensional trans-Sasakian manifold satisfying the hypothesis. Then, using equation (5), we have

$$\mathrm{grad}\,\beta = F(\mathrm{grad}\,\alpha) - Q\zeta + 2\left(\alpha^2 - \beta^2\right)\zeta - \zeta(\beta)\zeta, \tag{54}$$

and taking covariant derivative in above equation with respect to $U \in \Gamma(TM)$, while using equation (3), we get

$$\begin{aligned} A_\beta U = {} & (\nabla F)(U, grad\alpha) + FA_\alpha U - (\nabla Q)(U,\zeta) - Q(-\alpha FU + \beta U - \beta\eta(U)\zeta) \\ & + 2U\left(\alpha^2 - \beta^2\right)\zeta + 2\left(\alpha^2 - \beta^2\right)(-\alpha FU + \beta U - \beta\eta(U)\zeta) \\ & - U\zeta(\beta)\zeta - \zeta(\beta)(-\alpha FU + \beta U - \beta\eta(U)\zeta). \end{aligned} \tag{55}$$

□

Taking trace in above equation and noting the following outcome of equation (2),

$$\sum_{i=1}^{3}(\nabla F)(e_i, e_i) = 2\alpha\zeta, \tag{56}$$

for a local orthonormal frame $\{e_1, e_2, e_3\}$ on M, we get

$$\begin{aligned} \Delta\beta = {} & -2\alpha\zeta(\alpha) - \frac{1}{2}\zeta(\tau) - \beta\tau + \beta Ric(\zeta,\zeta) + 2\zeta\left(\alpha^2 - \beta^2\right) \\ & + 4\beta\left(\alpha^2 - \beta^2\right) - \zeta\zeta(\beta) - 2\beta\zeta(\beta), \end{aligned} \tag{57}$$

where we have used $TrFA_\alpha = 0$, $TrQF = 0$, $TrF = 0$, and well known formula

$$\sum_{i=1}^{3}(\nabla Q)(e_i, e_i) = \frac{1}{2}\,\mathrm{grad}\,\tau. \tag{58}$$

Now, using equation (4) and $\mathrm{Ric}(\zeta,\zeta) = 2(\alpha^2 - \beta^2 - \zeta(\beta))$ in equation (57), we have

$$\Delta\beta = -\frac{1}{2}\zeta(\tau) - \beta\tau - 6\beta^3 + 10\alpha^2\beta - 8\beta\zeta(\beta) - \zeta\zeta(\beta), \tag{59}$$

that is,

$$\Delta\beta = -\frac{1}{2}\zeta(\tau) - \beta\tau - 6\beta^3 + 10\alpha^2\beta - \zeta\left(\zeta(\beta) + 4\beta^2\right). \tag{60}$$

Note that on using equation (6), we have $1/2\ \mathrm{div}\,(\tau\zeta) = 1/2\zeta(\tau) + \beta\tau$ and

$$\mathrm{div}\left(\left(\zeta(\beta) + 4\beta^2\right)\zeta\right) = \zeta\left(\zeta(\beta) + 4\beta^2\right) + 2\beta\left(\zeta(\beta) + 4\beta^2\right). \tag{61}$$

Inserting these equations in equation (60), we arrive at

$$\Delta\beta = -\frac{1}{2}\,\mathrm{div}\,(\tau\zeta) - 6\beta^3 + 10\alpha^2\beta + 2\beta\left(\zeta(\beta) + 4\beta^2\right) - \mathrm{div}\left(\left(\zeta(\beta) + 4\beta^2\right)\zeta\right), \tag{62}$$

and integrating the above equation while keeping in mind equation (8), we get

$$\int_M \left(\zeta\left(\beta^2\right) + 2\beta^3\right) = 0. \tag{63}$$

Using the condition in the hypothesis, we conclude $\zeta($

$\beta^2) = -2\beta^3$ and $\beta\zeta(\beta) = -\beta^3$; that is, $3\beta^2\zeta(\beta) = -3\beta^4$. We get $\zeta(\beta^3) = -3\beta^4$, which in view of equation (6) implies

$$\operatorname{div}\left(\beta^3\zeta\right) = -\beta^4. \tag{64}$$

Integrating the above equation yields $\beta = 0$. Thus, equations (27) and (28) are now available to us. Taking covariant derivative in second equation of equation (28) with respect to $U \in \Gamma(TM)$, we get

$$(\nabla Q)(U,\zeta) - \alpha Q(FU) = (\nabla F)(U, \operatorname{grad}\alpha) + FA_\alpha U + 4\alpha U(\alpha)\zeta - 2\alpha^3 FU, \tag{65}$$

where we have used the second equation in equation (27). Now, using equation (27) and noting that $\zeta(\alpha) = 0$ in above equation, we conclude

$$(\nabla Q)(U,\zeta) - \alpha Q(FU) = 5\alpha U(\alpha)\zeta + FA_\alpha U - 2\alpha^3 FU. \tag{66}$$

Taking the inner product with ζ in above equation, we get

$$5\alpha U(\alpha) = g((\nabla Q)(U,\zeta),\zeta) - \alpha g(FU, Q\zeta). \tag{67}$$

Now, using equation (28), we have

$$g(FU, Q\zeta) = g\left(FU, F(\operatorname{grad}\alpha) + 2\alpha^2\zeta\right) = U(\alpha), \tag{68}$$

and inserting it in equation (67), we get

$$6\alpha U(\alpha) = g((\nabla Q)(U,\zeta),\zeta), \quad U \in \Gamma(TM). \tag{69}$$

Taking $U = \operatorname{grad}\alpha$ in above equation and using the condition in the hypothesis, we conclude

$$\alpha\|\operatorname{grad}\alpha\|^2 = 0. \tag{70}$$

Note that M being compact and simply connected, α is not allowed to be zero. Hence, the above equation implies that α is nonzero constant. Thus, we have by virtue of equation (27) that

$$\nabla_{U_1}\nabla_{U_2}\zeta - \nabla_{\nabla_{U_1}U_2}\zeta = \alpha^2(g(U_2,\zeta)U_1 - g(U_1,U_2)\zeta), \quad U_1, U_2 \in \Gamma(TM). \tag{71}$$

This proves that M is homothetic to a Sasakian manifold. The converse is trivial.

Data Availability

The data used to support the findings of this study are available from the corresponding author upon request.

Conflicts of Interest

The authors declare that they have no conflicts of interest.

Acknowledgments

This research is supported by the Deanship of Scientific Research, Imam Mohammed Ibn Saud Islamic University, Saudi Arabia, Grant No. 20-13-12-001.

References

[1] D. E. Blair, "Contact manifolds," in *Contact Manifolds in Riemannian Geometry*, vol. 509, Springer, Berlin, Heidelberg, 1976.

[2] D. E. Blair and J. A. Oubiña, "Conformal and related changes of metric on the product of two almost contact metric manifolds," *Publicacions Matemàtiques*, vol. 34, no. 1, pp. 199–207, 1990.

[3] A. Fujimoto and H. Muto, "On cosymplectic manifolds," *Tenso*, vol. 28, pp. 43–52, 1974.

[4] A. Gray and L. M. Hervella, "The sixteen classes of almost Hermitian manifolds and their linear invariants," *Annali Di Matematica Pura Ed Applicata*, vol. 123, no. 1, pp. 35–58, 1980.

[5] J. A. Oubiña, "New classes of almost contact metric structures," *Universitatis Debreceniensis*, vol. 32, no. 3-4, pp. 187–193, 1985.

[6] J. C. Marrero, "The local structure of trans-Sasakian manifolds," *Annali di Matematica Pura ed Applicata*, vol. 162, no. 1, pp. 77–86, 1992.

[7] W. P. Thurston, "Three dimensional manifolds, Kleinian groups and hyperbolic geometry," *Bulletin (New Series) of The American Mathematical Society*, vol. 6, no. 3, pp. 357–382, 1982.

[8] S. Deshmukh and M. M. Tripathi, "A note on trans-Sasakian manifolds," *Mathematica Slovaca*, vol. 63, no. 6, pp. 1361–1370, 2013.

[9] S. Deshmukh, U. C. De, and F. Al-Solamy, "Trans-Sasakian manifolds homothetic to Sasakian manifolds," *Universitatis Debreceniensis*, vol. 88, no. 3-4, pp. 439–448, 2016.

[10] S. Deshmukh, "Trans-Sasakian manifolds homothetic to Sasakian manifolds," *Mediterranean Journal of Mathematics*, vol. 13, no. 5, pp. 2951–2958, 2016.

[11] S. Deshmukh and F. al-Solamy, "A note on compact trans-Sasakian manifolds," *Mediterranean Journal of Mathematics*, vol. 13, no. 4, pp. 2099–2104, 2016.

[12] S. Deshmukh and U. C. De, "A note on trans-Sasakian manifolds," *Universitatis Debreceniensis*, vol. 92, no. 1-2, pp. 159–169, 2018.

[13] S. Deshmukh, A. Ishan, O. Belova, and S. B. Al-Shaikh, "Some conditions on trans-Sasakian manifolds to be homothetic to Sasakian manifolds," *Mathematics*, vol. 9, no. 16, p. 1887, 2021.

[14] W. Wang and X. Liu, "Ricci tensors on trans-Sasakian 3-manifolds," *Univerzitet u Nišu*, vol. 32, no. 12, pp. 4365–4374, 2018.

[15] Y. Wang and W. Wang, "A remark on trans-Sasakian 3-manifolds," *Revista de La Union Mat. Argentina*, vol. 60, no. 1, pp. 257–264, 2019.

[16] C. Boyer and K. Galicki, *Sasakian Geometry; Oxford Mathematical Monographs*, Oxford University Press, Oxford, NY, USA, 2007.

[17] M. Okumura, "Certain almost contact hypersurfaces in Kaehlerian manifolds of constant holomorphic sectional curvatures," *Tohoku Mathematical Journal, Second Series*, vol. 16, no. 3, pp. 270–284, 1964.

[18] A. E. Fischer and J. E. Marsden, "Manifolds of Riemannian metrics with prescribed scalar curvature," *Bulletin of the American Mathematical Society*, vol. 80, no. 3, pp. 479–485, 1974.

Hindawi
Advances in Mathematical Physics
Volume 2022, Article ID 3182116, 14 pages
https://doi.org/10.1155/2022/3182116

Research Article

A Study on Vague Graph Structures with an Application

Zheng Kou,[1] **Maryam Akhoundi**,[2] **Xiang Chen**,[1] **and Saber Omidi**[3]

[1]*Institute of Computing Science and Technology, Guangzhou University, Guangzhou 510006, China*
[2]*Clinical Research Development Unit of Rouhani Hospital, Babol University of Medical Sciences, Babol, Iran*
[3]*Ministry of Education Iran, Department of Education, Tehran, Iran*

Correspondence should be addressed to Maryam Akhoundi; maryam.akhoundi@mubabol.ac.ir

Received 13 January 2022; Accepted 10 February 2022; Published 2 March 2022

Academic Editor: Meraj Ali Khan

Fuzzy graph (FG) models take on the presence being ubiquitous in environmental and fabricated structures by human, specifically the vibrant processes in physical, biological, and social systems. Owing to the unpredictable and indiscriminate data which are intrinsic in real-life, problems being often ambiguous, so it is very challenging for an expert to exemplify those problems through applying an FG. Vague graph structure (VGS), belonging to FGs family, has good capabilities when facing with problems that cannot be expressed by FGs. VGSs have a wide range of applications in the field of psychological sciences as well as the identification of individuals based on oncological behaviors. Therefore, in this paper, we apply the concept of vague sets (VSs) to GS. We define certain notions, VGS, strong vague graph structure (SVGS), and vague β_i-cycle and describe these notions by several examples. Likewise, we introduce ψ-complement, self-complement (SC), strong self-complement (SSC), and totally strong self-complement (TSSC) in VGS and investigate some of their properties. Finally, an application of VGS is presented.

1. Introduction

The FG concept serves as one of the most dominant and extensively employed tools for multiple real-word problem representations, modeling, and analysis. To specify the objects and the relations between them, the graph vertices or nodes and edges or arcs are applied, respectively. Graphs have long been used to describe objects and the relationships between them. Many of the issues and phenomena around us are associated with complexities and ambiguities that make it difficult to express certainty. These difficulties were alleviated by the introduction of fuzzy sets by Zadeh [1]. A GS, proposed by Sampathkumar [2], refers to the generalization of undirected graph being relatively beneficial in investigating some structure including graphs, signed graphs, and graphs in which every edge is labeled or colored. A GS facilitates studying the different relations and the equivalent edges simultaneously. The FS focuses on the membership degree of an object in a particular set. The existence of a single degree for a true membership could not resolve the ambiguity on uncertain issues, so the need for a degree of membership was felt. Afterward, to overcome the existing ambiguities, Gau and Buehrer [3] introduced false-membership degrees and defined a VS as the sum of degrees not greater than 1. Kaufmann [4] represented FGs based on Zadeh's fuzzy relation [5, 6]. Rosenfeld [7] described the structure of FGs obtaining analogs of several graph theoretical concepts. Harinath and Lavanya [8] studied new concepts in fuzzy graph structures. Bhattacharya [9] gave some remarks on FGs. Several concepts on FGs were introduced by Mordeson and Nair [10]. Dinesh [11] investigated the notion of a FGS and studied some related properties. Ghorai et al. [12, 13] presented fuzzy tolerance graphs and planarity in VGs. Ramakrishna [14] defined VGs. Kosari et al. [15–18] investigated domination set, equitable domination set, and new concepts of domination in vague graphs and vague incidence graphs. Pal and Rashmanlou [19, 20] have given several concepts in FGs. Akram et al. [21, 22] introduced certain fuzzy graph structures. Sunitha and Vijayakumar [23] presented some properties of complement on FGs. Muhiuddin et al. [24–26] investigated new results in cubic graphs.

A VGS is concerned with the generalized structure of an FG that expresses more exactness, adaptability, and

compatibility to a system when synchronized with systems operating on FGs. Correspondingly, a VGS is capable of focusing on determining the uncertainly combined with the inconsistent and indeterminate information of any real-world problem, in which FGs may not lead to adequate results. Hence, in this paper, we define the certain notions including VGS, SVGS, and vague β_i-cycle and describe these notions by several examples. We study ψ-complement, SC, and SSC in VGSs and investigate some of their properties. Finally, an application of VGS has been presented.

2. Preliminaries

A GS $G^* = (V, R_1, R_2, \ldots, R_k)$, consists of a nonempty set V together with relations $R_1, R_2, \ldots, R_k$ on V, which are mutually disjoint so that each R_i is irreflexive and symmetric. If $(a, b) \in R_i$ for some i, $1 \le i \le k$, we name it an R_i-edge and write it as "ab."

A GS $G^* = (V, R_1, R_2, \ldots, R_k)$ is CGS, if,

(i) every edge R_i, $1 \le i \le k$ appears at least once in G^*

(ii) among every pair of nodes ab in V, ab is an E_i-edge for some i, $1 \le i \le k$

Definition 1 (see [1]). A fuzzy subset σ on a set X is a map $\sigma: X \longrightarrow [0, 1]$. A fuzzy binary relation on X is a fuzzy subset σ on $X \times X$. By a fuzzy relation, we mean a fuzzy binary relation given by $\sigma: X \times X \longrightarrow [0, 1]$.

Definition 2 (see [11]). Let $G^* = (V, R_1, R_2, \ldots, R_k)$ be a GS and let $\nu, \lambda_1, \lambda_2, \ldots, \lambda_k$ be the fuzzy subset of $V, R_1, R_2, \ldots, R_k$, respectively, so that $0 \le \lambda_i(xy) \le \sigma(x) \wedge \sigma(y)$, $\forall x, y \in V$, $i = 1, 2, \ldots, k$. Then, $G = (\nu, \lambda_1, \lambda_2, \ldots, \lambda_k)$ is an FGS of G^*.

Definition 3 (see [11]). Let $G = (\nu, \lambda_1, \lambda_2, \ldots, \lambda_k)$ be an FGS of a GS $G^* = (V, R_1, R_2, \ldots, R_k)$. Then, $F = (\nu, \tau_1, \tau_2, \ldots, \tau_k)$ is a PFSSGS of G if G, for $i = 1, 2, \ldots, k$.

Definition 4 (see [11]). The strength of a λ_i-path $a_0 a_1, \cdots a_n$ of a FGS G is $\wedge_{j=1}^{n} \lambda_i(a_{j-1}a_j)$, for $i = 1, 2, \ldots, k$.

Definition 5 (see [11]). In a FGS G, $\lambda_i^2(ab) = (\lambda_i \circ \lambda_i)(ab) = \vee_c\{\lambda_i(ac) \wedge \lambda_i(bc)\}$, $\lambda_i^j(ab) = (\lambda_i^{j-1} \circ \lambda_i)(ab) = \vee_c\{\lambda_i^{j-1}(ac) \wedge \lambda_i(bc)\}$, $j = 1, 2, \ldots, n$, for any $n \ge 2$. Also, $\lambda_i^{\infty}(ab) = \vee\{\lambda_i^j(ab), j = 1, 2, \ldots\}$.

Definition 6 Reference [11] $G = (\nu, \lambda_1, \lambda_2, \ldots, \lambda_k)$ is a λ_i-cycle if and only if $(\mathrm{Supp}(\nu), \mathrm{Supp}(\lambda_1), \mathrm{Supp}(\lambda_2), \ldots, \mathrm{Supp}(\lambda_k))$ is a R_i-cycle.

Definition 7. Reference [11] $G = (\nu, \lambda_1, \lambda_2, \ldots, \lambda_k)$ is a fuzzy λ_i-cycle if and only if $(\mathrm{Supp}(\nu), \mathrm{Supp}(\lambda_1), \mathrm{Supp}(\lambda_2), \ldots, \mathrm{Supp}(\lambda_k))$ is a E_i-cycle and $\exists$ no unique ab in $\mathrm{Supp}(\lambda_i)$ so that

$$\lambda_i(ab) = \wedge\{\lambda_i(cd) \mid cd \in \mathrm{Supp}(\lambda_i)\}. \tag{1}$$

Definition 8 (see [3]). A VS A is a pair (t_A, f_A) on set X where t_A and f_A are taken as real valued functions which can be defined on $V \longrightarrow [0, 1]$ so that $t_A(a) + f_A(b) \le 1$, $\forall a \in X$.

Definition 9 (see [14]). A VG is a pair $G = (A, B)$, where $A = (t_A, f_A)$ is a VS on V and $B = (t_B, f_B)$ is a VS on $E \subseteq V \times V$ so that $t_B(ab) \le \min(t_A(a), t_A(b))$ and $f_B(ab) \ge \max(f_A(a), f_A(b))$, for $ab \in E$.

All the basic notations are shown in Table 1.

3. New Concepts in Vague Graph Structure

Definition 10. $\widehat{G}_v = (A, B_1, B_2, \ldots, B_n)$ is said to be a VGS of a GS $G^* = (V, R_1, R_2, \ldots, R_n)$, if $A = (t_A, f_A)$ is a VS on V and for every $i = 1, 2, \ldots, n$; $B_i = (t_{B_i}, f_{B_i})$ is a VS on R_i so that

$$\begin{aligned} t_{B_i}(ab) &\le t_A(a) \wedge t_A(b), \\ f_{B_i}(ab) &\ge f_A(a) \vee f_A(b). \end{aligned} \tag{2}$$

$\forall ab \in R_i \subseteq V \times V$. Note that $t_{B_i}(ab) = 0 = f_{B_i}(ab)$, $\forall ab \in V \times V - R_i$ and $0 \le t_{B_i}(ab) \le 1$, $0 \le f_{B_i}(ab) \le 1$, $\forall ab \in R_i$, where V and R_i, $(i = 1, 2, \ldots, n)$ are named UVS and underlying i-edge set of $\widehat{G}_v$, respectively.

Example 1. Let $G^* = (V, R_1, R_2)$ be a GS so that $V = \{a_1, a_2, a_3, a_4\}$, $R_1 = \{a_1a_2, a_2a_3\}$, and $R_2 = \{a_3a_4, a_1a_4\}$. Let A, B_1, and B_2 be vague subsets of V, R_1, and R_2, respectively, so that

$$\begin{aligned} A &= \{(a_1, 0.4, 0.5), (a_2, 0.4, 0.6), (a_3, 0.3, 0.4), (a_4, 0.4, 0.4)\}, \\ B_1 &= \{(a_1a_2, 0.4, 0.6), (a_2a_3, 0.3, 0.6)\}, \\ B_2 &= \{(a_3a_4, 0.3, 0.4), (a_1a_4, 0.3, 0.5)\}. \end{aligned} \tag{3}$$

Then, $\widehat{G}_v = (A, B_1, B_2)$ is a VGS of G^* drawn in Figure 1.

Definition 11

(i) AVGS $\breve{H}_v = (C, D_1, D_2, \ldots, D_n)$ is said to be a VSGS of a VGS $G_v = (A, B_1, B_2, \ldots, B_n)$ with UVS V, if $C \subseteq A$ and $D_i \subseteq C_i$, $\forall i$, that is,

$$t_C(a) \le t_A(a), f_C(a) \ge f_A(a); \quad \text{for all } a \in V, \tag{4}$$

and for $i = 1, 2, \ldots, n$,

$$t_{D_i}(ab) \le t_{B_i}(ab), f_{D_i}(ab) \ge f_{B_i}(ab); \quad \text{for all } ab \in V \times V. \tag{5}$$

(ii) $\breve{H}_v$ is named a VSSGS of a VGS $\breve{G}_v$, if $C = A$.

(iii) $\breve{H}_v$ is named a VPSSGS of a VGS $\breve{G}_v$, if it excludes some edges of $\breve{G}_v$.

Table 1: Some basic notations.

Notation	Meaning
FG	Fuzzy graph
FS	Fuzzy set
VS	Vague set
GS	Graph structure
CGS	Complete graph structure
VGS	Vague graph structure
VSGS	Vague subgraph structure
SGS	Subgraph structure
FGS	Fuzzy graph structure
SVGS	Strong vague graph structure
UG	Underlying graph
EN	End node
SC	Self-complementary
SSC	Strong self-complementary
TSC	Totally self-complementary
TSSC	Totally strong self-complement
PFSSGS	Partial fuzzy spanning subgraph structure
UVS	Underlying vertex set
TSSC	Totally strong self-complementary

Example 2. Consider a VGS $\breve{G}_v = (A, B_1, B_2)$ as shown in Figure 1. Let

$$\begin{aligned} C &= \{(a_1, 0.3, 0.6), (a_2, 0.0, 0.7), (a_3, 0.3, 0.4), (a_4, 0.3, 0.5)\}, \\ D_1 &= \{(a_1a_2, 0, 0.7), (a_2a_3, 0, 0.7)\}, \\ D_2 &= \{(a_3a_4, 0.2, 0.5), (a_1a_4, 0.3, 0.6)\}, \\ C_1 &= \{(a_1a_2, 0.2, 0.6), (a_2a_3, 0.3, 0.6)\}, \\ C_2 &= \{(a_3a_4, 0.2, 0.4), (a_1a_4, 0.3, 0.7)\}, \\ F_1 &= \{(a_1a_2, 0.4, 0.6), (a_2a_3, 0.3, 0.6)\}, \\ F_2 &= \{(a_1a_4, 0.3, 0.6)\}. \end{aligned} \tag{6}$$

It is easy to see that $\breve{H}_v = (C, D_1, D_2)$, $\breve{J}_v = (A, C_1, C_2)$, and $\breve{K}_v = (A, F_1, F_2)$ are the VSGS, VSSGS, and VPSSGS of $\breve{G}_v$, respectively.

Their corresponding graphs are drawn in Figures 2–4.

Definition 12. Let $\breve{G}_v = (A, B_1, B_2, \ldots, B_n)$ be a VGS with UVS V. Then, there exists a B_i-edge among two nodes a and b of V so that we have

(i) $t_{B_i}(ab) > 0$, $f_{B_i}(ab) > 0$, or
(ii) $t_{B_i}(ab) > 0$, $f_{B_i}(ab) = 0$, or
(iii) $t_{B_i}(ab) = 0$, $f_{B_i}(ab) > 0$, for some i.

Definition 13. For a VGS $\breve{G}_v = (A, B_1, B_2, \ldots, B_n)$, the support of B_i is described as

$$\operatorname{Supp}(B_i) = \left\{ab \in V \times V : t_{B_i}(ab) \neq 0 \text{ or } f_{B_i}(ab) \neq 0\right\}, \quad i = 1, 2, \ldots, n. \tag{7}$$

Definition 14. B_i-path of a VGS $\breve{G}_v$ with UVS V is a sequence of distinct nodes $v_1, v_2, \ldots, v_m \in U$ (except the choice $v_m = v_1$) so that $v_{j-1}v_j$ is a B_i-edge, $\forall\, j = 2, 3, \ldots, m$.

Definition 15. In a VGS $\breve{G}_v = (A, B_1, B_2, \ldots, B_n)$ with UVS V, two nodes a and b called B_i-connected, if they are connected by a B_i-path, for some $i \in \{1, 2, 3, \ldots, n\}$.

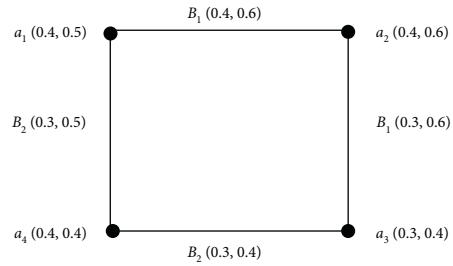

Figure 1: VGS $\widehat{G}_v = (A, B_1, B_2)$.

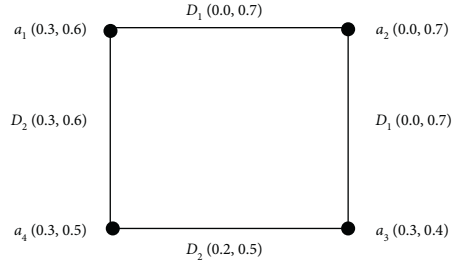

Figure 2: Vague subgraph structure $\breve{H}_v = (C, D_1, D_2)$.

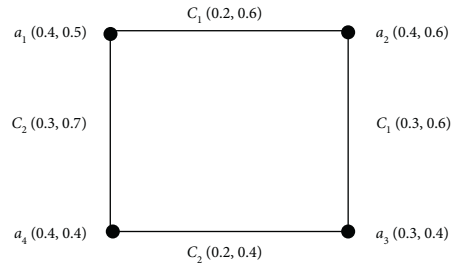

Figure 3: Vague spanning subgraph structure $\breve{J}_v = (A, C_1, C_2)$.

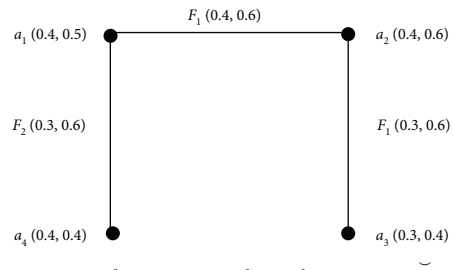

Figure 4: Vague partial spanning subgraph structure $\breve{K}_v = (A, F_1, F_2)$.

Definition 16. A VGS $\breve{G}_v = (A, B_1, B_2, \ldots, B_n)$ with UVS V is called to be B_i-strong, if $\forall\, B_i$-edges ab,

$$t_{B_i}(ab) = t_A(a) \wedge t_A(b),\ f_{B_i}(ab) = f_A(a) \vee f_A(b), \tag{8}$$

for some $i \in \{1, 2, 3, \ldots, n\}$.

Example 3. Consider the VGS $\breve{G}_v = (A, B_1, B_2)$, drawn in Figure 1. Then,

(i) a_1a_2, a_2a_3 are B_1-edges and a_3a_4, a_1a_4 are B_2-edges

(ii) $a_1a_2a_3$ and $a_3a_4a_1$ are B_1 and B_2 paths, respectively

(iii) a_1 and a_3 are B_1-connected nodes of U

(iv) $\breve{G}_v$ is a B_1-strong since $\mathrm{Supp}(B_1) = \{a_1a_2, a_2a_3\}$ and we have

$$\begin{aligned} t_{B_1}(a_1a_2) &= 0.4 = (t_A(a_1) \wedge t_A(a_2)), \\ f_{B_1}(a_1a_2) &= 0.6 = (f_A(a_1) \vee f_A(a_2)), \\ t_{B_1}(a_2a_3) &= 0.3 = (t_A(a_2) \wedge t_A(a_3)), \\ f_{B_1}(a_2a_3) &= 0.6 = (f_A(a_2) \vee f_A(a_3)). \end{aligned} \tag{9}$$

Definition 17. A VGS $\breve{G}_v = (A, B_1, B_2, \ldots, B_n)$ is named to be strong, if it is B_i-strong, $\forall i \in \{1, 2, 3, \ldots, n\}$.

Definition 18. A VGS $\breve{G}_v = (A, B_1, B_2, \ldots, B_n)$ with UVS V, is named complete or $B_1, B_2, \ldots, B_n$-complete if

(i) $\breve{G}_v$ is a SVGS

(ii) $\mathrm{Supp}(B_i) \neq \varnothing$, $\forall i = 1, 2, 3, \ldots, n$

(iii) For each nodes $a, b \in V$, ab should be a B_i-edge

Example 4. Suppose $\breve{G}_v = (A, B_1, B_2)$ drawn in Figure 5, be VGS of the GS $G^* = (V, R_1, R_2)$ where $V = \{a_1, a_2, a_3, a_4\}$, $R_1 = \{a_1a_2, a_2a_3, a_1a_3\}$, and $R_2 = \{a_1a_4, a_3a_4, a_2a_4\}$. Then, $\breve{G}_v$ is a SVGS, since it is both B_1-strong and B_2-strong. Moreover, $\mathrm{Supp}(B_1) \neq \varnothing$, $\mathrm{Supp}(B_2) \neq \varnothing$, and each nodes in V, is either a B_1-edge or a B_2-edge, so $\breve{G}_v$ is a complete or B_1B_2-complete-VGS as well.

Definition 19. In a VGS $\breve{G}_v = (A, B_1, B_2, \ldots, B_n)$ with UVS V, t_{B_i} and f_{B_i}-strength of a B_i-path "$P_{B_i} = v_1v_2, \ldots, v_m$" are denoted by $\delta \cdot P_{B_i}$ and $\Delta \cdot P_{B_i}$, respectively, so that $\delta \cdot P_{B_i} = \wedge_{j=2}^{m}[t_{B_i}(a_{j-1}a_j)]$ and $\Delta \cdot P_{B_i} = \vee_{j=2}^{m}[f_{B_i}(a_{j-1}a_j)]$.

Then, we write strength of the path $P_{B_i} = (\delta \cdot P_{B_i}, \Delta \cdot P_{B_i})$.

Example 5. In $\breve{G}_v = (A, B_1, B_2)$ shown in Figure 5, $P_1 = a_1a_2a_3a_1$ is a B_1-path, and $a_1a_4a_3$ is a B_2-path, we have

$$\begin{aligned} &\delta \cdot P_1 = t_{B_1}(a_1a_2) \wedge t_{B_1}(a_2a_3) \wedge t_{B_1}(a_3a_1) = 0.2 \wedge 0.3 \wedge 0.2 = 0.2, \\ &\Delta \cdot P_1 = f_{B_1}(a_1a_2) \vee f_{B_1}(a_2a_3) \vee f_{B_1}(a_3a_1) = 0.3 \vee 0.5 \vee 0.5 = 0.5, \\ &\delta \cdot P_2 = t_{B_2}(a_1a_4) \wedge t_{B_2}(a_4a_3) = 0.2 \wedge 0.4 = 0.2, \\ &\Delta \cdot P_2 = f_{B_2}(a_1a_4) \vee f_{B_2}(a_4a_3) = 0.6 \vee 0.6 = 0.6. \end{aligned} \tag{10}$$

Thus, strength of B_1-path is $P_1 = (0.2, 0.5)$, and strength of P_2-path is $P_2 = (0.2, 0.6)$.

Definition 20. In a VGS $\breve{G}_v = (A, B_1, B_2, \ldots, B_n)$ with UVS V,

(i) t_{B_i}-strength of connectedness between a and b is defined by $t^{\infty}_{B_i}(ab) = \vee_{j\geq 1}\{t^{j}_{B_i}(ab)\}$, where $t^{j}_{B_i}(ab) = (t^{j-1}_{B_i} \circ \mathrm{t}_{B_i})(\mathrm{ab})$, for $j \geq 2$ and $t^{2}_{B_i}(ab) = (t_{B_i} \circ \mathrm{t}_{B_i})(\mathrm{ab}) = \vee_{\mathrm{z}}\{\mathrm{t}_{B_i}(\mathrm{ac}) \wedge \mathrm{t}_{B_i}(\mathrm{bc})\}$;

(ii) f_{B_i}-strength of connectedness among a and b is described by $f^{\infty}_{B_i}(ab) = \wedge_{j\geq 1}\{f^{j}_{B_i}(ab)\}$, where $f^{j}_{B_i}(ab) = (f^{j-1}_{B_i} \circ \mathrm{f}_{B_i})(\mathrm{ab})$, for $j \geq 2$ and $f^{2}_{B_i}(ab) = (f_{B_i} \circ \mathrm{f}_{B_i})(\mathrm{ab}) = \vee_{\mathrm{z}}\{\mathrm{f}_{B_i}(\mathrm{ac}) \vee \mathrm{f}_{B_i}(\mathrm{bc})\}$.

Example 6. Let $\breve{G}_v = (A, B_1, B_2)$ be a VGS of GS $G^* = (V, R_1, R_2)$ as shown in Figure 6 so that $V = \{a_1, a_2, a_3\}$, $R_1 = \{a_1a_2, a_1a_3\}$, and $R_2 = \{a_2a_3\}$. Since $t_{B_1}(a_1a_2) = 0.2$, $t_{B_1}(a_1a_3) = 0.2$, and $t_{B_1}(a_2a_3) = 0$, therefore,

$$\begin{aligned} t^{2}_{B_1}(a_1a_2) &= \left(t_{B_1} \circ \mathrm{t}_{B_1}\right)(a_1a_2) = t_{B_1}(a_1a_3) \wedge t_{B_1}(a_3a_2) = 0.2 \wedge 0.3 = 0.2, \\ t^{2}_{B_1}(a_2a_3) &= \left(t_{B_1} \circ \mathrm{t}_{B_1}\right)(a_2a_3) = t_{B_1}(a_2a_1) \wedge t_{B_1}(a_1a_3) = 0.2 \wedge 0.2 = 0.2, \\ t^{2}_{B_1}(a_1a_3) &= \left(t_{B_1} \circ \mathrm{t}_{B_1}\right)(a_1a_3) = t_{B_1}(a_1a_2) \wedge t_{B_1}(a_2a_3) = 0.2 \wedge 0.3 = 0.2, \\ t^{3}_{B_1}(a_1a_2) &= \left(t^{2}_{B_1} \circ \mathrm{t}_{B_1}\right)(a_1a_2) = t^{2}_{B_1}(a_1a_3) \wedge t_{B_1}(a_3a_2) = 0.2 \wedge 0.3 = 0.2, \\ t^{3}_{B_1}(a_2a_3) &= \left(t^{2}_{B_1} \circ \mathrm{t}_{B_1}\right)(a_2a_3) = t^{2}_{B_1}(a_2a_1) \wedge t_{B_1}(a_1a_3) = 0.2 \wedge 0.2 = 0.2, \\ t^{3}_{B_1}(a_1a_3) &= \left(t^{2}_{B_1} \circ \mathrm{t}_{B_1}\right)(a_1a_3) = t^{2}_{B_1}(a_1a_2) \wedge t_{B_1}(a_2a_3) = 0.2 \wedge 0.3 = 0.2. \end{aligned} \tag{11}$$

Thus, we have,

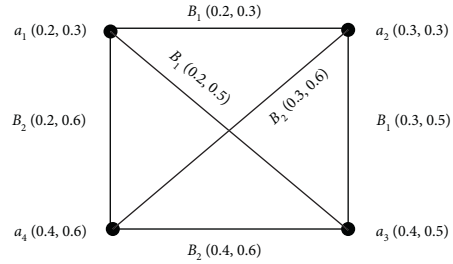

Figure 5: VGS $\breve{G}_v = (A, B_1, B_2)$.

$$\begin{aligned} t^{\infty}_{B_1}(a_1a_2) &= \vee\{0.2, 0.2, 0.2\} = 0.2, \\ t^{\infty}_{B_1}(a_2a_3) &= \vee\{0.2, 0.2, 0.2\} = 0.2, \\ t^{\infty}_{B_1}(a_1a_3) &= \vee\{0.2, 0.2, 0.2\} = 0.2. \end{aligned} \tag{12}$$

Since $f_{B_1}(a_1a_2) = 0.6$, $f_{B_1}(a_1a_3) = 0.7$, and $f_{B_1}(a_2a_3) = 0$, therefore,

$$\begin{aligned} f^2_{B_1}(a_1a_2) &= \left(f_{B_1} \circ \mathrm{f}_{B_1}\right)(a_1a_2) = f_{B_1}(a_1a_3) \vee f_{B_1}(a_3a_2) = 0.7 \vee 0.7 = 0.7, \\ f^2_{B_1}(a_2a_3) &= \left(f_{B_1} \circ \mathrm{f}_{B_1}\right)(a_2a_3) = f_{B_1}(a_2a_1) \vee f_{B_1}(a_1a_3) = 0.6 \vee 0.7 = 0.7, \\ f^2_{B_1}(a_1a_3) &= \left(f_{B_1} \circ \mathrm{f}_{B_1}\right)(a_1a_3) = f_{B_1}(a_1a_2) \vee f_{B_1}(a_2a_3) = 0.6 \vee 0 = 0.6, \\ f^3_{B_1}(a_1a_2) &= \left(f^2_{B_1} \circ \mathrm{f}_{B_1}\right)(a_1a_2) = f^2_{B_1}(a_1a_3) \vee f_{B_1}(a_3a_2) = 0.6 \vee 0.7 = 0.7, \\ f^3_{B_1}(a_2a_3) &= \left(f^2_{B_1} \circ \mathrm{f}_{B_1}\right)(a_2a_3) = f^2_{B_1}(a_2a_1) \vee f_{B_1}(a_1a_3) = 0.7 \vee 0.7 = 0.7, \\ f^3_{B_1}(a_1a_3) &= \left(f^2_{B_1} \circ \mathrm{f}_{B_1}\right)(a_1a_3) = f^2_{B_1}(a_1a_2) \vee f_{B_1}(a_2a_3) = 0.7 \vee 0.7 = 0.7, \end{aligned} \tag{13}$$

and

$$\begin{aligned} f^4_{B_1}(a_1a_2) &= \left(f^3_{B_1} \circ \mathrm{f}_{B_1}\right)(a_1a_2) = f^3_{B_1}(a_1a_3) \vee f_{B_1}(a_3a_2) = 0.7 \vee 0.7 = 0.7, \\ f^4_{B_1}(a_2a_3) &= \left(f^3_{B_1} \circ \mathrm{f}_{B_1}\right)(a_2a_3) = f^3_{B_1}(a_2a_1) \vee f_{B_1}(a_1a_3) = 0.7 \vee 0.7 = 0.7, \\ f^4_{B_1}(a_1a_3) &= \left(f^3_{B_1} \circ \mathrm{f}_{B_1}\right)(a_1a_3) = f^2_{B_1}(a_1a_2) \vee f_{B_1}(a_2a_3) = 0.7 \vee 0.7 = 0.7. \end{aligned} \tag{14}$$

Thus, we have

$$\begin{aligned} f^{\infty}_{B_1}(a_1a_2) &= \vee\{0.6, 0.7, 0.7, 0.7\} = 0.7, \\ f^{\infty}_{B_1}(a_2a_3) &= \vee\{0.0, 0.7, 0.7, 0.7\} = 0.7, \\ f^{\infty}_{B_1}(a_1a_3) &= \vee\{0.7, 0.6, 0.7, 0.7\} = 0.7. \end{aligned} \tag{15}$$

By similarity way, we can calculate $t^{\infty}_{B_2}(a_1a_2)$, $t^{\infty}_{B_2}(a_2a_3)$, and $t^{\infty}_{B_2}(a_1a_3)$.

Definition 21. A VGS $\breve{G}_v = (A, B_1, B_2, \ldots, B_n)$ of a GS $G^* = (V, R_1, R_2, \ldots, R_n)$ is a B_i-cycle, if G^* is an R_i-cycle.

Definition 22. A VGS $\breve{G}_v = (A, B_1, B_2, \ldots, B_n)$ of a GS $G^* = (V, R_1, R_2, \ldots, R_n)$ is a vague B_i-cycle, for some i, if we have

(i) G is a B_i-cycle;

(ii) There is no unique B_i-edge ab in $\breve{G}_v$ so that $t_{B_i}(ab) = \min\{t_{B_i}(zw) : zw \in R_i = \mathrm{Supp}(B_i)\}$ or $f_{B_i}(ab) = \max\{f_{B_i}(zw) : zw \in R_i = \mathrm{Supp}(B_i)\}$.

Example 7. VGS $\breve{G}_v = (A, B_1, B_2)$ in Figure 7 is a B_1-cycle as well as vague B_1-cycle, since $(\mathrm{Supp}(A), \mathrm{Supp}(B_1), \mathrm{Supp}(B_2))$ is an R_1-cycle and there are two B_1-edges with minimum degree of membership and two B_1-edges with maximum degree of membership of all B_1-edges.

Definition 23. A VGS $\breve{G}_{v1} = (A_1, B_{11}, B_{12}, \ldots, B_{1n})$ of GS $G^*_1 = (V_1, R_{11}, R_{12}, \ldots, R_{1n})$ is isomorphic to a VGS $\breve{G}_{v2} = (A_2, B_{21}, B_{22}, \ldots, B_{2n})$ of $G^*_2 = (V_2, R_{21}, R_{22}, \ldots, R_{2n})$ $(G_{v1} \cong G_{v2})$ if $\exists$ a bijective $g: V_1 \longrightarrow V_2$ and a permutation ψ on the set $\{1, 2, \ldots, n\}$ so that

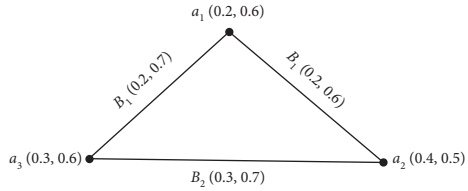

Figure 6: VGS $\breve{G}_v = (A, B_1, B_2)$.

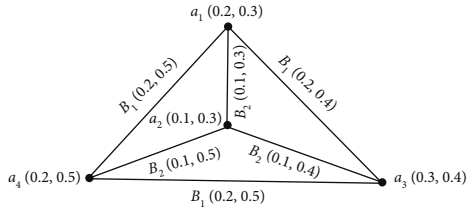

Figure 7: VGS $\breve{G}_v = (A, B_1, B_2)$.

$$t_{A_1}(u_1) = t_{A_2}(g(u_1)),$$
$$f_{A_1}(u_1) = f_{A_2}(g(u_1)), \tag{16}$$
$$\forall u_1 \in V_1, \text{ and for } \psi(i) = j,$$
$$t_{B_{1i}}(u_1u_2) = t_{B_{2j}}(g(u_1)g(u_2)), \quad f_{B_{1i}}(u_1u_2) = f_{B_{2j}}(g(u_1)g(u_2)), \text{ for all } u_1u_2 \in R_{1i},\ i = 1, 2, \ldots, n.$$

Definition 24. A VGS $\breve{G}_{v1} = (A_1, B_{11}, B_{12}, \ldots, B_{1n})$ of GS $G_1^* = (V, R_{11}, R_{12}, \ldots, R_{1n})$ is identical to a VGS $G_{v2} = (A_2, B_{21}, B_{22}, \ldots, B_{2n})$ of $G_2^* = (V, R_{21}, R_{22}, \ldots, R_{2n})$ if $\exists$ a bijection g: $V \longrightarrow V$ so that

$$t_{A_1}(u) = t_{A_2}(g(u)),$$
$$f_{A_1}(u) = f_{A_2}(g(u)), \text{for all } u \in V, \tag{17}$$

and

$$t_{B_{1i}}(u_1u_2) = t_{B_{2i}}(g(u_1)g(u_2)), f_{B_{1i}}(u_1u_2) = f_{B_{2i}}(g(u_1)g(u_2)), \text{ for all } u_1u_2 \in R_{1i}, \quad i = 1, 2, \ldots, n. \tag{18}$$

Example 8. Let $\breve{G}_{v1}$ and $\breve{G}_{v2}$ be two VGSs of GS $G_1^* = (V_1, R_1, R_2)$ and $G_2^* = (V_2, R_1', R_2')$, respectively, drawn in Figure 8. Here, $\breve{G}_{v1}$ is isomorphic (not identical) to $\breve{G}_{v2}$ under the mapping g: $V_1 \longrightarrow V_2$, defined by $g(a_1) = b_1$, $g(a_2) = b_2$, and $g(a_3) = b_3$ and a permutation ψ given by $\psi(1) = 2$, $\psi(2) = 1$ so that

$$t_{A_1}(a_i) = t_{A_2}(g(a_i)), f_{A_1}(a_i) = f_{A_2}(g(a_i)), \forall a_i \in V,$$
$$t_{B_k}(a_ia_j) = t_{B_{\psi(k)}}(g(a_i)g(a_j)),\ f_{B_k}(a_ia_j) = f_{B_{\psi(k)}}(g(a_i)g(a_j)), \quad \forall a_ia_j \in R_k,\ k = 1, 2. \tag{19}$$

Example 9. Let $\breve{G}_{v1} = (A, B_1, B_2)$ and $\breve{G}_{v2} = (A', B_1', B_2')$ be two VGSs of GSs $G_1^* = (V, R_1, R_2)$ and $G_2^* = (V', R_1', R_2')$, respectively, as shown in Figure 9. Here, $\breve{G}_{v1}$ is identical with $\breve{G}_{v2}$ under the mapping g: $V \longrightarrow V'$, defined by $g(a_1) = b_6$, $g(a_2) = b_2$, $g(a_3) = b_4$, $g(a_4) = b_5$, $g(a_5) = b_1$, and $g(a_6) = b_3$ so that

$$t_A(a_i) = t_{A'}(g(a_i)), f_A(a_i) = f_{A'}(g(a_i)), \quad \forall a_i \in V,$$
$$t_{B_k}(a_ia_j) = t_{B_k'}(g(a_i)g(a_j)), f_{B_k}(a_ia_j) = f_{B_k'}(g(a_i)g(a_j)), \quad \forall a_ia_j \in R_k,\ k = 1, 2. \tag{20}$$

Definition 25. Let $\breve{G}_v$ be a VGS of a GS G^*. Let ψ denote a permutation on the set $\{R_1, R_2, \ldots, R_n\}$ and the corresponding permutation on $\{B_1, B_2, \ldots, B_n\}$, i.e., $\psi(B_i) = B_j$ if $\psi(R_i) = E_j$, $\forall i$. If $ab \in B_r$ for some r and
$t_{B_i^\psi}(ab) = t_A(a) \wedge t_A(b) - \vee_{j \neq i} t_{\psi(B_j)}(ab)$,
$f_{B_i^\psi}(ab) = f_A(a) \vee f_A(b) - \vee_{j \neq i} f_{\psi(B_j)}(ab), \quad i = 1, 2, \ldots, n,$

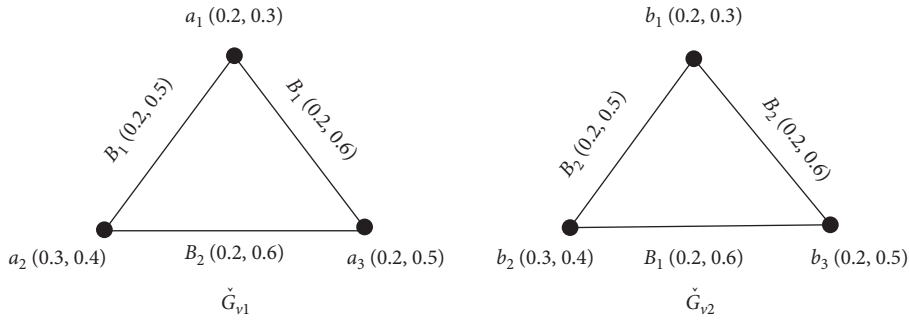

Figure 8: Isomorphic vague graph structures.

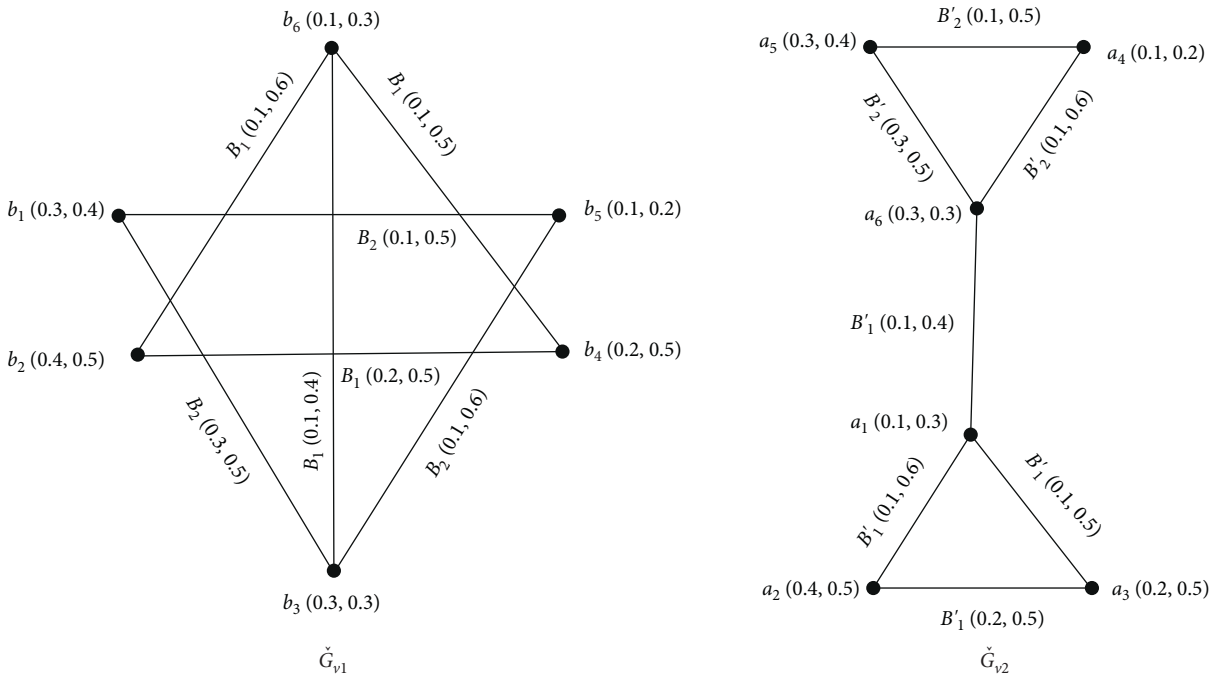

Figure 9: Identical vague graph structures.

then, $ab \in B_m^{\psi}$ while m is chosen so that $t_{B_m^{\psi}}(ab) \geq t_{B_i^{\psi}}(ab)$ and $f_{B_m^{\psi}}(ab) \geq f_{B_i^{\psi}}(ab)$, $\forall i$. Then, VGS $(A, B_1^{\psi}, B_2^{\psi}, \ldots, B_n^{\psi})$ denoted by $G_v^{\psi c}$, is named the ψ-complement of VGS.

Example 10. Consider VGS $\breve{G}_v = (A, B_1, B_2)$ shown in Figure 10 and let ψ be a permutation on the set $\{B_1, B_2\}$ so that $\psi(B_1) = B_2$ and $\psi(B_2) = B_1$. Now, for $a_1a_2 \in B_1$,

$$
\begin{aligned}
t^{\psi}_{B_1}(a_1a_2) &= t_A(a_1) \wedge t_A(a_2) - \bigvee_{j\neq 1}\left[t_{\psi B_j}(a_1a_2)\right] = 0.2 - 0.2 = 0,\\
f^{\psi}_{B_1}(a_1a_2) &= f_A(a_1) \vee f_A(a_2) - \bigvee_{j\neq 1}\left[f_{\psi B_j}(a_1a_2)\right] = 0.5 - 0.5 = 0,\\
t^{\psi}_{B_2}(a_1a_2) &= t_A(a_1) \wedge t_A(a_2) - \bigvee_{j\neq 2}\left[t_{\psi B_j}(a_1a_2)\right] = 0.2 - 0 = 0.2,\\
f^{\psi}_{B_2}(a_1a_2) &= f_A(a_1) \vee f_A(a_2) - \bigvee_{j\neq 2}\left[f_{\psi B_j}(a_1a_2)\right] = 0.5 - 0 = 0.5.
\end{aligned}
\tag{21}
$$

Clearly, $t_{B_2^\psi}(a_1a_2) = 0.2 > 0 = t_{B_1^\psi}(a_1a_2)$ and $f_{B_2^\psi}(a_1a_2) = 0.5 > 0 = f_{B_1^\psi}(a_1a_2)$, so $a_1a_2 \in B_2^\psi$.

$$\begin{aligned} t_{B_1^\psi}(a_1a_3) &= t_A(a_1)\wedge t_A(a_3) - \vee\left[t_{\psi B_2}(a_1a_3)\right] = 0.2 - 0.2 = 0,\\ f_{B_1^\psi}(a_1a_3) &= f_A(a_1)\vee f_A(a_3) - \vee\left[f_{\psi B_2}(a_1a_3)\right] = 0.4 - 0.4 = 0,\\ t_{B_2^\psi}(a_1a_3) &= t_A(a_1)\wedge t_A(a_3) - \vee\left[t_{\psi B_1}(a_1a_3)\right] = 0.2 - 0 = 0.2,\\ f_{B_2^\psi}(a_1a_3) &= f_A(a_1)\vee f_A(a_3) - \vee\left[f_{\psi B_1}(a_1a_3)\right] = 0.4 - 0 = 0.4. \end{aligned} \tag{22}$$

So, $a_1a_3 \in B_2^\psi$. Also, for a_2a_3, we have

$$\begin{aligned} t_{B_1^\psi}(a_2a_3) &= t_A(a_2)\wedge t_A(a_3) - \vee\left[t_{\psi B_2}(a_2a_3)\right] = 0.2 - 0 = 0.2,\\ f_{B_1^\psi}(a_2a_3) &= f_A(a_2)\vee f_A(a_3) - \vee\left[f_{\psi B_2}(a_2a_3)\right] = 0.5 - 0 = 0.5,\\ t_{B_2^\psi}(a_2a_3) &= t_A(a_2)\wedge t_A(a_3) - \vee\left[t_{\psi B_1}(a_2a_3)\right] = 0.2 - 0.2 = 0,\\ f_{B_2^\psi}(a_2a_3) &= f_A(a_2)\vee f_A(a_3) - \vee\left[f_{\psi B_1}(a_2a_3)\right] = 0.5 - 0.5 = 0. \end{aligned} \tag{23}$$

So, $a_2a_3 \in B_1^\psi$.

Theorem 1. *A ψ-complement of a VGS is a SVGS. In addition, if $\psi(i) = r$, for $r, i \in \{1, 2, \ldots, n\}$, then all B_r-edges in VGS $\breve{G}_v = (A, B_1, B_2, \ldots, B_n)$ become B_i^ψ-edges in $\breve{G}_v^{\psi c} = (A, B_1^\psi, B_2^\psi, \ldots, B_n^\psi)$.*

Proof. The proof of the first part is clear according to the definition of the ψ-complement $\breve{G}_v^{\psi c}$ of VGS $\breve{G}_v$, since for any B_i^ψ-edge ab, $t_{B_i}^\psi(ab)$ and $f_{B_i}^\psi(ab)$, respectively, have the maximum values of

$$\begin{aligned} &\left[t_A(a)\wedge t_A(b)\right] - \bigvee_{j\neq i} t_{\psi B_j}(ab)\\ &\left[f_A(a)\vee f_A(b)\right] - \bigvee_{j\neq i} f_{\psi B_j}(ab). \end{aligned} \tag{24}$$

That is,

$$\begin{aligned} t_{B_i}^\psi(ab) &= t_A(a)\wedge t_A(b),\\ f_{B_i}^\psi(ab) &= f_A(a)\vee f_A(b), \end{aligned} \tag{25}$$

for all edges ab in $\breve{G}_v^{\psi c}$; hence, $\breve{G}_v^{\psi c}$ is a SVGS. Now assume on contrary that $\psi(i) = r$, but ab is B_s-edge in $\breve{G}_v$ with $s \neq r$ that shows $\psi B_i \neq B_s$.

By comparing equations (24) and (25), we have

$$\begin{aligned} \bigvee_{j\neq i} t_{\psi B_j}(xy) &= 0,\\ \bigvee_{j\neq i} f_{\psi B_j}(xy) &= 0, \end{aligned} \tag{26}$$

that it is not true because $B_s = \psi B_j$, for some $j \in \{1, 2, \ldots, i-1, i+1, \ldots, n\}$. Therefore, our assumption is wrong and ab should be a B_r-edge. Thus, we get if $\psi(i) = r$, then, all B_r-edges in VGS $\breve{G}_v = (A, B_1, B_2, \ldots, B_n)$ become B_i^ψ-edges in $\breve{G}_v^{\psi c} = (A, B_1^\psi, B_2^\psi, \ldots, B_n^\psi)$, for $r, i \in \{1, 2, \ldots, n\}$. □

Definition 26. Let $\breve{G}_v = (A, B_1, B_2, \ldots, B_n)$ be a VGS and ψ be a permutation on the set $\{1, 2, \ldots, n\}$. Then,

(i) $\breve{G}_v$ is SC, if $\breve{G}_v \cong \breve{G}_v^{\psi c}$,
(ii) $\breve{G}_v$ is SSC, if it is identical to $\breve{G}_v^{\psi c}$.
(iii) $\breve{G}_v$ is TSC if $\breve{G}_v \cong \breve{G}_v^{\psi c}$, $\forall$ permutations ψ on the set $\{1, 2, \ldots, n\}$.
(iv) $\breve{G}_v$ is TSSC, if it is identical to $\breve{G}_v^{\psi c}$, $\forall$ permutations ψ on the set $\{1, 2, \ldots, n\}$.

Theorem 2. *A VGS $\breve{G}_v$ is strong if $\breve{G}_v$ is TSC.*

Proof. Assume $\breve{G}_v$ be a SVGS and ψ be a permutation on the set $\{1, 2, \ldots, n\}$. If $\psi^{-1}(i) = j$, then, by Theorem 1, all B_i-edges in $\breve{G}_v = (A, B_1, B_2, \ldots, B_n)$ become B_j^ψ-edges in $\breve{G}_v^{\psi c} = (A, B_1^\psi, B_2^\psi, \ldots, B_n^\psi)$. Also, $\breve{G}_v$ is strong, so,

$$\begin{aligned} t_{B_i}(a_1a_2) &= t_A(a_1)\wedge t_A(a_2) = t_{B_j^\psi}(a_1a_2),\\ f_{B_i}(a_1a_2) &= f_A(a_1)\vee f_A(a_2) = f_{B_j^\psi}(a_1a_2). \end{aligned} \tag{27}$$

Then, $\breve{G}_v$ is isomorphic to $\breve{G}_v^{\psi c}$, under the identity mapping g: $V \longrightarrow V$ and a permutation ψ, so that

$$t_A(a) = t_A(g(a)),\ f_A(a) = f_A(g(a)), \text{for all } a \in V, \tag{28}$$

and

$$\begin{aligned} t_{B_i}(a_1a_2) &= t_{B_j^\psi}(a_1a_2) = t_{B_j^\psi}(g(a_1)g(a_2)),\\ f_{B_i}(a_1a_2) &= f_{B_j^\psi}(a_1a_2) = f_{B_j^\psi}(g(a_1)g(a_2)), \end{aligned} \tag{29}$$

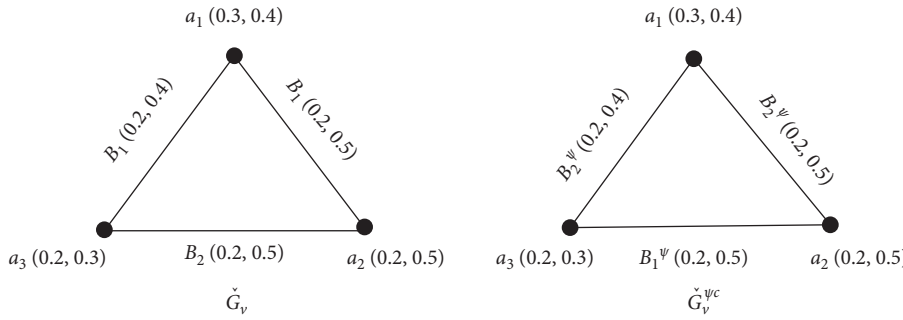

Figure 10: Vague graph structures $\breve{G}_v$ and $\breve{G}_v^{\psi c}$.

for all $a_1a_2 \in R_i$. This holds for all the permutation on the set $\{1, 2, \ldots, n\}$. Thus, $\breve{G}_v$ is TSC. Conversely, let ψ be any permutation on the set $\{1, 2, \ldots, n\}$ and $\breve{G}_v$ and $\breve{G}_v^{\psi c}$ be isomorphic. According to the definitions of ψ-complement and isomorphism, we get

$$\begin{aligned} t_{B_i}(a_1a_2) &= t_{B_j^{\psi}}(g(a_1)g(a_2)) = t_A(g(a_1)) \wedge t_A(g(a_2)) = t_A(a_1) \wedge t_A(a_2), \\ f_{B_i}(a_1a_2) &= f_{B_j^{\psi}}(g(a_1)g(a_2)) = f_A(g(a_1)) \vee f_A(g(a_2)) = f_A(a_1) \vee f_A(a_2), \end{aligned} \tag{30}$$

for all $a_1a_2 \in E_i$, $i = 1, 2, \ldots, n$. Hence, $\breve{G}_v$ is a SVGS. □

Theorem 3. *If GS $G^* = (V, R_1, R_2, \ldots, R_n)$ is TSSC and A is a VS of V with constant fuzzy mapping t_A and f_A, then, a SVGS $\breve{G}_v = (A, B_1, B_2, \ldots, B_n)$ of G^* is TSSC.*

Proof. Consider a SVGS $\breve{G}_v = (A, B_1, B_2, \ldots, B_n)$ of a GS $G^* = (V, R_1, R_2, \ldots, R_n)$. Assume that G^* is TSSC and that for some constants $s, t \in [0, 1]$, $A = (t_A, f_A)$ is a VS of u so that $t_A(u) = s$, $f_A(u) = t$, $\forall u \in V$. Then, we have to prove that $\breve{G}_v$ is TSSC. Let ψ be an arbitrary permutation on the set $\{1, 2, \ldots, n\}$ and $\psi^{-1}(j) = i$. Since G^* is TSSC, so $\exists$ a bijection $g: V \longrightarrow V$ so that for each R_i-edge a_1a_2 in G^*, $g(a_1)g(a_2)$ is an R_i-edge in $(G^*)^{\psi^{-1}c}$. Consequently, for every B_i-edge a_1a_2 in $\breve{G}_v$, $g(a_1)g(a_2)$ is a B_i^{ψ}-edge in $\breve{G}_v^{\psi c}$. From the definition of A and the definition of SVGS $\breve{G}_v$,

$$t_A(a) = s = t_A(g(a)), f_A(a) = t = f_A(g(a)), \text{ for all } a, g(a) \in V, \tag{31}$$

and

$$\begin{aligned} t_{B_i}(a_1a_2) &= t_A(a_1) \wedge t_A(a_2) = t_A(g(a_1)) \wedge t_A(g(a_2)) = t_{B_i^{\psi}}(g(a_1)g(a_2)), \\ f_{B_i}(a_1a_2) &= f_A(a_1) \vee f_A(a_2) = f_A(g(a_1)) \vee f_A(g(a_2)) = f_{B_i^{\psi}}(g(a_1)g(a_2)), \end{aligned} \tag{32}$$

for all $a_1a_2 \in B_i$, $i = 1, 2, \ldots, n$, which shows $\breve{G}_v$ is SSC. Hence, $\breve{G}_v$ is TSSC, since ψ is arbitrary. □

Example 11. A VGS $\breve{G}_v = (A, B_1, B_2, B_3)$ of GS $G^* = (V, R_1, R_2, R_3)$ as shown in Figure 11 is TSSC.

4. Application

Providing services to the people in the shortest possible time is one of the most important issues that governments strive to do in the best possible way. Unfortunately, in the past, due to the lack of medical and welfare services as well as the lack of educational centers, people had to travel to distant cities to provide these necessary facilities and equipment, and in this way, unfortunately, they incurred a lot of costs. But today, with the help of governments as well as the equipping of medical and welfare centers, people can move to their nearest neighboring city to benefit from these facilities. A vague graph structure helps us to understand which route is more appropriate for a particular service. It also shows us which service is increasing so that governments can strengthen it in the same way and also try to increase the rest of the services so that people can benefit from them. Most importantly, a VGS can also be useful to the mayor of the area, as it helps the mayor make appropriate policies for the city to develop appropriate services. For example, if one of

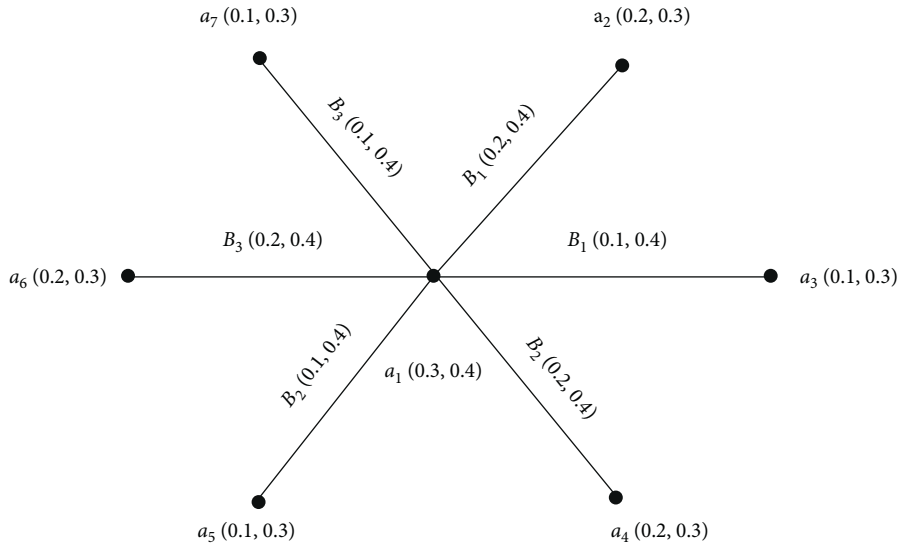

Figure 11: Totally strong self-complementary.

the welfare services in that area is more than other services (the number of people referring to that welfare center is higher), then, the VGS shows this issues and as a result, the mayor takes the necessary measures to maintain and increase this opportunity. Suppose A is a set consisting of 7 cities as $A = \{\text{Neka, Behshahr, Sari, Ghaemshahr, Babol, Bahnamir, Babolsar}\}$, and H is a VS on A as Table 2.

In Table 2, true membership value indicates the amount of welfare, educational, medical, and peace facilities in that area, and the false-membership value reveals the lack of necessary facilities in each of the medical services. In Tables 3–9, we show the membership rate of various welfare services on the route between each pair of cities. The relations that considered on set A are as follows:

R_1 = Grocery stores, R_2 = Banking services, R_3 = Car daelership, R_4 = Hospitals, and R_5 = University and Schools so that $(A, R_1, R_2, R_3, R_4, R_5)$ is a graph structure. Each object in a particular relation indicates the amount of services provided between the two cities. In these relations, each element is determined by its corresponding membership rate, and the corresponding sets are FSs on R_1, R_2, R_3, R_4, and R_5, respectively, which are shown by B_1, B_2, B_3, B_4, and B_5, respectively.

Suppose that

$$\begin{aligned}
R_1 &= \{(\text{Neka, Sari}), (\text{Sari, Behshahr})\},\\
R_2 &= \{(\text{Behshahr, Babol}), (\text{Babolsar, Babol})\},\\
R_3 &= \{(\text{Babol, Ghaemshar}), (\text{Sari, Ghaemshahr}), (\text{Bahnamir, Babolsar})\},\\
R_4 &= \{(\text{Neka, Bahnamir}), (\text{Sari, Bahnamir})\},\\
R_5 &= \{(\text{Ghaemshahr, Bahnamir}), (\text{Babolsar, Sari})\}.
\end{aligned} \tag{33}$$

Now, corresponding vague sets are

$$\begin{aligned}
B_1 &= \{((\text{Neka, Sari}), (0.6, 0.2)), ((\text{Sari, Behshahr}), (0.7, 0.2))\},\\
B_2 &= \{((\text{Behshahr, Babol}), (0.7, 0.2)), ((\text{Babolsar, Babol}), (0.8, 0.2))\},\\
B_3 &= \left\{ \begin{array}{c} ((\text{Babol, Ghaemshahr}), (0.5, 0.1)), ((\text{Sari, Ghaemshahr}), (0.7, 0.3)),\\ ((\text{Bahnamir, Babolsar}), (0.7, 0.2)) \end{array} \right\},\\
B_4 &= \{((\text{Neka, Bahnamir}), (0.7, 0.1)), ((\text{Sari, Bahnamir}), (0.6, 0.2))\},\\
B_5 &= \{((\text{Ghaemshahr, Bahnamir}), (0.7, 0.2)), ((\text{Babolsar, Sari}), (0.6, 0.3))\}.
\end{aligned} \tag{34}$$

Table 2: Vague set H on A.

City	Membership value
Neka	(0.3, 0.4)
Behshahr	(0.6, 0.3)
Sari	(0.8, 0.2)
Ghaemshahr	(0.5, 0.3)
Babol	(0.5, 0.2)
Bahnamir	(0.3, 0.2)
Babolsar	(0.6, 0.3)

Table 3: Vague set of services on roads connecting Neka and other cities.

Services	(Neka, Behshahr)	(Neka, Sari)	(Neka, Bahnamir)	(Neka, Babolsar)
Grocery store	(0.6, 0.2)	(0.5, 0.2)	(0.5, 0.2)	(0.7, 0.2)
Banking services	(0.6, 0.2)	(0.6, 0.2)	(0.4, 0.3)	(0.6, 0.3)
Car dealership	(0.5, 0.3)	(0.5, 0.2)	(0.3, 0.2)	(0.5, 0.4)
Hospitals	(0.6, 0.2)	(0.5, 0.3)	(0.4, 0.2)	(0.6, 0.3)
University and schools	(0.5, 0.4)	(0.5, 0.3)	(0.6, 0.2)	(0.5, 0.2)

Table 4: Vague set of services on roads connecting Behshahr and other cities.

Services	(Behshahr, Neka)	(Behshahr, Babol)	(Behshahr, Sari)
Grocery store	(0.7, 0.2)	(0.6, 0.2)	(0.7, 0.2)
Banking services	(0.8, 0.1)	(0.7, 0.2)	(0.4, 0.3)
Car dealership	(0.6, 0.2)	(0.6, 0.3)	(0.8, 0.2)
Hospitals	(0.8, 0.2)	(0.7, 0.2)	(0.6, 0.2)
University and schools	(0.7, 0.2)	(0.5, 0.3)	(0.6, 0.3)

Table 5: Vague set of services on roads connecting Sari and other cities.

Services	(Sari, Behshahr)	(Sari, Neka)	(Sari, Ghaemshahr)
Grocery store	(0.7, 0.2)	(0.5, 0.2)	(0.6, 0.2)
Banking services	(0.5, 0.3)	(0.4, 0.2)	(0.4, 0.3)
Car dealership	(0.6, 0.2)	(0.5, 0.3)	(0.6, 0.2)
Hospitals	(0.6, 0.4)	(0.4, 0.3)	(0.7, 0.3)
University and schools	(0.7, 0.2)	(0.5, 0.2)	(0.6, 0.2)

Table 6: Vague set of services on roads connecting Babol and other cities.

Services	(Babol, Behshahr)	(Babol, Babolsar)	(Babol, Ghaemshahr)
Grocery store	(0.5, 0.2)	(0.6, 0.2)	(0.4, 0.3)
Banking services	(0.6, 0.3)	(0.6, 0.1)	(0.4, 0.2)
Car dealership	(0.7, 0.2)	(0.5, 0.3)	(0.4, 0.3)
Hospitals	(0.6, 0.4)	(0.6, 0.2)	(0.4, 0.2)
University and schools	(0.6, 0.2)	(0.7, 0.1)	(0.5, 0.1)

Table 7: Vague set of services on roads connecting Ghaemshahr and other cities.

Services	(Ghaemshahr, Babol)	(Ghaemshahr, Sari)	(Ghaemshahr, Bahnamir)
Grocery store	(0.7, 0.1)	(0.7, 0.2)	(0.6, 0.2)
Banking services	(0.6, 0.3)	(0.8, 0.1)	(0.4, 0.3)
Car dealership	(0.6, 0.2)	(0.7, 0.3)	(0.7, 0.2)
Hospitals	(0.5, 0.4)	(0.6, 0.2)	(0.4, 0.2)
University and schools	(0.6, 0.2)	(0.5, 0.4)	(0.6, 0.3)

Table 8: Vague set of services on roads connecting Babolsar and other cities.

Services	(Babolsar, Babol)	(Babolsar, Sari)	(Babolsar, Bahnamir)
Grocery store	(0.7, 0.1)	(0.5, 0.2)	(0.6, 0.2)
Banking services	(0.5, 0.3)	(0.4, 0.3)	(0.4, 0.3)
Car dealership	(0.8, 0.2)	(0.6, 0.3)	(0.5, 0.2)
Hospitals	(0.8, 0.2)	(0.5, 0.3)	(0.4, 0.3)
University and schools	(0.7, 0.2)	(0.5, 0.3)	(0.5, 0.3)

Table 9: Vague set of services on roads connecting Bahnamir and other cities.

Services	(Bahnamir, Neka)	(Bahnamir, Sari)	(Bahnamir, Babolsar)
Grocery store	(0.5, 0.2)	(0.5, 0.3)	(0.5, 0.3)
Banking services	(0.6, 0.3)	(0.6, 0.2)	(0.6, 0.2)
Car dealership	(0.6, 0.3)	(0.5, 0.2)	(0.7, 0.2)
Hospitals	(0.7, 0.1)	(0.6, 0.2)	(0.5, 0.3)
University and schools	(0.6, 0.2)	(0.5, 0.3)	(0.4, 0.3)

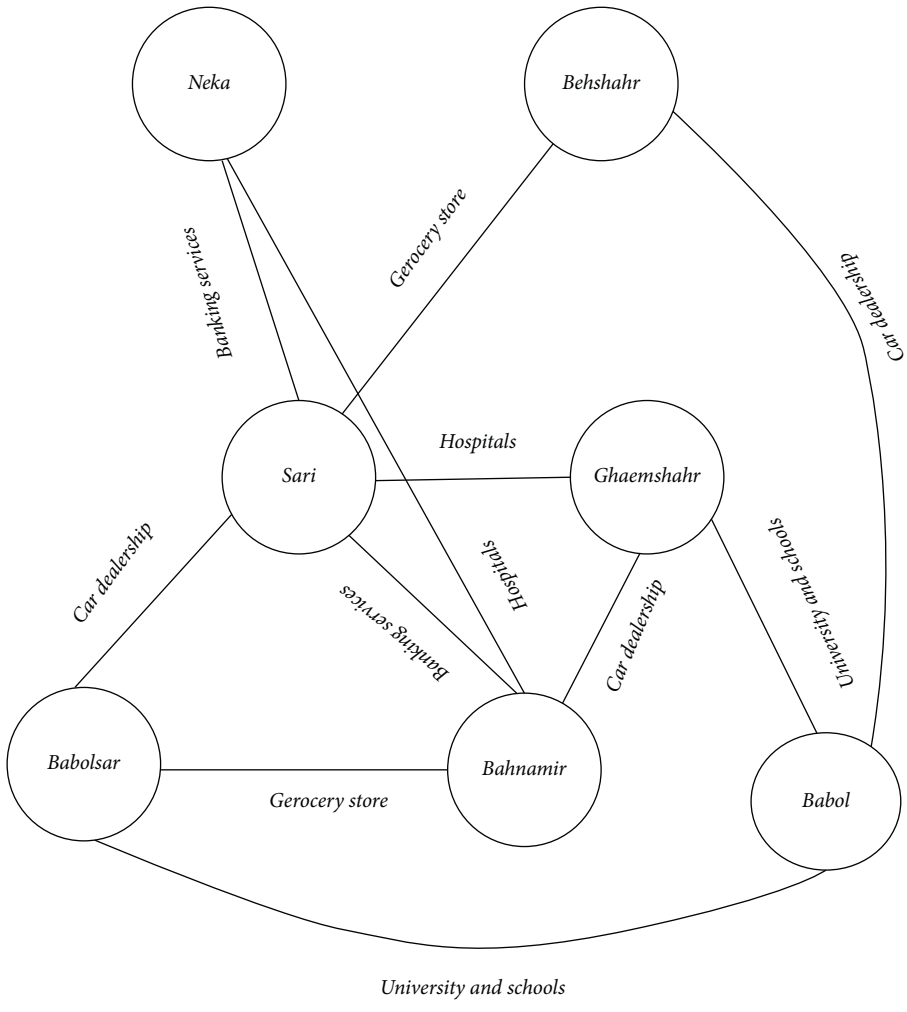

Figure 12: VGS showing the most important services along the roads connecting the two cities.

It is obvious that $(H, B_1, B_2, B_3, B_4, B_5)$ is a VGS and is denoted in Figure 12. In the VGS shown in Figure 12, each edge represents the most services that occur on the connecting route between the two cities. For example, most services on the way from Babolsar to Bahnamir are grocery services, and their membership value are $(0.7, 0.2)$. It is clear that the city of Sari has the highest membership in terms of banking services, which means that this city is the most

sensitive city for providing banking services. According to the VGS in Figure 12, the most common services is car dealership. Therefore, we conclude that government should identify places that are suitable for providing services between cities so that people can benefit from these services at the lowest cost and in the fastest possible time.

5. Conclusion

Fuzzy graph has various uses in modern science and technology, especially in the fields of neural networks, computer science, operation research, and decision making. VGS have more precision, flexibility, and compatibility, as compared to the fuzzy graphs. Today, VGSs play an important role in social networks and allow users to find the most effective person in a group or organization. So, in this paper, we presented certain notions, including VGS, SVGS, and vague B_i-cycle and illustrated these notions by several examples. We investigated ψ-complement, SC, SSC, and TSSC in VGS and studied some of their properties. Finally, an application of VGS has been introduced. In our future work, we will introduce neighborly irregular, highly irregular, strongly irregular, and edge irregularity in VGSs and investigate some of their properties.

Data Availability

No data were used to support this study.

Conflicts of Interest

The authors declare that they have no conflicts of interest.

References

[1] L. A. Zadeh, "Fuzzy sets," *Information and Control*, vol. 8, no. 3, pp. 338–353, 1965.
[2] E. Sampathkumar, "Generalized graph structures," *Bulletin of Kerala Mathematics Association*, vol. 3, no. 2, pp. 65–123, 2006.
[3] W.-L. Gau and D. J. Buehrer, "Vague sets," *IEEE Transactions on Systems, Man, and Cybernetics*, vol. 23, no. 2, pp. 610–614, 1993.
[4] A. Kaufmann, *Introduction a la Theorie des Sous-Emsembles Flous*, Vol. 1, Masson et Cie, , Échallens, Switzerland, 1973.
[5] L. A. Zadeh, "Similarity relations and fuzzy orderings," *Information Sciences*, vol. 3, no. 2, pp. 177–200, 1971.
[6] L. A. Zadeh, "Is there a need for fuzzy logic?" *Information Sciences*, vol. 178, no. 13, pp. 2751–2779, 2008.
[7] A. Rosenfeld, "Fuzzy graphs," in *Fuzzy Sets and Their Applications*, L. A. Zadeh, K. S. Fu, and M. Shimura, Eds., Academic Press, New York, NY, USA, pp. 77–95, 1975.
[8] P. Harinath and S. Lavanya, "Fuzzy graph structures and its properties," *Indian Journal of Science and Technology*, vol. 9, no. 43, pp. 1–7, 2016.
[9] P. Bhattacharya, "Some remarks on fuzzy graphs," *Pattern Recognition Letters*, vol. 6, no. 5, pp. 297–302, 1987.
[10] J. N. Mordeson and P. S. Nair, *Fuzzy Graphs and Fuzzy Hypergraphs: Second Edition 2001*, 2nd edition, 1998.
[11] T. Dinesh, *A study on graph structures, incidence algebras and their fuzzy analogues*, Ph.D. Thesis, Kannur University, Kannur, India, 2011.
[12] G. Ghorai and M. Pal, "Planarity in vague graphs with application," *Acta Mathematica Academiae Paedagogiace Nyregyhziensis*, vol. 33, no. 2, pp. 147–164, 2017.
[13] M. Pal, S. Samanta, and G. Ghorai, "Fuzzy tolerance graphs," in *Modern Trends in Fuzzy Graph Theory*, pp. 153–173, Springer, Singapore, 2020.
[14] N. Ramakrishna, "Vague graphs," *International Journal of Computational Cognition*, vol. 7, pp. 51–58, 2009.
[15] S. Kosari, Y. Rao, H. Jiang, X. Liu, P. Wu, and Z. Shao, "Vague graph structure with application in medical diagnosis," *Symmetry*, vol. 12, no. 10, p. 1582, 2020.
[16] Y. Rao, S. Kosari, Z. Shao, X. Qiang, M. Akhoundi, and X. Zhang, "Equitable domination in vague graphs with application in medical sciences," *Frontiers in Physics*, vol. 9, Article ID 635642, 2021.
[17] Y. Rao, S. Kosari, and Z. Shao, "Certain properties of vague graphs with a novel application," *Mathematics*, vol. 8, no. 10, p. 1647, 2020.
[18] Y. Rao, S. Kosari, Z. Shao, R. Cai, and L. Xinyue, "A study on domination in vague incidence graph and its application in medical sciences," *Symmetry*, vol. 12, no. 11, p. 1885, 2020.
[19] H. Rashmanlou, S. Samanta, M. Pal, and R. A. Borzooei, "A study on bipolar fuzzy graphs," *Journal of Intelligent and Fuzzy Systems*, vol. 28, no. 2, pp. 571–580, 2015.
[20] H. Rashmanlou and M. Pal, "Antipodal interval-valued fuzzy graphs," *International Journal of Applications of Fuzzy Sets and Artificial Intelligence*, vol. 3, pp. 107–130, 2013.
[21] M. Akram, A. Luqman, and A. B. Saeid, "Some types of hypergraphs for single-valued neutrosophic structures," *Fuzzy Hypergraphs and Related Extensions*, vol. 34, pp. 365–441, 2020.
[22] M. Akram and M. Sitara, "Certain fuzzy graph structures," *Journal of Applied Mathematics and Computing*, vol. 61, 2019.
[23] M. S. Sunitha and A. Vijayakumar, "Complement of fuzzy graphs," *Indian Journal of Pure and Applied Mathematics*, vol. 33, pp. 1451–1464, 2002.
[24] G. Muhiuddin, M. Mohseni Takallo, Y. B. Jun, and R. A. Borzooei, "Cubic graphs and their application to a traffic flow problem," *International Journal of Computational Intelligence Systems*, vol. 13, no. 1, pp. 1265–1280, 2020.
[25] H. Rashmanlou, G. Muhiuddin, S. Amanathulla, F. Mofidnakhaei, and M. Pal, "A study on cubic graphs with novel application," *Journal of Intelligent and Fuzzy Systems*, vol. 40, no. 1, pp. 89–101, 2021.
[26] S. Satham Hussain, R. Jahir Hussain, and G. Muhiuddin, "Neutrosophic vague line graphs," *Neutrosophic Sets and Systems*, vol. 36, pp. 121–130, 2020.

Hindawi
Advances in Mathematical Physics
Volume 2022, Article ID 7939654, 11 pages
https://doi.org/10.1155/2022/7939654

Research Article

$*$-Ricci Tensor on α-Cosymplectic Manifolds

M. R. Amruthalakshmi,[1] **D. G. Prakasha**,[1] **Nasser Bin Turki**,[2] **and Inan Unal**[3]

[1]*Department of Mathematics, Davangere University, Shivagangothri Campus, Davangere 577 007, India*
[2]*Department of Mathematics, College of Science, King Saud University, P.O. Box 2455, Riyadh 11451, Saudi Arabia*
[3]*Department of Computer Engineering, Munzur University, Tunceli, Turkey*

Correspondence should be addressed to Nasser Bin Turki; nassert@ksu.edu.sa

Received 19 December 2021; Accepted 28 January 2022; Published 21 February 2022

Academic Editor: Meraj Ali Khan

In this paper, we study α-cosymplectic manifold M admitting $*$-Ricci tensor. First, it is shown that a $*$-Ricci semisymmetric manifold M is $*$-Ricci flat and a ϕ-conformally flat manifold M is an η-Einstein manifold. Furthermore, the $*$-Weyl curvature tensor $\mathscr{W}^*$ on M has been considered. Particularly, we show that a manifold M with vanishing $*$-Weyl curvature tensor is a weak ϕ-Einstein and a manifold M fulfilling the condition $R(E_1, E_2) \cdot \mathscr{W}^* = 0$ is η-Einstein manifold. Finally, we give a characterization for α-cosymplectic manifold M admitting $*$-Ricci soliton given as to be nearly quasi-Einstein. Also, some consequences for three-dimensional cosymplectic manifolds admitting $*$-Ricci soliton and almost $*$-Ricci soliton are drawn.

1. Introduction

In the last few years, theory of almost contact geometry and related topics are an active branch of research due to elegant geometry and applications to physics. Nowadays, many attentions have been drawn towards the study of almost cosymplectic manifolds which are a special class of almost contact manifolds. This notion was initiated by Goldberg and Yano [1], in 1969, and then, a very systematic approach for the study of almost cosymplectic manifolds was carried forward by many geometers. A smooth manifold of $(2n+1)$-dimension with the condition $\eta \wedge d\eta^n \neq 0$ for a closed 1-form η is a cosymplectic manifold. A simple example of almost cosymplectic manifolds is given by the products of almost Kaehler manifolds and the real line $\mathbb{R}$ or the circle $\mathbb{S}^1$. At this moment, we refer the studies [2–5] and the references therein for a vast and exhaustive survey of the results on almost cosymplectic manifolds.

A new concept of the Ricci tensor named as $*$-Ricci tensor has been defined by Tachibana [6] and Hamada [7] in complex geometry. Similar to a complex case, the $*$-Ricci tensor of an almost contact metric manifold has been defined as follows:

$$S^*(E_1, E_2) = \frac{1}{2} Tr(E_3 \longrightarrow R(E_1, \phi E_2)\phi E_3), \tag{1}$$

for all $E_1, E_2 \in TM$, where R is the Riemannian curvature tensor. Naturally, Hamada also considered the notion of $*$-Einstein manifold. An Hermitian manifold is $*$-Einstein if we have $g(Q^*E_1, E_2) = \lambda g(E_1, E_2)$, where λ is a constant. Also, in the same study of Hamada, a classification of $*$-Einstein hypersurfaces was given. On the other hand, for an extension of Hamada's work, we refer to Ivey and Ryan [8]. The concept of the $*$-Ricci tensor has been studied in contact case. Venkatesha and his group ([9, 10]) recently studied some of the curvature properties on Sasakian manifold and contact metric generalized (κ, μ)-space form using the $*$-Ricci tensor.

In this study, the $*$-Ricci tensor within the framework of α-cosymplectic manifolds has been studied. In Section 2, we recall some basic formulas and results concerning α-cosymplectic manifold and $*$-Ricci tensor, which will be useful in further sections. An α-cosymplectic manifold satisfying $*$-Ricci semisymmetric and ϕ-conformally flat conditions are studied in Section 3 and shown that a ϕ-conformably flat α-cosymplectic manifold is η-Einstein

and a $*$-Ricci semisymmetric α-cosymplectic manifold is $*$-Ricci flat. In next section, the $*$-Weyl curvature tensor has been studied in the background of α-cosymplectic manifold, and several consequences are noticed. In the last section, we studied a special type of metric called $*$-Ricci soliton. Here, we have proved some important results of α-cosymplectic manifold admitting $*$-Ricci soliton.

2. Preliminaries

Here, we are going to recall some general facts on α-cosymplectic manifolds which are relevant to our work.

An almost contact metric manifold of $(2n+1)$-dimension is a 5-tuple (M, ϕ, ξ, η, g) with the following resources [11].

$$\begin{aligned} \phi^2 E_1 &= -E_1 + \eta(E_1)\xi, \\ \eta(\xi) &= 1, \\ \phi\xi &= 0, \\ \eta(\phi E_1) &= 0, \\ g(\phi E_1, \phi E_2) &= g(E_1, E_2) - \eta(E_1)\eta(E_2), \\ E_1, E_2 &\in TM, \end{aligned} \tag{2}$$

for a $(1,1)-$ tensor field ϕ, a characteristic vector field ξ, a 1-form η is dual of ξ, and g is a Riemannian metric. It is easily seen that

$$\begin{aligned} g(\phi E_1, E_2) &= -g(E_1, \phi E_2), \\ g(E_1, \xi) &= \eta(E_1), \\ E_1, E_2 &\in TM. \end{aligned} \tag{3}$$

It is well known that the fundamental 2-form ω is defined by $\omega(E_1, E_2) = g(\phi E_1, E_2)$ on M.

For an almost contact metric manifold M, we have the following classifications ([12, 13]):

(1) If $d\eta = \omega$, then M is a contact metric manifold

(2) If $d\eta = 0$ and $d\omega = 0$, then M is an almost cosymplectic manifold [1]

(3) If $d\eta = 0$ and $d\omega = 2\alpha\eta\wedge\omega$, then M is an almost α-Kenmotsu manifold for a nonzero scalar α

In the contact geometry, the notion is normality that is a contact analogue of the integrability of an almost complex structure. An almost cosymplectic metric manifold being normal, if we have $[\phi, \phi] = 0$ which is the Nijenhuis tensor of the tensor field ϕ, is defined by

$$[\phi, \phi] = \phi^2[E_1, E_2] + [\phi E_1, \phi E_2] - \phi[\phi E_1, E_2] - \phi[E_1, \phi E_2], \tag{4}$$

for all $E_1, E_2 \in TM$. A normal almost cosymplectic manifold is a cosymplectic manifold.

Almost $\alpha-$cosymplectic manifolds have been defined by Kim and Pak [14] by combining an almost α-Kenmotsu and almost cosymplectic structures by the following formula:

$$\begin{aligned} d\eta &= 0, \\ d\omega &= 2\alpha\eta\wedge\omega, \end{aligned} \tag{5}$$

for a constant α. On an α-cosymplectic manifold, we have

$$\left(\nabla_{E_1}\phi\right)E_2 = \alpha\left(g(\phi E_1, E_2)\xi - \eta(E_2)\phi E_1\right), \tag{6}$$

where ∇ denotes the Riemannian connection. From (6), it is easy to see that

$$\nabla_{E_1}\xi = -\alpha\phi^2 E_1 = \alpha[E_1 - \eta(E_1)\xi], \tag{7}$$

and

$$\left(\nabla_{E_1}\eta\right)E_2 = \alpha[g(E_1, E_2) - \eta(E_1)\eta(E_2)]. \tag{8}$$

On an α-cosymplectic manifold M of dimension $2n+1$, the following relationships are valid:

$$R(\xi, E_1)E_2 = \alpha^2\left(\eta(E_2)E_1 - g(E_1, E_2)\xi\right), \tag{9}$$

$$R(E_1, E_2)\xi = \alpha^2\left(\eta(E_1)E_2 - \eta(E_2)E_1\right), \tag{10}$$

$$S(E_1, \xi) = -2n\alpha^2\eta(E_1), \tag{11}$$

where R and S are the curvature and Ricci tensors, respectively.

By the following lemma, we obtain some derivational features of α-cosymplectic manifold.

Lemma 1. *On an $\alpha-$ cosymplectic manifold of dimension $2n+1$, we have*

$$\left(\nabla_{E_1}Q\right)\xi = -\alpha QE_1 - 2n\alpha^3 E_1, \tag{12}$$

$$\left(\nabla_{\xi}Q\right)E_1 = -2\alpha QE_1 - 4n\alpha^3 E_1, \tag{13}$$

$$\xi(r) = -2\alpha\left\{r + 2n(2n+1)\alpha^2\right\}. \tag{14}$$

Proof. Note that (11) implies $Q\xi = -2n\alpha^2\xi$, for Q defined by $S(E_1, E_2) = g(QE_1, E_2)$. Differentiating this along E_1 and using (7), we get (12). Next, differentiation of (10) with respect to T gives

$$\begin{aligned} (\nabla_T R)(E_1, E_2)\xi = &-\alpha R(E_1, E_2)T \\ &+ \alpha^3\{g(E_1, T)E_2 - g(E_2, T)E_1\}. \end{aligned} \tag{15}$$

Let $\{e_i\}_{i=1}^{2n+1}$ be a local basis on M. Replacing $E_1 = T = e_i$ in the foregoing equation with summing over i gives

$$\sum_{i=1}^{2n+1} g\left(\left(\nabla_{e_i}R\right)(e_i, E_2)\xi, E_3\right) = \alpha S(E_2, E_3) + 2n\alpha^3 g(E_2, E_3). \tag{16}$$

Using second Bianchi's identity leads to

$$\sum_{i=1}^{2n+1} g\left(\left(\nabla_{e_i}R\right)(E_3,\xi)E_2,e_i\right) = g\left(\left(\nabla_{E_3}Q\right)\xi,E_2\right) - g\left(\left(\nabla_{\xi}Q\right)E_3,E_2\right). \tag{17}$$

By considering (16) in (17) and then with the help of (12), we conclude

$$g\left(\left(\nabla_{\xi}Q\right)E_1,E_2\right) = -2\alpha S(E_1,E_2) - 4n\alpha^3 g(E_1,E_2), \tag{18}$$

which proves (13). Finally, contraction of (13) gives (14). □

From Riemannian geometry, the covariant derivative of a $(1,s)$-type of tensor field K is given by

$$(\mathrm{div}K)(E_1,E_1,\ldots,E_1s) = \sum_{i=1}^{2n+1} g\left(\left(\nabla_{e_i}K\right)(E_1,E_1,\ldots,E_1),e_i\right). \tag{19}$$

for all $E_1,E_1,\ldots,E_1 \in TM$, where div is stated for the divergence [15].

By following descriptions, we present some classification facts which come from the Ricci tensor and have been stated.

(1) An α–cosymplectic manifold M is called by weak ϕ-Einstein if we have

$$S^{\phi}(E_1,E_2) = \beta g^{\phi}(E_1,E_2), \quad \forall E_1,E_2 \in TM, \tag{20}$$

for some function β, where $g^{\phi}(E_1,E_2) = g(\phi E_1, \phi E_2)$, and S^{ϕ} is defined by

$$S^{\phi}(E_1,E_2) = \frac{1}{2}\{S^*(E_1,E_2) + Ric^*(E_2,E_1)\}, \quad E_1,E_2 \in TM, \tag{21}$$

In other words, S^{ϕ} denotes the symmetric part of S^*. If β is constant, then M is called ϕ-Einstein [16].

(2) M is called near quasi-Einstein manifold if the Ricci tensor is of the form

$$S(E_1,E_2) = ag(E_1,E_2) + bE(E_1,E_2), \quad \forall E_1,E_2 \in TM, \tag{22}$$

where a and b are the nonzero scalars and E is a nonzero $(0,2)$ tensor [17].

(3) M is called an η-Einstein manifold if we have

$$S(E_1,E_2) = \alpha g(E_1,E_2) + \gamma\eta(E_1)\eta(E_2), \quad \forall E_1,E_2 \in TM, \tag{23}$$

where α and γ are the constants [18].

By decomposition of Riemannian curvature tensor R, the Weyl conformal curvature tensor $\mathscr{W}$ has been obtained in this way:

$$\mathscr{W}(E_1,E_2)E_3 = R(E_1,E_2)E_3 - \frac{1}{2n-1}\{S(E_2,E_3)E_1 - S(E_1,E_3)E_2 + g(E_2,E_3)QE_1 - g(E_1,E_3)QE_2\} + \frac{r}{2n(2n-1)}\{g(E_2,E_3)E_1 - g(E_1,E_3)E_2\}. \tag{24}$$

for all $E_1,E_2,E_3 \in TM$ [15]. It is noted that, Weyl conformal curvature tensor vanishes whenever the metric is conformally identical to a flat metric, and it is one of the important curvature properties on a manifold.

3. $*$-Ricci Tensor on α-Cosymplectic Manifold

We are in a situation to confer the equation of the $*$-Ricci tensor in the framework of α-cosymplectic manifolds and then study its various properties. In [19], authors derived the expression of the $*$-Ricci tensor on α-cosymplectic manifold which is of the following form:

$$S^*(E_1,E_2) = S(E_1,E_2) + (2n-1)\alpha^2 g(E_1,E_2) + \alpha^2\eta(E_1)\eta(E_2), \tag{25}$$

for all $E_1,E_2 \in TM$.

Note that S^* is not symmetric. By contraction of (25), the $*$-scalar curvature is specified by

$$r^* = r + 4n^2\alpha^2. \tag{26}$$

If the $*$-Ricci tensor S^* is a constant multiple of the Riemannian metric g, then we say that the manifold is $*$-Einstein. Moreover, the $*$-scalar curvature is not constant on a $*$-Einstein manifold.

3.1. $*$-Ricci Semisymmetric α-Cosymplectic Manifolds. An α-cosymplectic manifold M satisfying the condition $R(E_1,E_2)\cdot S = 0$ for all $E_1,E_2 \in TM$ is called Ricci semi symmetric, where $R(E_1,E_2)$ acts as a derivation on S. This notion was introduced by Mirjoyan [20] for Riemann spaces and then studied by many authors. Analogous to this, an α-cosymplectic manifold is called $*$-Ricci semisymmetric if its $*$-Ricci tensor satisfies the condition $R(E_1,E_2)\cdot S^* = 0 \forall E_1,E_2 \in TM$.

Theorem 1. *If a $(2n+1)$-dimensional α-cosymplectic manifold M is $*$-Ricci semisymmetric, then M is $*$-Ricci flat. Moreover, it is an η-Einstein manifold, and the Ricci tensor is to be exhibited as*

$$S(E_1, E_2) = (1 - 2n)\alpha^2 g(E_1, E_2) - \alpha^2 \eta(E_1)\eta(E_2), \quad E_1, E_2 \in TM. \tag{27}$$

Proof. Let us consider $*$-Ricci semisymmetric α-cosymplectic manifold M. Then, condition $R(E_1, E_2).S^* = 0$ is equivalent to

$$S^*(R(E_1, E_2)E_3, E_4) + S^*(E_3, R(E_1, E_2)E_4) = 0. \tag{28}$$

Putting $E_1 = \xi$ in (28) and then recalling (9), we have

$$\begin{aligned}&\alpha^2\{S^*(E_2, E_4)\eta(E_3) - g(E_2, E_3)S^*(\xi, E_4)\}\\ &+ \alpha^2\{S^*(E_3, E_2)\eta(E_4) - g(E_2, E_4)S^*(E_3, \xi)\} = 0.\end{aligned} \tag{29}$$

It is well known that $Ric^*(E_1, \xi) = 0$. Making use of this in (29), we find

$$\alpha^2\{S^*(E_2, E_4)\eta(E_3) + S^*(E_3, E_2)\eta(E_4)\} = 0. \tag{30}$$

Again, plugging E_4 by ξ in (30) shows that M is $*$-Ricci flat, that is, $S^*(E_3, E_2) = 0, E_3, E_2 \in TM$. Moreover, in view of (25) and (30), we have the required result. □

3.2. ϕ-Conformally Flat α-Cosymplectic Manifolds. An α-cosymplectic manifold M is said to be ϕ-conformally flat if we have

$$\phi^2 \mathscr{W}(\phi E_1, \phi E_2)\phi E_3 = 0, \tag{31}$$

for all $E_1, E_2, E_3 \in TM$. Sasakian manifolds which are ϕ-conformally flat have been studied in [21]. In the following, we study a ϕ-conformally flat α-cosymplectic manifold.

Theorem 2. *An φ-conformally flat α-cosymplectic manifold is $* - \eta$-Einstein manifold. Moreover, M is weak φ-Einstein.*

Proof. Assume that an α-cosymplectic manifold is ϕ-conformally flat. So, it is easy to see that $\phi^2 C(\phi E_1, \phi E_2)\phi E_3 = 0$ carry if and only if $g(C(\phi E_1, \phi E_2)\phi E_3, \phi E_4) = 0\ \forall E_1, E_2, E_3, E_4 \in TM$. Hence, ϕ-conformally flat means

$$\begin{aligned}g(R(\phi E_1, \phi E_2)\phi E_3, \phi E_4) = {}& \frac{1}{2n-1}\{S(\phi E_2, \phi E_3)g(\phi E_1, \phi E_4) - S(\phi E_1, \phi E_3)g(\phi E_2, \phi E_4) + g(\phi E_2, \phi E_3)S(\phi E_1, \phi E_4)\\ &- g(\phi E_1, \phi E_3)S(\phi E_2, \phi E_4)\}\}\\ &- \frac{r}{2n(2n-1)}\{g(\phi E_2, \phi E_3)g(\phi E_1, \phi E_4)\\ &- g(\phi E_1, \phi E_3)g(\phi E_2, \phi E_4)\}.\end{aligned} \tag{32}$$

For a local orthonormal basis of TM with $\{e_1, \ldots, e_2 n, \xi\}$, if we put $E_1 = E_4 = e_i$ in (32) and sum up with respect to i, then we obtain

$$\begin{aligned}\sum_{i=1}^{2n} g(R(\phi e_i, \phi E_2)\phi E_3, \phi e_i) = {}& \frac{1}{2n-1}\sum_{i=1}^{2n}\{g(\phi e_i, \phi e_i)S(\phi E_2, \phi E_3) - g(\phi E_2, \phi e_i)S(\phi e_i, \phi E_3) + g(\phi E_2, \phi E_3)S(\phi e_i, \phi e_i)\\ &- g(\phi e_i, \phi E_3)S(\phi E_2, \phi e_i)\}\\ &- \frac{r}{2n(2n-1)}\sum_{i=1}^{2n}\{g(\phi e_i, \phi e_i)\\ &g(\phi E_2, \phi E_3) - g(\phi e_i, \phi E_3)g(\phi E_2, \phi e_i)\},\end{aligned} \tag{33}$$

and therefore,

$$S(\phi E_2, \phi E_3) - g(R(\xi, E_2)E_3, \xi) = \frac{2(n-1)}{2n-1}S(\phi E_2, \phi E_3) + \frac{1}{2n-1}\left[\frac{r}{2n} + \alpha^2\right]g(\phi E_2, \phi E_3). \tag{34}$$

From (9), we obtain $g(R(\xi, E_2)E_3, \xi) = -\alpha^2 g(\phi E_2, \phi E_3)$, and hence, from (34), we get

$$S(\phi E_2, \phi E_3) = \left[\frac{r}{2n} + \alpha^2\right] g(\phi E_2, \phi E_3). \tag{35}$$

Then, from (35), it follows from (32) that

$$g(R(\phi E_1, \phi E_2)\phi E_3, \phi E_4) = \frac{r + 4n\alpha^2}{2n(2n-1)}\{g(\phi E_2, \phi E_3)g(\phi E_1, \phi E_4) - g(\phi E_1, \phi E_3)g(\phi E_2, \phi E_4)\}. \tag{36}$$

In an α-cosymplectic manifold, in view of (3) and (9) for all $E_1, E_2, E_3, E_4 \in TM$, we can verify that

$$\begin{aligned} R\left(\varphi^2 E_1, \varphi^2 E_2, \varphi^2 E_3, \varphi^2 E_4\right) = R(E_1, E_2, E_3, E_4) + \alpha^2\{&g(E_2, E_3)\eta(E_1)\eta(E_2) - g(E_1, E_3)\eta(E_2)\eta(E_4) \\ &+ g(E_1, E_4)\eta(E_2)\eta(E_3) - g(E_2, E_4)\eta(E_1)\eta(E_3)\}. \end{aligned} \tag{37}$$

Taking $\varphi E_1, \varphi E_2, \varphi E_3, \varphi E_4$ instead of E_1, E_2, E_3, E_4 in (37), respectively, and making use of (36), we obtain

$$\begin{aligned} R(E_1, E_2, E_3, E_4) = &\frac{r + 4n\alpha^2}{2n(2n-1)}\{g(E_1, E_4)g(E_2, E_3) - g(E_2, E_4)g(E_1, E_3)\} \\ &- \frac{r + 2n(2n+1)\alpha^2}{2n(2n-1)}\{(g(E_2, E_3)\eta(E_1) - g(E_1, E_3)\eta(E_2))\eta(E_4) + (g(E_1, E_4)\eta(E_2) - g(E_2, E_4)\eta(E_1))\eta(E_3)\}. \end{aligned} \tag{38}$$

By the definition of S^*, direct computation yields

$$\begin{aligned} S^*(E_1, E_2) &= \sum_{i=1}^{2n+1} R(E_1, e_i, \phi e_i, \phi E_2) \\ &= \beta g(E_1, E_2) - \beta\eta(E_1)\eta(E_2), \end{aligned} \tag{39}$$

where $\beta = (r + 4n\alpha^2)/(2n(2n-1))$ reveals that M is $*-\eta$-Einstein. In view of (3), we have

$$S^*(E_1, E_2) = \frac{r + 4n\alpha^2}{2n(2n-1)} g^{\phi}(E_1, E_2), \quad E_1, E_2 \in TM. \tag{40}$$

Thus, $S^* = S^{\phi}$, and hence, it is weak ϕ-Einstein. This completes the proof. □

Next, for a constant scalar curvature of M, in view of (40), we state the following.

Corollary 1. *A ϕ-conformally flat α-cosymplectic manifold of constant scalar curvature is a ϕ--Einstein manifold.*

In an α-cosymplectic manifold, the $*$-Ricci tensor is given by (25), and so in view of (40), we state the following.

Corollary 2. *A ϕ-conformally flat α-cosymplectic manifold is η-Einstein.*

Furthermore, an α-cosymplectic manifold M is called to have the η-parallel Ricci tensor if its Ricci tensor S satisfies the condition $(\nabla_{E_1} S)(\phi E_2, \phi E_3) = 0$, $E_1, E_2, E_3 \in TM$. This notion was introduced in 1976 by Kon [22] in the framework of Sasakian manifolds and then studied by many authors. Analogous to this notion, we state the following:

Definition 1. An α-cosymplectic manifold M is said to have a η-parallel $*$-Ricci tensor if its $*$-Ricci tensor satisfies the condition $(\nabla_{E_1} S^*)(\phi E_2, \phi E_3) = 0\, \forall E_1, E_2, E_3 \in TM$.

Replacing E_1 by ϕE_1 and E_2 by ϕE_2 in (39), we obtain $S^*(\phi E_1, \phi E_2) = \beta g(\phi E_1, \phi E_2)$. Covariant derivative of the foregoing equation with respect to E_4, we get $(\nabla_{E_4} S^*)(\phi E_1, \phi E_2) = dr(E_4) g(\phi E_1, \phi E_2)$. Therefore, from Definition 1, we have the following.

Corollary 3. *Let M be a $(2n+1)$-dimensional ϕ-conformally flat α-cosymplectic manifold. If M admits a*

η-parallel $*$-Ricci tensor, then M has a constant scalar curvature.

4. $*$-Weyl Curvature Tensor on α-Cosymplectic Manifolds

The notion of $*$-Weyl curvature tensor $\mathscr{W}^*$ on real hypersurfaces of complex space forms (particularly, nonflat) is defined recently by Kaimakamis and Panagiotidou [23] in the following way:

$$\mathscr{W}^*(E_1,E_2)E_3 = R(E_1,E_2)E_3 + \frac{r^*}{2n(2n-1)}\{g(E_2,E_3)E_1 - g(E_1,E_3)E_2\} - \frac{1}{2n-1}\{g(Q^*E_2,E_3)E_1 - g(Q^*E_1,E_3)E_2 + g(E_2,E_3)Q^*E_1 - g(E_1,E_3)Q^*E_2\}, \tag{41}$$

for all $E_1, E_2, E_3 \in TM$, where Q^* is the $*$-Ricci operator and r^* is the $*$-scalar curvature corresponding to Q^*.

Using (25), we can write

$$Q^*E_1 = QE_1 + \alpha^2\{(2n-1)E_1 + \eta(E_1)\xi\}. \tag{42}$$

With the help of (41), (32), and (42), we obtain the expression for the $*$-Weyl curvature tensor on $(2n+1)$-dimensional α-cosymplectic manifold M as

$$\mathscr{W}^*(E_1,E_2)E_3 = \mathscr{W}(E_1,E_2)E_3 - \frac{2(n-1)\alpha^2}{2n-1}\{g(E_2,E_3)E_1 - g(E_1,E_3)E_2\} - \frac{\alpha^2}{2n-1}\{\eta(E_2)\eta(E_3)E_1 - \eta(E_1)\eta(E_3)E_2 + g(E_2,E_3)\eta(E_1)\xi - g(E_1,E_3)\eta(E_2)\xi\}. \tag{43}$$

4.1. α-Cosymplectic Manifold with Vanishing $*$-Weyl Curvature Tensor

Theorem 3. *An α-cosymplectic manifold with vanishing $*$-Weyl curvature tensor is an η-Einstein manifold.*

Proof. Let us consider an α-cosymplectic manifold M with vanishing $*$-Weyl curvature tensor, that is, $\mathscr{W}^*(E_1,E_2)E_3 = 0$. Thus, (43) infers that

$$\mathscr{W}(E_1,E_2)E_3 = \frac{2(n-1)\alpha^2}{2n-1}\{g(E_2,E_3)E_1 - g(E_1,E_3)E_2\} + \frac{\alpha^2}{2n-1}\{\eta(E_2)\eta(E_3)E_1 - \eta(E_1)\eta(E_3)E_2 + g(E_2,E_3)\eta(E_1)\xi - g(E_1,E_3)\eta(E_2)\xi\}. \tag{44}$$

Covariant differentiation of above relation along E_4 and then contracting the resultant equation over E_4 yields

$$\begin{aligned}\operatorname{div}\mathscr{W}(E_1,E_2)E_3 = {} & 2(n-1)\alpha^3\{g(E_1,E_3)\eta(E_2)\\ & -g(E_2,E_3)\eta(E_1)\},\end{aligned} \tag{45}$$

where "div" denotes the divergence. On the other side, differentiating $\mathscr{W}$ covariantly along E_4 and then contracting with the aid of following well-known formulas,

$$\begin{aligned}\operatorname{div}R(E_1,E_2)E_3 &= g\left(\left(\nabla_{E_1}Q\right)E_2,E_3\right)-g\left(\left(\nabla_{E_2}Q\right)E_1,E_3\right),\\ \operatorname{div}QE_1 &= \frac{1}{2}E_1(r),\end{aligned} \tag{46}$$

we easily obtain

$$\operatorname{div}\mathscr{W}(E_1,E_2)E_3 = \frac{2(n-1)}{2n-1}\left\{g\left(\left(\nabla_{E_1}Q\right)E_2,E_3\right)-g\left(\left(\nabla_{E_2}Q\right)E_1,E_3\right)\right\}-\frac{(n-1)}{2n(2n-1)}\{g(E_2,E_3)E_1(r)-g(E_1,E_3)E_2(r)\}. \tag{47}$$

By virtue of (45) and (47), we have

$$\begin{aligned}\frac{2(n-1)}{2n-1}\left\{g\left(\left(\nabla_{E_1}Q\right)E_2,E_3\right)-g\left(\left(\nabla_{E_2}Q\right)E_1,E_3\right)\right\} &= 2(n-1)\alpha^3\{g(E_1,E_3)\eta(E_2)-g(E_2,E_3)\eta(E_1)\}\\ &+\frac{(n-1)}{2n(2n-1)}\{g(E_2,E_3)E_1(r)-g(E_1,E_3)E_2(r)\}.\end{aligned} \tag{48}$$

Replacing E_2 by ξ in (48), we obtain

$$\begin{aligned}\frac{2(n-1)}{2n-1}\left\{g\left(\left(\nabla_{E_1}Q\right)\xi,E_3\right)-g\left(\left(\nabla_{\xi}Q\right)E_1,E_3\right)\right\} &= 2(n-1)\alpha^3\{g(E_1,E_3)-\eta(E_1)\eta(E_3)\}\\ &+\frac{(n-1)}{2n(2n-1)}\{\eta(E_3)E_1(r)-g(E_1,E_3)\xi(r)\}.\end{aligned} \tag{49}$$

Recalling Lemma 1 to find

$$\frac{2(n-1)}{2n-1}\alpha\left\{g(QE_1,E_3)+\alpha^2 g(E_1,E_3)\right\}+2(n-1)\alpha^3\eta(E_1)\eta(E_3)=\frac{n-1}{2n(2n-1)}\{\eta(E_3)E_1(r)-g(E_1,E_3)\xi(r)\}. \tag{50}$$

Writing ξ instead of E_3 by ξ in the foregoing equation and by making use of (11), we derive

$$X(r)=\xi(r)\eta(E_1). \tag{51}$$

Making use of this equation in (50) yields

$$\alpha g(QE_1,E_3)=-\left[\alpha^3+\frac{1}{4n}\xi(r)\right]g(E_1,E_3)+\left[-(2n-1)\alpha^3+\frac{1}{4n}\xi(r)\right]\eta(E_1)\eta(E_3). \tag{52}$$

Using (14) in (52), we get

$$S(E_1, E_3) = \left\{2n\alpha^2 + \frac{r}{2n}\right\} g(E_1, E_3) + \left\{-4n\alpha^2 - \frac{r}{2n}\right\} \eta(E_1)\eta(E_3). \tag{53}$$

This proves our result. □

Substituting (53) in (25), we have

$$S^*(E_1, E_3) = \gamma\{g(E_1, E_3) - \eta(E_1)\eta(E_3)\}, \tag{54}$$

where $\gamma = (1/2n) + (4n-1)\alpha^2$ shows that M is $*-\eta$-Einstein. In view of (3), we obtain

$$S^*(E_1, E_3) = \left[\frac{r}{2n} + (4n-1)\alpha^2\right] g^{\phi}(E_1, E_3), \quad E_1, E_3 \in TM. \tag{55}$$

Thus, $S^* = S^{\phi}$, and hence, it is weak ϕ-Einstein. Thus, we state the following.

Theorem 4. *An α-cosymplectic manifold with vanishing $*$-Weyl curvature tensor is a weak ϕ-Einstein manifold.*

4.2. α-Cosymplectic Manifold Satisfying the Condition $R(X,Y)\cdot\mathscr{W}^* = 0$. An α-cosymplectic manifold M is called semisymmetric if its curvature tensor satisfies the condition $R \cdot R = 0$. In [24], Szabo studied the intrinsic classification of semisymmetric spaces thoroughly. In this context, Venkatesha and Kumara [21] studied Sasakian manifolds satisfying condition $R(E_1, E_2)\cdot\mathscr{W}^* = 0$. In this section, we make an attempt to study this condition in the framework of α-cosymplectic manifolds and prove the following.

Theorem 5. *An α-cosymplectic manifold satisfying the condition $R(E_1, E_2)\cdot\mathscr{W}^* = 0$ is an η-Einstein manifold.*

Proof. Let M be an $(2n+1)$-dimensional α-cosymplectic manifold satisfying the condition $(R(E_1, E_2)\cdot\mathscr{W}^*)(U,V)E_4 = 0$. This infers that

$$R(E_1, E_2)\mathscr{W}^*(U,V)E_4 - \mathscr{W}^*(R(E_1, E_2)U, V)E_4 - \mathscr{W}^*(U, R(E_1, E_2)V)E_4 - \mathscr{W}^*(U,V)R(E_1, E_2)E_4 = 0. \tag{56}$$

Plugging ξ in place of E_1 in the previous equation and then picking inner product with ξ for the resultant equation, we obtain

$$\eta(R(\xi, E_2)\mathscr{W}^*(U,V)E_4) - \eta(\mathscr{W}^*(R(\xi, E_2)U, V)E_4) - \eta(\mathscr{W}^*(U, R(\xi, E_2)V))E_4 - \eta(\mathscr{W}^*(U,V)R(\xi, E_2)E_4) = 0. \tag{57}$$

In view of (9), it follows from (56) that

$$\alpha^2 \left\{ \begin{array}{c} \mathscr{W}^*(U,V,E_4,E_2) - g(E_2,U)\eta(\mathscr{W}^*(\xi,V)E_4) - \eta(\mathscr{W}^*(U,V)E_4)\eta(E_2) \\ -g(E_2,V)\eta(\mathscr{W}^*(U,\xi)E_4) + \eta(U)\eta(\mathscr{W}^*(E_2,V)E_4) + \eta(V)\eta(\mathscr{W}^*(U,E_2)E_4) \\ -g(E_2,E_4)\eta(\mathscr{W}^*(U,V)\xi) + \eta(E_4)\eta(\mathscr{W}^*(U,V)E_2) \end{array} \right\} = 0. \tag{58}$$

Replacing E_2 by U in the above equation, we have

$$\mathscr{W}^*(U,V,E_4,U) - g(U,U)\eta(\mathscr{W}^*(\xi,V)E_4) - g(U,V)\eta(\mathscr{W}^*(U,\xi)E_4) + \eta(E_4)\eta(\mathscr{W}^*(U,V)U) = 0, \tag{59}$$

provided $\alpha^2 \neq 0$. By virtue of (43), one can easily see that

$$\eta(\mathscr{W}^*(E_1,E_2)E_3) = -\frac{1}{2n-1}\{g(QE_2,E_3)\eta(E_1) - g(QE_1,E_3)\eta(E_2)\} + \left[\frac{r}{2n(2n-1)} - \frac{2(n-1)}{2n-1}\alpha^2\right] \{g(E_2,E_3)\eta(E_1) - g(E_1,E_3)\eta(E_2)\}, \eta(\mathscr{W}^*(E_1,E_2)\xi) = 0, \tag{60}$$

$$\eta(\mathscr{W}^*(E_1,\xi)E_3) = \frac{1}{2n-1}g(QE_1,E_3) + \frac{1}{2n-1}\left[2(n-1)\alpha^2 - \frac{r}{2n}\right]g(E_1,E_3) + \frac{1}{2n-1}\left[\frac{r}{2n} + 2\alpha^2\right]\eta(E_1)\eta(E_3), \tag{61}$$

$$\sum_{i=1}^{2n+1}\mathscr{W}^*(e_i,E_2,E_3,e_i) = -(2n-1)\alpha^2 g(E_2,E_3) - \alpha^2\eta(E_2)\eta(E_3), \tag{62}$$

where $\{e_i\}_{i=1}^{2n+1}$ is an orthonormal basis of the tangent space at any point of the manifold. Taking $U = e_i$ in (59) and summing over i and making use of (56)–(61), we get

$$S(V,E_4) = \frac{1}{2n}\left\{r + \alpha^2\right\}g(V,E_4) - \frac{1}{2n}\left\{r + \left(4n^2+1\right)\alpha^2\right\}\eta(V)\eta(E_4). \tag{63}$$

This completes the proof. □

5. α-Cosymplectic Manifolds Admitting $*$-Ricci Solitons

Hamilton [25] introduced the notion of Ricci solitons as fixed points of the Ricci flows on a Riemannian manifold, and they are also self-similar solutions. These self-similar solutions also generalize Einstein metrics. Ricci solitons also correspond to self-similar solutions of Hamilton's Ricci flow. A Ricci soliton with a potential vector field V is defined by

$$(E_V g)(E_1,E_2) + 2S(E_1,E_2) + 2\lambda g(E_1,E_2) = 0, \tag{64}$$

for some constant λ. The Ricci soliton is said to be shrinking, steady, and expanding accordingly as λ is negative, zero, and positive, respectively. The study of Ricci solitons and almost Ricci solitons on three-dimensional cosymplectic manifolds have been carried out by Wang [26] and De and Dey [27], respectively.

By taking the necessary modification (64), Kaimakamis and Panagiotidou [28] introduced the notion of a special type of metric called $*$-Ricci soliton on real hypersurfaces of nonflat complex space forms. A Riemannian metric g on M is called $*$-Ricci soliton, if the Lie derivative of a vector field V on M is given by

$$(E_V g)(E_1,E_2) + 2S^*(E_1,E_2) + 2\lambda g(E_1\cdot E_2) = 0, \forall E_1,E_2 \in TM. \tag{65}$$

Recently, the study of $*$-Ricci solitons within the context of almost contact and paracontact manifolds were carried out in the studies [18, 29–34] and drawn several interesting results. In this section, we intended to $*$-Ricci soliton on a α-cosymplectic manifold. Now, we prove the following result.

Theorem 6. *Let M be α-cosymplectic manifold admitting a $*$-Ricci soliton. If the potential vector field V is pointwise collinear with ξ, then M is a near quasi-Einstein manifold.*

Proof. Let V be a pointwise collinear vector field with ξ. Then, we have $V = b\xi$. From (7) and (65), we derive

$$\begin{aligned}(E_V g)(E_1,E_2) &= g\left(\nabla_{E_1}V,E_2\right) + g\left(\nabla_{E_2}V,E_1\right)\\ &= E_1(b)\eta(E_2) + E_2(b)\eta(E_1) + 2b\alpha\{g(E_1,E_2) - \eta(E_1)\eta(E_2)\}.\end{aligned} \tag{66}$$

Let M be an α-cosymplectic manifold admitting a $*$-Ricci soliton. Then, from (61) and (62), we obtain

$$S^*(E_1,E_2) = -\{\lambda + b\alpha\}g(E_1,E_2) + b\alpha\eta(E_1)\eta(E_2) - \frac{1}{2}\{E_1(b)\eta(E_2) + E_2(b)\eta(E_1)\}. \tag{67}$$

Let Db be a gradient of smooth function b on M, that is, $E_1(b) = g(Db, E_1)$ and $E_2(b) = g(Db, E_2)$. Then, by denoting the dual form of Db by v, we write

$$\begin{aligned} E_1(b) &= v(E_1), \\ E_2(b) &= v(E_2). \end{aligned} \tag{68}$$

By taking account of foregoing equations in (67), we get

$$S^*(E_1, E_2) = -\{\lambda + b\alpha\} g(E_1, E_2) + b\alpha\eta(E_1)\eta(E_2) - \frac{1}{2}\{v(E_1)\eta(E_2) + v(E_2)\eta(E_1)\}. \tag{69}$$

Then, from (25), equation (65) reduces to

$$S(E_1, E_2) = -\left\{\lambda + b\alpha + (2n-1)\alpha^2\right\} g(E_1, E_2) + \left\{b\alpha - \alpha^2\right\}\eta(E_1)\eta(E_2) - \frac{1}{2}\{v(E_1)\eta(E_2) + v(E_2)\eta(E_1)\}. \tag{70}$$

Let us take a nonvanishing symmetric $(0,2)$ tensor E in (66), such that

$$\begin{aligned} S(E_1, E_2) = &\left\{b\alpha - \alpha^2\right\}\eta(E_1)\eta(E_2) - \frac{1}{2}\{v(E_1)\eta(E_2) \\ &+ v(E_2)\eta(E_1)\}. \end{aligned} \tag{71}$$

Then, equation (66) yields

$$S(E_1, E_2) = ag(E_1, E_2) + E(E_1, E_2), \tag{72}$$

where $a = -\{\lambda + b\alpha + (2n-1)\alpha^2\}$. So, M is a near quasi-Einstein. □

As an immediate outcome of Theorem 6, we have the following corollary.

Corollary 4. *An α-cosymplectic manifold admitting a $*$-Ricci soliton is an η-Einstein manifold if $V = \xi$.*

A near quasi-Einstein manifold is not a manifold of nearly quasiconstant curvature. But, it is noted (Theorem 3.1 of [35]) that, a conformally flat near quasi-Einstein manifold is a manifold of nearly quasiconstant curvature. Hence, as immediate consequence of this fact, we obtain the following corollary:

Corollary 5. *A conformally flat α-cosymplectic manifold admitting a $*$-Ricci soliton is a manifold of near quasi-constant curvature if V is a pointwise collinear with ξ.*

However, since a 3-dimensional Riemannian manifold is conformally flat, we have following.

Corollary 6. *A 3-dimensional α-cosymplectic manifold admitting $*$-Ricci soliton is a manifold of nearly quasiconstant curvature if V is a pointwise collinear with ξ.*

6. Conclusions

Einstein manifolds which are arisen from Einstein field equations are very important classes of Riemann manifolds. Some generalizations of Einstein manifolds have been defined in the literature, and there have been obtained some applications of these kinds of manifolds in theoretical physics. Contact manifolds are special Riemann manifolds with almost contact structures. In theoretical physics, there are valuable applications of contact manifolds. Contact manifolds divided into many subclasses via the certain properties of the structure. An important one is α-cosymplectic manifold. This structure is also a generalization of some different contact structures. Many different characteristic properties of manifolds with structures have been arisen from their special structures. One of important notion is the $*$-Ricci tensor. This notion carries significant curvature features, and this feature gives valuable information about the geometry of the manifold. In this study, α-cosymplectic manifolds have been examined under the effect of the $*$-Ricci tensor. Important results have been obtained on some generalized Einstein manifolds, which emerged with the effect of the $*$-Ricci tensor. The notion of Ricci soliton comes from searching the solutions of Ricci flow equations. Ricci solitons have been effected from the structure of manifolds. We studied the concept of $*$-Ricci soliton for α-cosymplectic manifolds. By the way, important physical results have been stated in this study.

Data Availability

No data were used to support this study.

Conflicts of Interest

The authors declare that they have no conflicts of interest.

Authors' Contributions

M.R.A., D.G.P, N.B.T, and I.U. conceptualized the study, developed methodology, performed formal analysis. D.G.P., N.B.T., and I.U. wrote the original draft. M.R.A. and N.B.T. reviewed and edited the article. M.R.A., D.G.P., and I.U. supervised the study. D.G.P. administered the project. A.M.R. and N.B.T acquired fund .

Acknowledgments

This project was supported by the researchers supporting project number (RSP2022R413), King Saud University, Riyadh, Saudi Arabia. The first author M. R. Amruthalakshmi (MRA) is thankful to Department of Science and Technology, Ministry of Science and Technology, Government of India, for providing DST INSPIRE Fellowship (No: DST/INSPIRE Fellowship/(IF 190869)).

References

[1] S. I. Goldberg and K. Yano, "Integrability of almost cosymplectic structure," *Pacific Journal of Mathematics*, vol. 31, pp. 373–381, 1969.

[2] M. A. Akyol, "Conformal anti- invariant submersions from cosymplectic manifolds," *Hacettepe Journal of Mathematics and Statistics*, vol. 46, no. 2, pp. 177–192, 2017.

[3] G. Ayar and S. K. Chaubey, "M-$M-$ projective curvature tensor over cosymplectic manifolds," *Differential Geometry—Dynamical Systems*, vol. 21, pp. 23–33, 2019.

[4] S. Beyendi, G. Ayar, and G. N. Atkan, "On a type of $\alpha-$ cosymplectic manifolds," *Communications Faculty of Sciences University of Ankara Series A1 Mathematics and Statistics*, vol. 68, pp. 852–861, 2019.

[5] Z. Olszak, "On almost cosymplectic manifolds," *Kodai Mathematical*, vol. 4, no. 2, pp. 239–250, 1981.

[6] S. Tachibana, "On almost-analytic vectors in almost Kahlerian manifolds," *Tohoku Mathematical Journal*, vol. 11, pp. 247–265, 1959.

[7] T. Hamada, "Real hypersurfaces of complex space forms in terms of Ricci $*-$ tensor," *Tokyo Journal of Mathematics*, vol. 25, pp. 473–483, 2002.

[8] T. A. Ivey and P. J. Ryan, "The $*-$ Ricci tensor for hypersurfaces in $\mathbb{C}P^n$ and $\mathbb{C}H^n$," *Tokyo Journal of Mathematics*, vol. 34, pp. 445–471, 2011.

[9] H. Venkatesha and K. Aruna, *Sasakian Manifold and $*-$ Ricci Tensor*, https://arxiv.org/abs/1807.10541, 2018.

[10] A. K. Huchchappa, D. M. Naik, and V. Venkatesha, "Certain results on contact metric generalized $(\kappa, \mu)(\kappa, \mu)$-space forms," *Communications of the Korean Mathematical Society*, vol. 34, no. 4, pp. 1315–1328, 2019.

[11] D. E. Blair, "Contact manifolds in riemannian geometry," *Lecture Notes in Mathematics*, Springer-Verlag, vol. 509, Berlin, Germany, , 1976.

[12] D. E. Blair, "Riemannian geometry of contact and symplectic manifolds," *Progress in Mathematics*, Vol. 203, Birkhauser Boston, Inc., Boston, MA, USA, 2nd edition, 2010.

[13] B. Cappelletti-Montano, A. de Nicola, and I. Yudin, "A Survey on cosymplectic geometry," *Reviews in Mathematical Physics*, vol. 25, no. 10, Article ID 1343002, 2013.

[14] T. W. Kim and H. K. Pak, "Canonical foliations of certain classes of almost contact metric structures," *Acta Mathematica Sinica, English Series*, vol. 21, no. 4, pp. 841–846, 2005.

[15] K. Yano and M. Kon, *Structure on Manifold*, Vol. 3, World Scientific Publishing, , Singapore, 1984.

[16] J. T. Cho and J.-i. Inoguchi, "On $${{\varphi}}$$ -Einstein contact riemannian manifolds," *Mediterranean Journal of Mathematics*, vol. 7, no. 2, pp. 143–167, 2010.

[17] U. C. De and A. K. Gazi, "On nearly quasi-Einstein manifolds," *Novi Sad Journal of Mathematics*, vol. 38, no. 2, pp. 115–121, 2008.

[18] Y. Wang, "Contact 3-manifolds and $**$-Ricci soliton," *Kodai Mathematical Journal*, vol. 43, no. 2, pp. 256–267, 2020.

[19] A. Haseeb, D. G. Prakasha, and H. Harish, "$*-$Conformal $\eta-$Ricci solitons on $\alpha-$Cosymplectic manifolds," *International Journal of Analysis and Applications*, vol. 19, no. 2, pp. 165–179, 2021.

[20] V. A. Mirjoyan, "Structure theorems for Riemannian Ricci semisymmetric spaces," *Izvestiya Vysshikh Uchebnykh Zavedenii, Matematika*, vol. 6, pp. 80–89, 1992.

[21] V. Venkatesha and H. A. Kumara, "$*$-Weyl curvature tensor within the framework of sasakian and (κ,μ)-Contact manifolds," *Tamkang Journal of Mathematics*, vol. 52, 2021.

[22] M. Kon, "Invariant submanifolds in Sasakian manifolds," *Mathematische Annalen*, vol. 219, no. 3, pp. 277–290, 1976.

[23] G. Kaimakamis and K. Panagiotidou, "On a new type of tensor on real hypersurfaces in non-flat complex space forms," *Symmetry*, vol. 11, no. 4, p. 559, 2019.

[24] Z. I. Szabo, "Structure theorems on Riemannian spaces satisfying $R(X,Y)\ R{=}0R(X,Y)\cdot R=0$, I. the local version," *Journal of Differential Geometry*, vol. 17, no. 4, pp. 531–582, 1982.

[25] R. S. Hamilton, "The Ricci flow on surfaces," *Mathematics and General Relativity*, vol. 71, pp. 237–262, 1988.

[26] Y. Wang, "Ricci solitons on 3-dimensional cosymplectic manifolds," *Mathematica Slovaca*, vol. 67, no. 4, pp. 979–984, 2017.

[27] U. C. De and C. Dey, "On three dimensional cosymplectic manifolds admitting almost Ricci solitons," *Tamkang Journal of Mathematics*, vol. 51, no. 4, pp. 303–312, 2020.

[28] G. Kaimakamis and K. Panagiotidou, "$*$-Ricci solitons of real hypersurfaces in non-flat complex space forms," *Journal of Geometry and Physics*, vol. 86, pp. 408–413, 2014.

[29] D. G. Prakasha and P. Veeresha, "Para-Sasakian manifolds and $*$-$*-$ Ricci solitons," *Afrika Matematika*, vol. 30, pp. 989–998, 2018.

[30] A. Ghosh and D. S. Patra, "$*$-Ricci Soliton within the framework of Sasakian and (κ, μ)-contact manifold," *International Journal of Geometric Methods in Modern Physics*, vol. 15, no. 7, Article ID 1850120, 2018.

[31] X. Dai, Y. Zhao, and U. C. De, "$*$- Ricci soliton on (κ, μ)-$(\kappa, \mu)-$ almost Kenmotsu manifolds," *Open Mathematics*, vol. 17, pp. 874–882, 2019.

[32] X. Dai, "Non-existence of $$*$$-Ricci solitons on $$(\kappa ,\mu)$$-almost cosymplectic manifolds," *Journal of Geometry*, vol. 110, no. 2, p. 30, 2019.

[33] D. M. Venkatesha, H. Naik, D. M. Naik, and H. A. Kumara, "$*$-Ricci solitons and gradient almost $*$-Ricci solitons on Kenmotsu manifolds," *Mathematica Slovaca*, vol. 69, no. 6, pp. 1447–1458, 2019.

[34] V. Venkatesha, H. A. Kumara, and D. M. Naik, "Almost $$*$$-Ricci soliton on paraKenmotsu manifolds," *Arabian Journal of Mathematics*, vol. 9, no. 3, pp. 715–726, 2020.

[35] D. G. Prakasha and C. S. Bagewadi, "On nearly quasi-Einstein manifolds," *Mathematica Pannonica*, vol. 21, no. 2, pp. 265–273, 2010.